UAB
Universitat Autònoma de Barcelona

Eulàlia Nicolau Jiménez

Ultracold atoms in coupled ring potentials and flat-band lattices

Thesis supervisor:

Prof. Verònica Ahufinger Breto

Submitted in fulfillment of the requirements
for the degree of Doctor of Physics

Departament de Física
Universitat Autònoma de Barcelona

Bellaterra, September 2023

Als meus pares,
per l'educació que m'heu donat.

Reserve your right to think, for even to think
wrongly is better than not to think at all.

— HYPATIA OF ALEXANDRIA

ACKNOWLEDGMENTS

Although I find one thesis more than enough for a lifetime, it has been a wonderful ride thanks to the people that have accompanied me along the way.

First and foremost, this thesis would not exist without the careful guidance of Verònica Ahufinger. I met Verònica ten years ago when I was an eager undergraduate student starting the first year of the physics degree. I distinctly remember how, when I asked her to collaborate on some research project, she accepted even before I was able to build my case. From then on, Verònica has never doubted my ability to become a researcher and has done everything in her power to make that a reality. During my undergraduate studies, I learned by her side the joy of scientific research, while at the same time I discovered my preference for the abstract world of theoretical physics. Thanks to her I have learned not only a great deal of physics, but also the many skills that one requires to become a researcher: how to ask questions, how to write articles (through countless corrections that thankfully decreased with the years!), how to present results and, last but not least, to trust myself and my physical intuitions. You are the main reason today I call myself a physicist.

This thesis has also been marked by the incredibly fruitful collaboration with Anselmo Marques and Ricardo Dias. During my stay in Portugal, they welcomed me into their group and made me feel like one of their team. They introduced me to the field of topology in ultracold lattice gases, which allowed me to expand my physics background in a new direction and access a different line of research. I am especially grateful to Anselmo, with whom I had the pleasure to share the thrill and excitement of research through our many discussions about physics. I look forward to keep working with you.

To Jordi Mompart, who accompanied me through the first stages of my thesis, I thank his time, absolute faith in my work, and constant encouragement. I am also grateful to Bruno Juliá-Díaz, who kindly shared his expertise on Josephson oscillations and self-trapping. Also, I am indebted to David Marín and Armengol Gasull for their insights and discussion on mathematical topics that allowed me to further some of my works.

I am very thankful to Gerard Pelegrí and Joan Polo, from whom I inherited their line of research on ring potentials. My start in the field was smooth thanks to their patience in responding to my many questions about physics and numerical simulations. I am also grateful to Hong Yang, with whom I had the pleasure to coincide in the Boulder summer school, as our discussions eventually led me to the fascinating field of non-ergodic phenomena.

My journey into the world of science started many years before the PhD, through the

program Joves i Ciència of Fundació Catalunya La Pedrera, which gave me a first taste of the joy of discovery and understanding. I am especially thankful to Pelayo García de Arquer, Alejandra Valencia, and Zach Wissner-Gross for their role in that process.

I am grateful to all the QAOS family and the senior and junior members of the optics group for providing a nice and friendly environment in which to work. In particular, I am grateful to David Viedma for our discussions on photonic lattices, and to my other office colleagues, Josep Cabedo, Chris Hensel, Gerard Queraltó, and Gerard Pelegrí, for making the PhD student life a very positive experience.

I am thankful to Profs. Thomas Busch and Simon Gardiner for their encouraging and careful reports of this thesis, as well as to Profs. Anna Sanpera, Anna Minguzzi, and Matteo Rizzi for agreeing to take on the role of thesis committee. In addition, I would like to thank Prof. Maksym Serbyn for offering me a postdoc position, so that I can continue doing this peculiar job in which one is paid to learn.

I would like to thank all the people who have accompanied me through these four years from the outside of the academic world. I am thankful for my friends Queralt, Víctor, Marta, Silvia, and Eric, for filling my life with another dimension. To Marisa and Javier, for welcoming me into their family and taking care of me as one of their own. To Òscar, for giving me the opportunity to break free of the rational world of science and step with me into the music.

Finally, I owe my deepest gratitude to my family, Adriana, Maite, and Marcel, for their unconditional and loving support. I am grateful to my sister Adriana for her advice from the other side of the diploma. To my father Marcel, for our many discussions about physics, mathematics, and the intricacies of the academic world. To my mother Maite, for the constant logistical and emotional support, her encouragement and, of course, for her delicious and nutritious food.

And I am grateful to you, Maria, for making physics only one of the many things I learned during these four years.

Eulàlia Nicolau Jiménez
September of 2023

Contents

LIST OF PUBLICATIONS

The research contained in this thesis is supported by the following publications:

Chapter 3: Orbital angular momentum dynamics of Bose-Einstein condensates trapped in two stacked rings

1. Eulàlia Nicolau, Jordi Mompart, Bruno Juliá-Díaz, and Verònica Ahufinger, *Orbital angular momentum dynamics of Bose-Einstein condensates trapped in two stacked rings*, Physical Review A, **102**, 023331 (2020).

Chapter 4: Bosonic orbital Su-Schrieffer-Heeger model in a lattice of rings

2. Eulàlia Nicolau, Anselmo M. Marques, Jordi Mompart, Ricardo G. Dias, Verònica Ahufinger, *Bosonic orbital Su-Schrieffer-Heeger model in a lattice of rings*, Physical Review A, **108**, 023317 (2023).

Chapter 5: Many-body Aharonov-Bohm caging in a lattice of rings

3. Eulàlia Nicolau, Anselmo M. Marques, Ricardo G. Dias, Jordi Mompart, Verònica Ahufinger, *Many-body Aharonov-Bohm caging in a lattice of rings*, Physical Review A, **107**, 023305 (2023).

Chapter 6: Local Hilbert space fragmentation in bosonic flat-band lattices

4. Eulàlia Nicolau, Anselmo M. Marques, Jordi Mompart, Verònica Ahufinger, Ricardo G. Dias, *Local Hilbert space fragmentation and weak thermalization in Bose-Hubbard diamond necklaces*, Physical Review B, **107**, 094312 (2023).

5. Eulàlia Nicolau, Anselmo M. Marques, Ricardo G. Dias, Verònica Ahufinger, *Flat-band induced local Hilbert space fragmentation*, arXiv:2306.15660 (2023, under revision in Physical Review B).

LIST OF ACRONYMS

AQUID	Atomtronic quantum interference device
BEC	Bose-Einstein condensate
CLS	Compact localized state
EPT	Equitable partition theorem
ETH	Eigenstate thermalization hypothesis
FSM	Four-state model
GPE	Gross-Pitaevskii equation
IQHE	Integer quantum Hall effect
LIOM	Quasi-local integral of motion
MBL	Many-body localization
NN	Nearest-neighbor
OAM	Orbital angular momentum
QMBS	Quantum many-body scars
SQUID	Superconducting quantum interference device
SSH	Su-Schrieffer-Heeger
SSM	Six-state model
TSM	Two-state model

1

PREFACE

Since the first experimental realization of a Bose-Einstein condensate (BEC) in 1995 [1–3], predicted by A. Einstein 70 years earlier, the study of BECs has constituted a whole new field of physics. S. N. Bose developed a statistical description of photons to derive Planck's law of black-body radiation in 1924 [4], which Einstein generalized to massive bosons and used to predict their condensation into the ground state in the absence of interactions [5, 6]. At first, Bose-Einstein condensation was believed to be a pathological behavior of an ideal gas, which would be prevented by interatomic interactions, until 1938, when London suggested Bose-Einstein condensation as the cause for superfluidity in liquid helium [7]. However, the connection was uncertain, as the condensate fraction of helium was very low due to its strong interatomic interactions. After many advances in the techniques of cooling and trapping of atoms [8], which earned S. Chu, C. Cohen-Tannoudji, and W. D. Phillips a Nobel Prize in 1997, Bose-Einstein condensation of a weakly interacting gas was achieved in 1995 [1–3], earning E. A. Cornell, C. E. Wieman, and W. Ketterle a Nobel Prize in 2001.

In a BEC, a bosonic gas at very low temperatures presents a macroscopic population of the ground state, i.e., almost all particles occupy the same quantum state, and therefore exhibit a high degree of coherence. Because of the large population of the ground state and its long-range coherence, a Bose-Einstein condensate constitutes a giant matter wave, which exhibits macroscopic quantum effects. Besides more common quantum effects as interference patterns, demonstrated in [9], BEC presents features such as superfluidity, which enable, for instance, the existence of persistent currents in toroidal traps [10] or the formation of vortices [11], and nonlinearity, which drives the formation of solitons [12–15]. Since the first experimental realization of a BEC, further advances in cooling techniques made possible the condensation of Cooper pairs, thus reaching the quantum degenerate regime for fermionic gases [16–18].

The field of ultracold gases permeated into condensed matter physics when strongly correlated regimes were achieved through the use of optical lattices. In these systems, laser beams generate conservative dipole forces [19] that create a periodic potential where quantum tunneling effects compete with interatomic interactions. The transition from a superfluid, where tunneling effects dominate, to a Mott insulator, a phase ruled by interactions, was predicted [20, 21] and experimentally observed in a ultracold bosonic gas in 2002 [22]. The

appeal of ultracold lattice gases as an experimental platform is the high degree of controllability [23, 24]. The interactions in each site are governed by the s-wave scattering length, which can be modified through either optical [25–27] or magnetic [28–30] Feshbach resonances by harnessing excited molecular states. Long-range interactions are also within reach through the use of dipolar gases [31–33]. Also, one can achieve almost any desired lattice geometry by adjusting the parameters of the lasers, such as their direction, intensity, or frequency. For example, one can produce from simple cubic and square lattices to more complex geometries such as triangular [34], hexagonal [35], or kagome [36]. In addition, one can reduce the dimensionality to one or two dimensions by means of the optical lattice or by introducing additional potentials that freeze the dynamics in one or two axes [37].

As a result of their high tunability, ultracold lattice gases are a excellent candidate for quantum simulation [23, 24, 38], an idea originally envisioned by Feynman [39]. Classical simulation of a quantum system quickly becomes unfeasible for relatively small system sizes and particle numbers (even in state-of-the-art supercomputers) due to the rapid growth of the Hilbert space. Instead, one can use a quantum system to simulate another, such that the number of resources required to simulate the system scales linearly with its size instead of exponentially. The simulator must be a simpler quantum system with an analogous Hamiltonian that has highly controllable parameters and that is easy to measure. For example, ultracold fermions in an optical lattice described by the Fermi-Hubbard model are believed to serve as a quantum simulator of high temperature superconductivity [40]. However, one can take this idea a step further and ask: what phenomena are allowed by the laws of quantum mechanics? Ultracold lattice gases can also tackle this question with their capability to generate almost on-demand Hamiltonians. They have served to predict theoretically new exotic quantum phases that have later been reproduced experimentally and also allowed to design quantum systems without a parallel in nature [41–44].

A particularly important application of quantum simulation is the study of topological phases, which do not fit within the celebrated Landau-Ginzburg paradigm [45]. This highly successful theory describes phase transitions by expanding the free energy near the transition point in terms of a local order parameter. The generality of this formalism makes it applicable to a broad range of phase transitions, from the phase transitions of water to those of magnetic materials. The underlying principle behind these processes is symmetry breaking, which can be detected through the expectation value of the order parameter. Let us take for example the paramagnet to ferromagnet phase transition. As the temperature is lowered below the Curie temperature, the material acquires a non-zero magnetization as all the spins spontaneously align in a random direction, thus breaking rotational symmetry [46]. The main limitation of Landau's theory is the locality of the order parameter, which, in the case of the ferromagnet transition, is the local magnetization. Some phases cannot be distinguished by a local order parameter, rather, it is their global features that change from one phase to the other. These are known as topological phases, as their description relies on the mathematical field of topology, which deals with the global properties of geometrical objects that do not change under continuous deformations [47]. In this context, two objects are topologically equivalent when they can be continuously deformed into one another by twisting or bending them and are distinguished

from other topological classes by a topological invariant. In analogy, topological invariants also characterize physical systems, which take distinct values for different topological phases.

The observation of the integer quantum Hall effect (IQHE), a topological phase, marked a turning point in condensed matter physics [48]. For a cold two-dimensional electron gas pierced by a strong magnetic field, the Hall conductance exhibits quantized plateaus as a function of the magnetic field. The effect was understood through the Harper-Hofstadter model [49, 50], which describes spinless fermions in a square lattice, by Thouless, Kohmoto, Nightingale, and den Nijs [51]. The phases with a quantized Hall conductance are not characterized by a local order parameter (a continuous number), but correspond to the change in the Chern number (an integer) that characterizes the bulk of the material. This topological invariant predicts the presence of conducting edge states when the material has open boundary conditions, a connection known as the bulk-boundary correspondence. The IQHE turned out to be an example of a topological insulator, a material that is insulating in the bulk but conducting at the boundary. While it was originally thought that a magnetic field was required to obtain this type of phenomenology, Haldane showed through the anomalous quantum Hall effect that the breaking of time-reversal symmetry, even in the absence of a magnetic field, was sufficient [52]. Much later, Kane and Mele demonstrated that systems with time-reversal symmetry could also present topological phases through the study of graphene and the quantum spin-Hall effect [53]. All these results eventually crystallized into *The ten-fold way*, a classification of topological insulators and superconductors into ten classes in terms of their dimensionality and the time-reversal, particle-hole, and chiral symmetries [54, 55]. Far from leaving this field stale, the study of topological insulators has flourished since this result, as many topological phases have been found to escape this classification. For instance, crystalline symmetries can stabilize topological phases that would otherwise be trivial according to the previous classification, which leads to a much more nuanced and rich categorization [56]. Other types of topological phases have been discovered since, including Weyl semimetals [57], topological Anderson insulators [58] or floquet topological insulators [59], while many questions remain open, such as the effect of interactions on free-fermion topological phases [60]. These questions can be effectively tackled in ultracold lattice gases by using, for instance, synthetic dimensions [61, 62] or artificial gauge fields that simulate magnetic fluxes [63–65]. Using these and other techniques, many topological phases have been realized in this environment [66], including, for example, the Haldane [67] and the Hofstadter models [68–70].

This physical platform is also well-suited to explore out-of-equilibrium many-body dynamics. Instead of focusing on the ground state features, one can perform a global quench, i.e., prepare the system in a certain state (the ground state of a certain Hamiltonian), suddenly change the Hamiltonian parameters, and consider the unitary time evolution under the new Hamiltonian. The main question in this field is under which conditions and how does a quantum system out of equilibrium reach a thermal equilibrium state. Ultracold lattice gases present an excellent experimental platform to explore this question, as they are not only highly tunable, but also well isolated from their environment [71]. This feature stimulated a discussion around thermalization in isolated quantum many-body systems, which eventually gave birth to the eigenstate thermalization hypothesis (ETH) [72–74]. The ETH explains

thermalization through the presence of thermal eigenstates, which have microcanonical (i.e., thermal) expectation values for local observables. As a result, the system thermalizes as local observables acquire thermal expectation values. This occurs because the Hilbert space is able to act as a thermal reservoir for its subsystems, which enables the spread of entanglement and the initially local information. There is abundant numerical evidence of the validity of the ETH for a varied array of systems, including hard-core bosons and interacting spin chains [74–80], spinless and spinful fermions [81–84], or soft-core bosons [85–88]. However, not all quantum systems obey this hypothesis. The latter, usually referred to as non-ergodic, avoid thermalization (sometimes completely) by retaining some memory of the initial state even for a long time. For example, integrable systems fail to thermalize due to the presence of an extensive number of conserved quantities that constrain evolution [89] while in many-body localized systems, the interplay between disorder and interactions gives rise to emergent integrability [90]. Although these are fairly well-known examples, this domain has attracted a lot of attention recently with the discovery of quantum many-body scarred systems [91–108]. The non-ergodic behavior in these systems only emerges for some initial states, caused by a vanishing set of eigenstates with an anomalously low entanglement entropy. This phenomenon is closely related to a broader mechanism known as Hilbert space fragmentation, where the system fails to thermalize by virtue of having exponentially-many dynamically disconnected sectors in the Hilbert space [109]. This effect typically appears in constrained systems, such as those conserving the dipole moment or the center of mass [110–115], and, as is the case of scarred systems, the dynamics strongly depend on the initial state. Understanding quantum thermalization and the mechanisms that avoid this process is not only of fundamental interest, but also may result in applications in quantum computation [116, 117], where it is of critical importance to preserve the information of the initial state.

Thermalization is enabled by the exchange of particles and energy between subsystems, which makes localization a natural route to non-ergodic behavior [118]. As first discovered by Anderson, the presence of strong enough disorder localizes single-particle wavefunctions of a periodic medium [119]. The absence of extended states makes the system insulating, which precludes thermalization [118]. However, disorder is not the only route to localization. Electrons in a sufficiently strong magnetic field perform closed orbits that lead to quantized energy levels, effect known as Landau quantization [120]. A similar result can be achieved in an ultracold lattice gas breaking time-reversal symmetry in the absence of an external magnetic field. Within this context, synthetic gauge fields [63, 65] can be engineered to produce Aharonov-Bohm caging, which is characterized by the presence of compact localized states (CLSs) [121, 122]. These eigenstates have compact support on typically few nearby sites while their amplitude is exactly zero on the remainder of the lattice due to destructive interference. Due to the periodicity of the lattice, these eigenstates lead to the presence of flat bands. Alternatively, for an optical lattice with time reversal symmetry, the geometry of the lattice can be arranged to produce the destructive interference that leads to localization [123]. As it is the case with topological insulators, it is not yet well-understood what is the effect of interactions in a flat-band system. The single-particle kinetic energy becomes zero in a flat-band so that interactions have an outsized effect on the properties of the system.

Remarkably, flat-band lattices have been shown to host a variety of non-ergodic behavior, such as isolated quantum many-body scars [124] or disorder-free many-body localization [125, 126], and they have been proposed as candidates for the transfer of quantum states through a quantum network [127].

Interacting ultracold bosons are the leitmotiv of the research described in this thesis; the focus, however, is twofold. The first theme is ring potentials, which exhibit single-particle eigenstates with a well-defined orbital angular momentum (OAM). They play a major role in the developing field of atomtronics, that seeks to devise an alternative to electric circuits using ultracold atoms, while also providing a platform for quantum simulation and quantum technologies [128, 129]. Ring potentials are the simplest geometries that lead to non-trivial loop circuits, where the superfluidity of BECs acquires a fundamental role, allowing for the appearance of persistent currents [10, 130–136] as well as vortices [137]. For instance, they have been used to propose an Atomtronic Quantum Interference Device (AQUID) [138–143], the atomic analog of the superconductor device SQUID [144], that acts as a very precise magnetometer or as a rotation sensor. Another possible application is Sagnac interferometry, which provides rotation sensing through the collision of two solitons [145]. Within this context, we study the OAM states of a BEC trapped in two stacked rings coupled by quantum tunneling. As an alternative, one can also couple multiple coplanar ring potentials [146], which allows one to generate lattices of rings [147]. OAM plays a fundamental role within this platform, as it leads to complex tunneling amplitudes that can be controlled through the geometry of the lattice [147–150]. In this setting, we investigate strong correlated regimes hosting non-trivial topological phases, where interactions play a fundamental role. The second theme of this thesis is flat-band lattices that exhibit single-particle CLSs. We explore how on-site bosonic interactions modify the thermalization properties of the system and in particular we explore the emergence of Hilbert space fragmentation.

We begin this thesis by describing the physical models that we will later use, as well as the underlying theoretical foundations, in Chapter 2. We start with the main concepts behind Bose-Einstein condensation, from the role of quantum statistics to the mean-field description of BECs at zero temperature in terms of the Gross-Pitaevskii equation (GPE). Then, we explain how to generate optical lattices, briefly analyze their single-particle features, and introduce the many-body description by means of the Bose-Hubbard model. Regarding ring trapping potentials, we give an in-depth account of the single-particle problem and then discuss two toy models that allow us to describe arbitrary coplanar lattices of identical rings. To introduce the topic of topology, we revise its main concepts, with a special emphasis on the Berry phase, connection and curvature, and review their application to periodic systems. We also discuss topological insulators and the bulk-boundary correspondence and analyze in detail the Su-Schrieffer-Heeger model. Finally, we discuss thermalization in a classical and a quantum setting, introducing the main ideas of the ETH as well as the main routes to its violation.

In Chapter 3, we study a BEC confined in a two-stacked ring geometry by deriving the evolution equations for the amplitudes of each OAM mode from the GPE equation [151]. This system is governed by the interplay between the OAM, the tunneling between rings, and the repulsive interactions within each ring. Stationary solutions emerge when the two rings have

the same population in a single OAM mode, while self-trapping and Josephson oscillation regimes arise due to an initial population imbalance. However, these stationary solutions and dynamical regimes are not stable against Bogoliubov-type perturbations in higher order modes across the whole parameter space. We develop analytical models for both cases and validate our results through numerical simulations, showing, for instance, that the destabilization of the dynamical regimes are completely analogous to the Bogoliubov excitation dynamics of the stationary states.

In Chapter 4, we consider a one-dimensional lattice of tunnel-coupled ring potentials in a SSH-like configuration, where the local eigenstates with non-zero OAM endow each site with a synthetic dimension [152]. First, we establish the single-particle topological features of the model, which we characterize by performing a basis rotation that resolves the unitary symmetry inherent to the circulation of the OAM states. Then we explore the two-boson problem, where the presence of doublons (pairs of bosons bound by interactions) radically alters the topological phases of the system. We develop analytical models for two regimes: a strong-link model that characterizes the doublon bands in the dimerized regime, and, using perturbation theory for the strongly interacting limit, a model for each doublon subspace which exactly maps to either the single-particle SSH or the Creutz ladder.

In Chapter 5, we increase the complexity of the lattice of rings by introducing a tilting angle [153]. We demonstrate how the geometry of the lattice can be exploited to generate many-body Aharonov-Bohm caging on almost any N-boson subspace, by tuning the tilting angle, and how the extent of the cage can be chosen through the periodicity of this angle. In contrast with the previous lattice of in-line rings, the tunneling amplitudes here can take complex values, which allows one to map the lattice to a Creutz ladder with a synthetic flux. For a π flux, the system exhibits Aharonov-Bohm caging, which is characterized by single-particle CLSs that are induced by destructive interference. For N bosons with on-site interactions, we use perturbation theory to obtain a single-particle effective model for each subspace in the strongly interacting regime.

Chapter 6 also deals with flat-band lattices, but in this case, we shift our focus to time-reversal invariant systems, where the single-particle CLSs arise as a result of local symmetries. First, we prove Hilbert space fragmentation in a family of diamond necklaces with on-site interactions [154], and later demonstrate how this mechanism is general for a complete class of flat-band lattices [155]. We use graphs as a visual representation that reveals the fragmentation of the Hilbert space and its properties, as well as some recent results from graph theory, the equitable partition theorem, to define the class of flat-band lattices that we consider. The fragmentation of the Hilbert space is revealed upon a basis rotation that decouples the CLSs at the single-particle level. As a result, we are able to identify a conserved quantity in terms of the parity of the number of particles in the CLSs. Also, we explore the numerical signatures of this phenomenon, namely, a nested-dome distribution of entanglement entropies, thermalization restricted to each sub-sector, and both integrable and non-integrable sectors with a broad range of dimensions and entanglement scalings. Furthermore, we show this mechanism to be robust to generic long-range interactions.

Finally, in Chapter 7 we present the conclusions of this thesis and discuss possible new lines of research that stem from this work.

2

THEORETICAL FOUNDATIONS

In this chapter, we provide the theoretical foundations of this thesis and the physical models used throughout the following chapters. In Section 2.1, we give an overview of Bose-Einstein condensates (BEC) in which we discuss how bosonic particle statistics lead to condensation and we introduce the mean-field description of the interacting Bose gas at $T = 0$, the Gross-Pitaevskii equation (GPE). In Section 2.2, we review optical lattices in terms of the corresponding single-particle problem and we also explore the many-body scenario through the Bose-Hubbard model. Additionally, we present the use of matrices and graphs within this framework to investigate many-body Hamiltonians. In Section 2.3, we introduce the models used to study ring trapping potentials. We analyze the case of a single ring and then derive the tunneling amplitudes that arise when considering multiple coplanar rings. In Section 2.4, we explain the main concepts used to characterize the topology of discrete physics systems and describe a particular one-dimensional example, the Su-Schrieffer-Heeger model. Finally, in Section 2.5, we discuss thermalization in both classical and isolated quantum systems, we give an overview of the eigenstate thermalization hypothesis and briefly describe those systems that violate it.

2.1 Bose-Einstein condensates

In this section, we review the basics of BECs and briefly develop their mean-field treatment. First, we describe how bosonic quantum statistics underlie Bose-Einstein condensation and briefly explore the role of dimensionality. Then, we introduce the mean-field description of a weakly interacting BEC at zero temperature through the GPE. We discuss its derivation and also outline how to reduce its dimensionality to be able to describe low-dimensional condensates.

2.1.1   Identical particles

The notion of particle indistinguishability plays a fundamental role in Bose-Einstein condensation. Consider two particles, e.g., two electrons , that are identical, with the same intrinsic properties such as mass, electric charge, and spin. One might be able to assign labels to the particles (particle 1 and particle 2) by measuring them. For example, if the two particles are sufficiently far apart, one can distinguish them by measuring their position. Identical particles become indistinguishable when no such measurement exists. This has some important consequences on the wavefunction that represents these two particles, $\Psi\left(\xi_1, \xi_2\right)$, where ξ_i accounts for the spatial and spin coordinates of particle i, with $i = 1, 2$. If we permute the coordinates of two indistinguishable particles, the probability should not change. Therefore, the wavefunction can take one of two forms,

$$\Psi\left(\xi_1, \xi_2\right) = \frac{1}{\sqrt{2}}\left[\phi\left(\xi_1, \xi_2\right) \pm \phi\left(\xi_2, \xi_1\right)\right], \tag{2.1}$$

where $\phi\left(\xi_1, \xi_2\right)$ and $\phi\left(\xi_2, \xi_1\right)$ are eigenfunctions of the Schrödinger equation, and the probability density reads

$$\left|\Psi\left(\xi_1, \xi_2\right)\right|^2 = \frac{1}{2}\left[\left|\phi\left(\xi_1, \xi_2\right)\right|^2 + \left|\phi\left(\xi_2, \xi_1\right)\right|^2 \pm 2\mathrm{Re}\left\{\phi^*\left(\xi_1, \xi_2\right)\phi\left(\xi_2, \xi_1\right)\right\}\right]. \tag{2.2}$$

Bosons are symmetric with respect to particle exchange, $\Psi\left(\xi_1, \xi_2\right) = \Psi\left(\xi_2, \xi_1\right)$, and have integer spin, while fermions are antisymmetric, $\Psi\left(\xi_1, \xi_2\right) = -\Psi\left(\xi_2, \xi_1\right)$, and have half-integer spin. This connection to the spin of the particles is known as the spin-statistics theorem, which was formulated by M. Fierz and W. Pauli and later conceptually developed by J. Schwinger [156–158]. As a consequence of the permutation symmetry, fermions follow Fermi-Dirac statistics, while bosons follow Bose-Einstein statistics, whose characteristic traits can already be seen from the two-particle probability density, Eq. (2.2). For fermions, one recovers the Pauli exclusion principle: two indistinguishable fermions cannot occupy the same quantum state, $\left|\Psi\left(\xi, \xi\right)\right|^2 = 0$. In contrast, indistinguishable bosons can occupy the same state and do so with a probability twice the probability for distinguishable bosons, $\left|\Psi\left(\xi, \xi\right)\right|^2 = 2\left|\phi\left(\xi, \xi\right)\right|^2$. That is, fermions tend to be apart, while bosons tend to bunch together. In this thesis, we will focus on the latter.

Let us discuss the consequences of the bunching effect in a large number of bosons. For N bosons, the wavefunction is a symmetric superposition of all possible particle permutations [159],

$$\Psi\left(\xi_1, \xi_2, \cdots, \xi_N\right) = \frac{1}{\sqrt{N!}}\sum_{i_1, \cdots, i_N}\phi\left(\xi_{i_1}, \cdots, \xi_{i_N}\right), \tag{2.3}$$

and the probability of finding all N particles in the same coordinates is

$$\left|\Psi(\xi, \xi, \cdots, \xi)\right|^2 = N!\left|\phi(\xi, \xi, \cdots, \xi)\right|^2. \tag{2.4}$$

Therefore, the tendency of bosons of occupying the same state rapidly increases with the number of bosons. However, this quantum statistics effect only takes place if the identical

particles are indistinguishable. For a three-dimensional gas of identical bosons at room temperature, the particles can be distinguished by measuring their positions, as their associated wavepackets do not overlap. The size of this wavepacket at a temperature T can be quantified through the de Broglie wavelength,

$$\lambda_T = \frac{h}{p} = \frac{h}{\sqrt{2\pi M k_B T}},$$
(2.5)

where h is the Planck constant, p is the momentum of the particle, M is the mass of the particles, and k_B is the Boltzmann constant. If we lower the temperature of the gas, λ_T will increase as the momenta of the bosons decreases, and the wavepackets will begin to overlap when the following condition is fulfilled,

$$\eta \lambda_{T_c}^3 \simeq 1,$$
(2.6)

where $\eta = N/V$ is the particle density, N is the number of bosons, and V is the volume of the gas. This condition gives an estimate of the transition temperature T_c at which the quantum interference effects begin to take place and the bosons tend to macroscopically occupy the single-particle ground state, forming a BEC. The number of particles in the ground state, N_0, increases as the temperature is lowered down until there is a complete occupation of the ground state at $T = 0$. For a three-dimensional box, the condensate fraction reads [160]

$$\frac{N_0}{N} = 1 - \left(\frac{T}{T_c}\right)^{3/2}.$$
(2.7)

The particles that do not occupy the ground state and instead populate other excited states form the depletion of the condensate. This phase transition is remarkable as it occurs at a temperature where the first excited state is accessible to classical (i.e., distinguishable) particles. Therefore, it is a high-temperature effect driven by quantum statistics that occurs for both interacting and non-interacting Bose gases. However, this phase of matter is metastable, as the transition temperature typically corresponds to a solid phase. It can be achieved, for instance, in dilute gases of neutral atoms, where the three-body collisions driving the formation of molecules are rare [1–3].

The transition to a condensate phase, which also occurs in the presence of interactions, is highly dependent on the dimensionality of the system and the trapping potential. While true condensation always occurs below T_c for three dimensions both in free space and in the presence of a trapping potential, the transition is more nuanced for two-dimensional (2D) and one-dimensional (1D) systems [37]. One of the main characteristics of BECs is off-diagonal long-range order: the single-particle density matrix, $\rho(\mathbf{r}, \mathbf{r}') = \langle \hat{\Psi}(\mathbf{r}) \hat{\Psi}(\mathbf{r}') \rangle$, does not vanish for increasing particle distances, $\lim_{|\mathbf{r}-\mathbf{r}'| \to \infty} \rho(\mathbf{r}, \mathbf{r}') \neq 0$ [161]. This is a direct consequence of the overlapping de Broglie wavepackets of individual bosons, which become indistinguishable even for macroscopic distances. For 2D and 1D systems at $T > 0$, phase fluctuations can destroy long-range order [162], giving distinct phases such as quasi-condensates [163, 164]. However, phase fluctuations are suppressed at $T = 0$, making true condensation possible in any dimension.

2.1.2   The Gross-Pitaevskii equation

Let us consider a gas of interacting bosons in the condensed state and under the action of an external potential $V_{ext}(\mathbf{r})$. We assume that the gas fulfills the dilutness condition: the range of the interactions is much smaller than the average distance between atoms, $\eta^{-1/3}$. In this case, three-body collisions are highly improbable and they can be safely neglected. The many-body Hamiltonian in second quantization for a system of N bosons interacting through two-body collisions reads [165]

$$\hat{\mathcal{H}} = \int d\mathbf{r}\hat{\Psi}^\dagger(\mathbf{r})\left[-\frac{\hbar^2}{2M}\nabla^2 + V_{ext}(\mathbf{r})\right]\hat{\Psi}(\mathbf{r}) + \frac{1}{2}\iint d\mathbf{r}d\mathbf{r}'\hat{\Psi}^\dagger(\mathbf{r})\hat{\Psi}^\dagger(\mathbf{r}')V(\mathbf{r}-\mathbf{r}')\hat{\Psi}(\mathbf{r}')\hat{\Psi}(\mathbf{r}),$$
(2.8)

where $\hat{\Psi}(\mathbf{r})$ and $\hat{\Psi}^\dagger(\mathbf{r})$ are the boson field annihilation and creation operators, respectively. These operators fulfill the following commutation relations, $[\hat{\Psi}(\mathbf{r}'),\hat{\Psi}^\dagger(\mathbf{r})] = \delta^3(\mathbf{r}'-\mathbf{r})$ and $[\hat{\Psi}(\mathbf{r}'),\hat{\Psi}(\mathbf{r})] = [\hat{\Psi}^\dagger(\mathbf{r}'),\hat{\Psi}^\dagger(\mathbf{r})] = 0$. The first integral of the Hamiltonian describes the single-particle contribution to the energy, which includes the kinetic and external potential contributions, while the second describes the two-body interactions between particles. For a cold and dilute gas, the de Broglie wavelength is much larger than the range of the interactions, such that the exact form of the interaction potential $V(\mathbf{r}-\mathbf{r}')$ does not play an important role [160, 165, 166]. In addition, the momenta of the particles is very small at $T \ll T_c$ [see Eqs. (2.5) and (2.6)], such that the only relevant scattering processes are s-wave two-body collisions, which yield an isotropic interaction potential. Then, the potential $V(\mathbf{r}-\mathbf{r}')$ can be replaced by an effective contact interaction $V(\mathbf{r}-\mathbf{r}') = g\delta^3(\mathbf{r}-\mathbf{r}')$ with a strength $g = 4\pi\hbar^2 a_s/M$ that depends on a single parameter, the s-wave scattering length a_s [167], which is positive (negative) for repulsive (attractive) interactions. Introducing this interaction potential into Eq. (2.8), and integrating over $\mathbf{r}'$ yields the second quantization Hamiltonian for contact interactions,

$$\hat{\mathcal{H}} = \int d\mathbf{r}\hat{\Psi}^\dagger(\mathbf{r})\left[-\frac{\hbar^2}{2M}\nabla^2 + V_{ext}(\mathbf{r})\right]\hat{\Psi}(\mathbf{r}) + \frac{g}{2}\int d\mathbf{r}\hat{\Psi}^\dagger(\mathbf{r})\hat{\Psi}^\dagger(\mathbf{r})\hat{\Psi}(\mathbf{r})\hat{\Psi}(\mathbf{r}).$$
(2.9)

The time evolution of operator is given within Heisenberg's picture as $i\hbar\partial_t\hat{A}(t) = [\hat{A}(t),\hat{\mathcal{H}}]$ with $\hat{A}(t) = e^{i\hat{\mathcal{H}}t/\hbar}\hat{A}e^{-i\hat{\mathcal{H}}t/\hbar}$, where we have assumed an explicitly time-independent operator. For the bosonic field operator, one arrives at the following evolution equation [165],

$$i\hbar\frac{\partial\hat{\Psi}(\mathbf{r})}{\partial t} = \left(-\frac{\hbar^2}{2M}\nabla^2 + V_{ext}(\mathbf{r})\right)\hat{\Psi}(\mathbf{r}) + g|\hat{\Psi}(\mathbf{r})|^2\hat{\Psi}(\mathbf{r}),$$
(2.10)

where we have used the commutation relations given above. The field operator can be decomposed as $\hat{\Psi}(\mathbf{r},t) = \langle\hat{\Psi}(\mathbf{r},t)\rangle + \delta\hat{\Psi}(\mathbf{r},t)$, where the first term is the expectation value (i.e., a complex number with a well-defined phase) and the second term accounts for the thermal and quantum fluctuations [165]. For a large number of particles at zero temperature, one can neglect these fluctuations and obtain the so-called condensate wavefunction, $\hat{\Psi}(\mathbf{r},t) \approx \langle\hat{\Psi}(\mathbf{r},t)\rangle \equiv \Psi(\mathbf{r},t)$, which is normalized to the total number of bosons,

$\int d\mathbf{r}\,|\Psi(\mathbf{r},t)|^2 = N$. Applying this approximation to Eq. (2.10) yields the Gross-Pitaevskii equation (GPE) [168, 169],

$$i\hbar\frac{\partial\Psi(\mathbf{r})}{\partial t} = \left(-\frac{\hbar^2}{2M}\nabla^2 + V_{ext}(\mathbf{r})\right)\Psi(\mathbf{r}) + g|\Psi(\mathbf{r})|^2\Psi(\mathbf{r}), \qquad (2.11)$$

which describes a weakly interacting BEC at $T = 0$ in three dimensions (3D) in terms of a macroscopic wavefunction. The time-independent version of the GPE can be obtained by using the Ansatz $\Psi(\mathbf{r}, t) = \Psi(\mathbf{r})e^{-i\mu t/\hbar}$ [165],

$$\left(-\frac{\hbar^2}{2M}\nabla^2 + V_{ext}(\mathbf{r}) + g|\Psi(\mathbf{r})|^2\right)\Psi(\mathbf{r}) = \mu\Psi(\mathbf{r}), \qquad (2.12)$$

where μ is the chemical potential, the energy necessary to extract one particle from the condensate. One can reduce the dimensionality of the GPE (2.11) to describe 2D or 1D condensates by introducing a anisotropic harmonic trap that freezes the dynamics of one (for a 2D BEC) or two (for a 1D BEC) dimensions. For a tight confinement ($\mu \ll \hbar\omega$, with ω the frequency of the trap in the directions of confinement), the condensate wavefunction can be factorized. Then, one can obtain a reduced GPE in which the condensate wavefunction only depends on the unfrozen degrees of freedom. In Chapter 3, we will analyze a quasi-one dimensional BEC at $T = 0$ in terms of the one-dimensional version of the GPE.

2.2 Optical lattices

In this section, we continue exploring ultracold bosons but shift our attention to optical lattices, which will appear in Chapters 4 - 6, and analyze them both from a single-particle and a many-body perspective. First, we describe how the optical dipole force can be used to create periodic potentials for neutral atoms and then describe the single-particle solutions in such potentials in terms of Bloch functions. Then, we explore the bosonic many-body case by outlining the derivation of the Bose-Hubbard model. We discuss how the Fock basis formalism in second quantization allows one to represent Hamiltonians of finite systems as matrices. Finally, we make a connection to graph theory, which can be used to reveal some properties of a physical system by representing its Hamiltonian matrix as a graph.

2.2.1 Single particle description

The dynamics of a neutral atom trapped in an optical lattice are closely related to those of an electron in a solid-state crystal. While periodic potentials arise naturally in solid-state physics from the periodicity of the crystalline lattice, optical lattices are artificially engineered through the use of conservative light-matter interactions. A neutral atom subject to a far off-resonant oscillating electric field undergoes an energy shift proportional to the intensity and inversely proportional to the detuning, $\Delta E(\boldsymbol{r}) \propto I(\boldsymbol{r})/\Delta$ [19]. In 1D, two counter-propagating lasers along the x direction can create a standing wave, such that the atoms feel a position dependent

energy shift. Depending on the sign of the detuning, they become attracted to either the maxima (for red detuned lasers) or minima (for blue detuned lasers) of the position-dependent intensity. This leads to an effective sinusoidal potential,

$$V(x) = V_0 \sin^2 (2\pi/\lambda x),\tag{2.13}$$

where λ is the wavelength of the lasers and V_0 is proportional to their intensity. The minima of $V(x)$ constitute the sites of the lattice while the maxima define potential barriers between sites through which quantum tunneling can occur. Although we describe here the one-dimensional case, one can generate square (in 2D) and cubic (in 3D) optical lattices by using additional pairs of counter-propagating lasers [170]. Additionally, one can exploit the direction, polarization, phase and frequency of the laser beams, to engineer more complex geometries [34–36].

It is instructive to first analyze the 1D single particle case, which is described by the time-independent Schrödinger equation,

$$\left(-\frac{\hbar^2}{2M}\frac{\partial^2}{\partial x^2} + V(x)\right)\Psi_q^n(x) = E_q^n\Psi_q^n(x).\tag{2.14}$$

This equation also describes an electron in a periodic potential, which allows us to borrow some well known results from solid-state physics. The Bloch theorem states that the wavefunction of a particle in a periodic potential takes the following form [171, 172],

$$\Psi_q^n(x) = e^{iqx}u_q^n(x),\tag{2.15}$$

where the functions $u_q^n(x + D) = u_q^n(x)$ have the same periodicity as the lattice potential $V(x)$, defined by the lattice spacing D. They are modulated by plane waves, where q is the quasimomentum, a quantum number characterizing the translation symmetry of the potential. Due to the periodicity of the lattice, not all values of q yield unique solutions to Eq. (2.14), so that one can restrict the quasimomentum to the first Brillouin zone, $-\pi/D < q \le \pi/D$, without loss of generality. Similarly to the electronic band structure, a particle in an optical potential presents a series of energy bands n and energy gaps. As one increases the potential depth V_0 with respect to the gapless free-particle limit (at $V_0 = 0$), energy gaps grow and the energy bands flatten as the eigenstates become more localized at each site of the lattice.

The Bloch wavefunctions are orthonormal with respect to each energy band n and quasimomentum q, for a finite system, they fulfill, $\int [\Psi_{q'}^{n'}(x)]^*\Psi_q^n(x)dx = \delta_{n'n}\delta_{q'q}$. Another convenient basis is formed by the Wannier states, which are constructed as linear superpositions of Bloch waves [170],

$$w_n(x - x_i) = \frac{1}{\sqrt{\mathcal{M}}}\sum_q e^{-iqx_i}\Psi_q^n(x),\tag{2.16}$$

where $\mathcal{M}$ is the number of sites. While Bloch waves are delocalized through the lattice, Wannier functions are localized at each site of the lattice x_i. The Wannier functions are a useful description in the tight binding regime, where the lattice depth is large, and can be used to derive the Bose-Hubbard model that describes the many-body scenario, as shown in the next section.

2.2.2 Bose-Hubbard model

The Bose-Hubbard model [20] is the simplest model that captures the dynamics of interacting bosons in an optical lattice potential. Its main feature is the interplay between the kinetic energy and the interactions between particles. In Section 2.1.2, we described weakly-interacting ultracold bosonic gases through a mean-field approach yielding the GPE (2.11). In an optical lattice, one can reach strongly correlated regimes where the interactions play an important role in the dynamics of the system. The Bose-Hubbard model can be derived from the second quantization Hamiltonian with contact interactions, Eq. (2.9), in the presence of a periodic potential. When the lattice depth is large enough, the Wannier functions are highly localized at each site, and for low temperatures interband transitions are suppressed. Then, the bosonic field operators can be expanded as a linear combination of the Wannier functions of the lowest energy band as

$$\hat{\Psi}(\mathbf{r}) = \sum_i w_0 \left(\mathbf{r} - \mathbf{r}_i\right) \hat{a}_i, \tag{2.17}$$

where $\hat{a}_i$ and $\hat{a}_i^\dagger$ are the annihilation and creation operators acting on each site i of the lattice. These operators fulfill the bosonic commutation relations $[\hat{a}_{i'}, \hat{a}_i^\dagger] = \delta_{i'i}$, and $[\hat{a}_{i'}, \hat{a}_i] = [\hat{a}_{i'}^\dagger, \hat{a}_i^\dagger] = 0$. Introducing Eq. (2.17) into (2.9), yields the Bose-Hubbard model [23]

$$\hat{\mathcal{H}}_{\mathrm{BH}} = -\sum_{i,i'} J_{i,i'} \left(\hat{a}_{i'}^\dagger \hat{a}_i + \hat{a}_i^\dagger \hat{a}_{i'}\right) + \frac{1}{2} \sum_i U_i \hat{n}_i \left(\hat{n}_i - 1\right) - \sum_i \mu_i \hat{n}_i \tag{2.18}$$

where $\hat{n}_i = a_i^\dagger a_i$ is the boson number operator. The properties of the different terms of the model are described below:

1. The first term acts as a kinetic energy, it contains the hopping terms that annihilate one particle in one site and create another in a different site. The tunneling matrix elements are given by the following overlap integral

$$J_{i,i'} = -\int w_0^* \left(\mathbf{r} - \mathbf{r}_i\right) \left[-\frac{\hbar^2 \nabla^2}{2M} + V(\mathbf{r})\right] w_0 \left(\mathbf{r} - \mathbf{r}_{i'}\right) d\mathbf{r}. \tag{2.19}$$

2. The second term gives the interaction energy, it results from the contact interactions between bosons populating the same site. The strength of the interaction U_i depends on the Wannier function on a single site i

$$U_i = g \int \left|w_0 \left(\mathbf{r} - \mathbf{r}_i\right)\right|^4 d\mathbf{r}, \tag{2.20}$$

   where g is given in Section 2.2.1.

3. The last term describes the on-site potential μ_i, the energy required to remove a particle located at a given site i of the lattice. It arises when an external potential is added to the optical lattice and varies the potential at each site,

$$\mu_i = \int w_0^* \left(\mathbf{r} - \mathbf{r}_i\right) \left[-\frac{\hbar^2 \nabla^2}{2M} + V(\mathbf{r})\right] w_0 \left(\mathbf{r} - \mathbf{r}_i\right) d\mathbf{r}. \tag{2.21}$$

The simplest and most typical form of the Bose-Hubbard model is restricted to nearest neighbor tunnelings, as the tunneling amplitude $J_{i,i'}$ decays exponentially with the distance, such that the first sum only includes the terms $\langle i, i' \rangle$. Additionally, in the absence of an external potential on top of the optical lattice, the sites become identical, which yields a homogeneous interaction strength $U_i = U$, chemical potential $\mu_i = \mu$, and tunneling amplitude $J_i = J$. In that case, one typically removes the last term of (2.18), as it becomes a constant energy shift. All these parameters, J, U, and μ, depend on the form of the Wannier functions, which are, in turn, determined by the trapping potential. As the depth of the lattice increases, the Wannier functions become more localized, which causes the tunneling J to decrease and the interaction strength U to increase. Therefore, in an optical lattice, one can continuously tune the ratio U/J by modifying the parameters of the laser that creates the lattice, which allows one to reach strongly correlated regimes even in a weakly interacting gas. Depending on the ratio U/J, the bosonic gas is either in a superfluid phase, when the hopping dominates over the interactions, or in a Mott insulator phase, when repulsive interactions predominate [20–22]. However, many variations and extensions of this model have been considered in the literature [23, 24, 173]. For example, the addition of a position-dependent on-site potential can be used to model disorder and study bosonic many-body localized phases [174]. Also, one might consider interactions involving bosons in different sites of the lattice to model dipolar interactions [175] or the population of excited states instead of the ground-state at each site of the lattice [176]. In Chapters 4 and 5, we will explore lattices where we populate excited states, the states with orbital angular momentum $l = 1$ of a ring trapping potential that forms each site of the lattice.

2.2.3   Fock states, matrices, and graphs

The quantum state of a single-particle problem is well-described by the single-particle wavefunction. For two indistinguishable particles or more, a wavefunction description needs to enforce symmetrization (anti-symmetrization) for bosons (fermions) to take into account the effect of particle exchange symmetry (discussed in Section 2.1.1). This description, which remains quite simple for two particles [see Eq. (2.1)], quickly becomes cumbersome when the number of particles increases. In the second quantization formalism, used to introduce the Bose-Hubbard model (Sec. 2.2.2), quantum many-body states are described by Fock states [177]. These states specify the number of particles occupying a certain state (in this case a site), instead of denoting the state that each individual particle occupies, which greatly simplifies the notation. In an optical lattice with $\mathcal{M}$ sites, each Fock state $|f_s\rangle$ is obtained through the creation operator $a_j^\dagger$ acting on the vacuum state,

$$|f_s\rangle \equiv |n_1, n_2, \ldots, n_i, \ldots, n_{\mathcal{M}}\rangle = \prod_{j=1}^{\mathcal{M}} \frac{\left(a_j^\dagger\right)^{n_j}}{\sqrt{n_j!}} |\varnothing\rangle, \tag{2.22}$$

(a)

(b)

$$\begin{pmatrix} 0 & 1 & 0 & 0 & 1 & 0 \\ 1 & 0 & 1 & 1 & 1 & 0 \\ 0 & 1 & 0 & 1 & 0 & 0 \\ 0 & 1 & 1 & 0 & 0 & 1 \\ 1 & 1 & 0 & 0 & 0 & 1 \\ 0 & 0 & 0 & 1 & 1 & 0 \end{pmatrix}$$

(c)

$|100\rangle$ $|010\rangle$ $|001\rangle$

(d)

$|300\rangle$ $|210\rangle$ $|120\rangle$ $|030\rangle$ $|021\rangle$ $|012\rangle$ $|003\rangle$ $|201\rangle$ $|111\rangle$ $|102\rangle$
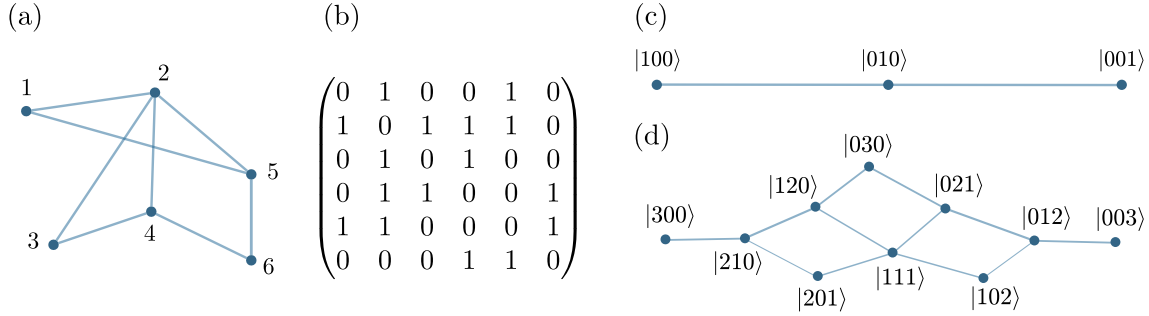
Figure 2.1: (a) Example of a simple graph and (b) corresponding adjacency matrix. (c,d) Graph representing a Hamiltonian of a three-site linear optical lattice loaded with bosons where each vertex represents a Fock state $|f_s\rangle$. (c) For a single boson, each vertex of the graph indicates the position of a site. (d) For three bosons, the geometrical structure of the lattice becomes hidden in the many-body Fock space.

where n_i is the number of particles in site i and s denotes a unique set of indices n_i. The Fock states fulfill the following orthonormality condition

$$\langle n'_1, \ldots, n'_\mathcal{M} \mid n_1, \ldots, n_\mathcal{M} \rangle = \prod_{j=1}^{\mathcal{M}} \delta_{n'_j n_j} \quad \Rightarrow \quad \langle f_{s'} \mid f_s \rangle = \delta_{ss'}. \qquad (2.23)$$

For a given number of sites $\mathcal{M}$ and a total number of particles $N = \sum_{k=1}^{\mathcal{M}} n_k$, the Fock states $\{|f_s\rangle\}$ constitute a basis that allows one to cast the Hamiltonian into a matrix form, where the matrix elements of the Hamiltonian are given by $\mathcal{H}_{ss'} = \langle f_{s'}|\hat{\mathcal{H}}|f_s\rangle$. Then, one can use exact diagonalization to find numerically all or some of the eigenvalues and eigenstates of the Hamiltonian [178]. Throughout this thesis, we will use this method to analyze lattice systems, which works well for a small number of sites $\mathcal{M}$ and particles N, where the dimension of the Hilbert space is relatively small. However, the rapid growth of the Hilbert space dimension with $\mathcal{M}$ and N makes this method impracticable for larger system sizes. For these cases, one might use other numerical methods such as tensor networks [179, 180], where one does not represent the whole Hilbert space but instead only a fraction of it that obeys certain entanglement constraints.

The representation of Hamiltonians as matrices suggests a connection to graph theory, from which we will borrow some tools in Chapter 6. A simple graph is a set of vertices $\mathcal{V}$ and a set of edges $\mathcal{E}$ that indicate connections between pairs of distinct vertices, $\mathcal{E} \subseteq \{\{x, y\} \mid x, y \in \mathcal{V} \text{ and } x \neq y\}$ [181]. Such a structure can be represented visually through a series of points representing the vertices, and straight lines representing the edges between such vertices (see some examples in Fig. 2.1). Note that the exact location of each vertex does not alter the graph, which is independent of its visual representation. Choosing an order for the vertices $\mathcal{V}$ yields a one-to-one correspondence between graphs and square matrices. One can define many associated matrices to a given graph, but the most relevant matrix for our purposes is the adjacency matrix. The off-diagonal elements of this matrix that take a value of 1 indicate the edges of the corresponding graph and are known as adjacency relations, while

disconnected pairs of vertices are represented by zeros. Figure 2.1(b) shows the adjacency matrix associated to the graph in Fig. 2.1(a), as a simple example.

Graphs are ubiquitous in many fields beyond physics, representing a myriad of structures such as metabolic networks, neural networks, the World Wide Web, ecological networks and others [182]. These networks often have a degree of complexity that cannot be captured by a simple graph, and require an extension of the concept. For example, weighted graphs have edges with a certain value, which are reflected in the value of the off-diagonal elements of the corresponding adjacency matrix. Also, colored graphs can include numerical labels for each vertex and other types of graphs can include loops, which correspond to adjacency relations that start and end in the same vertex. In this thesis, we will make use of an extended notion of a graph to represent Hamiltonian matrices visually by treating them as an adjacency matrix. These matrices will correspond to weighted and colored graphs that might include loops. We will refer to these objects simply as graphs.

The correspondence between matrices and graphs provides a common ground between mathematics and physics in this context. In mathematics, spectral graph theory deals with the properties of graphs in relation with the eigenstates and eigenvalues of their associated matrices [183]. In analogy, in physics one is often concerned with solving the eigenvalue problem given by the time-independent Schrödinger equation. This connection motivates the interdisciplinary use of graph theory tools to analyze quantum systems. Let us consider a many-body Hamiltonian representing particles in an optical lattice [Eq. (2.18), for instance]. The associated Hamiltonian matrix can have non-zero diagonal elements corresponding to the on-site potentials or interactions, and also off-diagonal elements with different weights given by the different tunneling amplitudes. Figures 2.1(c) and (d) show the graph of the Hamiltonian for a three-site linear optical lattice with one and three bosons, respectively, where the vertices are the Fock states forming the product-state basis of the Hamiltonian. These graphs reveal different information for the single-particle and the many-body cases. For a single particle, each basis state denotes the site that the particle occupies. For example, a Fock state reads $|0, \ldots, 0, 1, 0, \ldots, 0\rangle$, and thus it represents the position of the particle in the lattice. Thus, by locating each vertex of the graph appropriately, the graph can represent schematically the geometric structure of the lattice [see the case of 3 sites in Fig. 2.1(c)], or manifest visually the symmetries of the Hamiltonian. We will use this kind of visual representation to analyze compact localized states in terms of the symmetries of the graph in Chapter 6. Note also that the graph representation of a Hamiltonian critically depends on the basis we choose for the Hamiltonian, which determines the information that we can extract from it. For example, a set of completely decoupled vertices correspond to the eigenstates of a diagonalized Hamiltonian, but this picture does not highlight any new information. For a many-body Hamiltonian, the Fock states indicate the number of particles in each site of the lattice, for example $|3, 0, 2, 1, 0, \ldots\rangle$ [Eq. (2.22)]. As a result, the geometry of the lattice becomes hidden in the graph of the corresponding Hamiltonian [see the case of 3 bosons in 3 sites in Fig. 2.1(d)]. However, this representation might reveal other properties, such as the presence of densely linked clusters leading to quantum many-body scars [184] or highly symmetric graphs leading to time crystals [185]. We will use this many-body graph representation of Hamiltonians in

Chapter 6 to analyze the fragmentation of the Hilbert space.

2.3 Single particle in ring potentials

In the previous section, we discussed conventional optical lattices, where the dynamics are typically restricted to the local ground states of each lattice site. However, in this thesis we will study excited orbital angular momentum (OAM) states in ring-trapping potentials. In this section, we describe the physical models used to analyze these states from a single-particle perspective. First, we solve the Schrödinger equation to find the solutions for a single ring. Then, we consider the case of multiple coplanar rings by considering two toy models: two inline rings and three rings in a triangular configuration. These models are the basis to study arbitrary lattices of identical coplanar rings, where complex tunnelings naturally arise as a consequence of the OAM. We also outline a method to compute these tunneling amplitudes and we give an overview of the experimental techniques that can be used to implement these trapping potentials.

2.3.1 Single ring potential

We have seen in the previous section that counter-propagating lasers can be used to generate optical lattice potentials, that, in 1D, take a sinusoidal form. However, one might consider distinct trapping geometries forming each site of the lattice, such as ring potentials, which we will explore in Chapters 4 and 5. In this section, we compute the single-particle eigenstates of a two-dimensional toroidal trap, generated by a displaced harmonic potential of frequency ω that reads $V(\rho) = \frac{M\omega^2}{2}(\rho - \rho_0)^2$, where M is the mass of the particles, ρ is the radial coordinate, and ρ_0 is the radius of the ring. The time-independent Schrödinger equation in cylindrical coordinates for this potential reads

$$\left[-\frac{\hbar^2 \nabla^2}{2M} + \frac{M\omega^2 (\rho - \rho_0)^2}{2} \right] \phi = E\phi. \tag{2.24}$$

Due to the cylindrical symmetry of the external potential, the eigenstates are also eigenstates of the $\hat{L}_z = -i\hbar \frac{\partial}{\partial \varphi}$ operator, where φ is the azimuthal coordinate. Therefore, they have a well-defined OAM l and take the form

$$\phi_p^\nu(\rho, \varphi) = \psi_p^l(\rho) e^{i\nu\varphi}, \tag{2.25}$$

where $\nu = \pm l$ is the winding number and p labels the radial excitations. Introducing this Ansatz (2.25) into (2.24), one obtains an equation for the radial part of the wavefunction,

$$-\frac{\hbar^2}{2M} \left[\frac{d^2 \psi_p^l}{d\rho^2} + \frac{1}{\rho} \frac{d\psi_p^l}{d\rho} + \frac{l^2}{\rho^2} \psi_p^l \right] + \frac{M\omega^2 (\rho - \rho_0)^2}{2} \psi_p^l = E\psi_p^l. \tag{2.26}$$

We will use the following two assumptions:

1. We assume that there are no radial excitations (we fix $p = 0$), such that the states occupy the ground state of the radial potential. As this potential takes a displaced harmonic form, the ground state can be obtained variationally by taking the following displaced Gaussian as an Ansatz: $\psi_0^0(\rho) \simeq Ce^{-\alpha(\rho-\rho_0\beta)^2}$, with $\alpha \sim 1/2\sigma^2$ and $\beta \sim 1$ [186].

2. When the term $\frac{l^2}{\rho^2}\psi_p^l$ in Eq. (2.26) is small, the radial wavefunction for a mode l can be approximated by the ground state radial wavefunction $\psi_0^l(r) \approx \psi_0^0(r)$. This is valid for $p = 0$, low values of l and radii ρ_0 a few times σ or larger [187].

Given these assumptions, the wavefunction simplifies to $\phi_0^\nu(\rho, \varphi) = \psi_0^0(\rho)e^{i\nu\varphi}$. Then, the energy of an eigenstate, which can be obtained from Eq. (2.24), reads

$$
\begin{aligned}
E(l) &= \int d^2r \left[V(\rho)\left|\phi_0^\nu(\rho, \varphi)\right|^2 + \frac{\hbar^2}{2M}\left|\nabla\phi_0^\nu(\rho, \varphi)\right|^2 \right] \\
&= \int d^2r \left[V(\rho)\left|\psi_0^0\right|^2 + \frac{\hbar^2}{2M}\left|\frac{d\psi_0^0}{d\rho}\right|^2 \right] + l^2\frac{\hbar^2}{2M}\int d^2r \left|\frac{\psi_0^0}{\rho}\right|^2 = E_0 + E_c l^2.
\end{aligned}
$$

(2.27)

Thus, the energy has a ground state contribution common to all OAM modes, E_0, and a term that increases with l^2. Therefore, the system presents a non-degenerate ground state with $l = 0$, while the excited states form pairs of degenerate states with orbital angular momentum l and opposite winding numbers $\nu = \pm l$ [see Fig. 2.2(b)]. In Chapters 4 and 5, we will consider lattices where each site is a ring potential and bosons populate the states $l = 1$ of each ring trap, which remain decoupled from the other manifolds of states.

2.3.2   Tunneling amplitudes in coupled ring potentials

In order to study a lattice where each site is a ring potential, one must first consider the simplest case of a single particle trapped in two tunnel-coupled coplanar rings [see Fig. 2.2(a)]. The dynamics of this system are governed by the time-dependent Schrödinger equation,

$$
i\hbar\frac{\partial\Psi(\mathbf{r}, t)}{\partial t} = -\frac{\hbar^2}{2M}\nabla^2\Psi(\mathbf{r}, t) + V(\mathbf{r})\Psi(\mathbf{r}, t).
$$

(2.28)

We consider the case of two identical rings, L and R, with radius ρ_0 and frequency ω, where the potential minima of the two rings are separated by a distance d. We define the local polar coordinates at each ring, (ρ_j, φ_j) with $j = R, L$, to write the local eigenstates of the system in position representation [Eq. (2.25)] as

$$
\phi_{\pm l}^j(\rho_j, \varphi_j) = \langle\mathbf{r} \mid j, \pm l\rangle = \psi_l(\rho_j)e^{\pm il(\varphi_j-\varphi_0)},
$$

(2.29)

where we have introduced φ_0 as the arbitrary phase origin and l denotes the OAM. For a large enough distance d, each set of local eigenstates with OAM l form (to a good approximation) an orthonormal basis. As the different sets of states with OAM l are separated in energy [see Eq. (2.27) and Fig. 2.2(b)], each set of states can be analyzed independently. We assume that
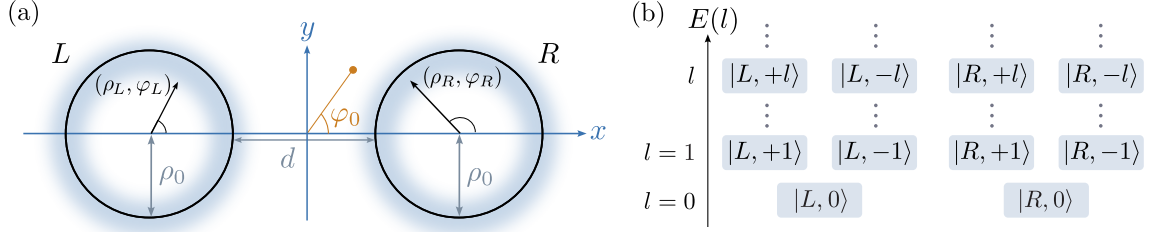
(a)

(b)

$E(l)$

	$\vdots$	$\vdots$	$\vdots$	$\vdots$
l	$|L,+l\rangle$	$|L,-l\rangle$	$|R,+l\rangle$	$|R,-l\rangle$
	$\vdots$	$\vdots$	$\vdots$	$\vdots$
$l=1$	$|L,+1\rangle$	$|L,-1\rangle$	$|R,+1\rangle$	$|R,-1\rangle$
$l=0$		$|L,0\rangle$	$|R,0\rangle$	

Figure 2.2: (a) Schematic of the two-identical ring configuration (L and R) with radii ρ_0 and separated by a distance d. Each ring has local polar coordinates (ρ_j, φ_j) with $j = L, R$ and the origin of the phase φ_0 is indicated in orange. (b) Qualitative representation of the energies for each set of states with OAM l.

given an initial state that is a superposition of the states $\{|L, +l\rangle, |L, -l\rangle, |R, +l\rangle, |R, -l\rangle\}$, the dynamics of the system will not drive excitations to other states. Then, the total state of the particle at a time t for a given OAM l can be written as

$$\left|\Psi^l(t)\right\rangle = a_{+l}^L(t)|L, +l\rangle + a_{-l}^L(t)|L, -l\rangle + a_{+l}^R(t)|R, +l\rangle + a_{-l}^R(t)|R, -l\rangle, \quad (2.30)$$

where the amplitudes $a_{\pm l}^j$ fulfill $\sum_{j=L,R} \sum_{\nu=\pm l} |a_\nu^j|^2 = 1$, such that $\left\langle \Psi^l(t) \mid \Psi^l(t) \right\rangle = 1$. Introducing this expression into the Schrödinger equation (2.28) and projecting for the different states $|j, \pm l\rangle$ with $j = L, R$, one can find a set of linearly-coupled evolution equations for the amplitudes $a_{\pm l}^j$,

$$i\hbar \frac{da_\nu^j}{dt} = \sum_{j,j'=L,R} \sum_{\nu,\nu'=\pm l} J_{j,\nu}^{j',\nu'} a_{j'}^{\nu'}, \quad (2.31)$$

where the parameters $J_{j,\nu}^{j',\nu'}$ are given by

$$J_{j,\nu}^{j',\nu'} = \int d^2r [\phi_\nu^j]^* \left[-\frac{\hbar^2 \nabla^2}{2M} + V(\mathbf{r}) \right] \phi_{\nu'}^{j'}. \quad (2.32)$$

The evolution equations (2.31) can be written in matrix form by ordering the corresponding states, $\{|L, +l\rangle, |L, -l\rangle, |R, +l\rangle, |R, -l\rangle\}$. This defines the Hamiltonian of the four-state model (FSM), $i\hbar\partial_t\mathbf{a}(t) = \hat{\mathcal{H}}_{\mathrm{FSM}}^l \mathbf{a}(t)$, where $\mathbf{a} = (a_{+l}^L, a_{-l}^L, a_{+l}^R, a_{-l}^R)^T$.

The parameters $J_{j,\nu}^{j',\nu'}$ are constrained by the global symmetries of the system, which where thoroughly analyzed in [186]. We briefly review their arguments here. One might note from Fig. 2.2(a), that the external potential $V(\mathbf{r})$ is invariant under x and y reflections,

$$\mathcal{M}_x : (x, y) \to (x, -y), \qquad \mathcal{M}_y : (x, y) \to (-x, y), \quad (2.33)$$

which modify the complex factor of the local eigenstates of the two rings while leaving its radial term invariant,

$$\mathcal{M}_x \left(\phi_{\pm l}^j\right) = e^{\mp 2il\varphi_0} \phi_{\mp l}^j, \qquad \mathcal{M}_y \left(\phi_{\pm l}^j\right) = e^{\mp 2il\varphi_0} e^{\pm il\pi} \phi_{\mp l}^k, \quad k \neq j. \quad (2.34)$$

Therefore, the Hamiltonian $\hat{\mathcal{H}}^l_{\mathrm{FSM}}$ is invariant under $\mathcal{M}_x$ and $\mathcal{M}_y$, and consequently, it is also invariant under parity, $\mathcal{M}_x\mathcal{M}_y$. Applying these operators to the Hamiltonian and using their effect on the local eigenstates, Eq. (2.34), constraints the possible values of the parameters $J^{j',\nu'}_{j,\nu}$, leaving only three independent tunnelings:

(i) $J^{L,\mp l}_{L,\pm l} \equiv J^l_1 e^{\pm 2il\varphi_0}$, couples opposite winding number states within a single ring.

(ii) $J^{R,\pm l}_{L,\pm l} \equiv J^l_2$, couples same winding number states in adjacent rings.

(iii) $J^{R,\mp l}_{L,\pm l} \equiv J^l_3 e^{\pm 2il\varphi_0}$, couples opposite winding number states in adjacent rings.

There is also a self-energy term that is equal for all the states $\{|j,\pm l\rangle\}$, $J^{j,\pm l}_{j,\pm l} \equiv E^l$, and we have defined $J^l_1, J^l_2, J^l_3, E^l \in \mathbb{R}$. The tunnelings (i) and (iii) appear due to the presence of the second ring, which breaks cylindrical symmetry. While the self-energy and (ii) are always real, (i) and (iii) have a complex factor that is modulated by the origin of the phase φ_0, indicated in Fig. 2.2(a). However, this origin can be chosen arbitrarily, as any value will lead to identical dynamics. For two inline rings, one can choose φ_0 along the axis that crosses the center of the two rings such that all parameters $J^{j',\nu'}_{j,\nu}$ become real. For this choice of φ_0, the four-state model defined by the evolution equations (2.31) reads

$$i\hbar\frac{d}{dt}\begin{pmatrix} a^L_{+l} \\ a^L_{-l} \\ a^R_{+l} \\ a^R_{-l} \end{pmatrix} = \begin{pmatrix} E^l & J^l_1 & J^l_2 & J^l_3 \\ J^l_1 & E^l & J^l_3 & J^l_2 \\ J^l_2 & J^l_3 & E^l & J^l_1 \\ J^l_3 & J^l_2 & J^l_1 & E^l \end{pmatrix}\begin{pmatrix} a^L_{+l} \\ a^L_{-l} \\ a^R_{+l} \\ a^R_{-l} \end{pmatrix} \equiv \hat{\mathcal{H}}^l_{FSM}\begin{pmatrix} a^L_{+l} \\ a^L_{-l} \\ a^R_{+l} \\ a^R_{-l} \end{pmatrix}. \qquad (2.35)$$

In order to obtain a good quantitative agreement between the predictions of the four-state model and the integration of the 2D Schrödinger equation, one must accurately calculate the parameters $J^{j',\nu'}_{j,\nu}$. However, the overlap integral in Eq. (2.32) is strictly valid in the limit where the local eigenstates are orthogonal, as it does not take into account any overlap between them. Instead, one can compute the parameters $J^{j',\nu'}_{j,\nu}$ by diagonalizing the Hamiltonian matrix of the four-state model, which gives the following eigenstates and energies,

$$\begin{aligned}
\left|E^l_1\right\rangle &= \frac{1}{2}(-|L,+l\rangle - |L,-l\rangle + |R,+l\rangle + |R,-l\rangle), & E^l_1 &= E^l + J^l_1 - J^l_2 - J^l_3, \\
\left|E^l_2\right\rangle &= \frac{1}{2}(-|L,+l\rangle + |L,-l\rangle - |R,+l\rangle + |R,-l\rangle), & E^l_2 &= E^l - J^l_1 + J^l_2 - J^l_3, \\
\left|E^l_3\right\rangle &= \frac{1}{2}(|L,+l\rangle - |L,-l\rangle - |R,+l\rangle + |R,-l\rangle), & E^l_3 &= E^l - J^l_1 - J^l_2 + J^l_3, \\
\left|E^l_4\right\rangle &= \frac{1}{2}(|L,+l\rangle + |L,-l\rangle + |R,+l\rangle + |R,-l\rangle), & E^l_4 &= E^l + J^l_1 + J^l_2 + J^l_3.
\end{aligned}$$

(2.36)

Then, one can find the amplitudes of the self-energy and the tunneling from the energies E^l_i by inverting the above relations,

$$\begin{aligned}
E^l &= \frac{1}{4}\left(\tilde{E}^l_1 + \tilde{E}^l_2 + \tilde{E}^l_3 + \tilde{E}^l_4\right), & J^l_2 &= \frac{1}{4}\left(-\tilde{E}^l_1 + \tilde{E}^l_2 - \tilde{E}^l_3 + \tilde{E}^l_4\right), \\
J^l_1 &= \frac{1}{4}\left(\tilde{E}^l_1 - \tilde{E}^l_2 - \tilde{E}^l_3 + \tilde{E}^l_4\right), & J^l_3 &= \frac{1}{4}\left(-\tilde{E}^l_1 - \tilde{E}^l_2 + \tilde{E}^l_3 + \tilde{E}^l_4\right).
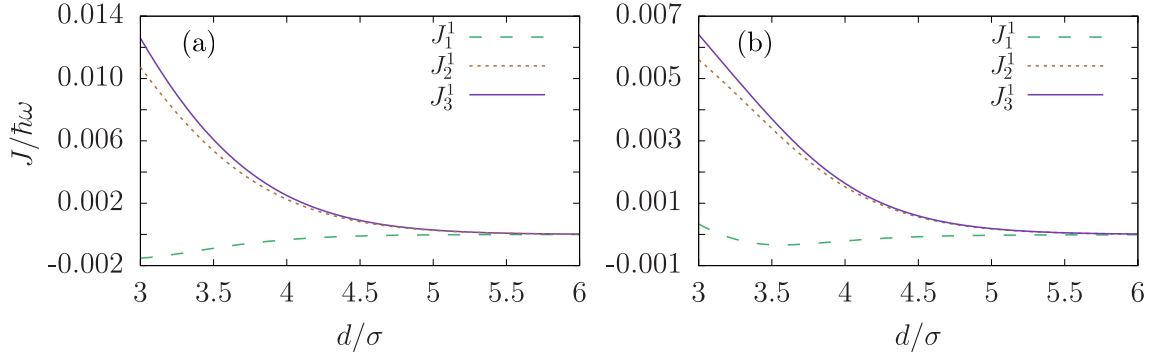\end{aligned}$$

(2.37)

Figure 2.3: Tunneling amplitudes J_1^1, J_2^1, and J_3^1 as a function of the separation distance between rings for (a) $\rho_0 = 2.5\sigma$ and (b) $\rho_0 = 5\sigma$ with $\sigma = \sqrt{\hbar/M\omega}$.

The exact eigenenergies of the system, $\{\tilde{E}_i^l\}$, can be obtained through imaginary-time evolution of the 2D Schrödinger equation, by subtracting at each step the projections of the lower energy states. To do that, we define the numerical external potential as the truncated sum of the ring potentials for the left and right rings,

$$V(\mathbf{r}) = \frac{M\omega^2}{2} \min \left[\left(\sqrt{(x - \rho_0 - d/2)^2 + y^2} - \rho_0 \right)^2, \left(\sqrt{(x + \rho_0 + d/2)^2 + y^2} - \rho_0 \right)^2 \right].$$

(2.38)

Figure 2.3 represents the tunneling amplitudes J_1^1, J_2^1, and J_3^1 as a function of the separation distance between rings for a ring radius (a) $\rho_0 = 2.5\sigma$ and (b) $\rho_0 = 5\sigma$ with $\sigma = \sqrt{\hbar/M\omega}$, as obtained through this method. For both radii, the difference between J_2^1 and J_3^1 decreases with the distance d, while the tunneling J_1^1 remains approximately one order of magnitude smaller than the others. For this reason, we will neglect J_1^1 in Chapters 4 and 5.

The two-ring model allows one to describe one-dimensional lattices of rings where all the ring centers are aligned, as those can be reduced to pairs of inline rings with tunneling amplitudes described by the four-state model. However, we need to study another system in order to be able to describe arbitrary coplanar geometries of identical rings: three coplanar identical rings L, R, and C forming a triangle, as shown in Fig. 2.4. Such structure can also be described by a few-state model, which in this case includes the six local eigenstates with OAM l in the rings L, R, and C: $\{|L, +l\rangle, |L, -l\rangle, |C, +l\rangle, |C, -l\rangle, |R, +l\rangle, |R, -l\rangle\}$. To simplify the model, we fix the origin of the phase along one of the axis uniting two of the rings, L - C, thus giving real tunneling amplitudes for this pair of rings. Necessarily, the other directions, L - R and C - R, form a non-zero angle with φ_0, which leads to complex values for the tunnelings (i) and (iii). We define the local coordinate system (x, y) for the pair L - C, such that φ_0 goes along the positive x axis (see Fig. 2.4). For the pair C - R, the origin of the phase measured in the local coordinate system (x', y') is $\varphi'_0 = \pi - \Theta$. This leads to a complex factor $e^{\pm 2il\varphi_0} = e^{\mp 2il\Theta}$ in the tunnelings between opposite circulation states that depends on the central angle Θ, and thus can be modified by changing the geometry of the lattice. For a central angle $\Theta > \pi/3$, the couplings along L - R can be neglected due to the rapid decay
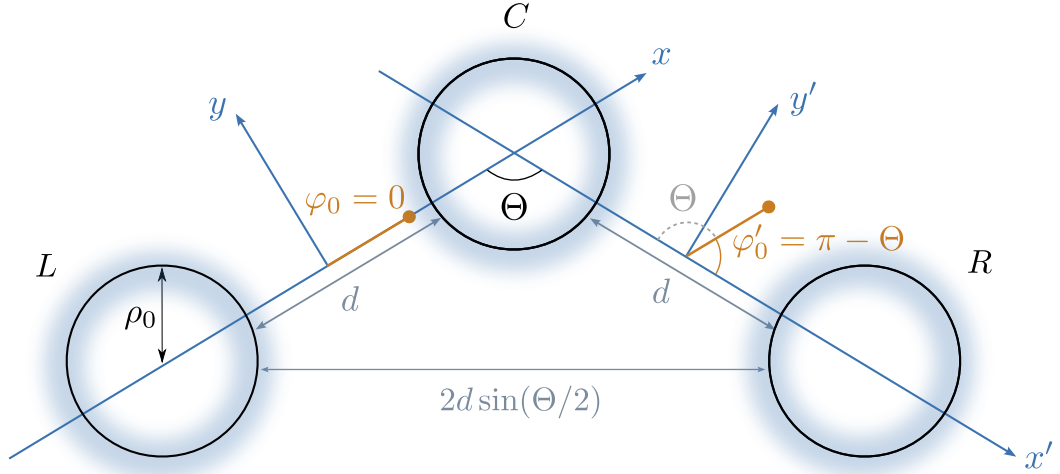
Figure 2.4: Schematic of the three-identical-rings configuration L - C - R forming a triangle with a central angle Θ. The origin of the phase φ_0 runs along the L - C axis, the rings L - C and C - R are separated a distance d from the potential minima at $\rho = \rho_0$.

of the tunneling strength J_2 and J_3 with the separation distance (see Fig. 2.3). In this case, ordering the amplitudes of the local eigenstates as $\{a_{+l}^L, a_{-l}^L, a_{+l}^C, a_{-l}^C, a_{+l}^R, a_{-l}^R\}$, yields the following six-state-model (SSM) Hamiltonian,

$$
\hat{\mathcal{H}}_{SSM}^l = \begin{pmatrix}
E^l & J_1^l & J_2^l & J_3^l & 0 & 0 \\
J_1^l & E^l & J_3^l & J_2^l & 0 & 0 \\
J_2^l & J_3^l & E^l & J_1^l \left(1 + e^{-2il\Theta}\right) & J_2^l & J_3^l e^{-2il\Theta} \\
J_3^l & J_2^l & J_1^l \left(1 + e^{2il\Theta}\right) & E^l & J_3^l e^{2il\Theta} & J_2^l \\
0 & 0 & J_2^l & J_3^l e^{-2il\Theta} & E^l & J_1^l e^{-2il\Theta} \\
0 & 0 & J_3^l e^{2il\Theta} & J_2^l & J_1^l e^{2il\Theta} & E^l
\end{pmatrix}. \quad (2.39)
$$

Any two-dimensional lattice of rings can be understood as a series of pairs of rings with either real or complex couplings, described by the four and six-state models, Eqs. (2.35) and (2.39), respectively. In Chapter 4 we will explore a lattice formed of inline rings, where the couplings are real, while in Chapter 5 we will study a lattice with complex couplings. In Chapter 3, we consider an entirely different configuration of tunnel coupled ring potentials: two rings stacked one on top of the other. In contrast with the case of coplanar rings, cylindrical symmetry is preserved in this configuration and the couplings J_3 and J_1 do not arise. In this case, we describe the system in the quasi-one dimensional regime by finding the evolution of the amplitudes of each OAM mode.

Isolated ring potentials can be created through a variety of techniques, including time-averaged potentials [188–190], painting potentials, [191, 192], static Laguerre-Gauss beams [193], magnetic traps [194–196], and conical refraction [197]. Once the trapping potential is in place, the excited states with non-zero OAM can be generated by rotating a weak link[10, 198], by transferring OAM from photons to atoms [133, 199], or using a temperature quench [200]. To generate tunnel-coupled geometries of rings, one can use digital micromirror devices,

which can create arbitrary potentials through a dense array of mirrors that can be controlled individually [201]. This technique has already been used to study a BEC trapped in two coplanar rings side by side [143]. Also, one can engineer a ring lattice using micro-lens arrays by combining them with conical refraction techniques [202], for which a 10×8 lattice was demonstrated. For the particular case of two stacked rings, one can use optical fibers [203]. Additionally, the dynamics of ultracold atoms in coplanar ring lattices are formally equivalent to those of the p_x and p_y excited states of a conventional lattice [204–207]. This corresponds to the limit $\rho_0 = 0$ in our description, and provides another route to observe the results described in Chapters 4 and 5.

2.4   Topology in physics

In this section, we discuss how topology arises in discrete physical systems with a focus on ultracold atoms in optical lattices. We start by making a connection between well-known mathematical results from topology and the main concepts used to analyze the topology of physical systems: the Berry phase, connection, and curvature. Then, we discuss the application of these concepts to periodic systems, which leads to the bulk-boundary correspondence and the concept of topological insulators. Finally, we introduce the Zak phase, used to analyze 1D systems, and describe in detail the simplest 1D topological insulator, the Su-Schrieffer-Heeger model.

2.4.1   Basic concepts

Topology is the field of mathematics that studies the properties of geometrical objects that remain invariant under continuous deformations [208]. Two objects are said to be topologically equivalent if they can be transformed from one to the other through a continuous deformation. These transformations can involve stretching or twisting the object without breaking it or joining any discontinuous parts. Within this mathematical context, an important result is the Gauss-Bonnet theorem, which links differential geometry and topology. It relates the local properties of a surface, the curvature at each point, to its topology, which is a global property [47]. In the particular case of a closed oriented surface S, it reads

$$\frac{1}{4\pi} \int_S \kappa \, dA = 1 - \mathfrak{g}, \tag{2.40}$$

where κ is the curvature, dA is the element of surface area of the object, and $\mathfrak{g} \in \mathbb{N}$ is the genus, the number of holes. The genus is a topological invariant, a quantity that remains invariant under topological deformations. Thus, two topologically equivalent objects share the same topological invariant. Recalling the most famous example, a doughnut and a cup are topologically equivalent ($\mathfrak{g} = 1$), as they can be continuously deformed into one another, while a sphere and a glass, constitute a different topological class ($\mathfrak{g} = 0$, they have no holes).

Topology also arises in quantum systems when considering a continuous variation of its Hamiltonian in parameter space [209]. In analogy with the Gauss-Bonnet theorem [47], the

varying parameters will define a geometrical object in which the so-called Berry curvature will play the role of the curvature κ and the Berry phase will be the resulting topological invariant. As a result, a Hamiltonian can have different topological phases characterized by distinct Berry phases. In this setting, two phases or Hamiltonians are said to be topologically equivalent if they can be continuously deformed into one another while maintaining its relevant symmetries and without closing the energy gap [210]. Consider a Hamiltonian $\hat{\mathcal{H}}(\mathbf{R})$ determined by some time-varying parameters $\mathbf{R} = \mathbf{R}(t)$ such that the instantaneous eigenstates at a given time t fulfill $\hat{\mathcal{H}}|m(\mathbf{R})\rangle = E_m(\mathbf{R})|m(\mathbf{R})\rangle$. Through the course of time evolution, the Hamiltonian changes as the parameters trace a path in parameter space. We take one of the instantaneous eigenstates as an initial state, $|\psi(t=0)\rangle = |m(\mathbf{R}_0)\rangle$ with $\mathbf{R}_0 = \mathbf{R}(t=0)$, and let it evolve. If the energy gaps around $E_m(\mathbf{R})$ remain open during time evolution and the evolution is slow enough compared to the frequencies associated with the energy gaps, the adiabatic theorem tells us that the system will remain in the instantaneous eigenstate without transitioning to other states [172]. Then, the time evolved state will only pick up a phase factor $|\psi(t)\rangle = e^{i\theta_m(t)}|m(\mathbf{R})\rangle$. The phase $\theta_m(t)$ can be obtained by introducing this expression into the Schrödinger equation [211]

$$\hat{\mathcal{H}}e^{i\theta_m}|m(\mathbf{R})\rangle = i\hbar\frac{\partial}{\partial t}e^{i\theta_m}|m(\mathbf{R})\rangle,$$

$$e^{i\theta_m}E_m(\mathbf{R})|m(\mathbf{R})\rangle = -\hbar e^{i\theta_m}\frac{\partial\theta_m}{\partial t}|m(\mathbf{R})\rangle + i\hbar e^{i\theta_m}\frac{\partial}{\partial t}|m(\mathbf{R})\rangle,$$

(2.41)

and projecting over $\langle m(\mathbf{R})|$,

$$\frac{\partial\theta_m}{\partial t} = i\langle m(\mathbf{R})|\frac{\partial}{\partial t}|m(\mathbf{R})\rangle - \frac{1}{\hbar}E_m(\mathbf{R}).$$

(2.42)

Integrating the above expression (2.42) over the time interval of the evolution yields

$$\theta_m(t) = i\int_0^t \langle m(\mathbf{R})|\frac{\partial}{\partial t'}|m(\mathbf{R})\rangle dt' - \frac{1}{\hbar}\int_0^t E_m(\mathbf{R})dt' = \gamma_m(t) + \beta_m(t).$$

(2.43)

Thus, the evolved state acquires a complex phase composed of two terms: $\beta_m(t)$ is the usual dynamical phase that any state acquires due to time evolution and $\gamma_m(t)$ is the geometrical or Berry phase, discovered by Berry in 1984 [212]. As Berry later stated in [213], $\beta_m(t)$ answers the question *how long did your journey take?* While $\gamma_m(t)$ answers *where did it take you?*

The geometrical nature of the Berry phase is revealed when rewriting it in terms of the Berry connection $\mathbf{A}_m(\mathbf{R})$ by using $\frac{\partial}{\partial t}|m[\mathbf{R}(t)]\rangle = \nabla_{\mathbf{R}}|m(\mathbf{R})\rangle\frac{d\mathbf{R}(t)}{dt}$, which gives

$$\gamma_m = i\int_{\mathbf{R}(0)}^{\mathbf{R}(t)} \langle m(\mathbf{R})|\nabla_{\mathbf{R}}|m(\mathbf{R})\rangle \cdot d\mathbf{R} = \int_{\mathbf{R}(0)}^{\mathbf{R}(t)} \mathbf{A}_m(\mathbf{R}) \cdot d\mathbf{R}.$$

(2.44)

One might note that the Berry connection is only gauge invariant for closed paths through parameter space. In this case, the Berry phase can be rewritten using Stokes theorem as

$$\gamma_m = \oint_{\mathcal{C}} \mathbf{A}_m(\mathbf{R}) \cdot d\mathbf{R} = \iint_{\mathcal{A}} [\nabla \times \mathbf{A}_m(\mathbf{R})] \cdot d\mathbf{S} \equiv \iint_{\mathcal{A}} \mathbf{\Omega}_m \cdot d\mathbf{S},$$

(2.45)

where $\boldsymbol{\Omega}_m = \nabla \times \mathbf{A}_m(\mathbf{R})$ is the Berry curvature and the integral is now performed over the surface $\mathcal{A}$ enclosed by the curve $\mathcal{C}$. The Berry curvature plays the role of the geometrical curvature in Gauss-Bonnet theorem, while the Berry phase becomes the topological invariant [214]. The surface of the geometrical object here becomes the surface $\mathcal{A}$ in parameter space. While the Berry phase is derived assuming that there are no degeneracies in the spectrum during the adiabatic time evolution, Wilczek and Zee proposed a generalization of this concept to take them into account [215, 216].

Periodic systems present a natural choice of parameters that affect the eigenstates of the system: the components of the quasimomentum $\boldsymbol{q}$. As discussed in Section 2.2.1, the Bloch theorem states that eigenstates of the Hamiltonian describing a single particle in a periodic potential can be written as a plane wave times a periodic function $u_{\boldsymbol{q}}^n$. The Brillouin zone, which contains unique eigenstates in quasimomentum space, has periodic boundaries, and thus can be regarded as a closed surface over which the eigenstates of the system vary. In this case, one might write the corresponding Berry phase for a given energy band n as [211]

$$\gamma_n = i \int_{BZ} \left\langle u_{\boldsymbol{q}}^n \left| \nabla_{\boldsymbol{q}} \right| u_{\boldsymbol{q}}^n \right\rangle \cdot d\boldsymbol{q}, \tag{2.46}$$

where now the integral is performed over the Brillouin zone. Remarkably, the value of the Berry phase of a periodic system predicts the presence or absence of states localized at the boundary when considering open boundary conditions. This is known as the bulk-boundary correspondence. Consider an insulator with a given topological invariant characterizing its bulk, surrounded by an insulator with a distinct topological invariant, such as air or vacuum. When considering the two insulators as a whole, the topological invariant changes from the inner medium to the outer one, which can only occur if the energy gap closes at the boundary. This is the origin of the edge states, which are conducting states that bridge the energy gap and are localized at the boundary of the inner medium. Then, the inner insulator is said to be in a topological phase, while the surrounding insulator is in a trivial one. Therefore, the topological invariant of the bulk, which is defined for periodic boundary conditions, determines the presence of states at the boundary when considering open boundary conditions. This effect can be observed in the integer quantum Hall effect [48], whose discovery gave rise to the field of topological insulators [217]. These materials are insulating in the bulk but conducting at the boundary of the material due to the presence of conducting edge states.

Zak phase

In Chapters 4 and 5, we will deal with 1D topological insulators, which are characterized through the Zak phase. This phase is the Berry phase in 1D, and was first used by J. Zak to analyze electronic energy bands in solids [218]. It reads

$$\mathcal{Z}_n = i \int_{-\frac{\pi}{D}}^{\frac{\pi}{D}} \left\langle u_q^n \left| \frac{d}{dq} \right| u_q^n \right\rangle dq, \tag{2.47}$$

where D is the lattice spacing. For inversion symmetric systems, J. Zak showed that $\mathcal{Z}_n$ is quantized, taking the values $\mathcal{Z}_n = 0, \pi \pmod{2\pi}$, which corresponds to the trivial and the

topological phase, respectively [218]. For a given energy gap, the total Zak phase is given by the sum of all Zak phases of the bands underneath that gap $\mathcal{Z} = \sum_n \mathcal{Z}_n$ [219]. This total Zak phase determines the presence of edge states when one considers open boundary conditions [220–222]. A convenient method to compute $\mathcal{Z}_n$ numerically is the Wilson-loop approach, where one approximates the integral by a summation of small segments [210, 220]. The Zak phase for a sufficiently small segment from q_j to q_{j+1} is $e^{-i\mathcal{Z}_n^j} \approx \langle u_{q_j}^n \mid u_{q_{j+1}}^n \rangle$, where we have approximated the differentiation by a finite difference. Then, the Zak phase over the whole Brillouin zone is the sum for all segments $\mathcal{Z}_n = \sum_j \mathcal{Z}_n^j$. However, the wavefunctions computed numerically can have arbitrary phases which affect the value of $\mathcal{Z}_n$. To avoid this problem, one can write the exponential in a gauge invariant form, i.e., invariant under transformations of the form $|u_q^n\rangle \to e^{if(q)}|u_q^n\rangle$,

$$\mathcal{W}_n = e^{-i\mathcal{Z}_n} = \prod_{j=1}^N e^{-i\mathcal{Z}_n^j} = \prod_{j=1}^N \langle u_{q_j}^n | u_{q_{j+1}}^n \rangle, \tag{2.48}$$

such that the Zak phase can be recovered as $\mathcal{Z}_n = \mathrm{Arg}\left(\lim_{N \to \infty} \mathcal{W}_n\right)$. Therefore, in order to compute the Zak phase, one needs to find the functions $|u_q^n\rangle$ by writing the Hamiltonian in quasimomentum space. The band structure of the Hamiltonian, described in Section 2.2.1, can be recovered in the tight binding formalism by considering periodic boundary conditions and letting the number of unit cells N_c tend to infinity so that one can expand the creation and annihilation operators as a Fourier integral. The expressions for the creation and annihilation operators read

$$\hat{c}_j^\dagger = \frac{1}{\sqrt{N_c}}\sqrt{\frac{D}{2\pi}} \int_{BZ} \hat{c}_q^\dagger e^{iqx_j} dq,$$
$$\hat{c}_j = \frac{1}{\sqrt{N_c}}\sqrt{\frac{D}{2\pi}} \int_{BZ} \hat{c}_q e^{-iqx_j} dq, \tag{2.49}$$

where D is the lattice spacing and $x_j = jD$ is the position of the unit cell j. For lattices with more than one site per unit cell, there are two conventions for the bulk Hamiltonian, sometimes called Basis I and Basis II in the literature. In Basis I, the most common and the one we use here [223, 224], the index x_j denotes the position of the unit cell (the external degree of freedom) without specifying the position of each site within the unit cell (the internal one). This restricts the amount of information of the associated Zak phase but simplifies its computation. In Basis II, one also takes into account the internal degrees of freedom [224, 225]. Both basis have been used to accurately characterize the topology of 1D systems in both theoretical and experimental studies (see [226] and references therein).

2.4.2 Su-Schrieffer-Heeger model

The simplest example of a topological insulator is the Su-Schrieffer-Heeger (SSH) model, a 1D lattice with alternating couplings t_1 and t_2. It was introduced by Su, Schrieffer, and Heeger for spinless fermions to explain the conductivity properties of the molecule polyacetylene [227].

Its tight binding Hamiltonian reads

$$\hat{\mathcal{H}}_{\text{SSH}} = \sum_{k=1}^{N_c} \left[t_1(\hat{a}_k^\dagger \hat{b}_k + \hat{b}_k^\dagger \hat{a}_k) + t_2(\hat{b}_k^\dagger \hat{a}_{k+1} + \hat{a}_{k+1}^\dagger \hat{b}_k) \right], \tag{2.50}$$

where N_c is the number of unit cells. Each unit cell k is composed of two sites A and B, with associated creation operators $\hat{a}_k^\dagger, \hat{b}_k^\dagger$ [see Fig. 2.5(a)]. The topological phase of this system is determined by the Zak phase, Eq. (2.47), which is quantized due to the inversion symmetry of this model [218]. In order to obtain it, we need to compute the bulk Hamiltonian, which is a function of the annihilation and creation operators in quasimomentum space. We introduce Eq. (2.49) with $\hat{c} = \hat{a}, \hat{b}$ into the SSH Hamiltonian (2.50) and compute first the terms of the Hamiltonian proportional to $\hat{a}^\dagger \hat{b}$:

$$
\begin{aligned}
\hat{\mathcal{H}}_{\text{SSH}}^{red} &= \sum_{j=1}^{N_c} t_1 \hat{a}_j^\dagger \hat{b}_j + t_2 \hat{a}_{j+1}^\dagger \hat{b}_j \\
&= \frac{D}{2\pi N_c} \sum_{j=1}^{N_c} \int_{\text{BZ}} \int_{\text{BZ}} dq\, dq'\, \hat{a}_q^\dagger \hat{b}_{q'} \left(t_1 e^{iqx_j} e^{-iq'x_j} + t_2 e^{iq(x_j+D)} e^{-iq'x_j} \right) \\
&= \frac{D}{2\pi N_c} \sum_{j=1}^{N_c} \int_{\text{BZ}} \int_{\text{BZ}} dq\, dq'\, \hat{a}_q^\dagger \hat{b}_{q'} \left(t_1 e^{ix_j(q-q')} + t_2 e^{ix_j(q-q')} e^{iqD} \right) \\
&= \int_{\text{BZ}} \int_{\text{BZ}} dq\, dq'\, \hat{a}_q^\dagger \hat{b}_{q'} \delta\left(q - q'\right) \left(t_1 + t_2 e^{iqD} \right) \\
&= \int_{\text{BZ}} dq\, \hat{a}_q^\dagger \hat{b}_q \left(t_1 + t_2 e^{iqD} \right)
\end{aligned}
\tag{2.51}
$$

Performing the same computation for the terms of $\hat{\mathcal{H}}_{\text{SSH}}$ proportional to $\hat{b}^\dagger \hat{a}$, one obtains $\hat{\mathcal{H}}_{\text{SSH}}$ (2.50) in terms of the creation and annihilation operators in quasimomentum space,

$$\hat{\mathcal{H}}_{\text{SSH}} = \int_{\text{BZ}} dq \left[\hat{a}_q^\dagger \hat{b}_q \left(t_1 + t_2 e^{iqD} \right) + \hat{b}_q^\dagger \hat{a}_q \left(t_1 + t_2 e^{-iqD} \right) \right], \tag{2.52}$$

and the real space Hamiltonian can be written as

$$\hat{\mathcal{H}}_{\text{SSH}} = \int_{\text{BZ}} \hat{\boldsymbol{\Psi}}_q^\dagger H_q \hat{\boldsymbol{\Psi}}_q dq, \qquad \text{where} \qquad \hat{\boldsymbol{\Psi}}_q = \begin{pmatrix} \hat{a}_q \\ \hat{b}_q \end{pmatrix}. \tag{2.53}$$

Thus, the bulk Hamiltonian takes a matrix form that reads

$$H_q = \begin{pmatrix} 0 & t_1 + t_2 e^{iqD} \\ t_1 + t_2 e^{-iqD} & 0 \end{pmatrix}. \tag{2.54}$$

Due to the internal degree of freedom of the SSH model, spanned by the sites A and B [see Fig. 2.5(a)], the bulk-Hamiltonian is a 2×2 matrix with two eigenvalues $E_{1(2)}(q) =$
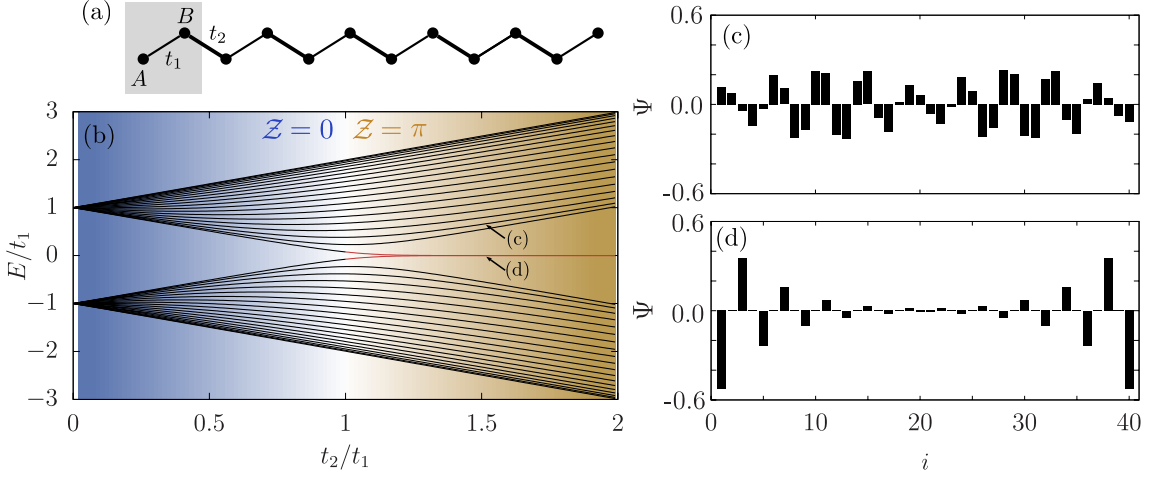
Figure 2.5: (a) Representation of the SSH model where the shadowed region indicates the unit cell with sites A and B, and t_1 and t_2 indicate the intra and intercell couplings, respectively. (b) Energy spectrum for $N_c = 20$ unit cells as a function of t_2/t_1 with the trivial ($\mathcal{Z} = 0$) and topological ($\mathcal{Z} = \pi$) phases indicated in blue and orange, respectively, and the edge states indicated in red. Amplitude at each site i of (c) an extended state and of (d) an hybridized edge state, for $t_2/t_1 = 1.5$ as indicated in (b).

$\overset{(+)}{_{(-)}}\sqrt{t_1^2 + t_2^2 + 2t_1 t_2 \cos(qD)}$, that define the band structure of the model. The associated eigenvectors are

$$|u_q^1\rangle = \frac{1}{\sqrt{2}} \begin{pmatrix} \frac{\sqrt{t_1^2 + t_2^2 + 2t_1 t_2 \cos(qD)}}{t_1 + t_2 e^{-iqD}} \\ -1 \end{pmatrix}, \quad |u_q^2\rangle = \frac{1}{\sqrt{2}} \begin{pmatrix} \frac{\sqrt{t_1^2 + t_2^2 + 2t_1 t_2 \cos(qD)}}{t_1 + t_2 e^{-iqD}} \\ +1 \end{pmatrix}.$$

$$(2.55)$$

From the eigenvectors (2.55), one can compute the Zak phase, which takes a value of 0 for $t_1 > t_2$ and a value of π for $t_1 < t_2$. Due to the bulk-boundary correspondence, a phase of π predicts the presence of two edge states for open boundary conditions [228, 229]. Figure 2.5(b) shows the energy spectrum for $N_c = 20$ unit cells as a function of t_2/t_1 with the trivial ($\mathcal{Z} = 0$) and topological ($\mathcal{Z} = \pi$) phases indicated in blue and orange, respectively. Two states depart from the bulk bands when the Zak phase changes from 0 to π and remain separated from them at zero energy. The presence of these edge states becomes intuitive when considering the dimerized limit, when either t_1 or t_2 are zero and the chain is composed of a series of decoupled dimers. For $t_1 = 0$, there is a single site completely disconnected at each boundary, which generates two strictly localized eigenstates. For $t_2 = 0$, the complete lattice is composed of dimers, which generate degenerate eigenstates with energies $\pm t_1$. For $t_1 < t_2$ with $t_1 \neq 0$, the edge states penetrate into the bulk while maintaining an exponential localization with respect to the edge [shown in Fig. 2.5(d)]. Thus, the model presents two edge states whenever the lattice starts and ends with the weaker coupling. These edge states are topologically protected by chiral symmetry, also known as sublattice symmetry, which keeps them locked at zero energy [210]. For a chirally symmetric lattice, one can divide the

chain into two sublattices containing the sites A or B such that there are no couplings, either hopping terms or on-site potentials, within each sublattice (in graph theory, this corresponds to a bipartite graph). This symmetry is defined by a unitary and Hermitian operator $\hat{\Gamma}$ that anti-commutes with the Hamiltonian $\hat{\Gamma}\hat{\mathcal{H}}\hat{\Gamma}^{\dagger} = -\hat{\mathcal{H}}$. For the SSH model, it takes the same form at each unit cell j, $\hat{\Gamma} = \oplus_{j=1}^{N_c}\sigma_z$, where σ_z is the z Pauli matrix. This operator can also be written in terms of the orthogonal sublattice projectors $\hat{P}_A = \frac{1}{2}(\mathbb{I} + \hat{\Gamma})$ and $\hat{P}_B = \frac{1}{2}(\mathbb{I} - \hat{\Gamma})$, where $\mathbb{I}$ is the identity operator. Note that the total action of $\hat{P}_A$ and $\hat{P}_B$ spans the whole Hilbert space, $\hat{P}_A + \hat{P}_B = \mathbb{I}$, as they project on the subset of sites $A(B)$. The presence of this symmetry has some important consequences on the energy spectrum. Given a chirally symmetric Hamiltonian with a set of eigenstates $\hat{\mathcal{H}}|\psi_n\rangle = E_n|\psi_n\rangle$, the energy spectrum is symmetric,

$$\hat{\mathcal{H}}\hat{\Gamma}|\psi_n\rangle = -\hat{\Gamma}\hat{\mathcal{H}}|\psi_n\rangle = -\hat{\Gamma}E_n|\psi_n\rangle = -E_n\hat{\Gamma}|\psi_n\rangle, \tag{2.56}$$

where $\hat{\Gamma}|\psi_n\rangle$ is the chiral partner of $|\psi_n\rangle$, with energy $-E_n$. Thus, each zero-energy edge state is the chiral partner of the other edge state. Additionally, the edge states have support on a single sublattice. As $\hat{\mathcal{H}}|\psi_n\rangle = 0$ for the edge states,

$$\hat{\mathcal{H}}\hat{P}_{A(B)}|\psi_n\rangle = \hat{\mathcal{H}}\left(|\psi_n\rangle \overset{+}{\underset{(-)}{}} \hat{\Gamma}|\psi_n\rangle\right) = \left(\hat{\mathcal{H}}|\psi_n\rangle \overset{(+)}{\underset{-}{}} \hat{\Gamma}\hat{\mathcal{H}}|\psi_n\rangle\right) = 0. \tag{2.57}$$

In contrast, the non-zero energy eigenstates have non-degenerate chiral pairs, and thus must be orthogonal. As a consequence, they have equal support on both sublattices

$$0 = \langle\psi_n|\hat{\Gamma}|\psi_n\rangle = \langle\psi_n|\hat{P}_A|\psi_n\rangle - \langle\psi_n|\hat{P}_B|\psi_n\rangle. \tag{2.58}$$

In the thermodynamic limit (i.e., $N_c \to \infty$), one can find approximate solutions that are exponentially localized at the edge and that occupy a single sublattice. For a finite lattice, these solutions are hybridized under the action of the Hamiltonian, which produces a small energy splitting that decays exponentially with the size of the system. The eigenstates for a finite system can be approximated as symmetric and antisymmetric superpositions of the edge states localized at each boundary [210]. This energy splitting can be seen in Fig. 2.5(b) at $t_2/t_1 \gtrsim 1$ due to the small size of the lattice ($N_c = 20$). Figures 2.5(c) and (d) represent the amplitudes at each site i of two eigenstates for $t_2/t_1 = 1.5$. Fig. 2.5(c) corresponds to an extended state which occupies both sublattices, while Fig. 2.5(d) represents one hybridized edge state which mostly occupies one sublattice on the left half of the chain and the other sublattice on the right half.

2.5 Thermalization

In this section, we explore the concept of thermalization in quantum systems. We first take a step back to introduce classical thermalization, which is closely related to the notions of ergodicity, mixing, and chaos, and that relies on the concept of phase space. We also discuss how classical integrable systems fail to thermalize. Then, we explain the obstacles that arise when going from a classical to a quantum description and outline the main ideas behind the

eigenstate thermalization hypothesis (ETH). Finally, we briefly discuss the different kinds of systems that violate this hypothesis and thus fail to thermalize.

2.5.1 Classical thermalization

A classical system (e.g., a gas) in thermal equilibrium can be well-characterized by macroscopic quantities such as the temperature and the chemical potential. Remarkably, this description is independent of the positions and momenta of each particle as it is compatible with many microscopic configurations. Given a particular initial state, thermalization is the process by which a system reaches an equilibrium state defined by macroscopic quantities. Therefore, the process of thermalization can be thought of as the erasure of the information of the initial state [230].

The description of classical thermalization relies on the notion of phase space. Consider a collection of N particles with positions $\{\mathbf{r}_1, \mathbf{r}_2, ..., \mathbf{r}_N\}$ and momenta $\{\mathbf{p}_1, \mathbf{p}_2, ..., \mathbf{p}_N\}$. These $2N$ degrees of freedom are the continuous variables that define the phase space $\{\mathbf{r}_1, \mathbf{r}_2, ..., \mathbf{r}_N, \mathbf{p}_1, \mathbf{p}_2, ..., \mathbf{p}_N\}$. Given an initial state with a certain energy, time evolution will define a trajectory $\vartheta(t)$ through the phase space. However, the trajectory $\vartheta(t)$ will be restricted to a constant-energy hypersurface in the phase space due to energy conservation. Such a system can be analyzed through the lens of dynamical systems theory and its subfield, ergodic theory. There are mainly three properties of dynamical systems underlying classical thermalization [231]: ergodicity, mixing and chaos.

- Ergodicity. For (almost) all initial states, the trajectory gets arbitrarily close to all points in phase space for sufficiently long times. Additionally, Liouville's theorem [232] implies that the system will spend equal amounts of time in equal volumes of phase space [231]. As a consequence, long-time averages of observables can be computed as phase-space averages, which are far easier to calculate.

- Mixing. Given an initial state with a small spread in phase space it eventually acquires a uniform spread over the whole phase space, as correlations to the initial state decay through time evolution. This is the same process by which a drop of dye in a glass of water eventually gives the water a uniform color when the water is stirred, which corresponds to time evolution [233].

- Chaos. Initial states that are arbitrarily close in phase space exhibit exponentially diverging trajectories in phase space, thus presenting a high sensitivity to perturbations in the initial state. The strength of the chaotic behavior can be quantified through the so-called Lyapunov exponents, which measure the rate of divergence of the trajectories. Given the separation $\delta(t) = \vartheta(t) - \vartheta'(t)$ between two nearby trajectories, the maximal Lyapunov exponent, $\lambda = \lim_{t\to\infty} \lim_{|\delta(0)|\to 0} \frac{1}{t} \ln \frac{|\delta(t)|}{|\delta(0)|}$, gives the mean exponential rate of divergence [234]. Then, a positive value of λ is taken as a strong indicator of chaos and serves as a measure of the predictability of the system.

These concepts can be classified into the Ergodic Hierarchy [235], which can be conceptually simplified to

$$\text{Chaotic} \subset \text{Mixing} \subset \text{Ergodic}, \tag{2.59}$$

where we have included chaos following [236, 237] (the interested reader can find a much more nuanced classification and discussion in [233]). Ergodicity is the first level of this hierarchy, which implies that ergodic systems need not be mixing or chaotic. Then, mixing is a stronger condition that implies ergodicity, and chaos implies both mixing and ergodicity. However, for classical systems with a large number of particles, one generally expects chaos, mixing and ergodicity [231]. Therefore, classical systems thermalize through the course of time evolution, which adequately scrambles the phase space such that the information on the initial state effectively disappears.

However, not all classical systems thermalize. Integrable systems present as many conserved quantities as degrees of freedom, which exactly determine the trajectories through the phase space. As a consequence, these systems do not explore the whole phase space, they are not ergodic. The difference between chaotic and integrable systems can be intuitively visualized in dynamical billiards. Consider a classical particle moving at a fixed constant velocity and trapped in a region with zero external potential that is enclosed by infinite potential walls. When the particle encounters a wall, it bounces off elastically producing a specular reflection. In two dimensions, such systems represent an ideal model of a billiard game that ignores effects such as friction and thus conserves kinetic energy. The dynamics in these geometrical enclosures, referred to as stadiums, critically depend on the geometry [238]. In Figure 2.6, we compare trajectories in a circular stadium [Fig. 2.6(a)] and a Bunimovich stadium, which is composed of two parallel lines united by circular sections at both ends [Fig. 2.6(b) and (c)] [239]. In Fig. 2.6(a) and (b), dark blue lines indicate the first 50 reflections, while the gray lines beneath show up to the 200th reflection. For the Bunimovich stadium, almost all initial states lead to the particle eventually exploring the complete surface of the stadium, such that the trajectory eventually covers the whole stadium uniformly. Note that one can find trajectories that do not explore the whole stadium, such as one that bounces perpendicularly to the parallel walls without touching the circular ones. Those trajectories form the set of measure zero of initial states that do not explore the whole phase space in this ergodic system. In contrast, the circular stadium is an integrable system: it conserves not only energy, but also angular momentum, due to the presence of cylindrical symmetry. As a result, the trajectories are a superposition of radial and angular periodic motions such that the trajectory leaves some regions of the stadium unexplored. Fig. 2.6(c) illustrates chaos in the Bunimovich stadium by representing the first 6 reflections for slightly different initial conditions. The trajectories are highly sensitive to perturbations in the initial conditions: they rapidly diverge and their positions and direction of motion become uncorrelated.

2.5.2   Quantum thermalization

In this section we explore how the notion of classical thermalization is translated into the realm of quantum physics. Due to Heisenberg's uncertainty principle, position and momentum
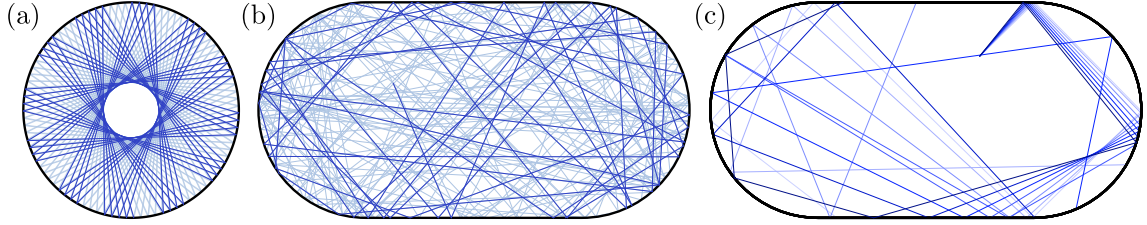
Figure 2.6: Trajectories exemplifying (a) integrability in the circular stadium and (b) ergodicity and (c) chaos in the Bunimovich stadium. (a,b) The first 50 reflections are indicated in blue and gray lines indicate up to the 200th reflection. (c) First 6 reflections for slightly different initial conditions illustrating the rapidly diverging trajectories in a chaotic system.

in a quantum system cannot be determined simultaneously with arbitrary precision, $\Delta_x \Delta_p \geq \hbar/2$. As a consequence, there is no notion of phase space and trajectories cannot be defined. Additionally, the Schrödinger equation is linear, in contrast with the non-linearity that leads to chaos in classical systems. As discussed in Section 2.5.1, classical systems thermalize through the course of time evolution and the description of this process relies on the notion of phase space [74]. In contrast, here we will see that quantum systems thermalize due to the presence of thermal eigenstates and that unitary time evolution only reveals their presence [89].

The eigenstate thermalization hypothesis (ETH) provides a framework to understand thermalization in an isolated quantum many-body system [72–74]. However, it is not immediately obvious what thermalization means in this context. Statistical quantum mechanics often deals with quantum systems in contact with an environment that acts as a reservoir [240]. In these systems, thermalization is enabled by the exchange of energy and particles between the system and the environment [see Fig. 2.7(a)]. However, isolated quantum many-body systems, by definition, lack this reservoir, such that thermalization requires a slightly different conceptualization. Let us consider a bipartition of the Hilbert space H into two subsystems $\mathcal{A}$ and $\mathcal{B}$ such that $\dim(\mathcal{A}) \ll \dim(\mathcal{B})$ [see Fig. 2.7(b)]. This could correspond, for example, to an optical lattice of L sites subdivided into two subsystems spanning $L_\mathcal{A}$ and $L_\mathcal{B}$ sites such that $L_\mathcal{A} \ll L_\mathcal{B}$. This bipartition is physically relevant because the measurement of global operators in a thermodynamically large system (with an exponentially large Hilbert space) is not experimentally feasible [241, 242]. Instead, one can measure local operators acting on a finite subset of the Hilbert space, for example, on subsystem $\mathcal{A}$. The system thermalizes if the subsystem $\mathcal{B}$ acts as a reservoir for the subsystem $\mathcal{A}$, such that local operators acting on $\mathcal{A}$ acquire thermal expectation values. Now we can understand how the erasure of information underpinning classical thermalization also seems to arise in quantum systems, where unitary evolution prevents the loss of information (i.e., given an initial state with a density matrix ρ, the purity, $\mathrm{tr}(\rho^2)$, remains constant). Thermalization in an isolated quantum system occurs as entanglement spreads between subsystems $\mathcal{A}$ and $\mathcal{B}$ as they exchange energy and particles [90]. Thus, the information on the initial state is transferred to inaccessible highly-nonlocal observables, while the measurable local observables in $\mathcal{A}$ acquire thermal expectation val-
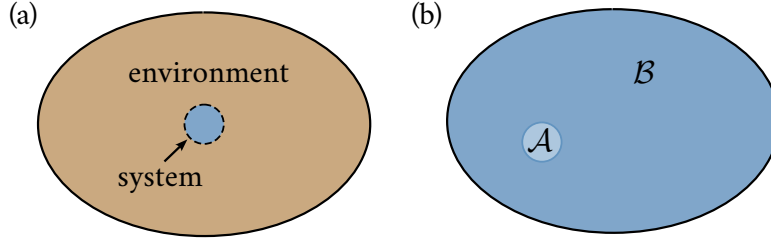
Figure 2.7: (a) Quantum system in contact with an environment in which thermalization is possible through the exchange of energy and particles with the thermal bath. (b) Isolated quantum system where thermalization takes place when a subsystem $\mathcal{B}$ acts as a reservoir for a much smaller subsystem $\mathcal{A}$.

ues. Let us explicitly write this argument to find the consequences of thermalization on the eigenstates of the system.

Consider a Hamiltonian $\hat{\mathcal{H}}$, with eigenstates $\hat{\mathcal{H}}|E_\alpha\rangle = E_\alpha|E_\alpha\rangle$, and an initial state $|\psi(0)\rangle = \sum_\alpha c_\alpha |E_\alpha\rangle$ with a small energy variance,

$$\langle\psi(0)|\hat{\mathcal{H}}|\psi(0)\rangle = \bar{E}, \quad \sqrt{\langle\psi(0)|\hat{\mathcal{H}}^2|\psi(0)\rangle - \bar{E}^2} = \Delta \ll W, \tag{2.60}$$

where W is the bandwidth of the energy spectrum. The system thermalizes if local observables reach equilibrium expectation values given by the microcanonical ensemble [89]. At a time t, the state is given by $|\psi(t)\rangle = \sum_\alpha c_\alpha e^{-iE_\alpha t/\hbar}|E_\alpha\rangle$, such that the expectation value of a local observable $\hat{O}$ can be written as

$$\langle\hat{O}(t)\rangle = \langle\psi(t)|\hat{O}|\psi(t)\rangle = \sum_\alpha |c_\alpha|^2 O_{\alpha\alpha} + \sum_{\alpha\neq\beta} c_\alpha^* c_\beta O_{\alpha\beta} e^{i(E_\alpha - E_\beta)t}. \tag{2.61}$$

Assuming that the expectation value $\langle\hat{O}(t)\rangle$ eventually reaches equilibrium and stays near the equilibrium value with small fluctuations, the equilibrium value of $\langle\hat{O}(t)\rangle$ can be well approximated by its infinite-time average, which reads

$$\langle\hat{O}\rangle_\infty \equiv \lim_{t\to\infty} \frac{1}{t}\int_0^t dt\, \langle\hat{O}(t)\rangle = \sum_\alpha |c_\alpha|^2 \langle E_\alpha|\hat{O}|E_\alpha\rangle. \tag{2.62}$$

We have assumed a non-extensive number of degeneracies such that the off-diagonal terms in Eq. (2.61) cancel due to dephasing when computing the infinite-time average. Thus, $\langle\hat{O}\rangle_\infty$ is exclusively determined by the so-called diagonal ensemble, which only depends on the probabilities $|c_\alpha|^2$ determining the initial state and the expectation values of the eigenstates, $\langle E_\alpha|\hat{O}|E_\alpha\rangle$. The system thermalizes if $\langle\hat{O}\rangle_\infty$ equals the microcanonical prediction for a microcanonical shell around the mean energy of the initial state, $\bar{E}$,

$$\langle\hat{O}\rangle_{\mathrm{mc}}|_{\bar{E}} \equiv \frac{1}{\mathcal{N}} \sum_{\{E_\alpha|\Delta E > |\bar{E} - E_\alpha|\}} \langle E_\alpha|\hat{O}|E_\alpha\rangle, \tag{2.63}$$

where the sum includes the $\mathcal{N}$ eigenstates with energies inside the microcanonical shell $\left|\bar{E} - E_\alpha\right| < \Delta E$. Comparing equations (2.62) and (2.63), we note that $\langle\hat{O}\rangle_\infty$ depends on the initial state through the probabilities $|c_\alpha|^2$, while $\langle\hat{O}\rangle_{\mathrm{mc}}\big|_{\bar{E}}$ only depends on the energy $\bar{E}$. However, if the expectation values of the eigenstates $\langle E_\alpha|\hat{O}|E_\alpha\rangle$ fluctuates only weakly for eigenstates with nearby energies, they can be taken out of the sum in Eq. (2.62) [74]. Then, one can use the normalization of the probabilities $|c_\alpha|^2$ to see that $\langle\hat{O}\rangle_\infty = \langle\hat{O}\rangle_{\mathrm{mc}}\big|_{\bar{E}}$. This leads to the main idea of the ETH, that can be stated as follows [72–74]:

> For a large interacting and isolated quantum many-body system, the expectation values of a local observable $\hat{O}$ on the eigenstates of the Hamiltonian, $\langle E_\alpha|\hat{O}|E_\alpha\rangle$, coincide with the microcanonical ensemble average around the corresponding energy $\langle\hat{O}\rangle_{\mathrm{mc}}\big|_{E_\alpha}$.

Then, the eigenstates themselves are said to be thermal, and their presence explains the thermalization of isolated quantum many-body systems.

2.5.3   Non-ergodic systems

In analogy with classical systems, not all isolated quantum many-body systems obey the ETH and thermalize. Such systems violate this hypothesis either weakly or strongly, depending on the relative number of eigenstates that are non-thermal. The main examples are briefly discussed below.

- **Quantum integrable systems** are those that present at least as many conserved quantities as degrees of freedom in the system. There must be an extensive number of local operators that commute with the Hamiltonian and with each other, thus excluding the projectors to the eigenstates of the system [89]. The presence of these conservation laws exactly determines the eigenstates and eigenvalues of the system and prevents it from thermalizing, analogously to what occurs for classical systems [243]. There are many integrable non-interacting many-body systems, such as one-dimensional spin chains solvable by Bethe Ansatz. In contrast, integrable interacting models are fine-tuned and hard to implement, as even small perturbations can shift the model away from integrability [89, 243]. In nearly-integrable models, those with small terms breaking integrability, the system rapidly relaxes to a steady state determined by the integrable model and only reaches the true thermal equilibrium at a much longer timescale. This phenomenon is known as prethermalization [244].

- Systems exhibiting **many-body localization** [245] (MBL) also fail to thermalize as predicted by the ETH due to the interplay between interactions and strong disorder [90]. As thermalization requires the exchange of energy and particles, MBL systems prevent thermalization due to their insulating nature, in analogy with the non-interacting case of Anderson insulators [118]. This causes the emergence of integrability through an extensive set of quasi-local integrals of motion (LIOMS). Many-body localization is stable within a broad range of interactions and variation of the parameters of the Hamiltonian, thus, it constitutes an stable phase of matter, in contrast with integrable systems [246, 247].

- Both in integrable systems and MBL the ETH is violated strongly by all the eigenstates of the system. More recently, it has been shown that the ETH can be weakly violated by a vanishing subset of states in the thermodynamic limit. These states have a very low entanglement entropy compared to the states at the same energy density. **Quantum many-body scars** (QMBS) where discovered experimentally in one-dimensional Rydberg arrays [91] and theoretically in the underlying PXP model [92, 93], while also being shown in the AKTL model [94, 95]. A tower of energy-equispaced scarred states leads to revivals in fidelity and to a slow entanglement growth for certain initial states with an anomalously high overlap with the scarred eigenstates. Additionally, there are also other kinds of non-thermal states that do not lead to fidelity revivals, such as isolated quantum many-body scars or some states generated through projector embedding formalisms [248].

- The ETH can also be violated either weakly or strongly in systems exhibiting **Hilbert space fragmentation** [109] (which has also received the name of Hilbert space shattering [111] and Krylov fracture [113]). The Hilbert space H of a system exhibiting Hilbert space fragmentation is composed of a series of dynamically disconnected sectors. This can be formalized as [113]

$$H = \bigoplus_{j=1}^{K} \mathcal{K}_j, \quad \mathcal{K}_j = \operatorname{span}_t \left\{ e^{-i\hat{\mathcal{H}}t} \ket{\psi_0} \right\}, \tag{2.64}$$

where $\operatorname{span}_t \left\{ e^{-i\hat{\mathcal{H}}t} \ket{\psi_0} \right\} \equiv \operatorname{span} \left\{ \ket{\psi_0}, \hat{\mathcal{H}} \ket{\psi_0}, \hat{\mathcal{H}}^2 \ket{\psi_0}, \cdots \right\}$ denotes the set of states that can be reached through time evolution, i.e., through the action of the Hamiltonian $\hat{\mathcal{H}}$, given an initial state $\ket{\psi_0}$. The state $\ket{\psi_0}$ is usually taken as a product state, as those are easily preparable in an experiment. Any Hamiltonian possessing a symmetry with an associated conservation law takes a block diagonal form where each sector is spanned by the states sharing the same quantum number. What differentiates Hilbert space fragmentation from the effect of conventional symmetries is the exponential growth of the number of sectors with the size of the system. In contrast, conventional symmetries yield either a constant number of sectors (e.g., systems with discrete global symmetry) or one that grows at most polynomially (e.g., systems with a continuous global symmetry) [249]. The sectors in a fragmented system usually have a wide range of dimensions, from frozen (i.e., one-dimensional) sectors to exponentially-large sectors, and they can include both integrable and non-integrable sectors [109]. The fractured structure of the Hilbert space prevents the system from exploring all states and thermalizing as predicted by the ETH. Such blocks usually arise due to kinetic constraints which forbid specific transitions, as the ones arising in a Rydberg blockade, where adjacent atoms cannot be transferred to the Rydberg state. In Chapter 6, we will explore local Hilbert space fragmentation, which arises due to a local conservation law driven by the presence of compact localized states [250].

3

ORBITAL ANGULAR MOMENTUM DYNAMICS OF BOSE-EINSTEIN CONDENSATES TRAPPED IN TWO STACKED RINGS

In this chapter, we study a Bose-Einstein condensate (BEC) trapped in two coupled rings within the mean-field description, using the Gross-Pitaevskii equation (GPE) that we introduced in Section 2.1.2. In particular, we focus on the stationary states and dynamical regimes that arise when the same orbital angular momentum (OAM) mode is populated in both rings. For both cases, we study these regimes in the presence of small perturbations in other OAM modes by using analytical models and numerical simulations.

Ultracold atoms trapped in ring potentials are one of the most promising systems in the emerging field of atomtronics [128, 129, 251, 252]. They have been considered for quantum sensing applications such as rotation sensing [188, 189], magnetometry [253], Sagnac interferometry [145, 254–258], or the atomic analog to superconducting quantum interference devices (SQUIDs) [10, 138–141, 198, 259–261]. Rings are the simplest geometries that lead to non-trivial loop circuits, in which the superfluidity of BECs gives rise to persistent currents [132, 262]. One can transfer OAM to the trapped BEC either by rotating a weak link [10, 198], by coherent transfer of angular momentum from photons to the atoms [133, 199], or by a temperature quench [200]. Regarding the implementation of the ring trapping potential, several techniques have been implemented or proposed: magnetic traps [194–196], conical refraction [197], pairs of optical fibers [203], static Laguerre-Gauss Beams [193], and time-averaged [188–190] or painting [191, 192] potentials (see also [128] and references therein).

On the other hand, the Josephson effect is a fundamental phenomenon in quantum mechanics that has been widely explored in superconductors, and its study has been recently extended to bosonic ultracold atomic systems [263–270]. Josephson oscillations can arise in weakly coupled BECs trapped in a double-well potential: when there is a non-zero population imbalance, quantum tunneling allows the particles to oscillate periodically from one well to the other. However, repulsive interactions can suppress tunneling such that the atoms remain mostly trapped in one of the wells, regime known as macroscopic quantum self-trapping [265]. Weakly coupled condensates have been proposed as basic building blocks for quantum

technologies [271–274]. In particular, the dynamics of BECs in tunnel-coupled ring potentials have been thoroughly explored in a variety of geometries such as stacked rings with [275, 276] or without lattices [277–285], concentric rings [186, 286], or coplanar rings [146, 287].

In this chapter, we investigate a BEC trapped in two rings in a stack configuration to study the interplay between the OAM, the tunneling dynamics, and the repulsive nonlinear interactions. First, we consider an initial state with a single OAM mode equally populated in both rings, which gives rise to symmetric and antisymmetric stationary states. The stability conditions for these states against OAM perturbations were derived within the mean-field theory and using Bogoliubov analysis in [278]. Here, we revisit the problem and demonstrate that the system can be described by a two-state model with fixed point solutions. In particular, one can derive a classical Hamiltonian that characterizes the dynamics of the system in terms of the orbits around the critical points. Second, we consider an initial state where a single OAM mode is populated with a non-zero population imbalance between rings, such that tunneling and interactions give rise to different dynamical regimes. We derive analytically the boundary condition between Josephson oscillations and self-trapping, and study numerically the stability of these regimes against perturbations in higher order OAM modes.

This chapter is organized as follows. In Section 3.1, we describe the physical system and introduce the few-state model of OAM modes derived from the GPE. Section 3.2 deals with the stability of the stationary states: after presenting briefly the Bogoliubov analysis, we derive a two-state model, find its critical points and analyze its associated classical Hamiltonian. The model is then compared against numerical simulations of the complete system of equations derived in Section 3.1. Section 3.3 focuses on the dynamical regimes of Josephson oscillations and self-trapping: we first study the case of populating a single mode in each ring and then explore the role of higher order OAM perturbations. Finally, the conclusions are presented in Section 3.4.

3.1 Physical system

The system under consideration is shown in Fig. 3.1. It consists of two coaxial annular traps around the z-axis separated by a distance $2z_0$, where a BEC of N atoms is trapped. The BEC is described within the mean-field theory by the GPE, Eq. (2.11), which in cylindrical coordinates reads

$$i\hbar\frac{\partial\Psi(\mathbf{r},t)}{\partial t} = \left[\frac{\hbar^2}{2M}\left(-\frac{\partial^2}{\partial\rho^2} - \frac{1}{\rho}\frac{\partial}{\partial\rho} - \frac{\partial^2}{\partial z^2} + \frac{L_z^2}{\hbar^2\rho^2}\right) + V(\mathbf{r}) + g|\Psi(\mathbf{r},t)|^2\right]\Psi(\mathbf{r},t), \quad (3.1)$$

where $V(\mathbf{r})$ is the external potential, M is the atomic mass, $L_z = -i\hbar\frac{\partial}{\partial\phi}$ is the z component of the OAM, and $g = 4\pi\hbar^2 a_s/M$ accounts for the contact interactions characterized by the s-wave scattering length a_s. The wavefunction, $\Psi(\mathbf{r},t)$, is normalized to the total number of particles, N. Henceforth, we will consider exclusively repulsive interactions, $g > 0$, and rings with large enough radii such that the term $\frac{1}{\rho}\frac{\partial}{\partial\rho}$ can be neglected in Eq. (3.1). The trapping potential in (3.1) is defined as $V(\mathbf{r}) = V_z(z) + V_\rho(\rho)$, where V_z is a symmetric double-well
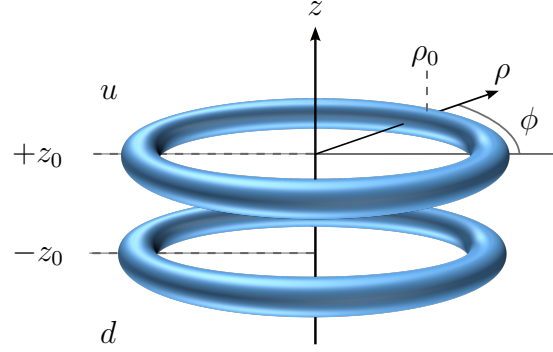
Figure 3.1: Schematic representation of the geometry of the system. The trapping potential consists of two ring traps, up, u, and down, d, that are located in the planes $\pm z_0$, centered at $\rho = 0$, and have radius ρ_0.

harmonic potential with minima at $\pm z_0$, and V_ρ is a harmonic radial potential centered at ρ_0. We assume weak coupling between the rings and that V_z and V_ρ are steep enough such that the BEC only presents azimuthal excitations. Then, the wavefunction can be factorized as

$$\Psi(\mathbf{r}, t) = \Psi(\rho) \left[\Phi^u(z)\chi^u(\phi, t) + \Phi^d(z)\chi^d(\phi, t) \right], \tag{3.2}$$

where $\Psi(\rho)$ is the ground state of the radial harmonic potential and the functions $\chi^u(\phi, t)$ and $\chi^d(\phi, t)$ contain the dependence of the BEC wavefunction with respect to time. The functions $\Phi^u(z)$ and $\Phi^d(z)$ are two modes localized in the wells up (u) and down (d) constructed as a superposition of the ground and first excited stationary solutions of the GPE equation. The total number of particles in each ring is $\int d\phi |\chi^{u/d}(\phi, t)|^2 = N^{u/d}(t)$ and the functions $\Psi(\rho)$, $\Phi^u(z)$ and $\Phi^d(z)$ are normalized to 1. The functions $\chi^u(\phi, t)$ and $\chi^d(\phi, t)$ for the upper and lower rings can be written as a linear combination of the OAM eigenstates,

$$\chi^{u/d}(\phi, t) = \frac{1}{\sqrt{2\pi}} \sum_{\nu=-\infty}^{\infty} \alpha_\nu^{u/d}(t) \, e^{i\nu\phi}, \tag{3.3}$$

with amplitudes $\alpha_\nu^{u/d}(t)$. For each eigenstate, the condensate has a quantized OAM $\nu\hbar$. The OAM mode coefficients are normalized to the number of particles in the ν-th angular mode in each ring, $|\alpha_\nu^{u/d}(t)|^2 = N_\nu^{u/d}(t)$, such that $N^{u/d}(t) = \sum_\nu N_\nu^{u/d}(t)$. Henceforth, we will omit the explicit time dependence in $\alpha_\nu^{u/d}(t)$. The evolution equations for the amplitudes of each OAM mode, $\alpha_\nu^{u/d}$, read [277, 278]:

$$i\frac{\partial \alpha_\nu^{u/d}}{\partial \tau} = \nu^2 \alpha_\nu^{u/d} - \kappa \alpha_\nu^{d/u} + \gamma \sum_{nn'} \alpha_n^{u/d}(\alpha_{n'}^{u/d})^* \alpha_{\nu-n+n'}^{u/d}, \tag{3.4}$$

where $\tau = \hbar t/(2MR^2)$ is the scaled time, $\kappa = R^2 \int dz \, (\Phi^d(z))^* \left[\frac{\partial^2}{\partial z^2} - \frac{2M}{\hbar^2}V_z\right]\Phi^u(z)$ is the tunneling rate between the two rings, and $\gamma = MR^2 g/(\pi\hbar^2) \int d\rho\rho |\Psi(\rho)|^4 \int dz |\Phi^u(z)|^4$ is

the interatomic interaction parameter with $R^{-2} = \int d\rho \rho^{-1} |\Psi(\rho)|^2$. The first term of the RHS in (3.4) corresponds to the kinetic energy of the ν-th mode, the second term, to the tunneling between the two rings, which only couples OAM modes with the same ν, and the third term is the nonlinear interaction that couples different OAM modes within each ring. The parameters τ, κ, γ and the other magnitudes appearing on the figures of this chapter are dimensionless.

3.2 Stability of the stationary states

Let us consider that only one OAM mode n is initially populated in both rings: $|\alpha_n^{u/d}(\tau = 0)|^2 \neq 0$, $|\alpha_{\nu \neq n}^{u/d}(\tau = 0)|^2 = 0$. Then, stationary solutions only exist for equal number of particles between rings, $N_n^u = N_n^d = N/2$, and Eq. (3.4) simplifies to

$$i\dot{\alpha}_n^{u/d} = n^2 \alpha_n^{u/d} - \kappa \alpha_n^{d/u} + \epsilon \alpha_n^{u/d}, \tag{3.5}$$

where $\epsilon = \gamma N/2$ and the dot indicates the derivative with respect to τ. By diagonalizing this system of equations, we find the following symmetric and antisymmetric stationary solutions with energies $\mu_\pm$:

$$(\alpha_n^u, \alpha_n^d)_s = \sqrt{N} e^{-i\mu_+\tau}(1,1), \qquad\qquad \mu_+ = n^2 + \epsilon - \kappa, \tag{3.6a}$$

$$(\alpha_n^u, \alpha_n^d)_a = \sqrt{N} e^{-i\mu_-\tau}(1,-1), \qquad\qquad \mu_- = n^2 + \epsilon + \kappa. \tag{3.6b}$$

3.2.1 Bogoliubov analysis

In order to study the stability of the states (3.6a) and (3.6b), we fix $n = 0$ and add a small amplitude symmetric perturbation in an arbitrary mode $\nu \neq 0$, of the form

$$\alpha_\nu^{u/d} = e^{-i\mu_\pm\tau}(u_\nu^{u/d} e^{-i\omega\tau} + (v_\nu^{u/d})^* e^{i\omega\tau}). \tag{3.7}$$

By introducing this Ansatz together with (3.6) into (3.4) and linearizing for small amplitudes of $u_\nu^{u/d}$ and $(v_\nu^{u/d})^*$, we obtain the following Bogoliubov-de Gennes equations

$$\omega u_\nu^{u/d} = (\nu^2 - \mu_\pm + 2\epsilon) u_\nu^{u/d} + \epsilon v_{-\nu}^{u/d} - \kappa u_\nu^{d/u}, \tag{3.8a}$$

$$-\omega v_{-\nu}^{u/d} = (\nu^2 - \mu_\pm + 2\epsilon) v_{-\nu}^{u/d} + \epsilon u_\nu^{u/d} - \kappa v_{-\nu}^{d/u}. \tag{3.8b}$$

By diagonalizing (3.8), one finds that only the antisymmetric state can be unstable against perturbations in higher order modes. The corresponding excitation branch, ω, determines the regions of the parameter space for which the antisymmetric state is unstable [278]:

$$\omega = \sqrt{(\nu^2 + \epsilon - 2\kappa)^2 - \epsilon^2}. \tag{3.9}$$

For real values of ω, the perturbations (3.7) remain periodic and thus bounded, while, for imaginary values, the perturbations in mode ν grow exponentially, destabilizing the stationary
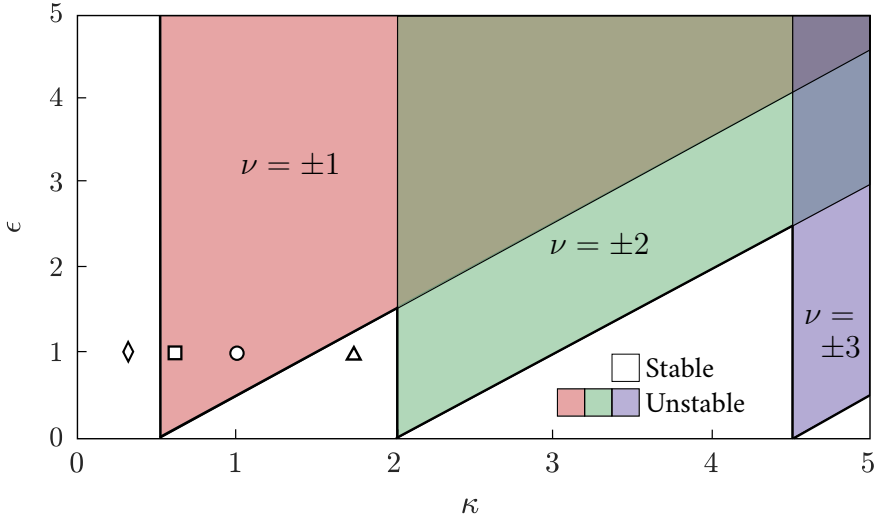
Figure 3.2: Real (white) and imaginary (color) regions of ω for the antisymmetric state with $n = 0$ and perturbations in the modes $\nu = \pm 1, \pm 2, \pm 3$ in the parameter space $[\kappa, \epsilon]$. The points rhombus, square, circle and triangle correspond to the parameter values used in Fig. 3.3 with the circle also being used in Fig. 3.4.

state. Fig. 3.2 shows the real (white) and imaginary (colored) regions of ω for the stationary state with $n = 0$ and perturbations in $\nu = \pm 1, \pm 2, \pm 3$ as a function of κ and ϵ. Interactions increase the instability regions of the antisymmetric state. The spectrum in (3.9) also holds for stationary solutions with $n \neq 0$; in that case, the perturbation ν is the OAM difference with respect to n.

3.2.2 Two-state model

The Bogoliubov analysis predicts the stability regions of the stationary solutions in the parameter space. However, it does not describe the dynamics once the stationary state has been destabilized. In order to get an insight into the excitation process, we derive the simplest model that captures these dynamics: a two-state model that includes the antisymmetric stationary state mode and a pair of perturbation modes $\pm\nu$. We take for simplicity the mode $n = 0$ for the stationary state, with $|\alpha_0^u|^2 = N_0^u$ and $|\alpha_0^d|^2 = N_0^d$. Then, the system of equations (3.4) reduces to a set of six equations that can be expressed in matrix form as

$$
i \begin{pmatrix} \dot{\alpha}_0^u \\ \dot{\alpha}_\nu^u \\ \dot{\alpha}_{-\nu}^u \\ \dot{\alpha}_0^d \\ \dot{\alpha}_\nu^d \\ \dot{\alpha}_{-\nu}^d \end{pmatrix} = \hat{A} \cdot \begin{pmatrix} \alpha_0^u \\ \alpha_\nu^u \\ \alpha_{-\nu}^u \\ \alpha_0^d \\ \alpha_\nu^d \\ \alpha_{-\nu}^d \end{pmatrix},
\tag{3.10}
$$

where

$$
\hat{A} = \begin{pmatrix}
\gamma B_0^u & \gamma \alpha_{-\nu}^u (\alpha_0^u)^* & \gamma \alpha_\nu^u (\alpha_0^u)^* & -\kappa & 0 & 0 \\
\gamma \alpha_0^u (\alpha_{-\nu}^u)^* & \nu^2 + \gamma B_\nu^u & 0 & 0 & -\kappa & 0 \\
\gamma \alpha_0^u (\alpha_\nu^u)^* & 0 & \nu^2 + \gamma B_{-\nu}^u & 0 & 0 & -\kappa \\
-\kappa & 0 & 0 & \gamma B_0^d & \gamma \alpha_{-\nu}^d (\alpha_0^d)^* & \gamma \alpha_\nu^d (\alpha_0^d)^* \\
0 & -\kappa & 0 & \gamma \alpha_0^d (\alpha_{-\nu}^d)^* & \nu^2 + \gamma B_\nu^d & 0 \\
0 & 0 & -\kappa & \gamma \alpha_0^d (\alpha_\nu^d)^* & 0 & \nu^2 + \gamma B_{-\nu}^d
\end{pmatrix},
$$

(3.11)

where we have defined the factor $B_{\pm\nu}^{u(d)} = 2N^u - |\alpha_{\pm\nu}^{u(d)}|^2$ with $N^{u/d} = |\alpha_0^{u/d}|^2 + |\alpha_\nu^{u/d}|^2 + |\alpha_{-\nu}^{u/d}|^2$ being the total number of particles in the u and d rings. We impose the initial condition $\alpha_0^u = -\alpha_0^d$ and add small amplitude symmetric perturbations in the high order modes $\pm\nu$ such that $\delta\alpha_{\pm\nu}^u = \delta\alpha_{\pm\nu}^d$. Due to angular momentum conservation and the fact that the stationary state is in the mode $n = 0$, the conditions $|\alpha_\nu^u|^2 = |\alpha_{-\nu}^u|^2$ and $|\alpha_\nu^d|^2 = |\alpha_{-\nu}^d|^2$ are fulfilled. Assuming that the phase difference between the perturbed modes stays approximately constant during the time evolution and that $|\alpha_{\pm\nu}^d| \approx |\alpha_{\pm\nu}^u|$, we can define $\alpha_\nu \equiv \alpha_{\pm\nu}^u = \alpha_{\pm\nu}^d$. We will also assume that the initial condition $\alpha_0^u = -\alpha_0^d$ is maintained during the temporal evolution, so that we can also use $N^u \approx N^d = N/2$. Applying all these conditions, the expression (3.10) can be simplified to a set of three equations for α_0^u, α_ν and α_0^d, that in matrix form read:

$$
i \begin{pmatrix} \dot{\alpha}_0^u \\ \dot{\alpha}_\nu \\ \dot{\alpha}_0^d \end{pmatrix} = \hat{A}' \begin{pmatrix} \alpha_0^u \\ \alpha_\nu \\ \alpha_0^d \end{pmatrix},
$$

(3.12)

where the matrix $\hat{A}'$ is

$$
\begin{pmatrix}
\gamma\left(N - |\alpha_0^u|^2\left(1 - 2\left(\frac{\alpha_\nu}{\alpha_0^u}\right)^2\right)\right) & 0 & -\kappa \\
0 & -\kappa + \nu^2 + \gamma\left(N - |\alpha_\nu|^2\left(1 - \left(\frac{\alpha_0^u}{\alpha_\nu}\right)^2\right)\right) & 0 \\
-\kappa & 0 & \gamma\left(N - |\alpha_0^u|^2\left(1 - 2\left(\frac{\alpha_\nu}{\alpha_0^u}\right)^2\right)\right)
\end{pmatrix}.
$$

(3.13)

This system can be reduced further by noting that the first and last diagonal elements are equal. Then, defining $\alpha_0 \equiv \alpha_0^u$, we obtain the following two-state model (TSM):

$$
i \begin{pmatrix} \dot{\alpha}_0 \\ \dot{\alpha}_\nu \end{pmatrix} = \begin{pmatrix}
\gamma(N - |\alpha_0|^2\left(1 - 2\left(\frac{\alpha_\nu}{\alpha_0}\right)^2\right)) + \kappa & 0 \\
0 & -\kappa + \nu^2 + \gamma\left(N - |\alpha_\nu|^2\left(1 - \left(\frac{\alpha_0}{\alpha_\nu}\right)^2\right)\right)
\end{pmatrix} \begin{pmatrix} \alpha_0 \\ \alpha_\nu \end{pmatrix}.
$$

(3.14)

In order to understand the oscillatory dynamics of the system, we define $\alpha_0 = |\alpha_0|e^{i\phi}$ and $\alpha_\nu = |\alpha_\nu|e^{i\theta}$. By using particle conservation, $2|\alpha_0|^2 + 4|\alpha_\nu|^2 = N$, and defining the phase difference $\zeta = \theta - \phi$, the system reduces to two coupled real equations:

$$
\dot{|\alpha_\nu|^2} = 2\gamma|\alpha_\nu|^2\left(2|\alpha_\nu|^2 - \frac{N}{2}\right)\sin 2\zeta,
$$

(3.15a)

$$
\dot{\zeta} = 2\kappa - \nu^2 + \gamma\left(3|\alpha_\nu|^2 - \frac{N}{2}\right) + \gamma\left(4|\alpha_\nu|^2 - \frac{N}{2}\right)\cos 2\zeta.
$$

(3.15b)

Critical points

The critical points of the two-state model fulfill $|\dot{\alpha_\nu}|^2 = \dot{\zeta} = 0$. Imposing $|\dot{\alpha_\nu}|^2 = 0$ in Eq. (3.15a), we find $|\alpha_\nu|^2 = 0$, $|\alpha_\nu|^2 = N/4$, and $\sin 2\zeta = 0$, where the two first trivial solutions correspond to the minimum and maximum values of $|\alpha_\nu|^2$ that are due to particle conservation. The critical points can be then found imposing $\dot{\zeta} = 0$ in Eq. (3.15b). For the trivial cases, the critical points are

$$\left(\cos 2\zeta = \frac{2\kappa - \nu^2 - \epsilon}{\epsilon} \equiv \mathcal{A}, \qquad\qquad |\alpha_\nu|^2 = 0 \right), \qquad (3.16a)$$

$$\left(\cos 2\zeta = \frac{\nu^2 - 2\kappa - \epsilon/2}{\epsilon} \equiv \mathcal{B}, \qquad\qquad |\alpha_\nu|^2 = \frac{N}{4} \right). \qquad (3.16b)$$

Due to the boundedness of the cosine in (3.16a), the solution with $|\alpha_\nu|^2 = 0$ exists if

$$\frac{\nu^2}{2} \le \kappa \le \frac{\nu^2 + 2\epsilon}{2}, \qquad (3.17)$$

and similarly, the solution with $|\alpha_\nu|^2 = N/4$, Eq. (3.16b), exists if

$$\frac{\nu^2 - 3\epsilon/2}{2} \le \kappa \le \frac{\nu^2 + \epsilon/2}{2}. \qquad (3.18)$$

By studying the eigenvalues of the Jacobian at the critical points, these trivial solutions can be shown to be saddle points (see Appendix A.1). For the nontrivial solution, for which $|\alpha_\nu|^2$ takes values different from 0 or $N/4$, the critical points are

$$\left(\zeta = a\pi, \qquad\qquad |\alpha_\nu|^2 = \frac{\nu^2 - 2\kappa + 2\epsilon}{14\epsilon/N} \equiv \mathcal{C} \right), \qquad (3.19a)$$

$$\left(\zeta = (2a + 1)\frac{\pi}{2}, \qquad\qquad |\alpha_\nu|^2 = \frac{2\kappa - \nu^2}{2\epsilon/N} \equiv \mathcal{D} \right), \qquad (3.19b)$$

where $a \in \mathbb{Z}$. Taking into account the minimum and maximum values of $|\alpha_\nu|^2$ due to particle conservation, the solutions with $\zeta = a\pi$ exist if

$$\frac{\nu^2 - 3\epsilon/2}{2} \le \kappa \le \frac{\nu^2 + 2\epsilon}{2}, \qquad (3.20)$$

whereas the ones with $\zeta = (2a + 1)\pi/2$ exist if

$$\frac{\nu^2}{2} \le \kappa \le \frac{\nu^2 + \epsilon/2}{2}. \qquad (3.21)$$

Note that the second set of solutions, Eq. (3.19b), has a more restrictive condition than the first, Eq. (3.19a). Similarly as before, these solutions can be shown to be centers, with the trajectories orbiting around them (see Appendix A.1). Table 3.1 summarizes the critical points, their existence conditions and if they are saddle points or centers.

ζ	$\lvert\alpha_\nu\rvert^2$	κ_{min}	κ_{max}
$\mathcal{A} = \cos 2\zeta = \dfrac{-\nu^2 + 2\kappa - \epsilon}{\epsilon}$	0	$\dfrac{\nu^2}{2}$	$\dfrac{\nu^2 + 2\epsilon}{2}$
$\mathcal{B} = \cos 2\zeta = \dfrac{-\nu^2 + 2\kappa + \frac{\epsilon}{2}}{\epsilon}$	$\dfrac{N}{4}$	$\dfrac{\nu^2 - \frac{3\epsilon}{2}}{2}$	$\dfrac{\nu^2 + \frac{\epsilon}{2}}{2}$
$a\pi$	$\mathcal{C} = \dfrac{2\epsilon + \nu^2 - 2\kappa}{14\epsilon/N}$	$\dfrac{\nu^2 - \frac{3\epsilon}{2}}{2}$	$\dfrac{\nu^2 + 2\epsilon}{2}$
$(2a+1)\dfrac{\pi}{2}$	$\mathcal{D} = \dfrac{2\kappa - \nu^2}{2\epsilon/N}$	$\dfrac{\nu^2}{2}$	$\dfrac{\nu^2 + \frac{\epsilon}{2}}{2}$

Table 3.1: Critical points of the two-state model and corresponding existence conditions.

Two-state model Hamiltonian

Assuming that the variables $\lvert\alpha_\nu\rvert^2$ and ζ are canonical conjugates, they fulfill $\partial H/\partial(\lvert\alpha_\nu\rvert^2) = \dot{\zeta}$ and $\partial H/\partial\zeta = -\lvert\dot{\alpha}_\nu\rvert^2$, and thus the corresponding classical Hamiltonian H reads:

$$H(\lvert\alpha_\nu\rvert^2, \zeta) = \lvert\alpha_\nu\rvert^2 \left[2\kappa - \nu^2 - \frac{\gamma N}{2} + \frac{3}{2}\gamma\lvert\alpha_\nu\rvert^2 + \gamma\left(2\lvert\alpha_\nu\rvert^2 - \frac{N}{2}\right)\cos 2\zeta \right]. \tag{3.22}$$

Fig. 3.3 shows lines of constant $H(\lvert\alpha_1\rvert^2, \zeta)$ for various initial conditions and $\gamma = 1/2000$, $N = 4000$ (thus, $\epsilon = 1$), $\nu = 1$ and different values of κ. According to the existence conditions of the critical points, Eqs. (3.17, 3.18, 3.20, 3.21), there are four possible types of phase diagrams as a function of the tunneling κ:

- $(\nu^2 - 3\epsilon/2)/2 < \kappa < \nu^2/2$: there are saddle points at $(\mathcal{B}, \lvert\alpha_\nu\rvert^2 = N/4)$ and centers at $(\zeta = a\pi, \mathcal{C})$ [e.g., Fig. 3.3(a)]. The orbits around the centers are not accessible for the initial conditions $\lvert\alpha_\nu\rvert^2/N \simeq 0$ and $\zeta = 0$, thus, the stationary state is stable.

- $\nu^2/2 < \kappa < (\nu^2 + \epsilon/2)/2$: there are saddle points at $(\mathcal{A}, \lvert\alpha_\nu\rvert^2 = 0)$ and $(\mathcal{B}, \lvert\alpha_\nu\rvert^2 = N/4)$, and centers at $(\zeta = a\pi, \mathcal{C})$ and $(\zeta = (2a+1)\pi/2, \mathcal{D})$ [e.g., Fig. 3.3(b)]. Given Eq. (3.19), the value of $\lvert\alpha_\nu\rvert^2$ corresponding to the centers at $\zeta = a\pi$ diminishes with the tunneling κ while the one for the centers at $\zeta = (2a+1)\pi/2$ grows with κ. For the values of κ when the $\lvert\alpha_\nu\rvert^2$ value of the centers at $\zeta = a\pi$ is equal or inferior than those of $\zeta = (2a+1)\pi/2$, the system orbits around $(\zeta = a\pi, \mathcal{C})$. For lower values of κ, the contrary occurs, and the system performs open orbits around the centers $(\zeta = (2a+1)\pi/2, \mathcal{D})$ [e.g., Fig. 3.3(b)].

- $(\nu^2 + \epsilon/2)/2 < \kappa < (\nu^2 + 2\epsilon)/2$: there are saddle points at $(\mathcal{A}, \lvert\alpha_\nu\rvert^2 = 0)$ and centers at $(\zeta = a\pi, \mathcal{C})$ [e.g., Fig. 3.3(c)], which allows the system to perform orbits around these centers.
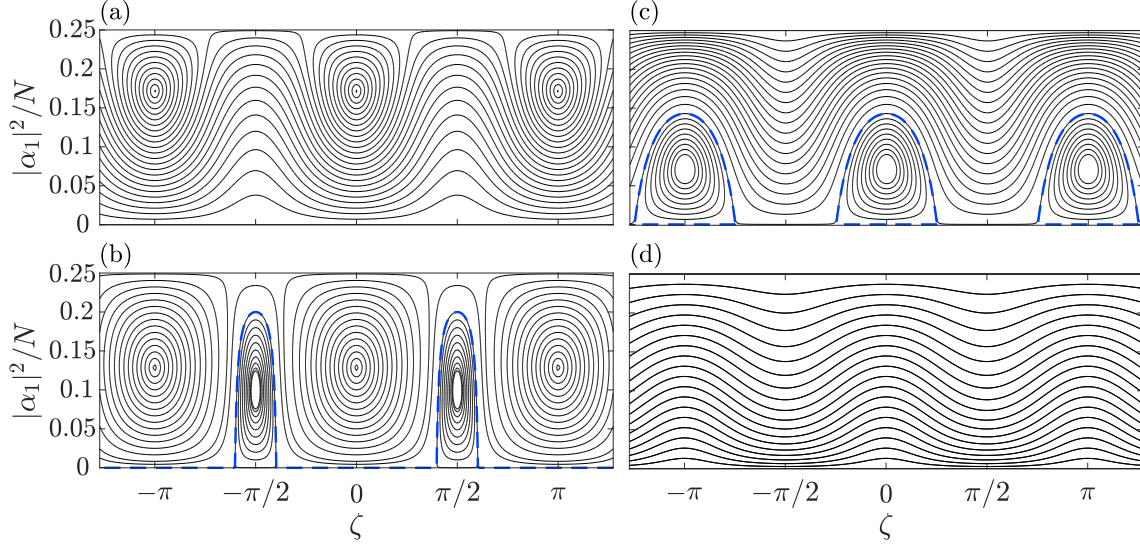
Figure 3.3: Lines of constant $H(|\alpha_1|^2, \zeta)$ for $\nu = 1$, $\gamma = 1/2000$, and $N = 4000$ (thus, $\epsilon = 1$) and (a) $\kappa = 0.3$, (b) $\kappa = 0.6$, (c) $\kappa = 1$, (d) $\kappa = 1.7$. In dashed blue, orbits corresponding to the stationary state excitations for the unstable cases, (b) and (c). The parameter values of the plots correspond to the points rhombus, square, circle and triangle in Fig. 3.2, respectively.

- For all other values of κ, i.e., $(\nu^2 + 2\epsilon)/2 < \kappa < (\nu^2 - 3\epsilon/2)/2$, there are neither saddle points nor centers [e.g., Fig. 3.3(d)], such that the stationary state is stable.

Combining all these conditions we find that the antisymmetric stationary state is unstable for $\nu^2/2 < \kappa < (\nu^2 + 2\epsilon)/2$, which coincides with the stability conditions predicted by the Bogoliubov analysis (see Fig. 3.2). The Bogoliubov excitations correspond to the open and closed orbits around the centers given the initial conditions $\zeta = 0$ and $|\alpha_\nu|^2/N \simeq 0$, as the ones shown in blue dashed lines in Figs. 3.3(b) and 3.3(c).

The population transfer between the states with $n = 0$ and the perturbations ν during the excitation is determined by the corresponding orbit. One can find an upper bound to the population transfer, $|\alpha_\nu|^2_{max}/N$, by considering the initial conditions $\zeta(\tau = 0) = 0$ and $|\alpha_\nu(\tau = 0)|^2/N = 0$, which correspond to the orbit with $H(|\alpha_\nu|^2, \zeta) = 0$. Taking into account the different possible orbits, either open or closed, and particle conservation in Eq. (3.22), one reaches

$$\frac{|\alpha_\nu|^2_{max}}{N} = \begin{cases} \dfrac{2\kappa - \nu^2}{\epsilon}; & \dfrac{\nu^2}{2} \leq \kappa \leq \dfrac{\nu^2 + \epsilon/4}{2}, \\ \dfrac{2}{7}\dfrac{\nu^2 - 2\kappa + 2\epsilon}{2\epsilon}; & \dfrac{\nu^2 + \epsilon/4}{2} \leq \kappa \leq \dfrac{\nu^2 + 2\epsilon}{2}. \end{cases} \tag{3.23}$$

The upper bound of the population transfer grows linearly with the tunneling κ, and reaches its maximum for $\kappa = \frac{\epsilon/4 + \nu^2}{2}$, when the centers at $\zeta = (2a + 1)\pi/2$ and $\zeta = a\pi$ have the same $|\alpha_\nu|^2$. Then, the upper bound of the population transfer decreases linearly with κ down to zero.
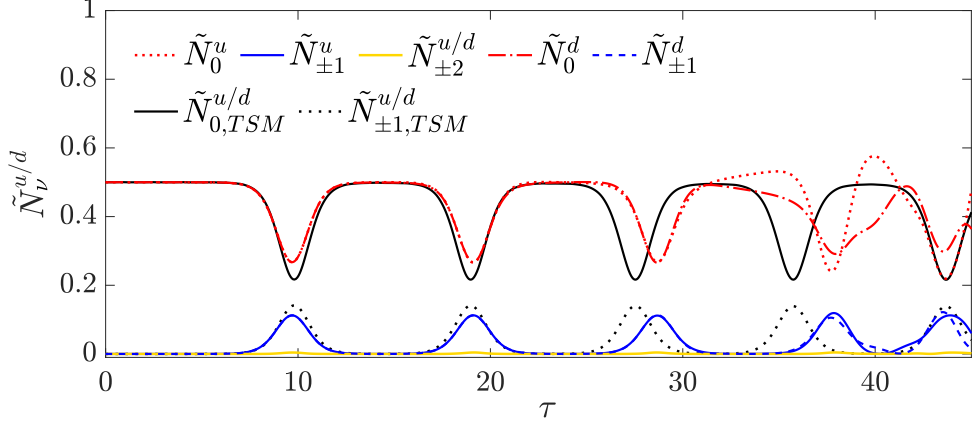
Figure 3.4: Temporal evolution of the populations, $\tilde{N}_\nu^{u/d} = N_\nu^{u/d}/N$, for $N = 4000$, $\kappa = 1$ and $\epsilon = 1$ (circle in Fig. 3.2) of the two-state model (TSM) with $\nu = 1$ (black) and the complete system of equations up to $\nu = \pm 15$ (color). Initial conditions: $\alpha_0^u = -\alpha_0^d = \alpha_0 = \sqrt{N/2}$ with perturbations of order $\sqrt{N/2} \cdot 10^{-4}$ [up to $\nu = \pm 5$ for the complete system of equations (3.4)].

For an initial state with $n \neq 0$, one observes analogous dynamics as the ones described above, where the pairs of excited modes have an OAM difference $\pm \nu$ with respect to n. For example, for $\kappa = 1$, $\epsilon = 1$ and the stationary state with $n = 0$, the states that form the excitation are $\nu = \pm 1$, whereas for $n = 1$, the excited modes are $\nu = 0$ and $\nu = 2$.

3.2.3   Numerical simulations

In this section, we will compare numerically the predictions of the two-state model (3.14) and the complete system of equations (3.4) for the stationary state with $n = 0$, $\kappa = 1$ and $\epsilon = 1$ (corresponding to the circle in Fig. 3.2). Fig. 3.4 shows the time evolution of the populations according to the two-state model (black) and by numerical integration of the system of equations (color).

For the two-state model, we initially set the amplitudes to $\alpha_0 = \sqrt{N/2}$ and $\alpha_1 = \sqrt{N/2} \cdot 10^{-4}$ in the system of equations (3.14). The population of the perturbation α_1 grows exponentially, in agreement with Eq. (3.9) of the Bogoliubov analysis. Then, the growth of the perturbation slows down, the population reaches a maximum closely bounded by Eq. (3.23), and the transfer of population is inverted; the population returns to α_0. This population transfer pattern is repeated periodically and, for small τ, it precisely captures the dynamics predicted by the complete set of equations.

For the full model, we populate equally the $n = 0$ modes, $\alpha_0^u = -\alpha_0^d = \sqrt{N/2}$, and introduce perturbations of order $\sqrt{N/2} \cdot 10^{-4}$ for $\nu \neq 0$ up to $\nu = \pm 5$ in Eq. (3.4). We include the first $\nu = \pm 15$ modes in the simulation, thus truncating the system of equations well above the highest relevant mode. In this case, the excitation is formed by the pair of modes $\nu = \pm 1$, which evolve with the same population within each ring, thus conserving angular

momentum. For long times, the periodic pattern in the evolution of the populations is no longer accurately described by the two-state model since the system does not keep the same population in the $n = 0$ modes of the two rings. However, the variations in the period and amplitude of the oscillations could be explained using the two-state model, which suggests that the dynamics of the system are highly sensitive to perturbations (see Fig. 3.3) i.e., a small perturbation can cause the system to change the orbit. Thus, by analogy, the perturbations appearing during the evolution in the full model would lead to oscillations presenting small changes in their period and amplitude. Also, the maximum population that the excitations reach is lower than the one of the two-state model due to secondary excitations: the higher order modes that are also excited modify the dynamics of the main excitation, $\nu = \pm 1$. In this case, the mode $\nu = \pm 2$ (yellow) reaches populations of order $O(10^{-3})$ while higher order modes have smaller contributions.

3.3   Dynamical regimes

Thus far, we have studied the destabilization of the stationary states, which have a single OAM mode n populated with the same number of particles in both rings. However, when the initial population in each ring is not the same, tunneling and interactions give rise to different dynamical regimes in the system.

   The dynamics of BECs trapped in double-well potentials are known to present either Josephson oscillations or self-trapping depending on the ratio between the tunneling and the nonlinear interactions [266]. In the Josephson oscillations regime, the population performs complete oscillations between the two wells while in the self-trapping regime, the population remains mostly trapped in one well. In order to find the self-trapping condition for our system, we initially populate a single mode n and factorize the amplitudes as $\alpha_n^{u/d} = \sqrt{N_n^{u/d}} e^{i\beta_n^{u/d}}$. The system of equations (3.4) can then be rewritten in terms of the population imbalance, $z_n = (N_n^u - N_n^d)/N$, and the phase difference, $\delta\phi_n = \beta_n^d - \beta_n^u$, as a set of two coupled equations:

$$\begin{cases} \dot{z}_n = -\sqrt{1 - z_n^2}\sin\delta\phi_n, \\ \dot{\delta\phi}_n = \Lambda z_n + \dfrac{z_n}{\sqrt{1 - z_n^2}}\cos\delta\phi_n, \end{cases} \tag{3.24}$$

where $\Lambda = \gamma N/(2\kappa) = \epsilon/\kappa$ and τ has been scaled to $2\kappa\tau$. Assuming that z_n and $\delta\phi_n$ are canonically conjugate variables, then, $\partial H/\partial z_n = \dot{\delta\phi}_n$ and $\partial H/\partial\delta\phi_n = -\dot{z}_n$, and the corresponding classical Hamiltonian reads

$$H = \frac{1}{2}\Lambda z_n^2 - \cos\delta\phi_n\sqrt{1 - z_n^2}. \tag{3.25}$$

Note that the Hamiltonian is equal for all n. Thus, the system presents identical dynamics for all OAM modes. In order to find the boundary between the regimes of self-trapping and Josephson oscillations, we impose $z_n(\tau) = 0$, which is only fulfilled in the Josephson
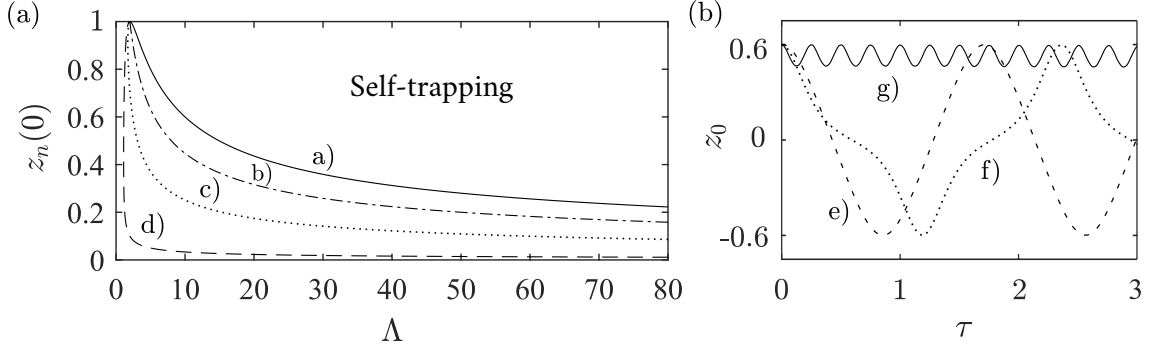
Figure 3.5: (a) Boundary between the self-trapping and the Josephson oscillations regimes as predicted by (3.26) for: a) $\delta\phi_n(0) = 0$, b) $\delta\phi_n(0) = \pi/2$, c) $\delta\phi_n(0) = 3\pi/4$, d) $\delta\phi_n(0) \to \pi$. (b) Time evolution of z_0 for $z_0(0) = 0.6$, $\delta\phi_0(0) = 0$, $N = 4000$, $\kappa = 1$ and e) $\Lambda = 4$, f) $\Lambda = 10$, g) $\Lambda = 24$.

oscillations regime. Using energy conservation in (3.25) and denoting the initial parameters as $z_n(\tau = 0) \equiv z_n(0)$ and $|\delta\phi_n(\tau = 0)| \equiv \delta\phi_n(0)$, one reaches

$$\Lambda_c = 2\left(\frac{\cos\delta\phi_n(0)\sqrt{1 - z_n^2(0)} + 1}{z_n^2(0)} \right), \tag{3.26}$$

which defines the phase boundary between the two regimes in terms of the initial population imbalance, the phase difference and the ratio Λ. This condition is a generalization of the one found in [265] for a BEC in a double-well potential. In addition, analogous dynamics are obtained for the total imbalance and phase difference in a system of stacked lattice rings in the deep superfluid limit [260, 275]. In this limit, the potential barriers between the sites of the lattices are small enough that the system resembles a couple of free rings. Fig. 3.5(a) shows the boundary given by (3.26) for different values of the initial phase difference $\delta\phi_n(0)$ as a function of $\Lambda = \epsilon/\kappa$ and the initial population imbalance $z_n(0)$. The self-trapping regime occurs for sufficiently large imbalance and ratio $\Lambda = \epsilon/\kappa$. As the phase difference grows from 0 to π, the region of parameters for which self-trapping occurs grows and, as one approaches the limit $\delta\phi_n(0) \to \pi$, the minimum population imbalance to obtain self-trapping approaches $z_n(0) = 0$.

Figure 3.5(b) shows the temporal evolution of the population imbalance, z_0, for $z_0(0) = 0.6$, $\delta\phi_n(0) = 0$ and for different values of Λ: e) $\Lambda = 4$, f) $\Lambda = 10$, g) $\Lambda = 24$. As the ratio $\Lambda = \epsilon/\kappa$ grows, the oscillations become anharmonic until the average population imbalance becomes non-zero. If one further increases Λ, the amplitude of the remaining oscillations decreases and they are eventually suppressed, then, the population remains at the initial imbalance.

3.3.1   Stability of the dynamical regimes

In this section we study numerically the stability of the dynamical regimes, Josephson oscillations and self-trapping, in the presence of perturbations in higher order modes. Initially,

we populate the mode $n = 0$ with a certain imbalance $z_0(0)$ between the rings and a phase difference of π, and introduce small amplitude perturbations in higher order modes of order $\sqrt{N/2} \cdot 10^{-4}$ for $\nu \neq 0$ up to $\nu = \pm 3$. Then, we also discuss the case in which the initial phase difference between the modes with $n = 0$ is 0.

Fig. 3.6 shows the different dynamics in the parameter space $[\kappa, \epsilon]$ for (a) $z_0(0) = 0.1$, (b) $z_0(0) = 0.4$ and (c) $z_0(0) = 0.75$. Black and blue indicate stable and unstable self-trapping, respectively, white indicates stable Josephson oscillations and green and yellow indicate unstable Josephson oscillations. The simulations run up to $\tau = 100$, and the color gradients indicate the decay times. The boundary between Josephson oscillations and self-trapping is not modified by the perturbations, and thus it is determined by Eq. (3.26) taking $\delta\phi_0(0) = \pi$. For small initial imbalance, Eq. (3.9) predicts accurately the regions of stability of the dynamical regimes, as the initial state resembles the stationary state [see Figs. 3.2 and 3.6(a)]. As the initial imbalance gets larger, the structure of the unstable regions becomes more involved [Figs. 3.6(b) and 3.6(c)].

The criteria for classification are the following. The stable regimes are those for which the population of the perturbed modes remains below 0.01. For stable Josephson oscillations, the population imbalance of the main mode becomes zero at some point during time evolution, whereas in the stable self-trapping regime it does not. The decay time of the unstable regimes is defined as the time for which the total mode populations, N_ν, of the main mode and the perturbation modes cross.

The Josephson oscillations and self-trapping dynamics decay into unstructured oscillations when higher order modes get excited. The system then remains in a state of non-periodic oscillations between the two rings that involves several modes. Fig. 3.7 presents examples of these dynamics for unstable (a) Josephson oscillations and (b) self-trapping, corresponding to the square in Fig. 3.6(c) and the circle in Fig. 3.6(b), respectively.

Close to the boundary between the stable and the unstable regimes, the system presents semistable Josephson oscillations and self-trapping. In these cases, the population of a single excited mode $\pm\nu$ grows and decays periodically, without destabilizing the dynamics of the main mode, $n = 0$. The upper plots of Figs. 3.8 and 3.9 show an example of semistable Josephson dynamics and semistable self-trapping dynamics, respectively. The lower plots of these figures show the corresponding total mode populations $\tilde{N}_\nu^u + \tilde{N}_\nu^d = (N_\nu^u + N_\nu^d)/N$, which present a pattern analogous to those shown by Bogoliubov excitations of the stationary state (see Fig. 3.4). Therefore, the semistable dynamics can be understood as Bogoliubov excitations of the dynamical states modulated by tunneling.

Figs. 3.6(d) and (e) show the different dynamics in the parameter space $[\kappa, \epsilon]$ for initial imbalance $z_0(0) = 0.75$ and $z_0(0) = 0.9$, respectively. For these cases, the initial phase difference between the modes with $n = 0$ is 0. In these cases the boundary between Josephson oscillations and self-trapping is given by Eq. (3.26) taking $\delta\phi_0(0) = 0$ [see Fig. 3.5(a)]. Consequently, the Josephson oscillations regimes are much larger than the ones with initial phase difference equal to π [see Figs. 3.6(a), (b), and (c)]. As the initial phase difference is 0, which corresponds to the symmetric state in the stationary case, there is no mechanism of Bogoliubov destabilization and the unstable regimes do not resemble the spectrum of Fig. 3.2.
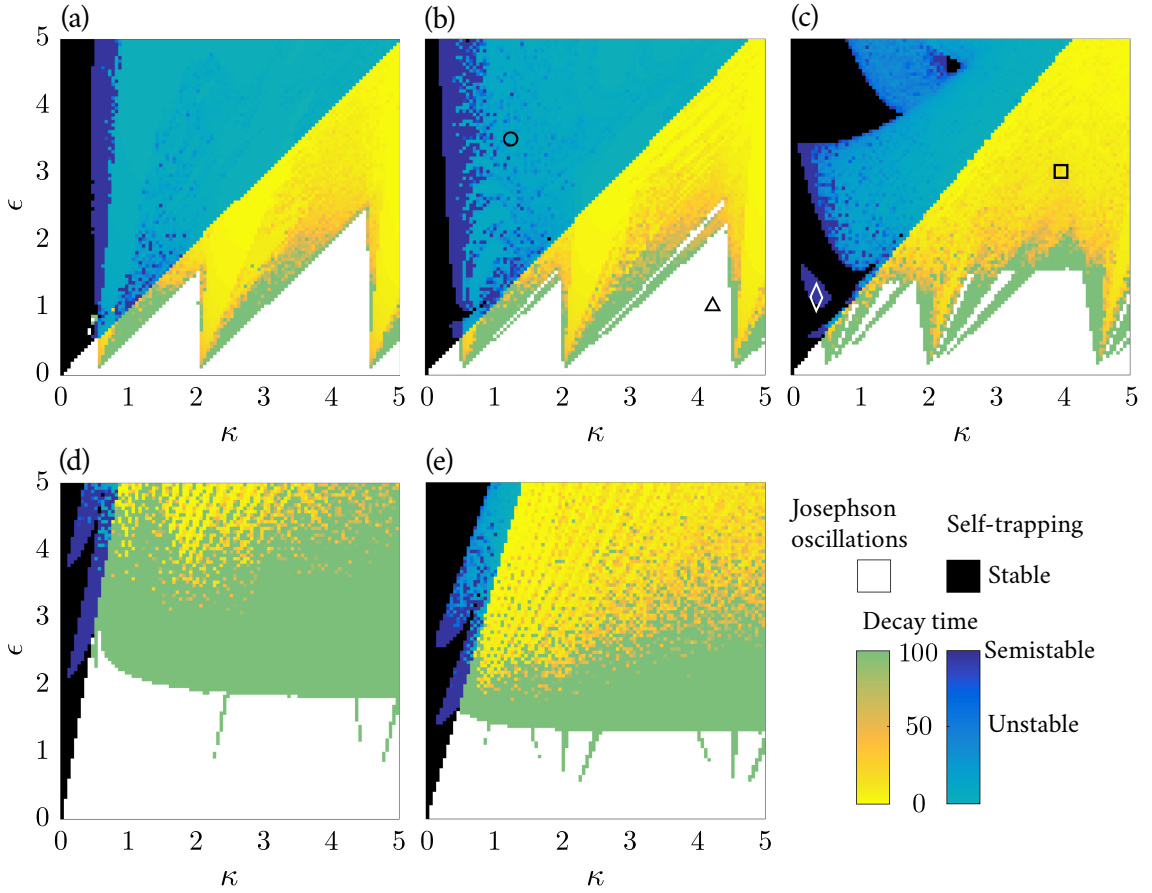
Figure 3.6: Dynamical regimes in the parameter space $[\kappa, \epsilon]$ up to $\tau = 100$ with $N = 4000$ for (a) $z_0(0) = 0.1$, (b) $z_0(0) = 0.4$, (c) $z_0(0) = 0.75$, (d) $z_0(0) = 0.75$, and (e) $z_0(0) = 0.9$. Initial phase difference π for (a), (b), and (c) and 0 for (d) and (e). The marked points correspond to: square [Fig. 3.7(a)], circle [Fig. 3.7(b)], triangle (Fig. 3.8) and white rhombus (Fig. 3.9). For the semistable cases, the dynamics do not decay up to $\tau = 100$.

Instead, there is an interactions threshold that depends mainly on the imbalance above which the Josephson oscillations become unstable. For initial imbalance $z_0(0) = 0.4$, both regimes are stable and the Josephson oscillations regime occupies the vast majority of the considered parameter space.

The time scales considered in this section, which go up to $\tau = 100$, reach the order of 8 s for ^{87}Rb, a ring radius of $\rho_0 = 5 \cdot 10^{-6}$ m and an oscillator length of the harmonic potentials $a = 1 \cdot 10^{-6}$ m. Within a time scale up to $\tau = 10$, which corresponds to 0.8 s, one would observe several Josephson oscillations, as can be seen in Figs. 3.7(a) and 3.8(a). Therefore, the described dynamics are within reach in state of the art experiments.
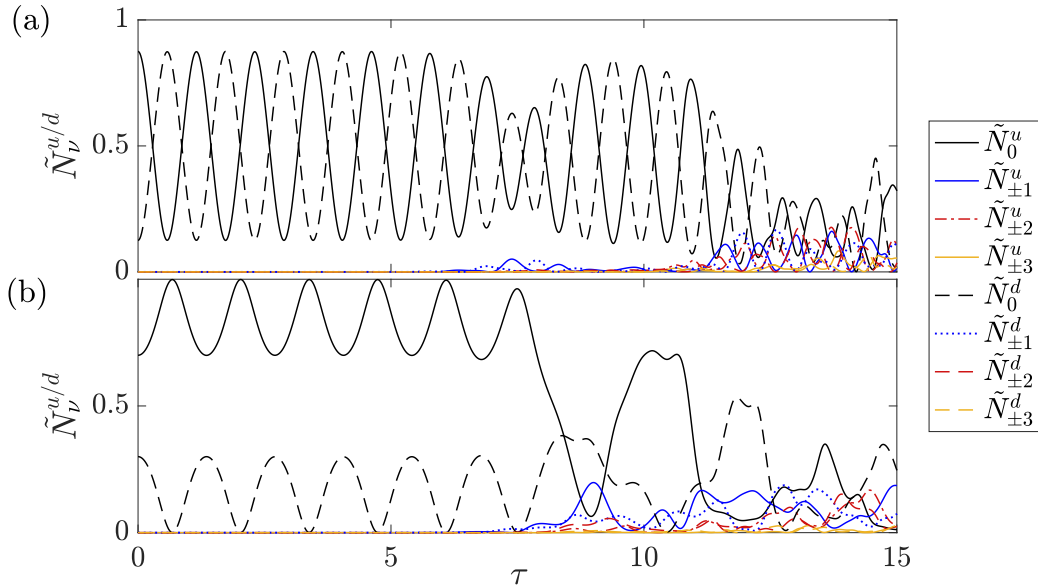
Figure 3.7: Temporal evolution of the populations, $\tilde{N}_\nu^{u/d} = N_\nu^{u/d}/N$ with $N = 4000$, for unstable Josephson oscillations (a) $\kappa = 4$, $\epsilon = 3$, $z_0(0) = 0.75$ [square in Fig. 3.6(c)] and self-trapping (b) $\kappa = 1.5$, $\epsilon = 3.5$, $z_0(0) = 0.4$ [circle in Fig. 3.6(b)]. The modes that grow from $\tau = 5$ onwards include $\nu = \pm 1, \pm 2, \pm 3$.

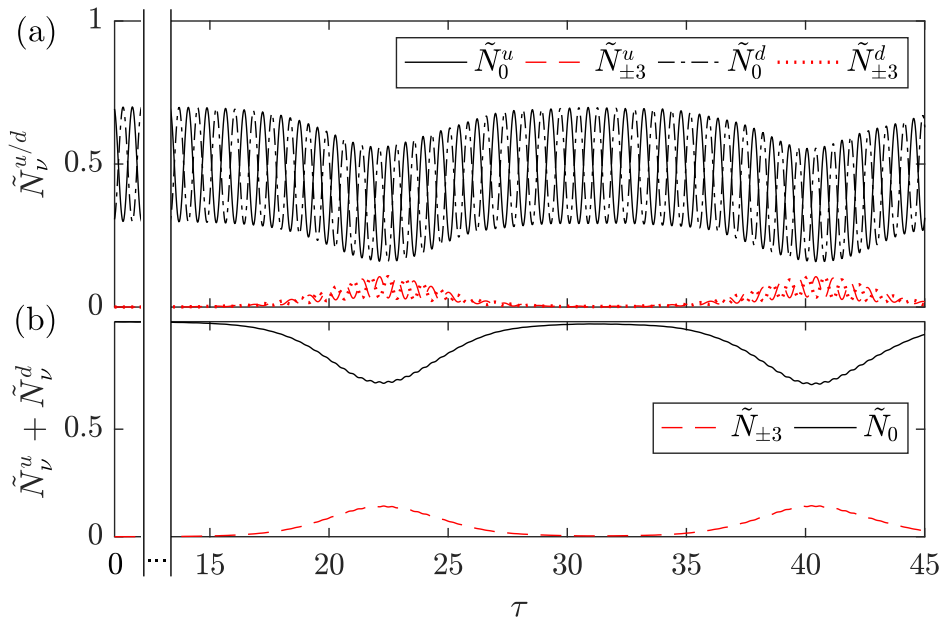Figure 3.8: Temporal evolution of semistable Josephson oscillations for $\kappa = 4.5$, $\epsilon = 1$, $N = 4000$, and $z_0(0) = 0.4$ [triangle in Fig. 3.6(b)] for (a) the populations in each mode and ring, $\tilde{N}_\nu^{u/d} = N_\nu^{u/d}/N$, and (b) the total mode populations, $\tilde{N}_\nu^u + \tilde{N}_\nu^d$. Note that the time axis has a gap between $\tau = 0$ and $\tau = 15$ to show the relevant dynamics.
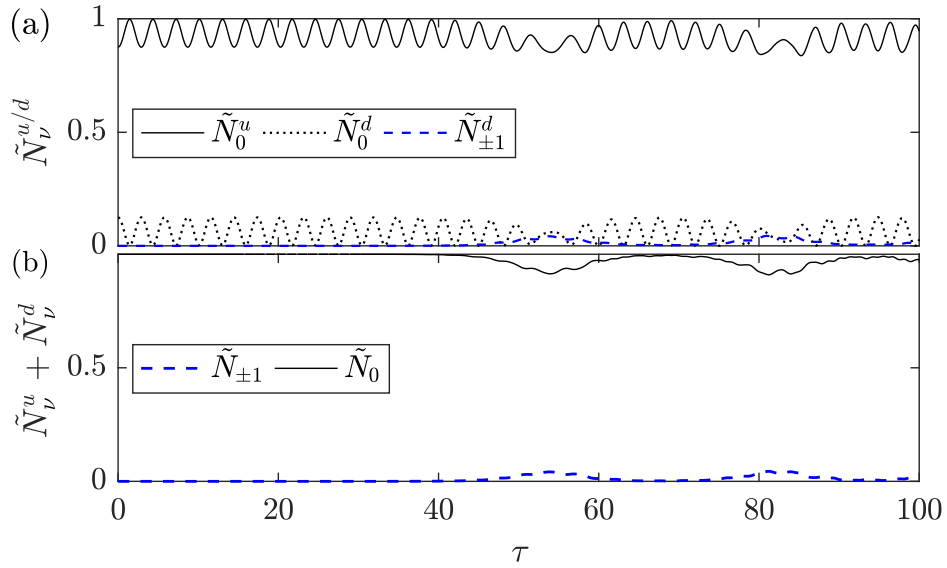
Figure 3.9: Temporal evolution of semistable self-trapping for $\kappa = 0.35$, $\epsilon = 1.25$, $N = 4000$ and $z_0(0) = 0.75$ [rhombus in Fig. 3.6(c)], for (a) the populations in each mode and ring, $\tilde{N}_\nu^{u/d} = N_\nu^{u/d}/N$, and (b) the total mode populations, $\tilde{N}_\nu^u + \tilde{N}_\nu^d$. The population of the modes $\alpha_{\pm 1}^u$ remain below 0.01.

3.4   Conclusions

In this chapter, we have investigated a BEC with repulsive interactions trapped in two rings in a stack configuration. The stability and dynamics of the BEC have been studied within mean-field theory and in terms of its OAM modes. For the case of a single mode equally populated in both rings and including small perturbations in other modes, we have derived a two-state model that predicts the regions of the parameter space supporting stable stationary states. This model also describes the dynamics of the system after destabilization, and characterizes accurately the features of the excitations. The analytical results of the two-state model have been contrasted with the numerical integration of the full model, finding a good qualitative and quantitative agreement.

Also, we have analyzed the dynamics of the system when a single OAM mode is populated with an arbitrary population imbalance between the two rings: the dynamical regimes of Josephson oscillations and self-trapping. The boundary condition between the two regimes has been analytically derived in terms of the population imbalance and the corresponding phase difference. We have found that the dynamics are equal for all OAM modes, and resemble the dynamics of a double-well system. By numerical analysis, we have characterized these dynamical regimes against perturbations in higher order OAM modes.

4

BOSONIC ORBITAL SU-SCHRIEFFER-HEEGER MODEL IN A LATTICE OF RINGS

In this chapter, we explore a one-dimensional lattice of in-line rings with local eigenstates in each site with a well-defined orbital angular momentum (OAM) by using a Bose-Hubbard-type model. The tunneling amplitudes between these states are well-described by the four-state model introduced in Section 2.3.2 and thus take real values. We analyze the single- and two-boson problems and focus on their topological characterization and the effect of on-site interactions.

A cornerstone idea behind topological insulators is the bulk-boundary correspondence. It relates the presence of robust edge states in a system with open boundary conditions with non-trivial values of topological invariants defined by the bulk bands. The symmetries and dimensionality of the non-interacting bulk restrict the possible topological phases that the system can host [54, 217]. However, interacting systems do not possess a well-defined band structure with an associated topological invariant. In contrast to the characterization of non-interacting topological phases, a systematic description of interacting topological phases has yet to be developed [288].

The simplest case where interactions already play a role is the two-body problem. Repulsive and attractive interactions can cause the formation of bound pairs of particles with energies outside the non-interacting energy bands [289, 290]. Such composite objects, usually called doublons [291–293], have very long lifetimes due to the finite energy bandwidth of the single-particle kinetic energy [294]. Doublons have been experimentally observed in ultracold atoms [291] and organic salts [295]. Also, they have been shown to arise in a variety of systems, including models with long range interactions [296–299], in superlattices [300], and in spinor gases [301].

Here we study a system of one or two bosons in a one-dimensional lattice of rings with alternating distances. This geometry mimics the Su–Schrieffer–Heeger (SSH) model [227, 302], which was initially proposed to describe solitons in polyacetylene, and was latter revealed as the simplest instance of a topological insulator. Each local potential has eigenstates with OAM l with winding numbers $\pm l$. The particles are loaded into the states with $l = 1$ providing

each site of the lattice with two internal states. The interacting two-particle SSH model was previously studied for both on-site and nearest-neighbor interactions [299, 303–305]. Here, the additional degree of freedom in each site leads to a richer array of bound-states, edge bound states and strongly interacting subspaces. There is a wide variety of techniques to generate ring potentials and to transfer angular momentum to the particles, thus exciting the states $l > 0$ (see discussion in Chapter 3). In addition, a ring lattice can be engineered for instance using micro-lens arrays by combining them with conical refraction techniques [202], for which a 10×8 lattice was demonstrated, or using digital micro-mirror devices, which provide a high degree of geometrical tunability [201]. Alternatively, the physics described here can also be observed in the p band of a conventional optical lattice [204–207]. Then, the atoms have to be loaded into the p-band orbitals of the form $p_x \pm i p_y$ [205, 207] which can be achieved using the following techniques: adiabatical deformation of an adjacent trap with resonant tunneling transfer [204], lattice shaking and shortcuts to adiabaticity [206], or OAM transfer from light to the atoms [199].

The rest of the chapter is organized as follows. In Sec. 4.1, we introduce the physical system and discuss the coupling strengths that appear between the different winding numbers. We analyze the single-particle case in Sec. 4.2, defining a basis rotation that decouples the system into two SSH chains that allow for a topological characterization of the system. We calculate their energy spectra and topologically-protected edge states for different distances. In Sec. 4.3, we explore the two-boson case by introducing on-site bosonic interactions in each site. We analyze the doublon bands in the energy spectrum in terms of a strong-link model. Additionally, we derive the effective Hamiltonians for the bound states in the regime of strong interactions, which lead to effective SSH and Creutz ladder models. Finally, we present our conclusions in Sec. 4.4.

4.1   Physical system

We consider bosons loaded into a one-dimensional lattice of ring potentials with alternating distances d and d'. Each unit cell, k, includes the sites A_k and B_k, as depicted in Fig. 4.1, where we define the local polar coordinates for each site, $(\rho_{j_k}, \varphi_{j_k})$ with $j = A, B$. The ring potential at each site is formed by a displaced harmonic potential in the radial coordinate, $V(\rho_{j_k}) = \frac{1}{2} M \omega^2 (\rho_{j_k} - \rho_0)^2$, where ω is the frequency of the radial potential, M, the mass of the atoms, and ρ_0, the radius of the ring. All the local potentials are identical, they have the same frequency ω and radius ρ_0. The distances $d^{(\prime)}$ are measured from one potential minima to the next, such that the distance that separates the unit cells is $D = d + d' + 4\rho_0$ (see Fig. 4.1).

As we saw in Sec. 2.3 of Chapter 2, the eigenstates of an isolated ring potential have well-defined OAM l with winding numbers $\nu = \pm l$ such that the sets of eigenstates with different OAM l are well-separated in energy. In a lattice structure, the states of a given manifold l are only resonant to states of the same manifold, and thus, effectively decoupled, so that one can study them separately [146, 147]. The total field operator for a given OAM l can be written as
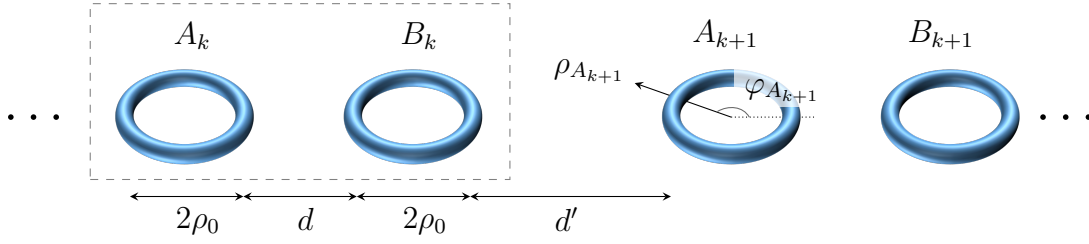
Figure 4.1: Representation of the considered one-dimensional lattice of rings. Each unit cell consists of two sites, A_k and B_k, formed by identical ring potentials where $(\rho_{j_k}, \varphi_{j_k})$ are the local radial and azimuthal coordinates at each site. The distance between adjacent sites alternates between d for consecutive sites within a unit cell and d' for the sites in adjacent unit cells.

a linear combination of the local OAM eigenstates at each site of the lattice,

$$\hat{\Psi}_l(\mathbf{r}) = \sum_{k=1}^{N_c} \sum_{\nu = \pm l} \phi_{A_k}^\nu (\rho_{A_k}, \varphi_{A_k}) \hat{a}_k^\nu + \phi_{B_k}^\nu (\rho_{B_k}, \varphi_{B_k}) \hat{b}_k^\nu, \tag{4.1}$$

where N_c is the number of unit cells and $\hat{a}_k^\nu$ and $\hat{b}_k^\nu$ are the annihilation operators of the local OAM states $|j_k^\nu\rangle$, where $j = A, B$ denotes the site and k labels the unit cell. We consider an integer number of unit cells N_c throughout this chapter. The wavefunctions of each state $|j_k^\nu\rangle$ are given by

$$\phi_{j_k}^\nu (\rho_{j_k}, \varphi_{j_k}) = \langle \mathbf{r} \mid j_k^\nu \rangle = \psi(\rho_{j_k}) \, e^{i\nu(\varphi_{j_k} - \varphi_0)}, \tag{4.2}$$

where $\psi(\rho_{j_k})$ is the radial part of the wavefunction and $e^{i\nu(\varphi_{j_k} - \varphi_0)}$ is the complex phase due to the non-zero OAM, where φ_0 indicates an arbitrary phase origin.

The total Hamiltonian that describes the bosonic system is $\hat{\mathcal{H}}_l = \hat{\mathcal{H}}_l^0 + \hat{\mathcal{H}}_l^{\text{int}}$, with a single-particle Hamiltonian

$$\hat{\mathcal{H}}_l^0 = \int d^2r \, \hat{\Psi}_l^\dagger(\mathbf{r}) \left[-\frac{\hbar^2 \nabla^2}{2M} + V(\mathbf{r}) \right] \hat{\Psi}_l(\mathbf{r}), \tag{4.3}$$

where the potential $V(\mathbf{r})$ is the sum of the truncated harmonic potentials of each site, and an interaction term that includes s-wave binary collisions

$$\hat{\mathcal{H}}_l^{int} = \frac{g}{2} \int d^2r \, \hat{\Psi}_l^\dagger(\mathbf{r}) \hat{\Psi}_l^\dagger(\mathbf{r}) \hat{\Psi}_l(\mathbf{r}) \hat{\Psi}_l(\mathbf{r}), \tag{4.4}$$

where g is proportional to the s-wave scattering length.

As we saw in Sec. 2.3.2 of Chapter 2, complex tunneling amplitudes can arise in coplanar rings for states with nonzero OAM. However, for a lattice of inline rings one can always choose the origin of the phase φ_0 along the lattice direction such that all couplings are real. Let us recall the three types of tunnelings: J_1 couples states with opposite winding numbers within a single ring, J_2 couples states with the same winding number in adjacent rings, and

J_3 couples states with opposite winding numbers in adjacent rings. Then, the tunneling strengths J_1, J_2, and J_3 can be computed from the eigenvalues of the four-state model (FSM) [see Eq. (2.37)], which can be obtained through imaginary time evolution of the single-particle FSM Hamiltonian for a particular ring separation d. As the coupling $|J_1|$ is approximately one order of magnitude smaller than the other two couplings for any distance d, it can be safely neglected in our analysis.

For the considered lattice of rings, the relevant tunneling amplitudes are J_2 and J_3, which correspond to the intra-cell distance d, and J_2' and J_3', which correspond to the inter-cell distance d' (see Fig. 4.1). In particular, we study the states with OAM $l = 1$ and winding numbers $\nu = \pm 1$, which we will denote by the circulation labels $\alpha = \pm$. We introduce the total bosonic field operator (4.1) in Eq. (4.3), use the above assumptions, and use harmonic oscillator units for the distances and energies, $\sigma = \sqrt{\hbar/M\omega}$ and $\hbar\omega$, respectively. Then, one arrives at the following single-particle Hamiltonian in terms of the creation and annihilation operators of the local OAM eigenstates

$$
\begin{aligned}
\hat{\mathcal{H}}_{l=1}^0 = {} & J_2 \sum_{k=1}^{N_c} \sum_{\alpha=\pm} \hat{a}_k^{\alpha\dagger} \hat{b}_k^{\alpha} + J_2' \sum_{k=1}^{N_c-1} \sum_{\alpha=\pm} \hat{b}_k^{\alpha\dagger} \hat{a}_{k+1}^{\alpha} + \\
& + J_3 \sum_{k=1}^{N_c} \sum_{\alpha=\pm} \hat{a}_k^{\alpha\dagger} \hat{b}_k^{-\alpha} + J_3' \sum_{k=1}^{N_c-1} \sum_{\alpha=\pm} \hat{b}_k^{\alpha\dagger} \hat{a}_{k+1}^{-\alpha} + \text{H.c.}
\end{aligned}
\tag{4.5}
$$

The interaction Hamiltonian can be obtained by introducing the total bosonic field operator restricted to an OAM l (4.1) into Eq. (4.4). As all rings are identical and we consider on-site interactions, the A and B sites yield identical interaction terms. The interaction term for a particular sublattice $j = a, b$ reads

$$
\begin{aligned}
\hat{\mathcal{H}}_{l,j}^{int} = {} & \frac{g}{2} \int d\mathbf{r}\, \hat{\Psi}_{l,j}^\dagger \hat{\Psi}_{l,j}^\dagger \hat{\Psi}_{l,j} \hat{\Psi}_{l,j} \\
= {} & \frac{g}{2} \int d\mathbf{r} \sum_{k=1}^{N_c} \left[(\phi_{j_k}^{+l})^* \hat{a}_{j_k}^{+l\dagger} + (\phi_{j_k}^{-l})^* \hat{a}_{j_k}^{-l\dagger} \right]^2 \left[\phi_{j_k}^{+l} \hat{a}_{j_k}^{+l} + \phi_{j_k}^{-l} \hat{a}_{j_k}^{-l} \right]^2 \\
= {} & \frac{g}{2} \sum_{k=1}^{N_c} \int d\mathbf{r}\, |\psi(\rho_{j_k})|^4 \left[e^{-il\varphi_{j_k}} \hat{a}_{j_k}^{+l\dagger} + e^{il\varphi_{j_k}} \hat{a}_{j_k}^{-l\dagger} \right]^2 \left[e^{il\varphi_{j_k}} \hat{a}_{j_k}^{+l} + e^{-il\varphi_{j_k}} \hat{a}_{j_k}^{-l} \right]^2 \\
= {} & \frac{g}{2} \sum_{k=1}^{N_c} \int d\mathbf{r}\, |\psi(\rho_{j_k})|^4 \left[e^{-2il\varphi_{j_k}} \left(\hat{a}_{j_k}^{+l\dagger} \right)^2 + e^{2il\varphi_{j_k}} \left(\hat{a}_{j_k}^{-l\dagger} \right)^2 + 2\hat{a}_{j_k}^{+l\dagger} \hat{a}_{j_k}^{-l\dagger} \right] \\
& \qquad\qquad\qquad\qquad \left[e^{2il\varphi_{j_k}} \left(\hat{a}_{j_k}^{+l} \right)^2 + e^{-2i\varphi_{j_k}} \left(\hat{a}_{j_k}^{-l} \right)^2 + 2\hat{a}_{j_k}^{+l} \hat{a}_{j_k}^{-l} \right] \\
= {} & \frac{U}{2} \sum_{k=1}^{N_c} \left(\hat{a}_{j_k}^{+l\dagger} \right)^2 \left(\hat{a}_{j_k}^{+l} \right)^2 + \left(\hat{a}_{j_k}^{-l\dagger} \right)^2 \left(\hat{a}_{j_k}^{-l} \right)^2 + 4\hat{a}_{j_k}^{+l\dagger} \hat{a}_{j_k}^{-l\dagger} \hat{a}_{j_k}^{+l} \hat{a}_{j_k}^{-l} \\
= {} & \frac{U}{2} \sum_{k=1}^{N_c} \hat{n}_{j_k}^{+l} \left(\hat{n}_{j_k}^{+l} - 1 \right) + \hat{n}_{j_k}^{-l} \left(\hat{n}_{j_k}^{-l} - 1 \right) + 4\hat{n}_{j_k}^{+l} \hat{n}_{j_k}^{-l},
\end{aligned}
\tag{4.6}
$$

where $\hat{n}_{j_k}^{\alpha} = \hat{j}_k^{\alpha\dagger}\hat{j}_k^{\alpha}$ are the number operators for each site j, unit cell k and circulation α, and $U \equiv g \int d\mathbf{r}\, |\psi\,(\rho_{j_k})|^4$ is the interaction strength. The total interaction Hamiltonian reads

$$\hat{\mathcal{H}}_{l=1}^{int} = \frac{U}{2} \sum_{j=a,b} \sum_{k=1}^{N_c} \left[\hat{n}_{j_k}^+ (\hat{n}_{j_k}^+ - 1) + \hat{n}_{j_k}^- (\hat{n}_{j_k}^- - 1) + 4\hat{n}_{j_k}^+ \hat{n}_{j_k}^- \right]. \tag{4.7}$$

Besides the conventional Bose-Hubbard like interaction terms for each circulation, there is an additional cross-circulation term with a greater strength.

4.2   Single particle

4.2.1   Band structure

Let us explore the single particle case. One can obtain the Hamiltonian in momentum space by considering the limit $N_c \to \infty$ and periodic boundary conditions and expanding the creation and annihilation operators in the Hamiltonian (4.5) as a Fourier integral [using Eq. (2.49) from Chapter 2]. In this case, the distance that separates the unit cells is $D = d + d' + 4\rho_0$ and $\hat{j}_q^{\alpha} = \hat{a}_q^{\alpha}, \hat{b}_q^{\alpha}$ are annihilation operators in quasimomentum space. Then, the Hamiltonian in Eq. (4.5) can be written in terms of the Hamiltonian in quasimomentum space as

$$\hat{\mathcal{H}}_{l=1}^0 = \int_{BZ} \hat{\mathbf{\Psi}}_q^{\dagger} \hat{\mathcal{H}}_q \hat{\mathbf{\Psi}}_q dq, \tag{4.8}$$

where $\hat{\mathbf{\Psi}}_q^{\dagger} = \left(\hat{a}_q^{+\dagger}, \hat{a}_q^{-\dagger}, \hat{b}_q^{+\dagger}, \hat{b}_q^{-\dagger} \right)$. For our system, the Hamiltonian $\hat{\mathcal{H}}_q$ reads

$$\hat{\mathcal{H}}_q = \begin{pmatrix} 0 & 0 & J_2 + J_2'e^{iqD} & J_3 + J_3'e^{iqD} \\ 0 & 0 & J_3 + J_3'e^{iqD} & J_2 + J_2'e^{iqD} \\ J_2 + J_2'e^{-iqD} & J_3 + J_3'e^{-iqD} & 0 & 0 \\ J_3 + J_3'e^{-iqD} & J_2 + J_2'e^{-iqD} & 0 & 0 \end{pmatrix}, \tag{4.9}$$

and has the following eigenvalues:

$$\begin{aligned} \epsilon_{1,2} &= \pm\sqrt{t_a'^2 + t_a^2 + 2t_a't_a \cos{(qD)}}, \\ \epsilon_{3,4} &= \pm\sqrt{t_s'^2 + t_s^2 + 2t_s't_s \cos{(qD)}}, \end{aligned} \tag{4.10}$$

where

$$\begin{aligned} t_a' &= J_2' - J_3', & t_a &= J_2 - J_3, \\ t_s' &= J_2' + J_3', & t_s &= J_2 + J_3. \end{aligned} \tag{4.11}$$

The system presents two sets of energy bands $\epsilon_{1,2}$ and $\epsilon_{3,4}$ that are symmetrical with respect to zero energy. The energy bands ϵ_1 and ϵ_2 tend to degeneracy at zero energy for large intertrap separations $d^{(\prime)}$, for which $J_2^{(\prime)} = J_3^{(\prime)}$. A direct topological characterization of the system does not respect the bulk-boundary correspondence, due to the presence of a unitary symmetry defined by the exchange of circulations $+ \leftrightarrow -$ in each site, which we will discuss later. In the next section we perform a basis rotation that leaves the Hamiltonian in block diagonal form, allowing for a topological characterization of the system within each block.

4.2.2   Mapping into two decoupled SSH chains

We consider the symmetric (s) and antisymmetric (a) superpositions of the positive and negative circulations in each site

$$\left|A_k^{s(a)}\right\rangle = \frac{1}{\sqrt{2}} \left(\left|A_k^+\right\rangle \underset{(-)}{+} \left|A_k^-\right\rangle\right),$$

$$\left|B_k^{s(a)}\right\rangle = \frac{1}{\sqrt{2}} \left(\left|B_k^+\right\rangle \underset{(-)}{+} \left|B_k^-\right\rangle\right). \tag{4.12}$$

In this new basis, the single particle Hamiltonian in (4.5) can be block diagonalized into two decoupled SSH chains. The symmetric chain is described by the Hamiltonian

$$\hat{\mathcal{H}}_s = t_s \sum_{k=1}^{N_c} \hat{a}_k^{s\dagger}\hat{b}_k^s + t'_s \sum_{k=1}^{N_c-1} \hat{a}_{k+1}^{s\dagger}\hat{b}_k^s + \text{H.c.}, \tag{4.13}$$

where $\hat{a}_k^s$ and $\hat{b}_k^s$ are the annihilation operators of the symmetric states defined in Eq. (4.12) and the couplings $t_s^{(\prime)}$ (4.11) define the energy bands $\epsilon_{3,4}$ of Eq. (4.10). Similarly, the antisymmetric chain is described by the Hamiltonian

$$\hat{\mathcal{H}}_a = t_a \sum_{k=1}^{N_c} \hat{a}_k^{a\dagger}\hat{b}_k^a + t'_a \sum_{k=1}^{N_c-1} \hat{a}_{k+1}^{a\dagger}\hat{b}_k^a + \text{H.c.}, \tag{4.14}$$

where $\hat{a}_k^a$ and $\hat{b}_k^a$ are the annihilation operators of the antisymmetric states defined in Eq. (4.12) and the couplings $t_a^{(\prime)}$ (4.11) define the energy bands $\epsilon_{1,2}$ of Eq. (4.10). Thus, each SSH chain contributes two energy bands to the whole system.

Figure 4.2 shows the couplings $t_a^{(\prime)}$ and $t_s^{(\prime)}$ as a function of the separation distance between two rings $d^{(\prime)}$ obtained numerically using Eqs. (4.11) and (2.37). We represent the cases of two ring radii, $\rho_0 = 2.5\sigma$ and 5σ, where $\sigma = \sqrt{\hbar/M\omega}$ is the harmonic oscillator length. All couplings decay with the separation distance, but due to the dependence of $t_s^{(\prime)}$ and $t_a^{(\prime)}$ on the couplings $J_2^{(\prime)}$ and $J_3^{(\prime)}$, $t_a^{(\prime)}$ remains much smaller than $t_s^{(\prime)}$ regardless of the ring radius ρ_0 and frequency ω.

In the SSH model [210], the topological phase of the system is determined by the ratio of the couplings, t/t' (see a detailed discussion in Sec. 2.4). This ratio determines the value of the Zak phase in each energy band p [Eq. (2.47)], which is obtained through the eigenstates of the bulk Hamiltonian. For $t < t'$, the Zak phase is $\mathcal{Z}_{1,2} = \pi$ and the system is in the topological phase, while for $t > t'$, the Zak phase is $\mathcal{Z}_{1,2} = 0$ and the system is in the trivial phase [see Fig. 4.3(a) and (b)]. As predicted by the bulk-boundary correspondence, the system with open boundary conditions presents two edge states in the topological phase that are not present in the trivial phase, shown in the next section.

One might try to compute the Zak phase using the eigenstates of the non-rotated Hamiltonian, Eq. (4.9), which presents four energy bands and three energy gaps. In that case, the presence of edge states at each gap would be given by the sum of the Zak phases of all the
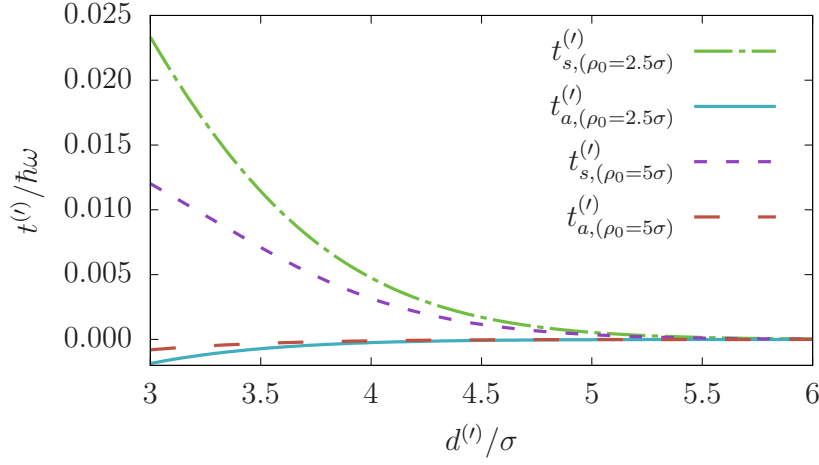
Figure 4.2: Couplings $t_a^{(\prime)}$ and $t_s^{(\prime)}$ as a function of the separation distance $d^{(\prime)}$ between rings for $\rho_0 = 2.5\sigma$ and $\rho_0 = 5\sigma$, where $\sigma = \sqrt{\hbar/M\omega}$ is the harmonic oscillator length.

bands below that gap. However, those results do not fulfill the bulk-boundary correspondence, as they do not correctly predict the presence of edge states. This is due to the fact that the Hamiltonian presents a unitary symmetry that exchanges the circulations $+ \leftrightarrow -$ at each site. As a result, the Hamiltonian can be block diagonalized such that each pair of bands arising from each symmetry sector have independent Zak phases associated to them.

Figure 4.3 shows the phases of the symmetric, $\hat{\mathcal{H}}_s$, and antisymmetric, $\hat{\mathcal{H}}_a$, chains as a function of the separation distances d and d' for $\rho_0 = 5\sigma$. The color represents the ratios (a) t_s/t'_s and (b) t_a/t'_a, and the solid black lines separate the trivial (above) and topological (below) phases. We define the nearly dimerized regimes of the trivial and topological phases by their lower boundaries at $t/t' = 10$ (dotted blue line) and upper boundaries at $t/t' = 0.1$ (dashed yellow line), respectively. In the nearly dimerized regime, the SSH model is well approximated by a set of decoupled dimers that correspond to the dimerized limit. Both chains are in the topological phase for $d > d'$, and in the trivial phase for $d < d'$, but the ratio t/t' varies for the symmetric and antisymmetric chains, as it is determined by the dependence of the couplings t_a, t_s on J_2 and J_3, Eq. (4.11). Thus, it is subject to their constraints, namely: (i) the couplings decay with the distance d, (ii) $J_3 > J_2$ with $J_3 \approx J_2$ for $d \gg 1$, (iii) $J_2, J_3 > 0$, valid for the considered range of distances.

Decoupled SSH chains also emerge in other physical platforms, such as the polariton micropillar system supporting the excited photonic modes p_x and p_y studied in [306]. The zigzag configuration of the micropillar structure gives rise to two decoupled SSH chains corresponding to the p_x and p_y modes, with a glide reflection symmetry between the chains [307], which are in opposite topological phases due to the geometry of the structure. In contrast, here both SSH chains are in the same topological phase for any pair of distances d and d'.
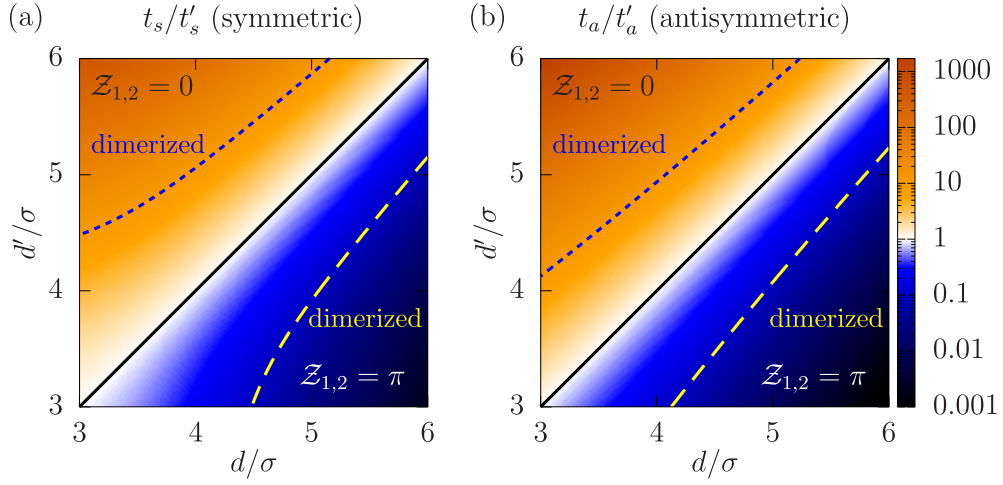
Figure 4.3: Phase diagram of the (a) symmetric, $\hat{\mathcal{H}}_s$, and (b) antisymmetric, $\hat{\mathcal{H}}_a$, chains as a function of the separation distances between rings, $d^{(\prime)}$, for $\rho_0 = 5\sigma$, where $\sigma = \sqrt{\hbar/M\omega}$ is the harmonic oscillator length. Color represents the ratios (a) t_s/t'_s and (b) t_a/t'_a, the black line separates the trivial phases with $\mathcal{Z}_{1,2} = 0$ (warm colors) and the topological phases with $\mathcal{Z}_{1,2} = \pi$ (cold colors). The dashed blue lines and dotted yellow lines bound the nearly dimerized regimes of the trivial and topological phases, respectively.

4.2.3   Exact diagonalization results

We consider a lattice of rings of $N_c = 20$ unit cells with $\rho_0 = 5\sigma$, $d' = 3.6\sigma$ and the two cases $d = 4\sigma$ and 5σ. Figure 4.4 shows the energy spectrum of the system for $d = 4\sigma$ (black dots) and $d = 5\sigma$ (blue crosses). The outer bands correspond to the symmetric chain $\hat{\mathcal{H}}_s$ [$\epsilon_{3,4}$ in (4.10)], while the inner bands correspond to the antisymmetric chain $\hat{\mathcal{H}}_a$ [$\epsilon_{1,2}$ in (4.10)]. This correspondence can be deduced from the values of t_s and t_a [see Eq. (4.11) and Fig. 4.2], as they fulfill $t_s > t_a$. Additionally, the condition $t_s > t_a$ also makes the outer bands more dispersive than the inner bands for both distances d [see $\epsilon_{1,2}$ and $\epsilon_{3,4}$ in Eq. (4.10)]. For both cases, the two chains are in the topological phase, which leads to the presence of four edge states, two for each chain. The dispersion of both models is reduced considerably for $d = 5\sigma$ compared to $d = 4\sigma$, as both chains enter the nearly dimerized regime.

Figure 4.5 shows (i) the amplitude of the left and right edge states of $\hat{\mathcal{H}}_s$ and $\hat{\mathcal{H}}_a$, and (ii) the real space densities $|\Psi|^2$ of the left edge state, taking $d' = 3.6\sigma$, $\rho_0 = 5\sigma$, and $N_c = 20$ for all cases. Figures (a) and (c) correspond to the symmetric chain for $d = 4\sigma$ and $d = 5\sigma$, respectively. Figures (b) and (d) correspond to the antisymmetric chain for $d = 4\sigma$ and $d = 5\sigma$, respectively. In subfigures (i), each bar represents the amplitude of the basis states in Eq. (4.12) for each site. In all cases, the edge states only populate one sublattice, either the A, or the B sites, with the population decaying exponentially from the edge. They are obtained as the symmetric and antisymmetric superpositions of their hybridized counterparts. The edge states for $d = 5\sigma$, show an almost complete localization of the population in the edge site as both $\hat{\mathcal{H}}_s$ and $\hat{\mathcal{H}}_a$ are within the nearly dimerized regime. However, for $d = 4\sigma$ all edge
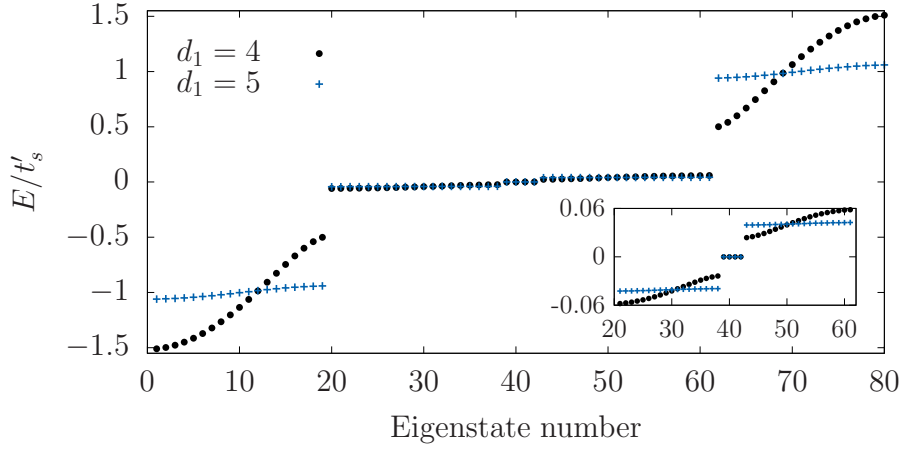
Figure 4.4: Single particle energy spectrum for a chain of $N_c = 20$ unit cells with $\rho_0 = 5\sigma$, distances $d' = 3.6\sigma$, $d = 4\sigma$ (black dots) and $d = 5\sigma$ (blue crosses). The inset shows the inner bands given by $\hat{\mathcal{H}}_a$ and the zero-energy edge states.

states penetrate considerably into the bulk. In subfigures (ii) that show the real space density plots, one can see the difference between the edge states of $\hat{\mathcal{H}}_s$ and $\hat{\mathcal{H}}_a$ in the orientation of the nodes that appear in the density $|\Psi|^2$. These nodes appear due to the superposition of the positive and negative circulations of the mode with OAM $l = 1$, Eq. (4.12).

4.3 Two-particle

In this section we investigate the role of on-site bosonic interactions by considering the simplest possible interacting case, a two-boson system. The total Hamiltonian is $\hat{\mathcal{H}}_{l=1} = \hat{\mathcal{H}}^0_{l=1} + \hat{\mathcal{H}}^{\text{int}}_{l=1}$, where the independent-particle term $\hat{\mathcal{H}}^0_{l=1}$ [interaction term $\hat{\mathcal{H}}^{\text{int}}_{l=1}$] is given in Eq. (4.5) [Eq. (4.7)]. Figure 4.6 shows the two-particle energy spectrum in gray lines as a function of the interaction strength to tunneling ratio U/t'_s for a chain of $N_c = 15$ unit cells with $\rho_0 = 5\sigma$ and the distances $d = 5\sigma$ and $d' = 3.6\sigma$. At zero interaction $U/t'_s = 0$, the spectrum presents five scattering continua, which correspond to the different two-particle combinations that occupy the different energy bands of the single-particle spectrum. As the particles occupy different sites, the energy bandwidth of these bands stays constant for any value of U. For a non-zero interaction strength, nine additional bands can be distinguished, for which the energy depends on the interaction strength U. On top of these bands we plot in color the eigenvalues of the strong-link Hamiltonian discussed in the next section. Those bands have contributions of basis states where two bosons occupy the same site, forming a bound state referred as doublon, that leads to a nonzero interaction energy [289–293].

In order to characterize the doublon bands, we analyze two regimes: (i) For the topological dimerized limit of the original lattice, where $d' < d$ and $J'_2, J'_3 \gg J_2, J_3$, we derive a strong-link model that describes the doublon bands at any interaction strength U, and (ii) For the limit of strong interactions, $U \gg J_2^{(\prime)}, J_3^{(\prime)}$, we use perturbation theory to describe the effective
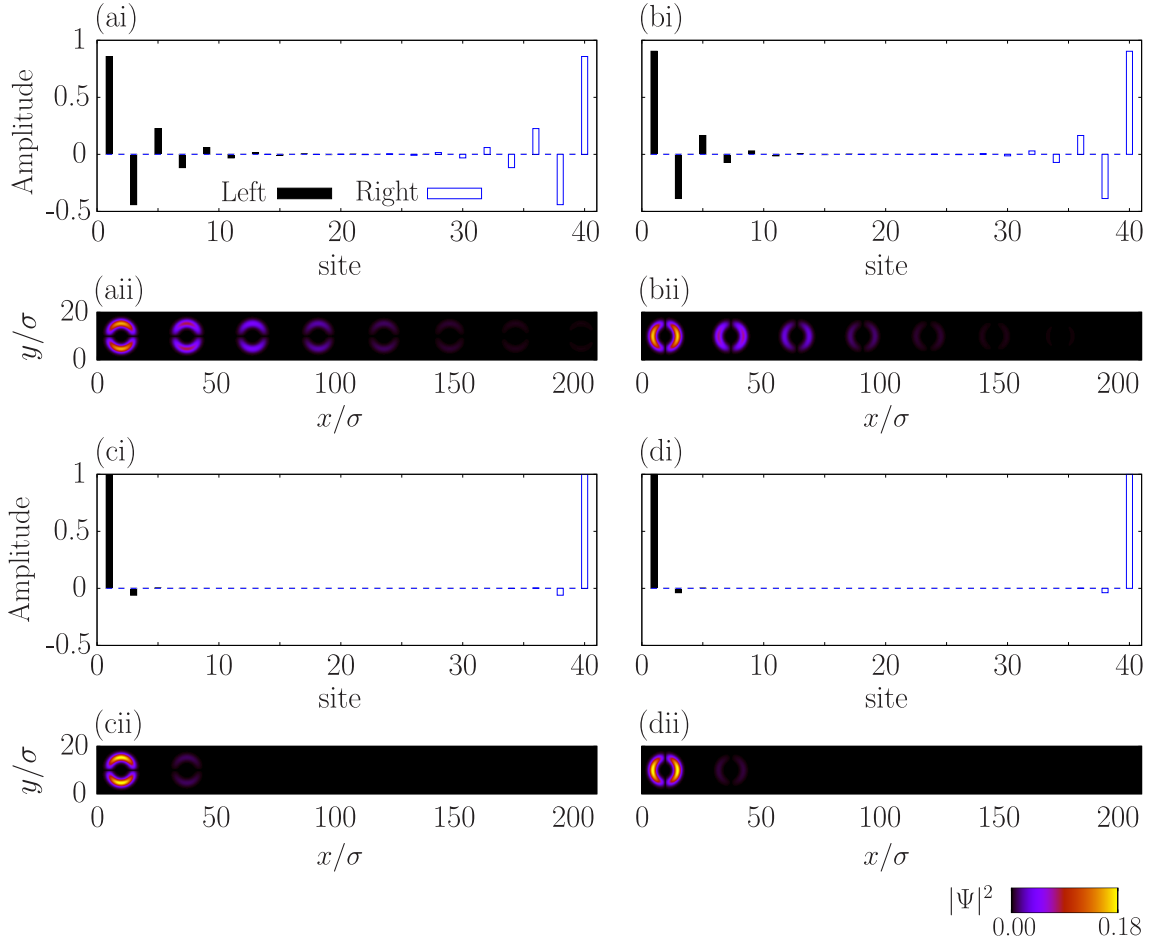
Figure 4.5: Edge states of (a,c) $\hat{\mathcal{H}}_s$ and (b,d) $\hat{\mathcal{H}}_a$. The distance is (a,b) $d = 4\sigma$ and (c,d) $d = 5\sigma$, with $d' = 3.6\sigma$, $\rho_0 = 5\sigma$, and $N_c = 20$ for all cases. (i) Amplitude of the left (filled black bars) and right (empty blue bars) edge states of the symmetric and antisymmetric states (4.12) at each site. (ii) Real space density, $|\Psi|^2$ of the first 15 sites of the left edge state. The edge states arise as the symmetric and antisymmetric superpositions of their hybridized counterparts.

subspaces that appear as a result of introducing the couplings $J_2^{(\prime)}$, $J_3^{(\prime)}$ as a perturbation.

Strong-link Hamiltonian

In this section we consider the dimerized limit of the real space SSH lattice. First, we consider the topological dimerization, for which $d' < d$, and such that the corresponding couplings can be neglected, $J_2', J_3' \gg J_2, J_3$. Thus, the symmetric $\hat{\mathcal{H}}_s$ and antisymmetric $\hat{\mathcal{H}}_a$ SSH lattices are also in the dimerized limit. In this regime, the doublon bands can be described by the reduced two-particle Hamiltonian of a single strong link in unit cells k and $k + 1$. This approach was used in [303] to analyze the doublon bands of the two-particle conventional SSH model. The basis states of this two-particle Hamiltonian are the ten two-particle combinations of the sites

A and B in the unit cells k and $s = k + 1$, namely:

$$\{ \left|A_s^+ A_s^+\right\rangle, \left|A_s^+ A_s^-\right\rangle, \left|A_s^+ B_k^+\right\rangle, \left|A_s^+ B_k^-\right\rangle, \left|A_s^- A_s^-\right\rangle,$$
$$\left|A_s^- B_k^+\right\rangle, \left|A_s^- B_k^-\right\rangle, \left|B_k^+ B_k^+\right\rangle, \left|B_k^+ B_k^-\right\rangle, \left|B_k^- B_k^-\right\rangle \}. \tag{4.15}$$

In this basis, the strong-link Hamiltonian reads

$$\hat{\mathcal{H}}_{SL} = \begin{pmatrix} U & 0 & \sqrt{2}J_2' & \sqrt{2}J_3' & 0 & 0 & 0 & 0 & 0 & 0 \\ 0 & 2U & J_3' & J_2' & 0 & J_2' & J_3' & 0 & 0 & 0 \\ \sqrt{2}J_2' & J_3' & 0 & 0 & 0 & 0 & 0 & \sqrt{2}J_2' & J_3' & 0 \\ \sqrt{2}J_3' & J_2' & 0 & 0 & 0 & 0 & 0 & 0 & J_2' & \sqrt{2}J_3' \\ 0 & 0 & 0 & 0 & U & \sqrt{2}J_3' & \sqrt{2}J_2' & 0 & 0 & 0 \\ 0 & J_2' & 0 & 0 & \sqrt{2}J_3' & 0 & 0 & \sqrt{2}J_3' & J_2' & 0 \\ 0 & J_3' & 0 & 0 & \sqrt{2}J_2' & 0 & 0 & 0 & J_3' & \sqrt{2}J_2' \\ 0 & 0 & \sqrt{2}J_2' & 0 & 0 & \sqrt{2}J_3' & 0 & U & 0 & 0 \\ 0 & 0 & J_3' & J_2' & 0 & J_2' & J_3' & 0 & 2U & 0 \\ 0 & 0 & 0 & \sqrt{2}J_3' & 0 & 0 & \sqrt{2}J_2' & 0 & 0 & U \end{pmatrix}. \tag{4.16}$$

To find the eigenvalues and eigenvectors of $\hat{\mathcal{H}}_{SL}$, we consider the regime of large distances where $J_2' \simeq J_3' \equiv J$. In this regime, the eigenvalues are

$$E_1 = 0, \qquad E_2 = U, \qquad E_3 = 2U,$$
$$E_{7,8} = \frac{U - \sqrt{16J^2 + U^2}}{2}, \qquad E_{9,10} = \frac{U + \sqrt{16J^2 + U^2}}{2},$$
$$E_{4+q} = \left[\cos\left(\frac{1}{3} \arccos\left[-\frac{U}{4\sqrt{2}J} \left(\frac{\frac{U^2}{8J^2} + 2}{3} \right)^{-\frac{3}{2}} \right] + \frac{2\pi q}{3} \right) \cdot 2\sqrt{\frac{\frac{U^2}{8J^2} + 2}{3}} + \frac{U}{2\sqrt{2}J} \right] 2\sqrt{2}J, \tag{4.17}$$

where $q = 0, 1, 2$. Table 4.1 presents the eigenvectors in the limit $|U| \gg J$ while the general expressions can be found in Table B.1 of the Appendix B.1. The strong-link model for the trivial dimerization is analogous to the topological dimerization model and it can be obtained by simply replacing the indices $s = k + 1$ of each A site in the basis states (17) by $s = k$. This yields the same eigenvectors and eigenvalues given in Eq. (4.17) and Tables 4.1 and B.1 in the regime of large distances.

Figure 4.6(a) shows the eigenvalues (in color) on top of the exact diagonalization results (in gray) as a function of the ratio U/t_s'. The exact diagonalization results correspond to the distances $d = 5\sigma$ and $d' = 3.6\sigma$, which determine the values of the couplings $J_2^{(')}$, $J_3^{(')}$ (see Fig. 4.2). To compare the analytical and numerical results, we fix the coupling J of $\hat{\mathcal{H}}_{SL}$ as the largest numerical coupling, J_3', which corresponds to the topological dimerization of the strong-link model. Thus, we consider the eigenvalues of $\hat{\mathcal{H}}_{SL}$ in the regime of large distances $(J_2' \simeq J_3' \equiv J)$, Eq. (19). The analytically obtained eigenvalues accurately predict the overall energy dependence of the doublon bands obtained numerically.
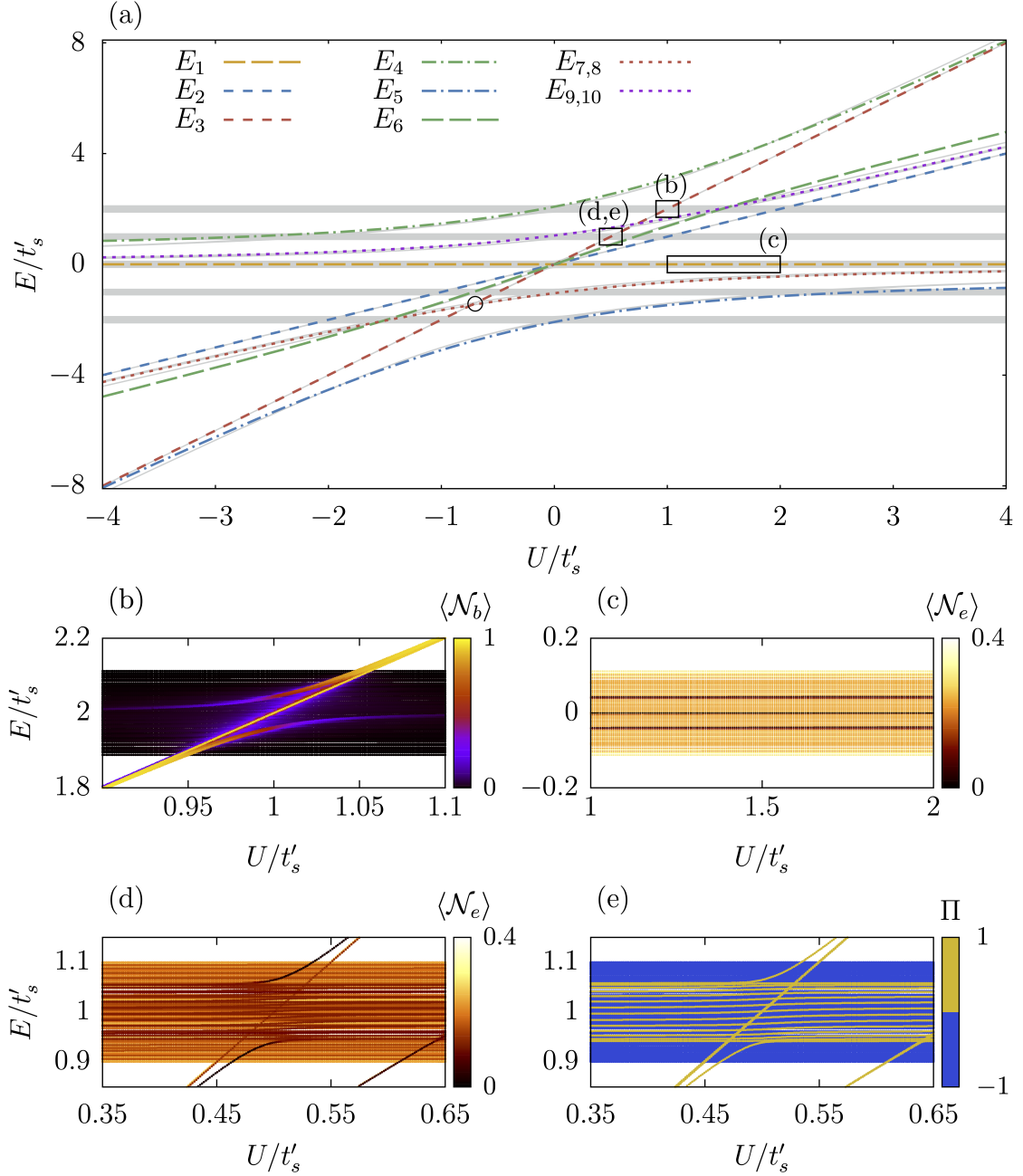
Figure 4.6: (a) Two-particle energy spectrum for a chain of $N_c = 15$ unit cells with $\rho_0 = 5\sigma$ and distances $d' = 3.6\sigma$, $d = 5\sigma$ obtained through exact diagonalization (gray lines) and eigenvalues of the strong-link Hamiltonian Eq. (4.16) for $J_3' = J$ in color. (b-e): Numerical results for various sections of the spectrum with the color indicating (b) the expectation value of the bound state population $\mathcal{N}_b$; (c,d), the expectation value of the average distance to the nearest edge $\mathcal{N}_e$, and (e) parity Π. The circle indicates a crossing between different doublon bands and the rectangles indicate the sections of the spectrum depicted in (b-e).

v_n	$E_{n,|U|\gg J}$	Π	$\lvert A_s^+A_s^+\rangle$	$\lvert A_s^+A_s^-\rangle$	$\lvert A_s^+B_k^+\rangle$	$\lvert A_s^+B_k^-\rangle$	$\lvert A_s^-A_s^-\rangle$	$\lvert A_s^-B_k^+\rangle$	$\lvert A_s^-B_k^-\rangle$	$\lvert B_k^+B_k^+\rangle$	$\lvert B_k^+B_k^-\rangle$	$\lvert B_k^-B_k^-\rangle$
v_1	0	$+$	0	0	$\frac{1}{2}$	$-\frac{1}{2}$	0	$-\frac{1}{2}$	$\frac{1}{2}$	0	0	0
v_2	U	$+$	$-\frac{1}{2}$	0	0	0	$-\frac{1}{2}$	0	0	$\frac{1}{2}$	0	$\frac{1}{2}$
v_3	$2U$	$+$	0	$-\frac{1}{\sqrt{2}}$	0	0	0	0	0	0	$\frac{1}{\sqrt{2}}$	0
v_4	$\{2U,0\}$	$+$	0	$\{\frac{1}{\sqrt{2}},0\}$	$\{0,\frac{1}{2}\}$	$\{0,\frac{1}{2}\}$		$\{0,\frac{1}{2}\}$	$\{0,\frac{1}{2}\}$		$\{\frac{1}{\sqrt{2}},0\}$	
v_5	$\{0,2U\}$	$+$	0	$\{0,\frac{1}{\sqrt{2}}\}$	$\{-\frac{1}{2},0\}$	$\{-\frac{1}{2},0\}$		$\{-\frac{1}{2},0\}$	$\{-\frac{1}{2},0\}$		$\{0,\frac{1}{\sqrt{2}}\}$	
v_6	U	$+$	$\frac{1}{2}$	0	0	0	$\frac{1}{2}$	0	0	$\frac{1}{2}$	0	$\frac{1}{2}$
v_7	$\{0,U\}$	$-$	$\{0,\frac{1}{2}\}$	0	0	$\{-\frac{1}{\sqrt{2}},0\}$	$\{0,-\frac{1}{2}\}$	$\{\frac{1}{\sqrt{2}},0\}$	0	$\{0,-\frac{1}{2}\}$	0	$\{0,\frac{1}{2}\}$
v_8	$\{0,U\}$	$-$	$\{0,\frac{1}{2}\}$	0	$\{-\frac{1}{\sqrt{2}},0\}$	0	$\{0,-\frac{1}{2}\}$	0	$\{\frac{1}{\sqrt{2}},0\}$	$\{0,\frac{1}{2}\}$	0	$\{0,-\frac{1}{2}\}$
v_9	$\{U,0\}$	$-$	$\{\frac{1}{2},0\}$	0	0	$\{0,\frac{1}{\sqrt{2}}\}$	$\{-\frac{1}{2},0\}$	$\{0,-\frac{1}{\sqrt{2}}\}$	0	$\{-\frac{1}{2},0\}$	0	$\{\frac{1}{2},0\}$
v_{10}	$\{U,0\}$	$-$	$\{\frac{1}{2},0\}$	0	$\{0,\frac{1}{\sqrt{2}}\}$	0	$\{-\frac{1}{2},0\}$	0	$\{0,-\frac{1}{\sqrt{2}}\}$	$\{\frac{1}{2},0\}$	0	$\{-\frac{1}{2},0\}$

Table 4.1: Normalized eigenvectors v_n and eigenvalues E_n of the strong-link Hamiltonian $\hat{\mathcal{H}}_{SL}$ in the regime of large distances, and the regime of strong interactions $|U| \gg J$. Two cases are considered, $\{U > 0, U < 0\}$, and a single number is given when it is the same for both cases. Note that the eigenvectors and eigenvalues $n = 1, 2, 3$ are independent of the ratio $|U|/J$. The third column indicates the parity Π of the eigenstate with respect to the exchange circulation symmetry $+ \leftrightarrow -$ in each site.

Table 4.1 gives the eigenvectors v_n of the strong-link Hamiltonian Eq. (4.16) in the regime of strong interactions $|U| \gg J$ for two cases, $\{U > 0, U < 0\}$, and specifies the corresponding eigenvalues E_n for the two regimes. The eigenvectors and eigenvalues $n = \{1 - 3\}$ do not depend on the coupling J and thus they do not change when increasing $|U|/J$. In both regimes, the eigenvalues form three groups, with energies 0, U and $2U$. This tendency can be observed even for relatively small ratios $|U|/t_s'$ in Fig. 4.6, where the energy difference between the different groups of doublon bands diminishes for increasing values of $|U|/t_s'$. The eigenvectors in Table 4.1 clarify the differences between these three groups. The eigenvectors with energy zero are a superposition of states where the two particles populate different sites, $|A_s^\alpha, B_k^{\alpha'}\rangle$. As there are four possible states, there are four bands with energy zero. In these states the two bosons do not interact, and their energy, which is given by the interaction Hamiltonian term (4.7), becomes zero. The group with energy U is composed of eigenstates that are a superposition of states with two bosons in the same site and the same circulation, $|j_k^\alpha, j_k^\alpha\rangle$, which also results in four possible states and four energy bands. Finally, the group with energy $2U$ is formed of states where the bosons occupy opposite circulations in the same site $|j_k^+, j_k^-\rangle$. In this case, there are only two available states and this results in only two energy bands.

Figure 4.7 represents the adjacency graph of the strong-link Hamiltonian $\hat{\mathcal{H}}_{SL}$ and its symmetries. Each vertex represents one of the basis states in Eq. (4.15) and the edges represent the off-diagonal (solid blue lines) and diagonal (solid blue loops) matrix elements of $\hat{\mathcal{H}}_{SL}$. The symmetries of the graph become explicit by locating the states $|B_k^+ B_k^-\rangle$ and $|A_s^+ A_s^-\rangle$ in the out-of-plane z axis, which is perpendicular to the plane where all the other basis states
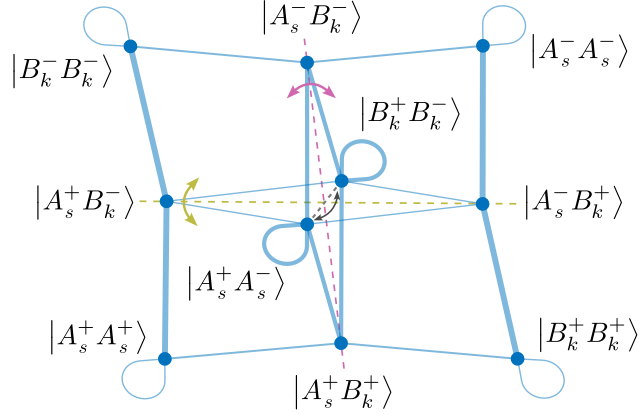
Figure 4.7: Adjacency graph of the strong-link Hamiltonian $\hat{\mathcal{H}}_{SL}$ Eq. (4.16). Each vertex represents one of the basis states in Eq. (4.15) and the edges represent the off-diagonal (solid blue lines) and diagonal (solid blue loops) matrix elements of $\hat{\mathcal{H}}_{SL}$. The dashed lines indicate the reflection symmetries with respect to the oxz (yellow), oyz (pink), and oxy planes, where the states $|B_k^+ B_k^-\rangle$ and $|A_s^+ A_s^-\rangle$ are located in the out-of-plane axis z (gray).

lie (where $s = k + 1$). Then, the graph explicitly exhibits three symmetries: (i) a reflection symmetry with respect to the oxz (yellow) plane that leaves the states $|B_k^+ B_k^-\rangle$, $|A_s^+ A_s^-\rangle$, $|A_s^+ B_k^-\rangle$, and $|A_s^- B_k^+\rangle$ invariant; (ii) a reflection symmetry with respect to the oyz (pink) plane that leaves the states $|B_k^+ B_k^-\rangle$, $|A_s^+ A_s^-\rangle$, $|A_s^- B_k^-\rangle$, and $|A_s^+ B_k^+\rangle$ invariant; and (iii) a reflection symmetry respect to oxy plane that only permutes the states $|B_k^+ B_k^-\rangle$ and $|A_s^+ A_s^-\rangle$ located in the out-of-plane axis z (gray). A single strong-link is symmetric with respect to the exchange of the sites A and B, regardless of the number of particles. This symmetry is reflected in the two-particle graph as the combined application of the symmetries (ii) and (iii). However, this symmetry disappears when we move away from the dimerized limit by introducing weak couplings between the different strong links. In contrast, there is a symmetry that originates in the total Hamiltonian [Eqs. (4.5) and (4.7)], the exchange of circulations $+ \leftrightarrow -$ in each site, which is inherited by $\hat{\mathcal{H}}_{SL}$. This symmetry can be obtained by applying the symmetries (i) and (ii) in the two-particle graph. Both the eigenstates of $\hat{\mathcal{H}}_{l=1}$ and $\hat{\mathcal{H}}_{SL}$ have well-defined parities Π with respect to the exchange of circulations in each site, and we indicate the latter in Table 4.1.

The spectrum in Fig. 4.6 shows a large number of intersections and avoided crossings between the doublon bands and the scattering continua, as well as between different doublon bands at $U/t_s' \simeq \pm 0.7$ [black circle in Fig. 4.6(a)]. The presence of avoided crossings can be understood in terms of the circulation exchange symmetry $+ \leftrightarrow -$ discussed above. They can appear for doublon states and extended states of the same parity that converge in energy. In contrast, states of opposite parities belong to different symmetry sectors and are therefore completely decoupled. Below we discuss two examples of avoided crossings.

Fig. 4.6(b) shows the avoided crossing of the state v_3 with the upper band of extended states. The color represents the expectation value of the bound state population in each strong

link $\mathcal{N}_b = \sum_{k=1}^{N_c-1} \hat{n}_k^b$, where

$$
\begin{aligned}
\hat{n}_k^b =&\hat{n}_{A_{k+1}}^+ \hat{n}_{A_{k+1}}^+ + \hat{n}_{A_{k+1}}^+ \hat{n}_{A_{k+1}}^- + \hat{n}_{A_{k+1}}^+ \hat{n}_{B_k}^+ + \hat{n}_{A_{k+1}}^+ \hat{n}_{B_k}^- + \hat{n}_{A_{k+1}}^- \hat{n}_{A_{k+1}}^- \\
&+ \hat{n}_{A_{k+1}}^- \hat{n}_{B_k}^+ + \hat{n}_{A_{k+1}}^- \hat{n}_{B_k}^- + \hat{n}_{B_k}^+ \hat{n}_{B_k}^+ + \hat{n}_{B_k}^+ \hat{n}_{B_k}^- + \hat{n}_{B_k}^- \hat{n}_{B_k}^-.
\end{aligned}
\tag{4.18}
$$

The number operators account for the ten state combinations that form the strong-link Hamiltonian basis in the topological dimerization. This avoided crossing occurs due to the strong hybridization between the state v_3, which has positive parity, and extended states of the upper band, where all states also have positive parity.

In the avoided crossing shown in Figs. 4.6(d) and (e), the strong resonance involves an edge bound state instead of the states of the band associated to the state v_3. The color in Fig. 4.6(d) gives the expectation value of $\mathcal{N}_e = \sum_{o=1}^{2N_c} \sum_{\alpha=\pm} \min((o-1)/2N_c, 1 - o/2N_c)\hat{n}_{o,\alpha}/2$ where $\hat{n}_{o,\alpha}$ is the number operator at site o for the circulation $\alpha = \pm$, so that it represents the average normalized distance to the nearest edge. There are two states below and above the doublon bands with high edge localization (dark lines), which indicates the presence of edge bound states associated to that doublon band. For the same avoided crossing, the color in Fig. 4.6(e) indicates the parity Π of each eigenstate. Embedded within the band of extended states, there is an inner band of extended states with a lower value of $\langle \mathcal{N}_e \rangle$, which correspond to those states where a particle occupies the upper single-particle band of the symmetric SSH spectrum and the other particle occupies an edge state [304]. Of these states, only some have a positive parity that allows for the avoided crossing to occur. Such embedded states are only present in the topological dimerization of the original chain, which possesses four topologically protected single-particle edge states. They are also present in the zero energy band [dark horizontal lines in Fig. 4.6(c)], in which either the two particles occupy an edge state, at exactly zero energy, or one occupies one edge state while the other occupies the single-particle bands of the antisymmetric SSH lattice.

To obtain the strong-link Hamiltonian we consider that each strong link is completely decoupled from the adjacent ones, such that every dimer yields exactly the same eigenvalues. This model is strictly valid in the dimerized limit, where the either the inter- or intra-cell couplings are exactly zero. As a result of the weak coupling between strong links, the doublon bands computed through exact diagonalization are not exactly degenerate, but present some dispersion [see Fig. 4.6(b)]. Additionally, the doublon bands obtained numerically can present edge bound states above or below the energy of the corresponding doublon band [dark lines in Fig. 4.6(d)]. They can be identified with Tamm-Shockley states as they are a result of the renormalized couplings at the edge sites that arise when one introduces the weak couplings as a perturbation [303, 308–310]. In the next section we are going to lift this degeneracy by moving away from the dimerized limit and we will consider the regime of strong interactions to better understand the emergence of the doublon subspaces.

Strong interactions limit

Consider the regime of strong interactions, where the interactions dominate over the tunneling processes, $U \gg J_2, J_3, J_2', J_3'$. The available states for $U \to \infty$, can be deduced from the

three groups of eigenvectors of the strong-link Hamiltonian for strong interactions (see Table 4.1). The two bosons can either occupy different sites or occupy the same site forming a doublon. The bosons can form two possible bound states: $\mathcal{A}$, where the two particles occupy the same site and the same circulation, $|j_k^\alpha, j_k^\alpha\rangle$, with $j = A, B$ and $\alpha = \pm$, and $\mathcal{B}$, where the two particles occupy the same site and opposite circulations $|j_k^+, j_k^-\rangle$. These bound states have energies $E_\mathcal{A} = U$ and $E_\mathcal{B} = 2U$, respectively, given by the interaction term (4.7).

If one introduces the couplings J_2, J_3, J_2', J_3' as a perturbation, the bound states in adjacent sites become coupled through second-order hopping processes, which creates an effective dispersive subspace for each bound state class. As the bound states are well separated in energy, these subspaces are decoupled and can be analyzed independently. The matrix elements of the effective Hamiltonian for each subspace up to second-order perturbation theory read [311, 312]

$$\langle u|\hat{\mathcal{H}}_{\text{eff}}|u'\rangle = E_u^0 \delta_{uu'} + \frac{1}{2} \sum_w \langle u|\hat{\mathcal{H}}_{l=1}^0|w\rangle \langle w|\hat{\mathcal{H}}_{l=1}^0|u'\rangle \left[\frac{1}{E_u^0 - E_w^0} + \frac{1}{E_{u'}^0 - E_w^0} \right],$$

(4.19)

where $|u\rangle$, $|u'\rangle$ are the bound-states, $|w\rangle$, $|w'\rangle$ are the mediating states in each hopping process, and E^0 are the unperturbed energies. Note that the first-order corrections are always zero. For $|u\rangle \neq |u'\rangle$, one obtains an effective tunneling term, while for $|u\rangle = |u'\rangle$, one obtains an effective on-site potential.

$\mathcal{B}$ subspace

Let us start with the $\mathcal{B}$ subspace, which is composed of only one bound state per site, $|j_k^+, j_k^-\rangle$. The existence of this bound state is due to the inter-circulation interaction term in the interaction Hamiltonian (4.7). Thus, it is a consequence of the ring structure of each site of the lattice [150, 153] and cannot appear in a conventional SSH lattice [303]. When we introduce the couplings J_2, J_3, J_2', J_3' as a perturbation, the bound states of the $\mathcal{B}$ subspace in adjacent sites become coupled through second-order hopping processes. These yield two effective couplings: an intra-cell coupling between the bound states $|A_k^+, A_k^-\rangle$ and $|B_k^+, B_k^-\rangle$, and an inter-cell coupling between $|B_k^+ B_k^-\rangle$ and $|A_{k+1}^+, A_{k+1}^-\rangle$. Additionally, each bound state acquires a self-energy term through second-order processes, yielding effective on-site potentials at each site. Note that in the edge sites there are half the mediating states present in the bulk sites [303, 304, 308]. Thus, the effective on-site potential in the edge V_E is smaller than the on-site potential in the bulk V_B. Using Eq. (4.19), the resulting effective subspace is an SSH chain with renormalized couplings and a bulk-edge on-site potential mismatch

$$\hat{\mathcal{H}}_\mathcal{B} = \left[\frac{J_2^2 + J_3^2}{U} \sum_{k=1}^{N_c} \hat{a}_k^{\mathcal{B}\dagger} \hat{b}_k^\mathcal{B} + \frac{J_2'^2 + J_3'^2}{U} \sum_{k=1}^{N_c-1} \hat{a}_{k+1}^{\mathcal{B}\dagger} \hat{b}_k^\mathcal{B} \right] + \text{H.c.}$$

$$+ \frac{J_2^2 + J_3^2 + J_2'^2 + J_3'^2}{U} \sum_{k=1}^{N_c} (\hat{a}_k^{\mathcal{B}\dagger} \hat{a}_k^\mathcal{B} + \hat{b}_k^{\mathcal{B}\dagger} \hat{b}_k^\mathcal{B}) - \frac{J_2'^2 + J_3'^2}{U} (\hat{a}_1^{\mathcal{B}\dagger} \hat{a}_1^\mathcal{B} + \hat{b}_{N_c}^{\mathcal{B}\dagger} \hat{b}_{N_c}^\mathcal{B}),$$

(4.20)

where the creation and annihilation operators $\hat{a}_k^{\mathcal{B}(\dagger)}$ and $\hat{b}_k^{\mathcal{B}(\dagger)}$ correspond to the bound states of
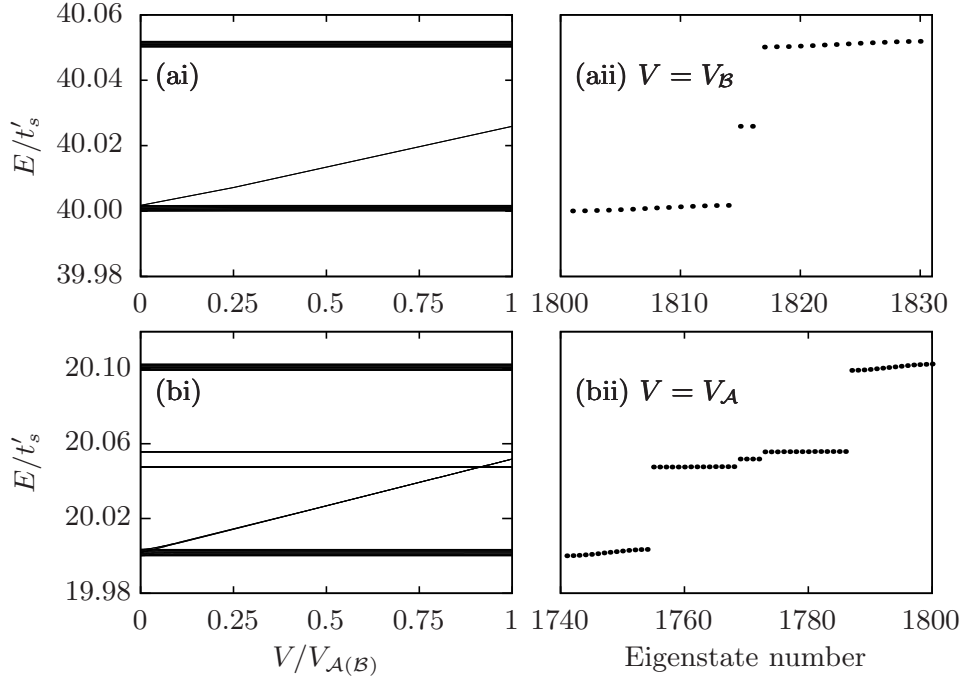
Figure 4.8: Two-particle energy spectrum for $N_c = 15$ unit cells with $\rho_0 = 5\sigma$, distances $d' = 3.6\sigma$, $d = 4.5\sigma$, and $U/t'_s = 20$ for the (a) $\mathcal{B}$ and (b) $\mathcal{A}$ subspaces. (i) Energies as a function of the edge on-site potential correction V in units of $V_{\mathcal{A}(\mathcal{B})}$ and (ii) energies for the exactly compensated on-site potential mismatch, (aii) $V = V_{\mathcal{B}}$ and (bii) $V = V_{\mathcal{A}}$.

the $\mathcal{B}$ subspace in the A and B sites, respectively. This mismatch can be exactly compensated by introducing an on-site potential V in the edge sites of the real space lattice. Figure 4.8(a) shows the energy spectrum of the $\mathcal{B}$ subspace for $N_c = 15$ unit cells with $\rho_0 = 5\sigma$, distances $d' = 3.6\sigma$, $d = 4.5\sigma$, and $U/t'_s = 20$. In Fig. 4.8(ai), the spectrum is represented as a function of the edge potential correction V in units of $V_{\mathcal{B}} = (J'^2_2 + J'^2_3)/2U$, the value of the potential that exactly compensates the mismatch. Figure 4.8(aii) shows the spectrum for the potential $V_{\mathcal{B}}$. For $V = 0$, the spectrum presents only two dispersive bands. The lower band contains two extra states that arise due to the impurity potentials at the edge sites of the SSH chain. When increasing the potential correction V, these Tamm-Shockley states depart from the lower chain as their energy grows linearly and become localized at the edge. For $V_{\mathcal{B}}$, the potential mismatch is compensated exactly, thus restoring the chiral symmetry of the model and yielding two topologically-protected edge states.

$\mathcal{A}$ subspace

In contrast with the $\mathcal{B}$ subspace, the $\mathcal{A}$ subspace presents two bound states per site instead of only one, $|j^\alpha_k, j^\alpha_k\rangle$ with $\alpha = \pm$. In the strong interactions regime, the bound states in adjacent sites become coupled through second-order hoppings, which yields four effective couplings between the adjacent bound states $|A^\alpha_k, A^\alpha_k\rangle$ and $|B^{\alpha'}_{k'}, B^{\alpha'}_{k'}\rangle$, thus forming a Creutz ladder

structure [313]. In analogy with the $\mathcal{B}$ subspace, each bound state also obtains an effective on-site potential that generates a bulk-edge on-site potential mismatch. Using Eq. (4.19), the effective model of this subspace reads

$$
\begin{aligned}
\hat{\mathcal{H}}_{\mathcal{A}} = \sum_{\alpha=\pm} \Bigg(& \sum_{k=1}^{N_c} \left[\frac{2J_2^2}{U} \hat{a}_k^{\mathcal{A}\alpha\dagger} \hat{b}_k^{\mathcal{A}\alpha} + \frac{2J_3^2}{U} \hat{a}_k^{\mathcal{A}\alpha\dagger} \hat{b}_k^{\mathcal{A}-\alpha} \right] + \text{H.c.} \\
& + \sum_{k=1}^{N_c-1} \left[\frac{2J_2'^2}{U} \hat{a}_{k+1}^{\mathcal{A}\alpha\dagger} \hat{b}_k^{\mathcal{A}\alpha} + \frac{2J_3'^2}{U} \hat{a}_{k+1}^{\mathcal{A}\alpha\dagger} \hat{b}_k^{\mathcal{A}-\alpha} \right] + \text{H.c.} \\
& + 2\frac{J_2^2 + J_3^2 + J_2'^2 + J_3'^2}{U} \sum_{k=1}^{N_c} \left[\hat{a}_k^{\mathcal{A}\alpha\dagger} \hat{a}_k^{\mathcal{A}\alpha} + \hat{b}_k^{\mathcal{A}\alpha\dagger} \hat{b}_k^{\mathcal{A}\alpha} \right] \\
& - 2\frac{J_2'^2 + J_3'^2}{U} \left[\hat{a}_1^{\mathcal{A}\alpha\dagger} \hat{a}_1^{\mathcal{A}\alpha} + \hat{b}_{N_c}^{\mathcal{A}\alpha\dagger} \hat{b}_{N_c}^{\mathcal{A}\alpha} \right] \Bigg),
\end{aligned}
\tag{4.21}
$$

where the creation and annihilation operators $\hat{a}_k^{\mathcal{A}\alpha(\dagger)}$ and $\hat{b}_k^{\mathcal{A}\alpha(\dagger)}$ correspond to the bound states of the $\mathcal{A}$ subspace with two particles in circulation α in the A and B sites, respectively. The effective model of the $\mathcal{A}$ subspace takes the same form as the original single-particle model in Eq. (4.5), with additional on-site potential terms. Figure 4.8(b) shows the energy spectrum of the $\mathcal{A}$ subspace for $N_c = 15$ unit cells with $\rho_0 = 5\sigma$, distances $d' = 3.6\sigma$, $d = 4.5\sigma$, and $U/t_s' = 20$ for (bi) an increasing potential correction V in units of $V_{\mathcal{A}}$ and for (bii) the exactly compensated spectrum at $V_{\mathcal{A}} = (J_2'^2 + J_3'^2)/U$. Figure 4.8(bi) shows four bands with the outer ones presenting a larger dispersion than the inner ones, and also four Tamm-Shockley states for which the energy increases linearly with the potential correction V. As in the $\mathcal{B}$ subspace, the impurity states coincide in energy with the dispersive band due to the edge-bulk potential mismatch, but here two of them are located within the bulk. The fact that these two states, in the absence of any edge potential compensation, naturally appear within a bulk continuum while remaining localized at the edge, suggests that they may be regarded as bound states in the continuum [314]. Once the on-site potential mismatch is exactly compensated, introducing $V_{\mathcal{A}}$, the single-particle [Eq. (4.5)] and two-particle [Eq. (4.21)] models become completely analogous. Then, one can apply the single-particle basis rotation (4.12) for the $\mathcal{A}$ bound states that transforms the system into two decoupled SSH chains with the following renormalized couplings

$$
\begin{aligned}
t_s^{\mathcal{A}} &= 2\frac{J_2^2 + J_3^2}{U} & t_s'^{\mathcal{A}} &= 2\frac{J_2'^2 + J_3'^2}{U} \\
t_a^{\mathcal{A}} &= 2\frac{J_2^2 - J_3^2}{U} & t_a'^{\mathcal{A}} &= 2\frac{J_2'^2 - J_3'^2}{U}.
\end{aligned}
\tag{4.22}
$$

The spectrum in Fig. 4.8(bii) is equivalent to the single-particle one shown in Fig. 4.4 with renormalized and shifted energies. The outer bands, which show a greater dispersion, belong to the symmetric chain, while the inner ones belong to the antisymmetric chain. As both models are in the same topological phase, both lattices contribute with two topologically-protected edge states.

4.4 Conclusions

In this chapter, we have studied a system of one or two bosons loaded into states with OAM $l = 1$ in a lattice of rings, with alternating distances d and d'. By selecting the states with a given OAM l, each site of the lattice presents two internal states given by the two circulations $+$ and $-$. At the single-particle level, this system presents non-trivial topological characteristics, that can be properly analyzed by resolving the exchange symmetry between the circulations $+$ and $-$. This leads to two decoupled SSH chains whose associated Zak phases determine the topological phase of the system. We analyze the parameter space in terms of the distances d and d', finding that both chains are always in the same topological phase but show different dispersion in their bands. Thus, the system can present four topologically-protected edge states.

Secondly, we study the case of two bosons with on-site interactions, which generate a rich landscape of doublon bands and edge bound states. In these bands, the two-particles occupy the same site, and we analyze them analytically in two limits. In the dimerized limit, one can reduce the system to a single strong link. The eigenvalues of the associated Hamiltonian accurately predict the overall energy dependence of the doublon bands obtained using exact diagonalization in the nearly dimerized regime. The strong-link eigenvectors are analyzed in the strong interactions limit, where we find that they form three distinct groups. They either tend to states where the two particles are in distinct sites, with energy zero, or to the same site in the same circulation (with energy U), or opposite circulations (energy $2U$). Additionally, we show that the avoided crossings between the doublon bands and the bands of extended states can only arise between eigenstates of the same exchange parity sector. In order to be able to capture the subspaces created by these doublon states away from the dimerized limit, we consider the strong interactions limit using second-order perturbation theory. The two doublon subspaces are well separated in energy and thus can be studied independently. We find effective models that map to an SSH model and a Creutz-like model with a bulk-edge on-site potential mismatch. We show how this mismatch can be corrected by introducing a potential at the edge sites, thus recovering the chiral symmetry that topologically protects the doublon edge states. The effective models are benchmarked using exact diagonalization.

5

MANY-BODY AHARONOV-BOHM CAGING IN A LATTICE OF RINGS

In this chapter, we explore a one-dimensional (1D) staggered lattice of rings within the Bose-Hubbard formalism. This lattice can be understood through the six-state-model presented in Sec. 2.3.2 of Chapter 2, which predicts that the tunneling amplitudes between orbital angular momentum (OAM) states with opposite circulations in each ring can take complex values. These complex couplings realize synthetic fluxes that can be exploited to generate flat bands created by Aharonov-Bohm caging. Within this context, we study the single-particle case and then analyze the role of on-site interactions in this phenomenon.

Neutral particles can emulate the dynamics of electrons in the presence of magnetic fields through the engineering of artificial gauge fields [63, 315]. In the well-known Aharonov-Bohm effect [316, 317], a charged particle performing a closed loop on a region with a non-zero electromagnetic potential acquires not only a dynamical phase but also an additional phase known as the Aharonov-Bohm phase. For particular periodic lattice geometries, single-particle wavefunctions undergo a sharp localization due to destructive interference known as Aharonov-Bohm caging [121, 122]. These localization effects arise in systems such as the $\mathcal{T}_3$ model [121, 318, 319] or the diamond chain [122], and it has been observed in several experimental platforms, such as networks of conducting wires [320, 321], ultracold atoms [322], and photonic lattices [216, 323, 324].

Of particular interest is the role that interactions play in a system with single-particle Aharonov-Bohm caging, which has been explored in different regimes [122, 150, 293, 325, 326]. The addition of interactions lifts the degeneracy of the single-particle flat bands, providing a mechanism for particles to avoid caging [122, 293, 325]. However, in the regime of strong interactions, Aharonov-Bohm caging of two particles can be recovered for appropriately tuned magnetic fluxes through the formation of bound states [293].

Here, we study a 1D lattice of ring potentials populated by OAM modes with $l = 1$ and winding numbers $\nu = \pm l$. Such states give rise to complex couplings that can be engineered by modifying the geometry of the lattice [146–150, 327]. Thus, it is a system where synthetic fluxes arise naturally. The physics described here can be observed either in a lattice of ring

potentials or in the p-band of a conventional lattice. For both cases, a variety of techniques exist to generate the potentials and transfer angular momentum to the particles (see discussions in Chapters 3 and 4). For the particular case of an optical lattice, a staggered geometry can be generated in a superlattice with commensurate wavelengths of light beams where the extra tunnelings are switched off with square lattices [328]. The local eigenstates with winding number $\nu = \pm l$ provide the system with a synthetic dimension, such that it can be mapped to a Creutz ladder model with a flux threading each plaquette. For this family of models, interaction induced effects have been studied for repulsive [307, 313, 329, 330] and attractive [331, 332] on-site interactions, and for nearest-neighbor interactions [333–335]. In particular, two-body Aharonov-Bohm caging was explored in [313], where a photonic lattice implementation was proposed. Here, we explore the N-boson case and further generalize the study to the case of non-uniform fluxes, which are known to enrich the Aharonov-Bohm caging phenomenology in single-particle diamond lattices [336].

The chapter is organized as follows. We introduce the system in Section 5.1 and analyze the single-particle case in Sec. 5.2. For the case in which a π-flux threads each plaquette, we analyze both the topology of the system and study the Aharonov-Bohm caging effect in terms of the compact localized states (CLSs) that compose the flat-band spectrum. In Section 5.3, we generalize this study to the case of N particles by introducing on-site repulsive interactions and studying the regime of strong interactions using perturbation theory. In Sec. 5.4, we generalize the study to the case of non-uniform fluxes and summarize our conclusions in Sec. 5.5.

5.1   Physical system

We consider a few bosons loaded into a 1D lattice where the adjacent sites are equally separated by a distance d. Each unit cell k is composed of two sites A_k and B_k, and we make the lattice staggered by introducing an angle ϕ as depicted in Fig. 5.1. Given the local polar coordinates of each site, $(\rho_{j_k}, \varphi_{j_k})$ with $j = A, B$, the local trapping potential is a ring potential of the form $V(\rho_{j_k}) = \frac{1}{2} M \omega^2 (\rho_{j_k} - \rho_0)^2$, where ω is the frequency of the radial potential, M is the mass of the particles, and ρ_0 is the radius. For $\rho_0 = 0$, the ring trap reduces to a harmonic potential. We consider identical local potentials at each site.

The eigenstates of each isolated ring have a well-defined OAM l. Each value of l corresponds to two degenerate eigenstates with winding numbers $\nu = \pm l$ (with the exception of $l = 0$, that corresponds to a single non-degenerate eigenstate). Therefore, they are eigenstates of the operator $\hat{L}_z = -i\hbar \frac{\partial}{\partial \varphi}$ with eigenvalue $\hbar \nu$. We will denote the local eigenstates as $|j_k^\nu\rangle$, where k is the unit cell index, $j = A, B$ is the site, and ν is the winding number. As we saw in Sec. 2.3 of Chapter 2, these sets of local eigenstates with different OAM l are well-separated in energy, which makes them effectively decoupled in a lattice structure [146, 147]. In analogy with the previous chapter, the total field operator for the states with OAM l in the lattice reads

$$\hat{\Psi}_l(\mathbf{r}) = \sum_{k=1}^{N_c} \sum_{\nu=\pm l} \phi_{A_k}^\nu (\rho_{A_k}, \varphi_{A_k}) \hat{a}_k^\nu + \phi_{B_k}^\nu (\rho_{B_k}, \varphi_{B_k}) \hat{b}_k^\nu, \tag{5.1}$$
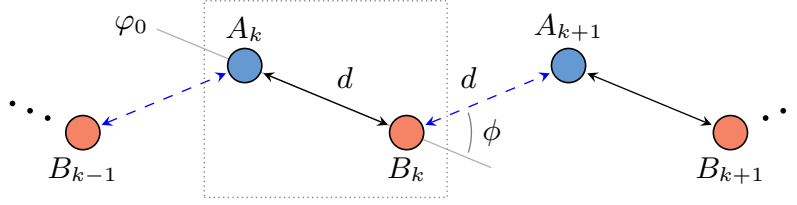
Figure 5.1: Diagram of the 1D staggered chain where the adjacent sites A and B are separated by a distance d. The unit cell is marked by a rectangle and the gray line indicates the origin of the phase φ_0. The black arrows denote real tunneling amplitudes while the blue ones indicate complex tunneling amplitudes between states of different winding number.

where N_c is the number of unit cells, and $\hat{a}_k^\nu$ and $\hat{b}_k^\nu$ are the annihilation operators of the local eigenstates $|A_k^\nu\rangle$ and $|B_k^\nu\rangle$, respectively. The wavefunctions of each state $|j_k^\nu\rangle$ are given by

$$\phi_{j_k}^\nu \left(\rho_{j_k}, \varphi_{j_k}\right) = \langle \mathbf{r} \mid j_k^\nu \rangle = \psi\left(\rho_{j_k}\right) e^{i\nu\left(\varphi_{j_k} - \varphi_0\right)}, \tag{5.2}$$

where $\psi\left(\rho_{j_k}\right)$ is the radial part of the wavefunction and $e^{i\nu\left(\varphi_{j_k} - \varphi_0\right)}$ is the complex phase due to the non-zero OAM, with φ_0 indicating the origin of the phase.

For an array of coplanar rings, the local OAM eigenstates become coupled through the tunneling amplitudes J_1 (for opposite circulations within a single ring), J_2 (for the same circulation in adjacent rings), and J_3 (for opposite circulations in adjacent rings), see Sec. 2.3.2. In Chapter 4, we investigated an array of inline rings, where the complex factors accompanying J_1 and J_3 vanish for an appropriately chosen φ_0. Here, we choose the origin of the phase along the A_k and B_k sites of the same unit cell (see Fig. 5.1), such that the corresponding couplings are real. The inter-cell couplings between the sites B_k and A_{k+1} form an angle ϕ with respect to the origin of the phase, such that the corresponding couplings between opposite circulations acquire a complex phase $e^{\pm i 2 l \phi}$. Therefore, one can tune the complex phase of these couplings by modifying the geometry of the staggered chain, i.e., the angle ϕ (see Fig. 5.1).

In this chapter, we focus on the regime of large distances, defining $J_2 = J_3 \equiv J$, and we neglect the J_1 coupling. Also, we study the states with OAM $l = 1$ and winding numbers $\nu = \pm 1$, that we denote with the circulation label $\alpha = \pm$, and consider an integer number of unit cells. Given the above assumptions and using harmonic oscillator units, the single-particle Hamiltonian of this system reads

$$\hat{\mathcal{H}}_{l=1}^0 = J \sum_{\alpha = \pm} \left[\sum_{k=1}^{N_c} \left(\hat{a}_k^{\alpha\dagger}\hat{b}_k^\alpha + \hat{a}_k^{\alpha\dagger}\hat{b}_k^{-\alpha}\right) + \sum_{k=1}^{N_c-1} \left(\hat{b}_k^{\alpha\dagger}\hat{a}_{k+1}^\alpha + e^{-2\alpha i\phi}\hat{b}_k^{\alpha\dagger}\hat{a}_{k+1}^{-\alpha}\right) + \text{H.c.} \right].$$
$$\tag{5.3}$$

By representing the two circulations $+$ and $-$ as separate sites, one can depict this system as the Creutz ladder with vanishing vertical couplings shown in Fig. 5.2. The two circulations $\alpha = \pm$ act as a synthetic dimension that constitutes the two legs of the ladder. Henceforward, we use the notation $|j_k^\alpha, n\rangle$ to denote the number of particles n in the local state $|j_k^\alpha\rangle$. In the following section, where we discuss the single-particle case, n will always be $n = 1$. For this case, the states in each site are $|A_k^\alpha, 1\rangle$ and $|B_k^\alpha, 1\rangle$, the couplings are $\mathcal{J} = J$ and $\theta = 2\phi$.

$$|B^+_{k-1}, n\rangle \quad |A^+_k, n\rangle \quad |B^+_k, n\rangle \quad |A^+_{k+1}, n\rangle$$

$$|B^-_{k-1}, n\rangle \quad |A^-_k, n\rangle \quad |B^-_k, n\rangle \quad |A^-_{k+1}, n\rangle$$

$$\longrightarrow \mathcal{J}$$
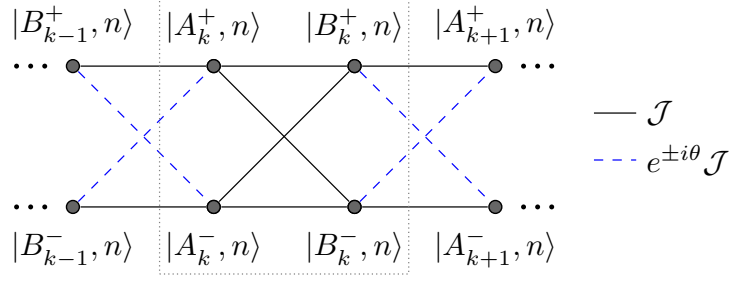$$\text{- - -} \; e^{\pm i\theta}\mathcal{J}$$

Figure 5.2: Schematic representation of the sites and couplings of the lattice formed by a real dimension and the synthetic dimension spanned by the two circulations $\pm$ in each site A_k and B_k. The unit cell is indicated as a dotted rectangle and the complex couplings are $e^{i\theta}\mathcal{J}$ from circulation $+$ to $-$ and its complex conjugate in the opposite direction.

5.2 Single particle

In this section, we will analyze in detail the single-particle case, which will be the basis to understand the generalization to N particles that we explore in Section 5.3. As we have seen, the complex factor $e^{\pm 2i\phi}$ that appears with the J_3 couplings can be tuned by modifying the real space angle ϕ of the staggered chain (see Fig. 5.1). We are interested in the case $\phi = \pi/2$, for which the J_3 inter-cell couplings are accompanied by a minus sign, thus generating a synthetic π-flux in each plaquette. Note that the couplings in the staggered chain can form either rhombus or triangle plaquettes with two configurations each, such that every one of them contains a π-flux (see Fig. 5.3). As a result, a particle cannot tunnel two sites to the right or to the left due to destructive interference. This destructive interference that leads to localization due to the presence of a flux is known as Aharonov-Bohm caging [121, 122]. For $\phi = \pi/2$, the Hamiltonian in Eq. (5.3) reduces to

$$\hat{\mathcal{H}}^0_{l=1} = J \sum_{\alpha=\pm} \left[\sum_{k=1}^{N_c} \left(\hat{a}^{\alpha\dagger}_k \hat{b}^\alpha_k + \hat{a}^{\alpha\dagger}_k \hat{b}^{-\alpha}_k \right) + \sum_{k=1}^{N_c-1} \left(\hat{b}^{\alpha\dagger}_k \hat{a}^\alpha_{k+1} - \hat{b}^{\alpha\dagger}_k \hat{a}^{-\alpha}_{k+1} \right) + \text{H.c.} \right]. \tag{5.4}$$

A topological characterization of this system can be obtained by analyzing the block-diagonalized Hamiltonian. We introduce the following basis change (with $n = 1$),

$$\left| A^{s(a)}_k, n \right\rangle = \frac{1}{\sqrt{2}} \left(\left| A^+_k, n \right\rangle \overset{+}{_{(-)}} \left| A^-_k, n \right\rangle \right),$$

$$\left| B^{s(a)}_k, n \right\rangle = \frac{1}{\sqrt{2}} \left(\left| B^+_k, n \right\rangle \overset{+}{_{(-)}} \left| B^-_k, n \right\rangle \right), \tag{5.5}$$

that decouples the system into the two following Hamiltonians,

$$\hat{\mathcal{H}}_s = 2J \sum_{k=1}^{N_c} \hat{a}^{s\dagger}_k \hat{b}^s_k + \text{H.c.},$$

$$\hat{\mathcal{H}}_a = 2J \sum_{k=1}^{N_c-1} \hat{a}^{a\dagger}_{k+1} \hat{b}^a_k + \text{H.c.}, \tag{5.6}$$
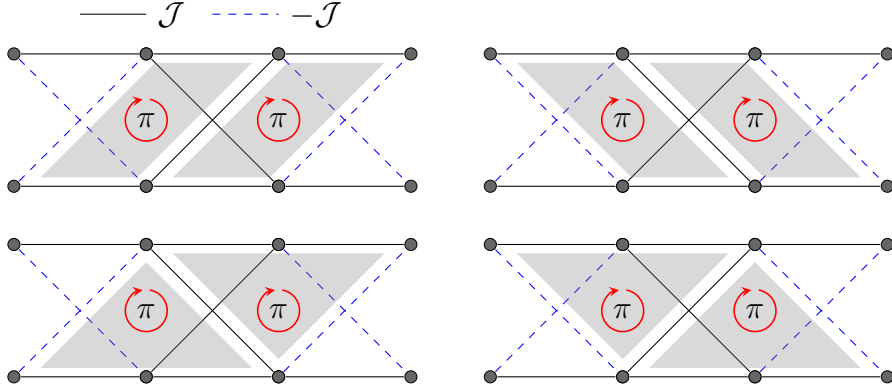
Figure 5.3: Schematic representation of the lattice with a π-flux in each plaquette, for which the cross-circulation couplings reduce to $-\mathcal{J}$ (blue dashed lines). The different diagrams highlight the plaquette configurations that enclose a π-flux: rhombi and triangles with two configurations each.

where $\hat{a}_k^{s(a)}$ and $\hat{b}_k^{s(a)}$ are the annihilation operators of the states in Eq. (5.5). The Hamiltonians $\hat{\mathcal{H}}_a$ and $\hat{\mathcal{H}}_s$ correspond to two Su-Schrieffer-Heeger (SSH) chains in the dimerized limit, i.e., linear chains with alternating couplings where either the inter or the intra-cell coupling is zero (see Fig. 5.4 with $n = 1$ and $\mathcal{J} = J$). The two models have the same couplings, $2J$ and 0, in opposite configurations.

We consider an integer number of unit cells and that the first site of the chain is a site A (and thus, the last, a site B), such that the edge couplings are real [see Fig. 5.4(a)]. In that case, the symmetric SSH chain, $\hat{\mathcal{H}}_s$, is in the trivial phase, characterized by a quantized Zak phase $\mathcal{Z} = 0$, and the antisymmetric chain, $\hat{\mathcal{H}}_a$, is in the topological phase with a quantized Zak phase, $\mathcal{Z} = \pi$. If we instead consider a lattice starting with a B site, the symmetric chain would be the one in the topological phase. Thus, for an integer number of unit cells, the two edge states come from the same SSH chain. For a non-integer number of unit cells, the Creutz ladder also presents two edge states [see Fig. 5.4(b)]. However, in this case each edge state comes from a different chain, as SSH models with an odd number of sites exhibit a single edge state [337].

In Fig. 5.5(a), we represent the energy spectrum of a chain with $N_c = 12$ unit cells and $\phi = \pi/2$ obtained through exact diagonalization. We obtain two flat bands and two zero-energy edge states that correspond to the superposition of the energy spectra of $\hat{\mathcal{H}}_s$ and $\hat{\mathcal{H}}_a$, in Eq. (5.6). The edge states are eigenstates of the antisymmetric chain and are completely localized at the edge sites (with $n = 1$),

$$
\begin{aligned}
|A_1^a, n\rangle_{edge} &= \frac{1}{\sqrt{2}} \left(|A_1^+, n\rangle - |A_1^-, n\rangle \right), \\
|B_{N_c}^a, n\rangle_{edge} &= \frac{1}{\sqrt{2}} \left(|B_{N_c}^+, n\rangle - |B_{N_c}^-, n\rangle \right).
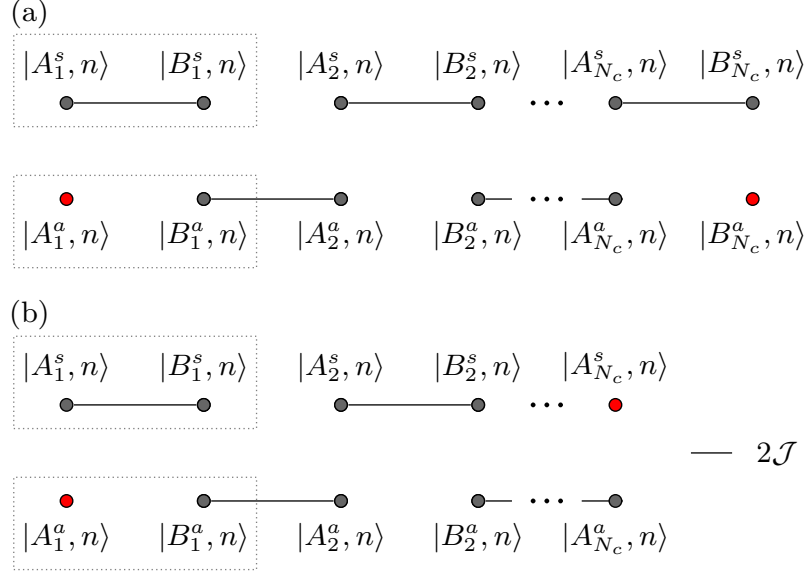\end{aligned}
\tag{5.7}
$$

(a)

(b)

Figure 5.4: Decoupled symmetric and antisymmetric SSH chains with alternating couplings $2\mathcal{J}$ and 0 for (a) an integer number of unit cells and (b) a non-integer number of unit cells. The unit cell of each chain is indicated by the dotted rectangles and the edge states are indicated in red.

5.2.1   Single-particle Aharonov-Bohm caging

In this section, we explore single-particle Aharonov-Bohm caging. The flat bands that appear in the spectrum when a π-flux threads each plaquette [see Fig. 5.5(a)], are characterized by the presence of compact localized states (CLSs). These eigenstates have high real space localization: their amplitude is non-zero in a few close-by sites while being exactly zero everywhere else. The smallest possible basis for the CLSs in this model spans the states of one unit cell and an extra site (where $n = 1$),

$$\left\{ |A_k^+, n\rangle, |A_k^-, n\rangle, |B_k^+, n\rangle, |B_k^-, n\rangle, |A_{k+1}^+, n\rangle, |A_{k+1}^-, n\rangle \right\}. \tag{5.8}$$

The CLSs are found to be [see Fig. 5.5(b)]

$$
\begin{aligned}
|\Upsilon_k^1, n\rangle &= \frac{1}{2} \left(|B_k^+, n\rangle + |B_k^-, n\rangle - |A_k^+, n\rangle - |A_k^-, n\rangle \right), \\
|\Upsilon_k^2, n\rangle &= \frac{1}{2} \left(|B_k^+, n\rangle - |B_k^-, n\rangle - |A_{k+1}^+\rangle + |A_{k+1}^-, n\rangle \right), \\
|\Upsilon_k^3, n\rangle &= \frac{1}{2} \left(|B_k^+, n\rangle + |B_k^-, n\rangle + |A_k^+, n\rangle + |A_k^-, n\rangle \right), \\
|\Upsilon_k^4, n\rangle &= \frac{1}{2} \left(|B_k^+, n\rangle - |B_k^-, n\rangle + |A_{k+1}^+, n\rangle - |A_{k+1}^-, n\rangle \right),
\end{aligned}
\tag{5.9}
$$

and their corresponding energies are $E_1 = E_2 = -2\mathcal{J}$ and $E_3 = E_4 = 2\mathcal{J}$ (where $\mathcal{J} = J$ in the single-particle case). Any initial state that can be written as a superposition of these states

(a)

(b) $|\Upsilon_k^3, n\rangle$ $|\Upsilon_k^4, n\rangle$

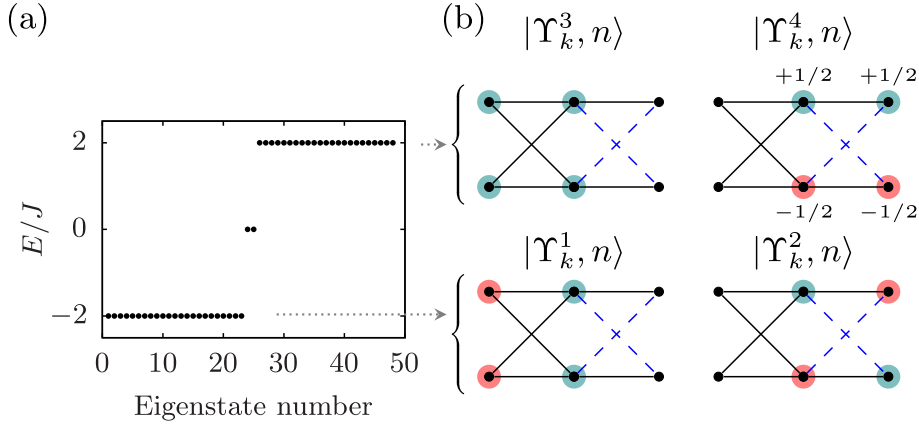$|\Upsilon_k^1, n\rangle$ $|\Upsilon_k^2, n\rangle$

Figure 5.5: (a) Single-particle energy spectrum for $N_c = 12$ unit cells and $\phi = \pi/2$. (b) Representation of the CLSs defined in Eq. (5.9) that are eigenstates of the Creutz ladder, see Fig. 5.2, when a π-flux threads each plaquette. The radius of each circle represents the amplitude and the color represents the phase, with red being a π phase, and green being a phase zero.

will remain localized in the caging cell defined in (5.8). We note that the π-flux case of this system exactly maps to the usual π-flux Creutz ladder with complex horizontal couplings [313] through a gauge transformation. In such models, the unit cell is composed of only two sites and presents two CLSs. One CLS corresponds to our two CLSs with energies $E_1 = E_2 = -2\mathcal{J}$ and the other, to the two CLSs with $E_3 = E_4 = 2\mathcal{J}$. For an arbitrary flux, the adjacent triangle plaquettes contain fluxes 2ϕ and -2ϕ, such that the model does not map to a Creutz ladder with only two sites per unit cell.

We consider an initial state where only a single site A_k in the bulk of the chain is populated. Fig. 5.6(a) shows the time evolution of the population of each local eigenstate, $P_{|j_k^\alpha, 1\rangle}$ (with $j = A, B$), for the initial state $\left(|A_k^+, 1\rangle + |A_k^-, 1\rangle\right)/\sqrt{2}$, which corresponds to the superposition $(|\Upsilon_k^3, 1\rangle - |\Upsilon_k^1, 1\rangle)/\sqrt{2}$. The population coherently oscillates between the sites A_k and B_k without populating any other sites due to destructive interference at B_{k-1} and A_{k+1}. Thus, the total caged population, $P_{cag} = P_{|A_k^+, 1\rangle} + P_{|A_k^-, 1\rangle} + P_{|B_k^+, 1\rangle} + P_{|B_k^-, 1\rangle}$, stays at $P_{cag} = 1$ throughout the time evolution. Additionally, the two circulations within each site maintain the same population at all times: $P_{|A_k^+, 1\rangle} = P_{|A_k^-, 1\rangle}$ and $P_{|B_k^+, 1\rangle} = P_{|B_k^-, 1\rangle}$. For the initial state $\left(|A_k^+, 1\rangle - |A_k^-, 1\rangle\right)/\sqrt{2} = (|\Upsilon_k^4, 1\rangle - |\Upsilon_k^2, 1\rangle)/\sqrt{2}$, one obtains identical dynamics but the exchange in population takes place between the sites A_k and B_{k-1}, as the sign of the superposition shifts the destructive interference to the sites B_k and A_{k-1}. Fig. 5.6(b) shows the time evolution for the initial state $|A_k^+, 1\rangle = (-|\Upsilon_k^1, 1\rangle + |\Upsilon_k^3, 1\rangle - |\Upsilon_{k-1}^2, 1\rangle + |\Upsilon_{k-1}^4, 1\rangle)/2$. As this initial state cannot be written as a superposition of CLSs of a single caging cell, the population reaches both the sites B_k and B_{k-1}. The total caged population, which in this case also stays constant, is $P_{cag} = P_{|A_k^+, 1\rangle} + P_{|A_k^-, 1\rangle} + P_{|B_k^+, 1\rangle} + P_{|B_k^-, 1\rangle} + P_{|B_{k-1}^+, 1\rangle} + P_{|B_{k-1}^-, 1\rangle}$. Also, we simulate a chain with $N_c = 12$ unit cells and choose the unit cell $k = 4$ for the initial state. The caging dynamics in Fig. 5.6 can also be understood in terms of the decoupled
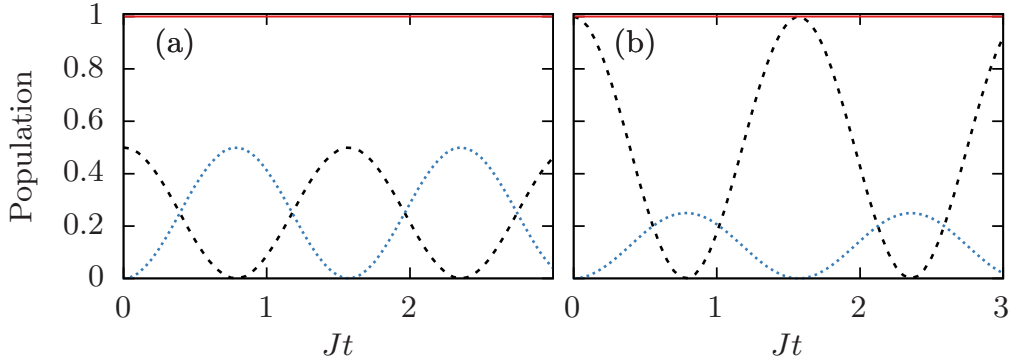
Figure 5.6: Time evolution of the population of the states $|j_k^\alpha, 1\rangle$ with $j = A, B$ and total caged population, obtained through exact diagonalization for $J = 1$, $N_c = 12$ unit cells and $\phi = \pi/2$. The continuous red line is the total caged population P_{cag}; the dashed black line is the population in the states $|A_4^\alpha, 1\rangle$, with $\alpha = \pm$; and the dotted blue line is the population in the states (a) $|B_4^\alpha, 1\rangle$, (b) $|B_3^\alpha, 1\rangle$ and $|B_4^\alpha, 1\rangle$. The initial states are (a) $\left(|A_4^+, 1\rangle + |A_4^-, 1\rangle \right)/\sqrt{2}$ and (b) $|A_4^+, 1\rangle$.

dimers of the SSH chains. For the symmetric and antisymmetric initial states, in Eq. (5.5), the population remains trapped in the corresponding dimer of the symmetric, $\hat{\mathcal{H}}_s$, or the antisymmetric, $\hat{\mathcal{H}}_a$, chain (see Fig. 5.4). In contrast, the initial state $|A_k^+, 1\rangle$ populates both the symmetric and antisymmetric SSH chains, such that the population reaches both dimers and as a consequence reaches a broader spatial extent.

5.3 N particles

In this section, we explore the many-body dynamics of the system for N bosons with repulsive interactions. As shown in Chapter 4, the interaction Hamiltonian describing on-site two-body collisions for the states with $l = 1$ reads

$$\hat{\mathcal{H}}_{l=1}^{int} = \frac{U}{2} \sum_{j=A,B} \sum_{k=1}^{N_c} \left[\hat{n}_{j_k}^+ (\hat{n}_{j_k}^+ - 1) + \hat{n}_{j_k}^- (\hat{n}_{j_k}^- - 1) + 4\hat{n}_{j_k}^+ \hat{n}_{j_k}^- \right], \tag{5.10}$$

where $\hat{n}_{j_k}^\alpha = \hat{j}_k^{\alpha\dagger} \hat{j}_k^\alpha$ is the number operator and the interaction strength is defined as $U \equiv g \int d^2r \, |\psi(\rho_{j_k})|^4$ [147]. The cross-circulation term induces a nearest-neighbor interaction term along the rungs of the Creutz ladder which was also considered in [334].

Henceforward, we will analyze the regime of strong interactions, in which the interaction term dominates over the tunneling term, $U \gg J$. We are interested in the bound-states where the N bosons occupy a single site of the lattice, $\{ |j_k^\alpha, n\rangle \otimes |j_k^{-\alpha}, m\rangle \}$, where there are n particles in one circulation and m particles in the other circulation (with $n + m = N$). In the regime of strong interactions, the kinetic Hamiltonian, $\hat{\mathcal{H}}_{l=1}^0$ [Eq. (5.3)], is introduced as a perturbation that couples the bound states $\{ |j_k^\alpha, n\rangle \otimes |j_k^{-\alpha}, m\rangle \}$ in adjacent sites. This effect

creates subspaces that are well-separated in energy, and thus, effectively uncoupled. We will analyze in detail the two and three-particle cases as an example in the next subsections. The matrix elements of the effective Hamiltonian of each subspace up to third order are given by [311, 312]

$$
\begin{aligned}
\langle d|\hat{\mathcal{H}}_{\text{eff}}|d'\rangle = & E_d^0 \delta_{dd'} + \frac{1}{2}\sum_w \langle d|\hat{\mathcal{H}}_{l=1}^0|w\rangle\langle w|\hat{\mathcal{H}}_{l=1}^0|d'\rangle \cdot \left[\frac{1}{E_d^0 - E_w^0} + \frac{1}{E_{d'}^0 - E_w^0}\right] + \\
& + \frac{1}{2}\sum_{ww'} \langle d|\hat{\mathcal{H}}_{l=1}^0|w\rangle\langle w|\hat{\mathcal{H}}_{l=1}^0|w'\rangle\langle w'|\hat{\mathcal{H}}_{l=1}^0|d'\rangle \cdot \\
& \cdot \left[\frac{1}{(E_d^0 - E_w^0)(E_d^0 - E_{w'}^0)} + \frac{1}{(E_{d'}^0 - E_w^0)(E_{d'}^0 - E_{w'}^0)}\right],
\end{aligned}
\tag{5.11}
$$

where $|d\rangle$, $|d'\rangle$ are the bound-states, $|w\rangle$, $|w'\rangle$ are the mediating states in each hopping process, and E^0 are the unperturbed energies. Note that the first-order corrections are always zero. For $|d\rangle \neq |d'\rangle$, one obtains an effective tunneling term, while for $|d\rangle = |d'\rangle$, one obtains an effective on-site potential. While Eq. (5.11) provides a good description up to $N = 3$, for $N > 3$, one would need to compute the higher-order terms of the perturbative expansion.

5.3.1   Two and three particles

For the two and three-particle cases, there are only two subspaces available that arise from the following bound-state classes:

(a) $\mathcal{A}$: N particles occupy the same site and the same circulation, $|j_k^\alpha, N\rangle$. These are the bound-states that minimize the interaction energy, which is $E_{\mathcal{A}} = N(N-1)U/2$.

(b) $\mathcal{B}$: these bound-states maximize the interaction energy and take the following two forms:

   (i) For N even, $N/2$ particles in each circulation,
   $$
   \left\{|j_k^+, N/2\rangle \otimes |j_k^-, N/2\rangle\right\},
   $$
   with energy $E_{\mathcal{B},\text{even}} = (3N^2/2 - N)U/2$.

   (ii) For N odd, $(N-1)/2$ particles in one circulation and $(N-1)/2 + 1$ in the other
   $$
   \left\{\begin{array}{l} |j_k^+, (N-1)/2\rangle \otimes |j_k^-, (N-1)/2 + 1\rangle, \\ |j_k^+, (N-1)/2 + 1\rangle \otimes |j_k^-, (N-1)/2\rangle \end{array}\right\},
   $$
   with a slightly lower energy, $E_{\mathcal{B},\text{odd}} = (3N^2/2 - N - 1/2)U/2$.

$\mathcal{A}$ subspace

We introduce the coupling J as a perturbation, i.e., $U \gg J$, such that the states of the $\mathcal{A}$ subspace in adjacent sites become coupled. The states for the two-particle case, e.g., $|A_k^\alpha, 2\rangle$

and $|B_k^{\alpha'}, 2\rangle$, become coupled through second-order hopping processes, while the states in the three-particle case, e.g., $|A_k^\alpha, 3\rangle$ and $|B_k^{\alpha'}, 3\rangle$, become coupled through third-order hopping processes. Additionally, each state is coupled to itself also through second-order hoppings, such that an effective on-site potential arises. Note that for both cases, the third-order contribution to the effective on-site potential is zero. Also, the on-site potential has different magnitudes for the bulk, V_B, and the edge, V_E, since the number of available mediating states for the bulk states is twice the number of the ones available for the states localized at the edge sites [303, 304, 308]. Using Eq. (5.11) up to second order for the two-particle case and up to third order for the three-particle case, the resulting effective chains become a Creutz ladder, depicted in Fig. (5.2) with $n = 2$ or 3. The parameters that characterize the two and three-particle effective models as well as those of the single-particle case are given in Table 5.1.

Parameters	Single-particle	$\mathcal{A}_2$	$\mathcal{A}_3$	$\mathcal{B}_3$
$\mathcal{J}$	J	$2J^2/U$	$3J^3/(2U^2)$	$121J^3/(72U^2)$
θ	2ϕ	4ϕ	6ϕ	2ϕ
ϕ	$\pi/2$	$\pi/4$	$\pi/2, \pi/6$	$\pi/2$
V_E	—	$4J^2/U$	$3J^2/U$	$11J^2/(6U)$
V_B	—	$8J^2/U$	$6J^2/U$	$11J^2/(3U)$
V	—	$2J^2/U$	J^2/U	—

Table 5.1: Summary of parameters that characterize the single-particle case and the two and three-particle effective subspaces that exhibit Aharonov-Bohm caging. Parameters of the Creutz ladder defined in Fig. 5.2: couplings $\mathcal{J}$, angle θ and real space angle ϕ that induces a π-flux. Effective on-site potential up to second-order corrections at the edge sites, V_E, and the bulk sites, V_B, and edge correction potential V.

The inter-cell cross couplings between the $\mathcal{A}$ subspace states with opposite circulations contain a complex factor $e^{\pm i\theta}$ (where θ takes different values for each subspace, see Table 5.1). Then, for two (three) particles and the real space angle $\phi = \pi/4$ ($\phi = \pi/2$ or $\pi/6$) (see Fig. 5.1), the complex factor becomes a π phase and the effective chain acquires a π-flux in each plaquette of the Creutz ladder, see Fig. 5.3. Due to the similarities between the single-particle model and the effective $\mathcal{A}$ subspace, we can apply the basis-change employed for the single-particle case, taking $n = 2$ or 3 in Eq. (5.5). As expected, one obtains two dimerized SSH-like decoupled systems with renormalized couplings [Fig. 5.4 with $n = 2$ or 3 and $\mathcal{J} = 2J^2/U$ or $3J^3/(2U^2)$], with additional on-site potentials inherited from the Creutz ladder, V_B and V_E.

Fig. 5.7 shows the energy spectrum of the $\mathcal{A}$ subspace for (a1) two particles and (b1) three particles for $U/J = 50$ and $N_c = 12$ unit cells. We choose the angle ϕ that induces a π-flux in each effective Hamiltonian, $\phi = \pi/4$ and $\phi = \pi/2$, respectively. In contrast with a regular SSH model, the effective chains are not chirally symmetric due to the presence of the bulk-edge on-site potential mismatch. Therefore, the four eigenstates that fall outside the bulk
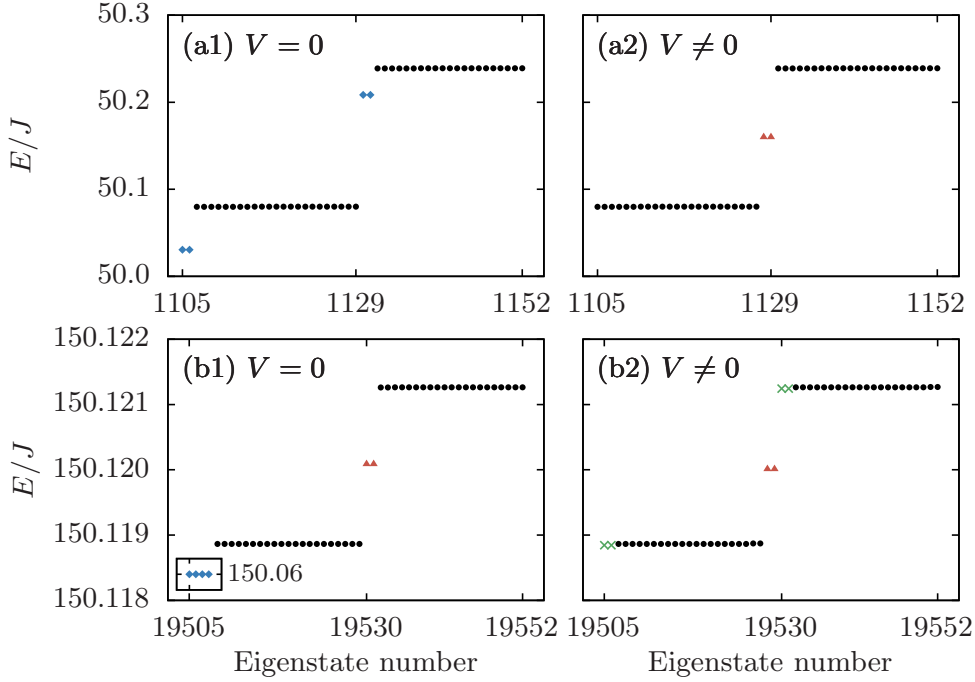
Figure 5.7: Energy spectrum of the $\mathcal{A}$ subspace for (a) two ($\phi = \pi/4$) and (b) three ($\phi = \pi/2$) particles, $U/J = 50$ and $N_c = 12$ unit cells with or without an on-site potential correction V at the edge sites: (a1,b1) $V = 0$, (a2) $V = 2J^2/U$, and (b2) $V = J^2/U$. We depict bulk states with black circles, Tamm-Shockley states with blue rhombi, topologically protected edge states with red triangles, and the green crosses indicate states slightly below the bulk bands.

bands (blue rhombi) are non-topological Tamm-Shockley edge states, i.e., states induced by interactions that are localized at the edge sites due to the bulk-edge on-site potential mismatch [303, 308–310]. One can recover chiral symmetry in the effective model by introducing an on-site potential V at the edge sites of the real space chain that exactly compensates the potential mismatch [308]. Figures 5.7(a2) and (b2) show the two and three-particle spectra of the $\mathcal{A}$ subspace when we introduce the on-site potential correction at the edge sites, $V = 2J^2/U$ and $V = J^2/U$, respectively. In this case, we recover the spectrum of an SSH model with two symmetry-protected edge states (red triangles).

There are some differences between the two and three-particles cases. For three particles, the processes that induce the bulk-edge on-site potential mismatch are one order of magnitude higher than the ones that generate the bulk bands. Thus, the bulk-edge mismatch effectively uncouples the edge sites from the rest of the lattice, which retains chiral symmetry. Given that the symmetric and antisymmetric SSH chains are in opposite topological phases, removing the edge sites from the lattice exchanges the topological phase between the two chains. Therefore, the spectrum in Fig. 5.7(b1) presents not only the four Tamm-Shockley edge states (blue rhombi), well-separated energetically from the bulk bands, but also two

topologically protected edge states (red triangles). When we introduce the potential correction $V = J^2/U$ in Fig. 5.7(b2), we exchange the topological phases of the symmetric and antisymmetric chains. The Tamm-Shockley states are absorbed by the bulk and two topologically protected edge states remain. We can also observe two states in each band (green crosses) with slightly lower energies than the others due to fourth-order corrections to the on-site potential. These corrections are not observable in the two-particle case, see Fig. 5.7(a2), as the fourth-order corrections are two orders of magnitude smaller than the couplings that generate the bulk bands.

Following the analogy with the single-particle case, the eigenstates of the flat-band spectra obtained for two and three particles are the CLSs in Eq. (5.9) taking $n = 2$ or 3, with energies $\pm 2\mathcal{J}$. Fig. 5.8 shows the time evolution of the population of the two-particle bound-states of the $\mathcal{A}$ subspace for different initial states. In particular, we consider the initial states analogous to the ones used in the single-particle case: in Fig. 5.8(a), $\left(\left|A_k^+, 2\right\rangle + \left|A_k^-, 2\right\rangle\right)/\sqrt{2}$, and in Fig. 5.8(b), $\left|A_k^+, 2\right\rangle$. One can see that the dynamical evolution is identical to the one observed for a single particle (see Fig. 5.6). In this case, the dynamics correspond to two-particle Aharonov-Bohm caging and they take place over a much longer timescale. This is because the couplings of the effective Creutz ladder are a second-order effect and, thus, much smaller in magnitude than the ones in the single-particle case (see Table 5.1). We define the total caged population as the sum of the population in a series of states: (a) $P_{cag} = P_{\left|A_k^+,2\right\rangle} + P_{\left|A_k^-,2\right\rangle} + P_{\left|B_k^+,2\right\rangle} + P_{\left|B_k^-,2\right\rangle}$; (b) $P_{cag} = P_{\left|A_k^+,2\right\rangle} + P_{\left|A_k^-,2\right\rangle} + P_{\left|B_k^+,2\right\rangle} + P_{\left|B_k^-,2\right\rangle} + P_{\left|B_{k-1}^+,2\right\rangle} + P_{\left|B_{k-1}^-,2\right\rangle}$. The total caged population reveals slight population losses that are due to higher-order corrections to the effective model that make the flat bands in Fig. 5.7 slightly dispersive.

For three particles and the analogous initial states, $\left(\left|A_k^+, 3\right\rangle + \left|A_k^-, 3\right\rangle\right)/\sqrt{2}$ and $\left|A_k^+, 3\right\rangle$, we obtain identical (albeit slower) dynamics that correspond to three-particle Aharonov-Bohm caging. The periods of the oscillations for the different numbers of particles and $U/J = 50$ are $JT_{N=1} = 1.55$, $JT_{N=2} = 39.5$, $JT_{N=3} = 2600$.

To further compare the two and three-particle Aharonov-Bohm caging, we consider an initial state in the $\mathcal{A}$ subspace, $(\left|B_k^+, n\right\rangle + \left|B_k^-, n\right\rangle)/\sqrt{2}$ (with $n = 2$ or $n = 3$), located at the middle of the lattice, and we let it evolve through time. The caged population for this initial state is $P_{cag} = P_{\left|A_k^+,n\right\rangle} + P_{\left|A_k^-,n\right\rangle} + P_{\left|B_k^+,n\right\rangle} + P_{\left|B_k^-,n\right\rangle}$. Fig. 5.8(c) shows the caged population after a time $3JT_N$, where JT_N is the period of the oscillations for $U/J = 100$, as a function of the ratio U/J for the two and three-particle cases. The caged population rapidly increases for $U > J$, reaching a value close to 1 as the system enters the regime of strong interactions. The growth of the caged population is faster for the three-particle subspace compared to the two-particle case, and it saturates at a smaller value of U/J. This can be understood by inspecting the higher-order terms of the perturbative expansion. As the ratio U/J decreases, higher-order terms of the perturbative expansion have to be taken into account. For two particles (and also for any subspace with an even number of particles), the odd-order perturbative corrections are always zero. Then, the next perturbative correction is fourth order, and it leads to effective on-site potentials, nearest-neighbor hoppings, and also next-nearest neighbor hoppings that destroy the CLSs. In contrast, the fourth-order correction to the three-particle case only induces an effective on-site potential, and the fifth
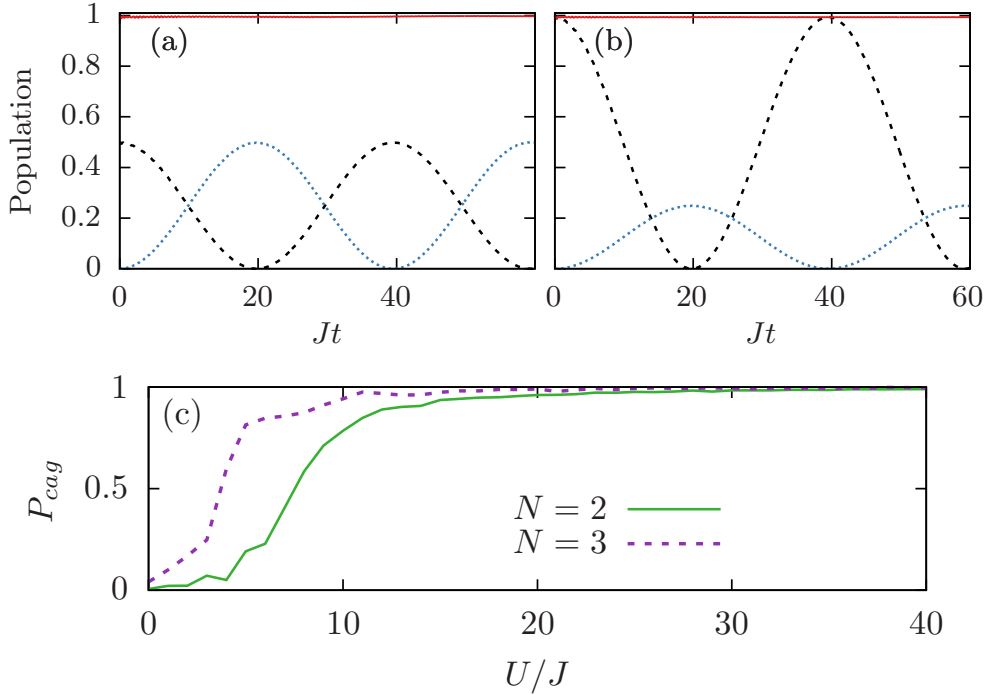
Figure 5.8: (a,b) Time evolution of the population of the states $|j_k^\alpha, 2\rangle$ with $j = A, B$ and total caged population, obtained through exact diagonalization for $U/J = 50$, $N_c = 12$ unit cells, and $\phi = \pi/4$. The continuous red line is the total caged population P_{cag}; the dashed black line is the population in the states $|A_4^\alpha, 2\rangle$, with $\alpha = \pm$; and the dotted blue line is the population in the states (a) $|B_4^\alpha, 2\rangle$, (b) $|B_3^\alpha, 2\rangle$ and $|B_4^\alpha, 2\rangle$. The initial states are (a) $\left(|A_4^+, 2\rangle + |A_4^-, 2\rangle\right)/\sqrt{2}$ and (b) $|A_4^+, 2\rangle$. (c) Caged population, P_{cag}, after a time $3JT_N$ for the $\mathcal{A}$ subspace with $N = 2$ and $N = 3$ as a function of the ratio U/J. JT_N is the period of the oscillations for $U/J = 100$, for the two and three-particle cases and taking ϕ from Table 5.1. The number of unit cells is $N_c = 10$ for $N = 2$ and $N_c = 6$ for $N = 3$.

order induces nearest-neighbor hopping terms that maintain the Creutz ladder structure that exhibits flat bands. It is not until the sixth-order correction, that the next-nearest neighbor hoppings appear, making the CLSs disappear. Thus, the three-particle subspaces are more resilient to deviations from the regime of strong interactions than the two-particle $\mathcal{A}$ subspace.

$\mathcal{B}$ subspace

The bound-states of the $\mathcal{B}$ subspace for the two-particles case have one particle in each circulation, $|j_k^+, 1\rangle \otimes |j_k^-, 1\rangle$. When we consider the couplings between states in adjacent sites, e.g., between $|A_k^+, 1\rangle \otimes |A_k^-, 1\rangle$ and $|B_k^+, 1\rangle \otimes |B_k^-, 1\rangle$, there is no complex factor, as any hopping process between opposite circulations will necessarily be followed by a hopping process with the opposite phase factor. This results in an effective linear chain with uniform couplings $2J^2/U$ and on-site potentials $V_B = 4J^2/U$ at the bulk and $V_E = 2J^2/U$ at
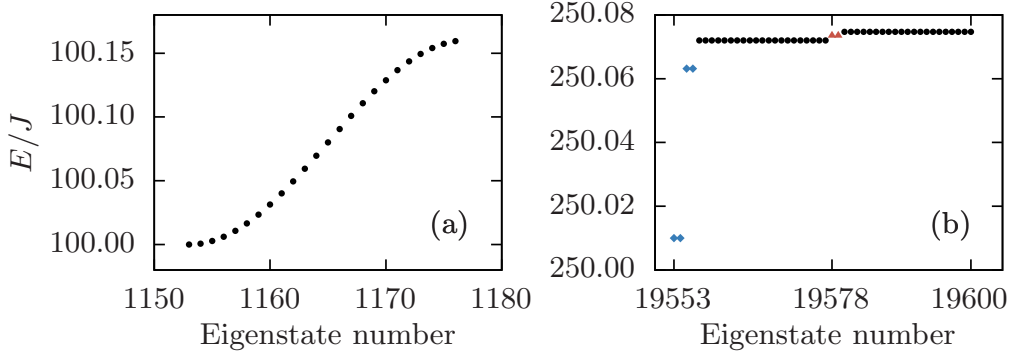
Figure 5.9: Energy spectrum of the $\mathcal{B}$ subspace for (a) two ($\phi = \pi/4$) and (b) three ($\phi = \pi/2$) particles, $U/J = 50$ and $N_c = 12$ unit cells. We depict bulk states with black circles, Tamm-Shockley states with blue rhombi, and topologically protected edge states with red triangles.

the edges. Therefore, the two-particle $\mathcal{B}$ subspace has a dispersive spectrum for any ϕ [see Fig. 5.9(a)] and therefore cannot exhibit Aharonov-Bohm caging.

The three-particle $\mathcal{B}$ subspace arises from bound states of the form $\left|j_k^\alpha, 2\right\rangle \otimes \left|j_k^{-\alpha}, 1\right\rangle$. In analogy with the $\mathcal{A}$ subspace cases, the $\mathcal{B}$ effective subspace is a Creutz ladder with a bulk-edge on-site potential mismatch that can be mapped to two decoupled SSH-like chains with the same on-site potential mismatch (see Table 5.1). Fig. 5.9(b) shows the energy spectrum for the three-particle $\mathcal{B}$ subspace for $U/J = 50$, $N_c = 12$ unit cells, and $\phi = \pi/2$. However, in this case there is an extra ingredient: the two bound-states in the same site, $\left|j_k^\alpha, 2\right\rangle \otimes \left|j_k^{-\alpha}, 1\right\rangle$ and $\left|j_k^\alpha, 1\right\rangle \otimes \left|j_k^{-\alpha}, 2\right\rangle$, are also coupled through second-order processes that generate a complex vertical coupling in the effective Creutz model. For the angle ϕ that induces a π-flux, $\phi = \pi/2$, the complex couplings of each mediating process cancel with the symmetric mediating process (i.e., inverting the direction of the hopping processes from right to left). This compensation does not occur on the edge sites, which results in an energy mismatch between the Tamm-Shockley states (blue rhombi) of the two edges. In analogy with the three-particle $\mathcal{A}$ subspace [see Fig. 5.7(b1)], there are two topologically protected edge states (red triangles) besides the Tamm-Shockley states.

5.3.2 N-particle generalization

From the above cases, one can deduce a recipe to obtain Aharonov-Bohm caging in any N-particle subspace by looking at the N-particle tunneling processes involving complex tunnelings, i.e., the cross-circulation couplings J_3. We define an arbitrary bound state $\left\{\left|j_k^\alpha, n\right\rangle \otimes \left|j_k^{-\alpha}, m\right\rangle\right\}$ with n particles in one circulation and m particles in the other circulation such that $n + m = N$. Note that similar bosonic bound-states have been studied in transmon arrays [338]. In the regime of strong interactions, Aharonov-Bohm caging can exist in the subspace generated by these bound-states if all the N-particle hopping processes involving a complex phase acquire the same total phase factor, such that by appropriately choosing the angle ϕ, one can induce a π-flux. The bound-states in the sites B_k will be coupled
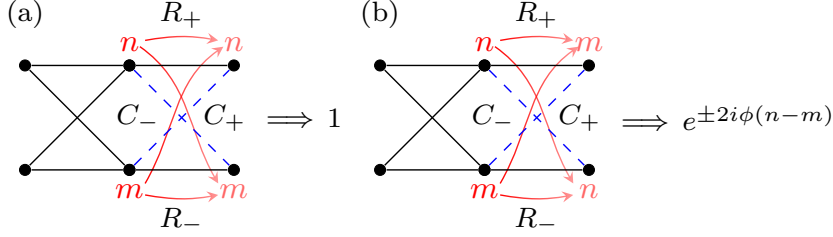
Figure 5.10: Hopping processes of an arbitrary N-particle bound state $\{|B_k^\alpha, n\rangle \otimes |B_k^{-\alpha}, m\rangle\}$ that couples to the bound-states in the adjacent site (a) $\{|A_{k+1}^\alpha, n\rangle \otimes |A_{k+1}^{-\alpha}, m\rangle\}$ and (b) $\{|A_{k+1}^\alpha, m\rangle \otimes |A_{k+1}^{-\alpha}, n\rangle\}$ and corresponding phase factors. R_α and C_α are the numbers of real and complex hopping processes, respectively, coming from each circulation and the labels n and m denote the number of particles in each site.

in the adjacent sites A_{k+1} (see Fig. 5.10) through the integer number of real hoppings from each circulation, R_α and $R_{-\alpha}$, and the integer number of complex hoppings from each circulation, C_α and $C_{-\alpha}$, such that

$$n = R_\alpha + C_\alpha \qquad \text{and} \qquad m = R_{-\alpha} + C_{-\alpha}. \tag{5.12}$$

Then, the total complex factor will be given by $e^{\pm 2i\phi(C_\alpha - C_{-\alpha})}$. These states are coupled to both the bound-states $\{|A_{k+1}^\alpha, n\rangle \otimes |A_{k+1}^{-\alpha}, m\rangle\}$ [Fig. 5.10(a)] and $\{|A_{k+1}^\alpha, m\rangle \otimes |A_{k+1}^{-\alpha}, n\rangle\}$ [Fig. 5.10(b)] in the adjacent site, thus fulfilling the following conditions for each case,

$$\{|A_{k+1}^\alpha, n\rangle \otimes |A_{k+1}^{-\alpha}, m\rangle\} : \begin{Bmatrix} n = C_{-\alpha} + R_\alpha \\ m = C_\alpha + R_{-\alpha} \end{Bmatrix},$$

$$\{A_{k+1}^\alpha, m\rangle \otimes |A_{k+1}^{-\alpha}, n\rangle\} : \begin{Bmatrix} n = R_{-\alpha} + C_\alpha \\ m = R_\alpha + C_{-\alpha} \end{Bmatrix}. \tag{5.13}$$

Combining Eqs. (5.12) and (5.13), we obtain the following relations between the number of complex couplings C_α and the corresponding phase factors (see Fig. 5.10),

$$\begin{aligned} \{|A_{k+1}^\alpha, n\rangle \otimes |A_{k+1}^{-\alpha}, m\rangle\} : C_\alpha = C_{-\alpha} &\implies 1, \\ \{|A_{k+1}^\alpha, m\rangle \otimes |A_{k+1}^{-\alpha}, n\rangle\} : C_\alpha - C_{-\alpha} = n - m &\implies e^{\pm 2i\phi(n-m)}. \end{aligned} \tag{5.14}$$

Therefore, one can obtain an effective Creutz ladder model up to N-th order perturbation theory for any subspace with $n \neq m$. In this case, the states in the same site $\{|j_k^\alpha, n\rangle \otimes |j_k^{-\alpha}, m\rangle\}$ and $\{|j_k^\alpha, m\rangle \otimes |j_k^{-\alpha}, n\rangle\}$ are also coupled, which produces an effective vertical coupling in the Creutz ladder. The order of these couplings is $2|n - m|$ and they are in general complex. The effect of these couplings can be neglected if $2|n - m| \gg n + m = N$, as N is the order of the other couplings that compose the Creutz ladder. Alternatively, the vertical couplings vanish in the bulk for $\phi = \pi/2$, as each N-particle hopping process cancels with its left-right symmetric counterpart. In the presence of a non-negligible complex vertical coupling, the

CLSs are no longer eigenstates and, consequently, the subspace does not exhibit Aharonov-Bohm caging. Then, considering the vertical coupling and using Eq. (5.14), one can obtain a π-flux through the plaquettes by choosing

$$\begin{cases} \phi = \dfrac{\pi}{2(n-m)}, & \text{if}\quad 2|n-m| \gg n+m = N \\ \phi = \dfrac{\pi}{2}, & \text{if}\quad n-m \text{ is odd.} \end{cases} \tag{5.15}$$

For $n = m$, there is only one type of bound state, $\left\{ |j_{k+1}^{\alpha}, n\rangle \otimes |j_{k+1}^{-\alpha}, n\rangle \right\}$, such that the effective model is a linear chain with real couplings, and the system cannot exhibit Aharonov-Bohm caging. For the N-particle subspaces that exhibit flat bands with $\phi \neq \pi/2$, the single-particle spectrum is dispersive, which makes these Aharonov-Bohm caging phenomena a many-body effect.

Let us see some examples. For the $\mathcal{A}$ subspaces, N particles will accumulate a complex phase $e^{\pm 2iN\phi}$ when coupling the states $|B_k^{\alpha}, N\rangle$ and $|A_{k+1}^{-\alpha}, N\rangle$. Flat bands arise for the angles $\phi = (1 + 2q)\pi/(2N)$ with $q \in \mathbb{Z}$ as long as ϕ remains small enough so that the sites A_k and A_{k+1} do not become coupled, i.e., $|\phi| \lesssim 2\pi/3$ [147]. Additionally, the vertical couplings are $2N$-order connections and thus, always negligible. For the $\mathcal{B}$ subspaces with an even number of particles, $N/2$, in each circulation, Aharonov-Bohm caging cannot occur. The complex phases accumulated by the particles cancel out such that all the couplings of the effective chain are real and the resulting energy bands are dispersive. However, for N odd, the tunneling process of one of the particles is not compensated, leading to a complex factor $e^{\pm 2i\phi}$. Then, a phase $\phi = \pi/2$ leads to a flat-band spectrum while at the same time canceling the vertical couplings. For a real space angle $\phi = \pi/2$, the single-particle spectrum exhibits flat bands, and both the N odd $\mathcal{A}$ and $\mathcal{B}$ subspaces also present a flat-band spectrum. However, for an angle $\phi = \pi/(2N)$ the $\mathcal{A}$ subspace presents flat bands in the absence of a single-particle flat-band spectrum, making this instance of Aharonov-Bohm caging a purely many-body effect.

As one increases the number of particles in the system, the number of bound-state configurations increases and, in particular, other semi bound-states appear where not all particles are located in a single-site, i.e., $\left\{ |j_k^{\alpha}, n\rangle \otimes |j_k^{-\alpha}, m\rangle \right\}$ with $n + m < N$ and $N - (n + m)$ particles not bound to the site j. The picture described above will hold as long as the subspaces induced by bound-states do not become degenerate with the subspaces induced by these semi bound-states. For the $\mathcal{B}$ subspaces, as their bound-states have the maximum possible energy, they will not become degenerate with any other subspace. The other subspaces can become degenerate with a subspace with some particles in a bound state in the same site, and some in other sites of the lattice. However, these instances are rare: up to ten particles, only 8 out of 34 bound-states are degenerate, for example, $\left\{ |j_i^{\alpha}, 5\rangle \right\}$ and $\left\{ |j_i^{\alpha}, 2\rangle \otimes |j_i^{-\alpha}, 2\rangle \right\}$. We have checked numerically the recipe to obtain π-fluxes in arbitrary subspaces given in Eq. (5.15) up to six particles.
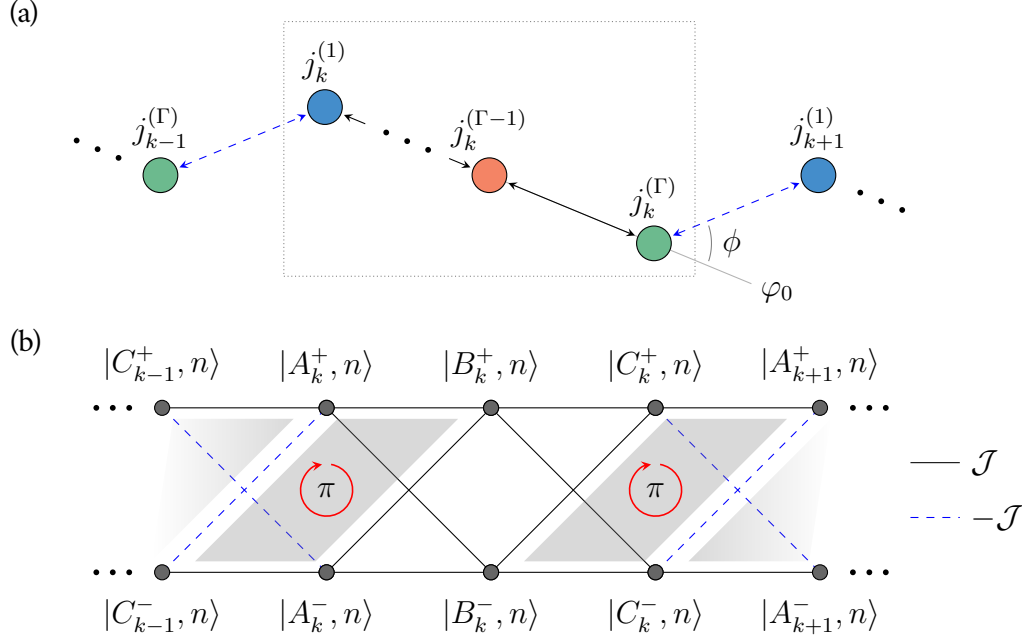
Figure 5.11: (a) Diagram of the 1D staggered chain for an arbitrary periodicity Γ. The unit cell k contains Γ sites $\{j_k^{(1)}, j_k^{(2)}, ..., j_k^{(\Gamma-1)}, j_k^{(\Gamma)}\}$ and is enclosed by a dotted rectangle. The gray line indicates the origin of the phase φ_0 such that an angle ϕ is introduced in the inter-cell couplings. The black arrows denote real tunneling amplitudes while the blue ones indicate complex tunneling amplitudes between states of different winding number. (b) Schematic representation of the sites and couplings of the lattice for $\Gamma = 3$ and an angle ϕ such that a non-uniform π-flux arises.

5.4 Generalization to non-uniform fluxes

In this section, we generalize the study to the family of models where the angle ϕ of the staggered chain is introduced with an arbitrary lattice periodicity Γ, thus increasing the number of sites per unit cell [see Fig. 5.11(a)]. The complex couplings between adjacent sites only occur between the last site of the unit cell and the first site of the next unit cell. Thus, the flux induced by this angle ϕ will not be present in each plaquette, with the exact flux pattern being a function of the number of sites in the unit cell. Non-uniform fluxes have been studied in diamond lattices [336, 339], where it has been shown to lead to an enriched Aharonov-Bohm caging phenomenology.

The analysis of Section 5.3 for the dynamics of N particles in the regime of strong interactions applies also to this family of models. In particular, the angles given in Eq. (5.15) for each N-particle subspace also yield π-fluxes, that, in this case, are non-uniform [see an example for $\Gamma = 3$ in Fig. 5.11(b)]. The non-uniform pattern is composed of $\Gamma - 2$ rhombi (or triangles) without a flux followed by two rhombi (or triangles) with a π-flux. For the case of $\Gamma = 2$, discussed in Sections 5.2 and 5.3, the number of rhombi plaquettes without flux is zero. As a
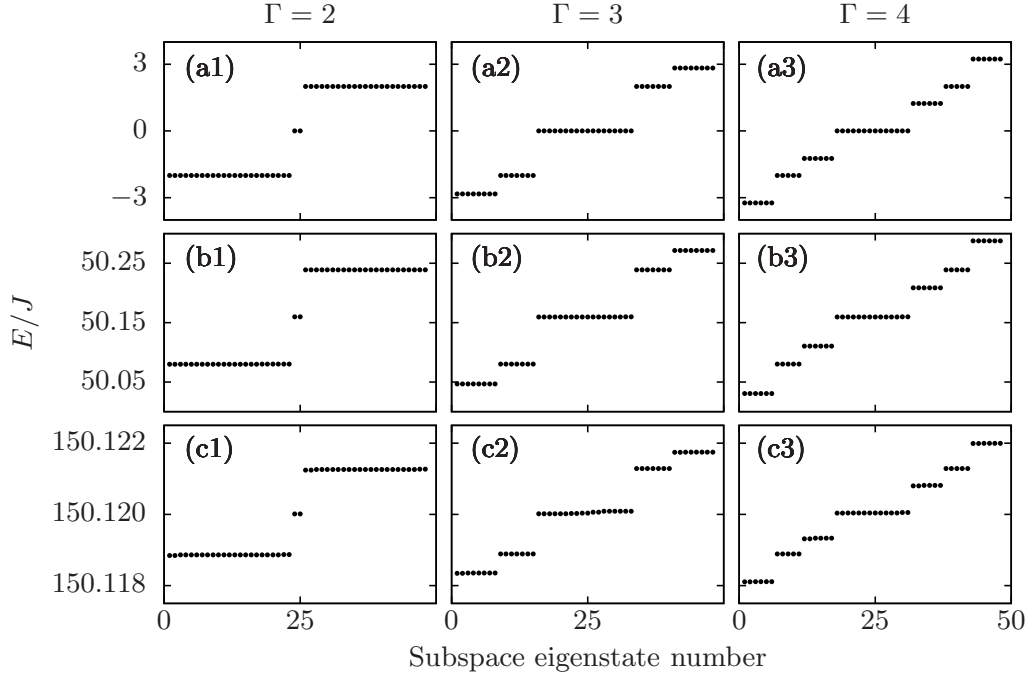
Figure 5.12: Energy spectrum for different number of particles (a) $N = 1$, (b) $N = 2$, (c) $N = 3$ and periodicities (1) $\Gamma = 2$, (2) $\Gamma = 3$, and (3) $\Gamma = 4$, for 24 sites. For the two and three-particle cases, only the $\mathcal{A}$ subspace is shown, and we fix $U/J = 50$ and introduce the on-site potential correction V at the edge sites. The angle ϕ is taken from Eq. (5.15) such that a π-flux is obtained in each subspace: (1) $\phi = \pi/2$, (2) $\phi = \pi/4$, and (3) $\phi = \pi/2$.

result of the non-uniform flux pattern, a particle cannot tunnel Γ sites to the right or the left due to destructive interference, and as a consequence, the spectrum is composed of a series of flat bands. Fig. 5.12 shows the energy spectrum for the single-particle case and the two and three-particle $\mathcal{A}$ subspaces for different periodicities, $\Gamma = 2, 3$ and 4. The angles ϕ, as given by Eq. (5.15), yield a π-flux, and we take $U/J = 50$ and simulate 24 sites for each case. Notably, by increasing the periodicity Γ, the number of flat bands increases, as the caging cell is enlarged and gives support to a larger number of CLSs. The zero-energy edge states that are present for $\Gamma = 2$, are buried in the central band of the spectrum for $\Gamma > 2$. As an example, we discuss the case of $\Gamma = 3$ in the next subsection.

5.4.1   Example: $\Gamma = 3$

For a periodicity $\Gamma = 3$, the unit cell has three sites that we will call A, B, and C. From Figures 5.12(a2), (b2), and (c2), one can see that the N-particle subspaces (with the appropriate π-flux inducing angle ϕ) present six flat bands with two degenerate zero-energy bands. The eigenstates in these flat bands consist of a series of CLSs that one can find through the diagonalization of a small lattice. Analogously to the $\Gamma = 2$ case, the basis states that compose the smallest caging cell are those within a unit cell and the next site
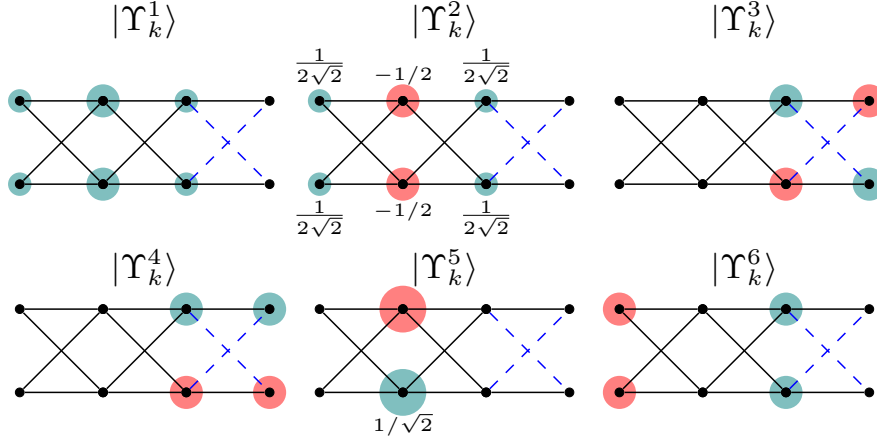
Figure 5.13: Representation of the CLSs for $\Gamma = 3$ defined in Eq. (5.17) that are eigenstates of the Creutz ladder with a non-uniform π-flux, see Fig. 5.11(b). The radius of each circle represents the amplitude and the color represents the phase, with red being a π phase, and green being a phase zero.

$$\left\{ |A_k^+, n\rangle, |A_k^-, n\rangle, |B_k^+, n\rangle, |B_k^-, n\rangle, |C_k^+, n\rangle, |C_k^-, n\rangle, |A_{k+1}^+, n\rangle, |A_{k+1}^-, n\rangle \right\}. \quad (5.16)$$

We give below the analytical expressions of the CLSs (dropping the label n for conciseness) and give a visual representation in Fig. 5.13,

$$
\begin{aligned}
|\Upsilon_k^1\rangle &= \frac{|A_+^k\rangle + |A_-^k\rangle + \sqrt{2}|B_+^k\rangle + \sqrt{2}|B_-^k\rangle + |C_+^k\rangle + |C_-^k\rangle}{2\sqrt{2}}, \\
|\Upsilon_k^2\rangle &= \frac{|A_+^k\rangle + |A_-^k\rangle - \sqrt{2}|B_+^k\rangle - \sqrt{2}|B_-^k\rangle + |C_+^k\rangle + |C_-^k\rangle}{2\sqrt{2}}, \\
|\Upsilon_k^3\rangle &= \frac{|C_+^k\rangle - |C_-^k\rangle - |A_+^{k+1}\rangle + |A_-^{k+1}\rangle}{2}, \\
|\Upsilon_k^4\rangle &= \frac{|C_+^k\rangle - |C_-^k\rangle + |A_+^{k+1}\rangle - |A_-^{k+1}\rangle}{2}, \\
|\Upsilon_k^5\rangle &= \frac{|B_-^k\rangle - |B_+^k\rangle}{\sqrt{2}}, \\
|\Upsilon_k^6\rangle &= \frac{|C_+^k\rangle + |C_-^k\rangle - |A_+^k\rangle - |A_-^k\rangle}{2}.
\end{aligned}
\quad (5.17)
$$

The energies of the CLSs are given by

$$
\begin{aligned}
E_1 &= 2\sqrt{2}\mathcal{J}, & E_2 &= -2\sqrt{2}\mathcal{J}, & E_3 &= -2\mathcal{J}, \\
E_4 &= 2\mathcal{J}, & E_5 &= 0, & E_6 &= 0.
\end{aligned}
\quad (5.18)
$$

Let us compare these CLSs with those obtained for $\Gamma = 2$, in Eq. (5.9). For $\Gamma = 3$, the unit cell is enlarged, and we obtain more CLSs (six for $\Gamma = 3$ vs. four for $\Gamma = 2$) that also
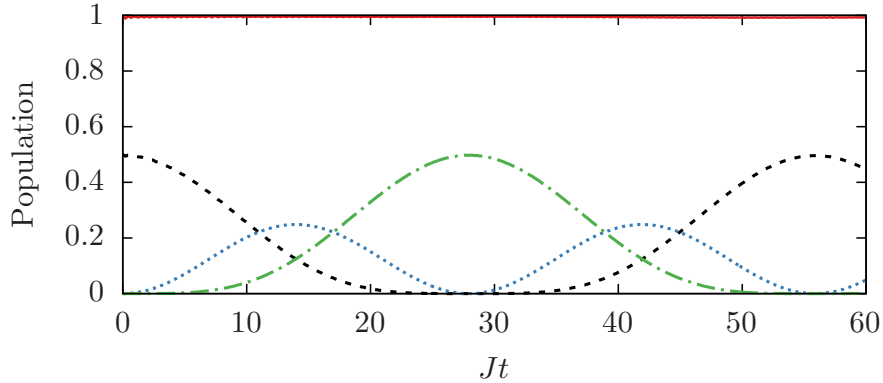
Figure 5.14: Time evolution of the population of the states $\left|j_k^\alpha, 2\right\rangle$ with $j = A, B, C$ and total caged population P_{cag} (continuous red line), obtained through exact diagonalization for $U/J = 50$, $N_c = 12$ unit cells and $\phi = \pi/4$. The dashed black line is the population in the states $\left|A_4^\alpha, 2\right\rangle$, with $\alpha = \pm$, the dotted blue line is the population in the states $\left|B_4^\alpha, 2\right\rangle$, and the dashed-dotted green line is the population in $\left|C_4^\alpha, 2\right\rangle$. The initial state is $\left(\left|A_4^+, 2\right\rangle + \left|A_4^-, 2\right\rangle\right)/\sqrt{2}$.

span a larger number of sites. As a direct consequence, the caging dynamics resulting from these flat bands have larger support over the lattice. To give an example, we consider the two-particle $\mathcal{A}$ subspace with $\phi = \pi/4$, $U/J = 50$ and $N_c = 12$ unit cells for $\Gamma = 3$. In Fig. 5.14, we show the time evolution of the population of the states, $P_{\left|j_k^\alpha, 2\right\rangle}$ for the initial state $\left(\left|A_4^+, 2\right\rangle + \left|A_4^-, 2\right\rangle\right)/\sqrt{2}$. The red line indicates the caged population $P_{cag} = P_{\left|A_k^+, 2\right\rangle} + P_{\left|A_k^-, 2\right\rangle} + P_{\left|B_k^+, 2\right\rangle} + P_{\left|B_k^-, 2\right\rangle} + P_{\left|C_k^+, 2\right\rangle} + P_{\left|C_k^-, 2\right\rangle}$. The population oscillates between the sites A_k, B_k, C_k of a single unit cell, as the destructive interference occurs at the sites C_{k-1} and A_{k+1}.

5.5   Conclusions

In this chapter, we have studied a system of bosons in a staggered lattice with ring traps in each site and considered the local eigenstates with orbital angular momentum $l = 1$. The system can be mapped to a Creutz ladder with a real and a synthetic dimension, in which the flux enclosed in each plaquette is determined by the angle ϕ that makes the lattice staggered. In the single-particle case, one can tune the angle ϕ to obtain a uniform π-flux threading each plaquette. This leads to a flat-band spectrum characterized by the presence of CLSs and the system exhibits Aharonov-Bohm caging.

For N particles in the regime of strong on-site interactions, bound-states arise where the N particles populate a single site. Using perturbation theory, most of the N-particle subspaces can be mapped to an effective Creutz ladder with a flux that depends on the angle ϕ. We have identified the conditions under which these subspaces present a π-flux that leads to flat bands and Aharonov-Bohm caging. Remarkably, some of these subspaces can exhibit

Aharonov-Bohm caging even in the presence of a single-particle dispersive spectrum, making these instances a purely many-body effect.

Finally, we have generalized this study to the case of non-uniform fluxes by introducing the angle ϕ at an arbitrary lattice periodicity Γ. In this case, one can engineer flat-band spectra for different N-particle subspaces and an arbitrary Γ. As the unit cell increases in size, the number of flat bands increases, resulting in a larger number of CLSs that also have a greater spatial extent. As a result, the caged particles can explore a broader region of the lattice before encountering destructive interference, making the periodicity Γ a tunable parameter that controls the spatial extent of the Aharonov-Bohm caging.

6

LOCAL HILBERT SPACE FRAGMENTATION IN BOSONIC FLAT-BAND LATTICES

In this chapter, we study local Hilbert space fragmentation in flat band lattices exhibiting single-particle compact localized states (CLSs). First, we analyze in detail a family of diamond necklace lattices with n central sites. We show how the fragmentation of the Hilbert space is revealed upon a certain basis rotation and that there is a conserved quantity related to the occupation of the single-particle CLSs. Second, we demonstrate that this is a general mechanism for a complete class of flat-band lattices with commutative local symmetries, which present a generalized conservation law.

CLSs are eigenstates of a Hamiltonian that have non-zero amplitudes on (typically few) close-by sites and whose amplitude strictly vanishes on the rest [123, 340]. CLSs arise due to geometrical frustration through the interplay between the geometry and the tunneling amplitudes of the model. If the system is periodic, CLSs lead to a macroscopic number of degenerate eigenstates that constitute a flat band. Flat bands have an energy independent of the quasimomentum, such that transport is strongly suppressed. They can generally be related to the presence of CLSs, as these can be constructed as a superposition of degenerate Bloch states [341].

There are multiple methods of construction to generate flat bands, such as the use of Fano lattices [123], origami rules [342], fractals [343, 344], bipartite graphs [345], and others [346–348]. More general procedures also exist, such as solving inverse eigenvalue problems [340, 349–351], performing band engineering [352], or using strictly local projectors [353, 354]. Although there is no framework capable of generating all systems known to exhibit flat bands, many CLSs arise as a result of local reflection symmetries in the Hamiltonian. For this class of CLSs, a general formalism has been proposed using the equitable partition theorem (EPT) from graph theory [181], and its generalization to complex matrices [355–357]. This theorem allows one to link the presence of commutative local symmetries to the presence of CLSs [358].

Systems with Hilbert space fragmentation avoid full thermalization due to the presence of exponentially many disconnected sectors in their Hilbert space. Remarkably, this mechanism

can lead both to a weak or a strong violation of the eigenstate thermalization hypothesis (ETH), that broadly states that the eigenstates of isolated quantum many-body systems have thermal expectation values for local observables. This effect can arise in a wide variety of systems, such as dipole moment or center-of-mass conserving systems [110–115], the 1D t-J_z model [359], the t-V and t-V_1-V_2 models [360, 361], models within the Fibonacci Hilbert space of the Rydberg blockade [362], and models with dipolar interactions [363]. All the above examples exhibit fragmentation of the Hilbert space in the product state basis [249], i.e., classical fragmentation. Quantum fragmentation, which occurs in an entangled basis, has been recently shown to arise in Temperley-Lieb spin chains [249] and in quantum East models [364]. However, it has yet to be determined if quantum fragmentation leads to different phenomenology than its classical analog.

In the first part of this chapter, we analyze in detail a family of Bose-Hubbard diamond necklaces [365] that exhibit quantum local Hilbert space fragmentation. In locally fragmented systems, the conserved quantities that shatter the Hilbert space are strictly local [125, 185, 250, 362, 366], in analogy with the conserved local quantities in disorder-free localization [367] and in lattice gauge theories [368–371]. In contrast, standard fragmentation is due to the presence of the recently coined crypto-local conserved quantities, those that cannot be expressed as sums of local operators [372]. Here, the presence of a single-particle flat band composed of CLSs gives rise to the fragmentation of the Hilbert space when introducing on-site interactions. As a consequence of this fragmentation, one finds a nested distribution of entanglement entropies, sub-sector-restricted thermalization, and a broad range of sub-sectors of the Hamiltonian that range from frozen sub-sectors following area-law to non-integrable sub-sectors with logarithmic scaling. Then, a natural question arises: Is there a general local fragmentation mechanism for flat-band lattices? In the second part of this chapter, we answer this question affirmatively for arbitrary flat-band lattices possessing commutative local symmetries that correspond to local reflection symmetries, and thus that obey the EPT theorem.

The chapter is structured as follows: in the first part of the chapter, Section 6.1, we study the family of diamond necklaces both analytically and numerically. In Sec. 6.1.1, we introduce the physical model and, in Sec. 6.1.2, we describe the basis rotation that reveals the fragmentation of the Hilbert space. In Sec. 6.1.3, we analyze the conserved quantity that characterizes the sub-sectors of the Hamiltonian, present the adjacency graphs of the fragmented Hamiltonian, and demonstrate that the system is strongly fragmented. The numerical results are discussed in Sec. 6.1.4, which include the distribution of entanglement entropies, the entanglement evolution and scaling, the level spacing analysis and a comparison between the different models of the diamond necklace family. In the second part of the chapter, Sec. 6.2, we generalize the analysis to other flat-band lattices. In Sec. 6.2.1, we define a class of flat-band systems with commutative local symmetries and, in Sec. 6.2.2, we demonstrate that they exhibit strong local Hilbert space fragmentation in the presence of on-site bosonic interactions. In Sec. 6.2.3, we explore the effect of long-range interactions on the conserved quantities. Finally, we provide a numerical example in Sec. 6.2.4, the 1D Pyrochlore lattice, and present the conclusions in Sec. 6.3.

6.1   Diamond necklaces

6.1.1   Physical system

We study a system of interacting bosons loaded onto a one-dimensional lattice of diamond necklaces with n central (i.e., spinal) sites [see Fig. 6.1(a)]. Each unit cell k is composed of the sites $C_{1,k} \cdots C_{n,k}$, U_k and D_k (with $k = 1, ..., N_c$), and all the couplings have the same magnitude $\mathcal{J}$. The Hamiltonian of this system is $\hat{\mathcal{H}}_n = \hat{\mathcal{H}}_n^0 + \hat{\mathcal{H}}_n^{int}$, where the single-particle Hamiltonian reads

$$\hat{\mathcal{H}}_n^0 = \mathcal{J} \sum_k \left[\hat{c}_{n,k}^\dagger (\hat{u}_k + \hat{d}_k) + (\hat{u}_k^\dagger + \hat{d}_k^\dagger) \hat{c}_{1,k+1} + \sum_{j=1}^{n-1} (\hat{c}_{j,k}^\dagger \hat{c}_{j+1,k}) \right] + \text{H.C.}, \qquad (6.1)$$

where $\hat{c}_{j,k}$ is the annihilation operator of the state $|C_{j,k}\rangle$ at the central site $j = 1, ..., n$ in each unit cell k, and $\hat{u}_k$ and $\hat{d}_k$ are the annihilation operators of the states $|U_k\rangle$ and $|D_k\rangle$ at the up and down sites of each diamond, respectively. In particular, the $n = 2$ case corresponds to a type of orthogonal dimer chain [226, 373–382] with absent vertical couplings. The interaction Hamiltonian reads

$$\begin{aligned} \hat{\mathcal{H}}_n^{int} &= \frac{U}{2} \sum_{k=1}^{N_c} \left[\hat{n}_{u,k}(\hat{n}_{u,k} - 1) + \hat{n}_{d,k}(\hat{n}_{d,k} - 1) + \sum_{j=1}^n \hat{n}_{j,k}(\hat{n}_{j,k} - 1) \right] \\ &= \hat{\mathcal{H}}_{n,\text{diam.}}^{int} + \hat{\mathcal{H}}_{n,\text{cent.}}^{int}, \end{aligned} \qquad (6.2)$$

where we distinguish the terms of the up and down sites of each diamond, $\hat{\mathcal{H}}_{n,\text{diam.}}^{int}$, and the central sites, $\hat{\mathcal{H}}_{n,\text{cent.}}^{int}$. The operators $\hat{n}_{u,k} = \hat{u}_k^\dagger \hat{u}_k$, $\hat{n}_{d,k} = \hat{d}_k^\dagger \hat{d}_k$ and $\hat{n}_{j,k} = \hat{c}_{j,k}^\dagger \hat{c}_{j,k}$ are the number operators at the up, down and central sites, respectively.

An interesting characteristic of this family of Hamiltonians is that each diamond presents a single-particle CLS that only populates the sites U_k and D_k, $(|U_k\rangle - |D_k\rangle)/\sqrt{2}$, [see Fig. 6.1(a)]. Due to the presence of the CLS in each diamond of the lattice, all models of this family exhibit a single-particle spectrum with a zero-energy flat band. We are interested in the many-body states where some of the particles occupy a CLS, and how the existence of these states modifies the thermalization properties of the whole system. The numerical results that we present in Section 6.1.4 can be better interpreted by performing a basis rotation and analyzing the symmetries of the system, which we discuss in the next subsection.

6.1.2   Basis rotation

Consider the symmetric and antisymmetric superpositions of the up and down states of each diamond,

$$|S_k\rangle = \frac{1}{\sqrt{2}} \left(|U_k\rangle + |D_k\rangle \right), \quad |A_k\rangle = \frac{1}{\sqrt{2}} \left(|U_k\rangle - |D_k\rangle \right), \qquad (6.3)$$
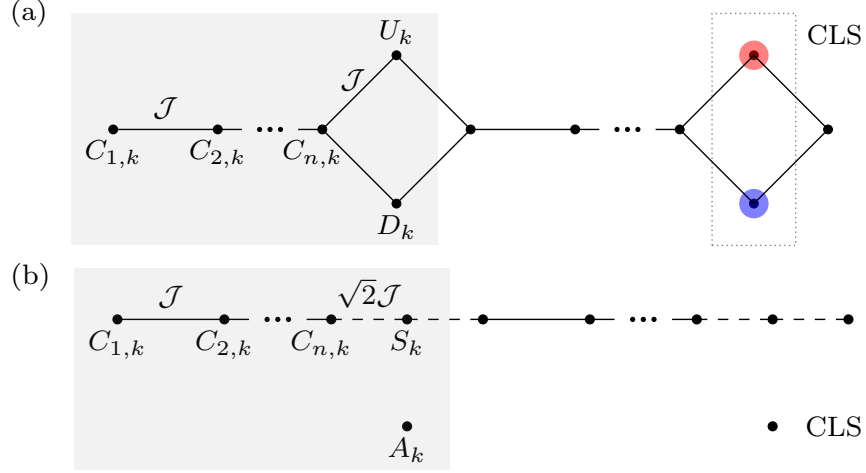
Figure 6.1: (a) Diagram of the one-dimensional diamond necklace model with n central sites. All couplings have a strength $\mathcal{J}$ and the unit cell is shadowed in gray. In the second unit cell we represent the CLS with the site amplitude being the radius of the circle and the phase being the color (zero, red; π, blue). (b) Diagram of the rotated model with the renormalized couplings, $\sqrt{2}\mathcal{J}$, denoted by a dashed line. The uncoupled states represent the CLSs, $|A_k\rangle$.

where $\hat{s}_k^\dagger$ and $\hat{a}_k^\dagger$ are the respective creation operators and $|A_k\rangle$ is the CLS in unit cell k. By using these states to perform a basis rotation on the single-particle Hamiltonian, in Eq. (6.1), only the couplings associated to the diamonds are altered,

$$\hat{\mathcal{H}}_n^{0'} = \sum_k \left[\sqrt{2}\mathcal{J}\left(\hat{c}_{n,k}^\dagger \hat{s}_k + \hat{s}_k^\dagger \hat{c}_{1,k+1} \right) + \mathcal{J} \sum_{j=1}^{n-1} (\hat{c}_{j,k}^\dagger \hat{c}_{j+1,k}) \right] + \text{H.C.} \tag{6.4}$$

One obtains a linear chain that includes the symmetric states, $|S_k\rangle$, and the central states $|C_{j,k}\rangle$, with renormalized couplings corresponding to the diamonds, $\sqrt{2}\mathcal{J}$. Additionally, the CLSs in each unit cell, $|A_k\rangle$, become decoupled, see Fig. 6.1(b). In analogy with the transformation of $\hat{\mathcal{H}}_n^0$, only the interaction term of the up and down sites of each diamond, $\hat{\mathcal{H}}_{n,\text{diam.}}^{int}$ in Eq. (6.2), is altered by the basis rotation,

$$\hat{\mathcal{H}}_{n,\text{diam.}}^{int'} = \frac{U}{4} \sum_{k=1}^{N_c} \left[4\hat{s}_k^\dagger \hat{a}_k^\dagger \hat{s}_k \hat{a}_k + \sum_{\sigma=a,s} \left(\hat{\sigma}_k^\dagger \hat{\sigma}_k^\dagger \hat{\sigma}_k \hat{\sigma}_k \right) + \hat{a}_k^\dagger \hat{a}_k^\dagger \hat{s}_k \hat{s}_k + \hat{s}_k^\dagger \hat{s}_k^\dagger \hat{a}_k \hat{a}_k \right], \tag{6.5}$$

where $\hat{\sigma}_k$ ($\hat{\sigma} = \hat{s}, \hat{a}$) are the annihilation operators of $|S_k\rangle$ and $|A_k\rangle$, respectively. The first term corresponds to a nearest-neighbor interaction that arises when there is at least one particle in $|S_k\rangle$ and one in $|A_k\rangle$, akin to the inter-circulation interaction term appearing in Hubbard models of excited orbital angular momentum states in optical lattices [150, 153]. The second term is an effective on-site interaction that occurs when there are at least two particles in either $|S_k\rangle$ or $|A_k\rangle$. Finally, the last two terms correspond to a two particle tunneling between the decoupled states $|A_k\rangle$ and the states $|S_k\rangle$. Therefore, on-site interactions induce a coupling between the CLSs and the dispersive linear chain through the two-particle tunneling.

6.1.3 Local and total CLS number parity

Let us consider the two-particle tunneling term that appears in the rotated interaction Hamiltonian of Eq. (6.5). As a consequence of this process, the system presents a conserved quantity, the local CLS number parity, that reads

$$\hat{\mathcal{P}}_k = e^{i\pi\hat{n}_{a,k}}, \tag{6.6}$$

where $\hat{n}_{a,k} = \hat{a}_k^\dagger \hat{a}_k$ is the CLS number operator at unit cell k. This operator commutes with the rotated interaction Hamiltonian, $[\hat{\mathcal{H}}_{n,\text{diam.}}^{int\prime}, \hat{\mathcal{P}}_k] = 0$, and consequently, with the total rotated Hamiltonian, $[\hat{\mathcal{H}}_n', \hat{\mathcal{P}}_k] = 0$. The operator $\hat{\mathcal{P}}_k$ can be evaluated at each unit cell k (which contains a single diamond) and takes the eigenvalues $\mathcal{P}_k = 1$, for an even number of particles, and $\mathcal{P}_k = -1$, for an odd number of particles. We define the local CLS number parity vector as the vector that contains the eigenvalues of $\hat{\mathcal{P}}_k$ at each unit cell, $\boldsymbol{\mathcal{P}} = (\mathcal{P}_1, \cdots, \mathcal{P}_{N_c})$. This conserved quantity corresponds to a $\mathbb{Z}_2$ local gauge symmetry governed by the two-particle tunneling term in Eq. (6.5) [332, 383, 384]. Additionally, one can define the total CLS number parity as the sum of the local operators in all unit cells, $\hat{\mathcal{P}} = \sum_k \hat{\mathcal{P}}_k$. Given that the rotated Hamiltonian commutes with the local operator, it is straightforward to see that it also commutes with the total CLS number parity, $[\hat{\mathcal{H}}_n', \hat{\mathcal{P}}] = 0$. The eigenvalues of the total parity are determined by the number of unit cells and the number of particles that can occupy the CLSs. If there are at least as many particles, N, as unit cells, $N \geq N_c$, there are $N_c + 1$ sectors with eigenvalues $\mathcal{P} = -N_c, -N_c + 2, ..., N_c - 2, N_c$. For $N < N_c$, the number of sectors reduces to $N + 1$ as the lowest eigenvalues become unavailable. We note that the $\mathbb{Z}_2$ local gauge symmetry makes the sub-sectors in this model similar to the superselection sectors present in lattice gauge theories, where the shattering of the Hilbert space naturally stems from the gauge field and leads to non-ergodicity [368, 369, 385].

Spinless fermions in diamond lattices with nearest-neighbor interactions present a locally fragmented Hilbert space where the number of particles occupying a CLS is conserved, which corresponds to a $U(1)$ local gauge symmetry [126]. The authors note there that for bosons or spinful fermions, the two-particle tunneling implies that the number of particles in a CLS is no longer conserved. Here, we show that for bosons with on-site interactions a new conserved quantity emerges, the CLS number parity, which preserves the fragmentation of the Hilbert space.

In Fig. 6.2, we represent three examples of the adjacency graph of the rotated Hamiltonian. Unless otherwise specified, we consider open boundary conditions, and for all simulations we fix $U = \mathcal{J} = 1$ and consider an integer number of unit cells. Henceforward, the eigenvalues $\mathcal{P}_k$ are denoted as $\pm$. The width of the lines indicates the strength of the couplings between basis states and, for Figs. 6.2(a) and (b), the color of the nodes indicates the diagonal terms of the rotated Hamiltonian, $\varepsilon = \langle f | \hat{\mathcal{H}}_n' | f \rangle$, where $|f\rangle$ is a basis state. Fig. 6.2(a) represents the diamond chain, $\hat{\mathcal{H}}_1'$, a known square-root topological insulator [226, 386], with $N = 2$ particles in $N_c = 2$ unit cells. Each basis state is represented by a node and labeled using the notation $|N_{C,1} N_{S,1} N_{A,1} N_{C,2} N_{S,2} N_{A,2}\rangle$, where $N_{j,k}$ is the number of particles in state $|j_k\rangle$ ($j = C, S, A$) in the unit cell k. We obtain several uncoupled clusters of basis states with
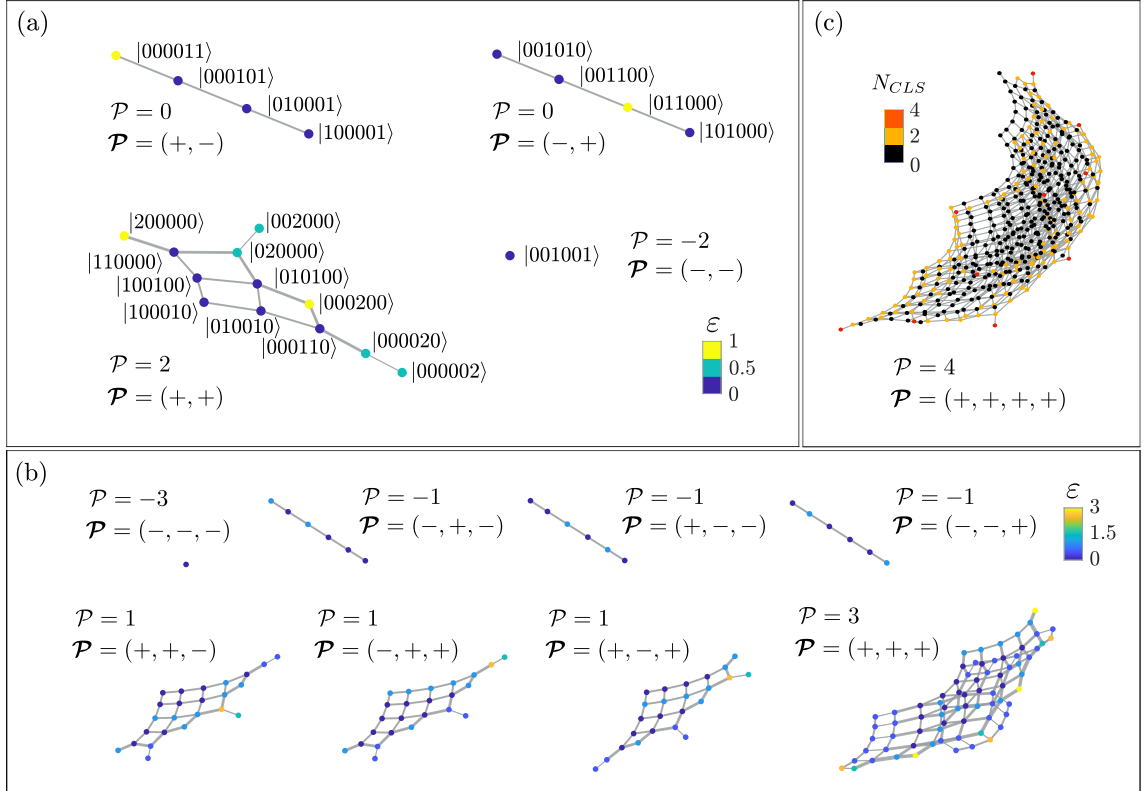
Figure 6.2: Adjacency graphs for open boundary conditions and $U = \mathcal{J} = 1$. (a) $\hat{\mathcal{H}}_1'$, with $N = 2$ particles in $N_c = 2$ unit cells, (b) $\hat{\mathcal{H}}_1'$, with $N = 3$ and $N_c = 3$, (c) largest sub-sector of $\hat{\mathcal{H}}_1'$, with $N = 4$ and $N_c = 4$. The width of the lines indicates the strength of the couplings between basis states and the color of the nodes represents the diagonal terms, ε, in (a,b), and the total number of particles in a CLS, N_{CLS}, in (c). For each cluster, the values of the total CLS number parity are given as well as the vector $\mathcal{P}$ for the local CLS number parity. In (a), each basis state is represented by a node and labeled using the notation $|N_{C,1}\, N_{S,1}\, N_{A,1}\, N_{C,2}\, N_{S,2}\, N_{A,2}\rangle$, where $N_{j,k}$ is the number of particles in state $|j_k\rangle$ ($j = C, S, A$) in the unit cell k.

distinct local eigenvalues $\mathcal{P}$, i.e., the Hilbert space is fragmented. Each sector with total parity eigenvalue $\mathcal{P}$ is composed of one or more uncoupled sub-sectors with eigenvalues $\mathcal{P}$. There is a one-dimensional (or frozen) sub-sector with a single basis state with the two particles occupying the two CLSs, $\mathcal{P} = -2$, and which is not coupled to any other basis state. There are two sub-sectors sharing the same total CLS parity value, $\mathcal{P} = 0$, where only one particle is in a CLS, while the other particle occupies the dispersive chain. The two sub-sectors arise due to the two CLSs that the particle can occupy, which leads to different orderings in the elements of the vector $\mathcal{P}$. Finally, most of the basis states of the largest sub-sector have the two particles in the dispersive chain and zero in a CLS. However, due to the two-particle tunneling, there are two special basis states with two particles occupying the same CLS, $|002000\rangle$ and $|000002\rangle$, which yield the same eigenvalue for the local and total CLS number parity, $\mathcal{P} = (+, +)$ and

$\mathcal{P} = 2$.

In Fig. 6.2(b), we present the same system, $\hat{\mathcal{H}}_1'$, for a larger lattice: $N_c = 3$ unit cells with $N = 3$ particles. The number of sub-sectors proliferates due to the presence of an additional CLS in the lattice. More precisely, for $N \geq N_c$, the number of sub-sectors is given by 2^{N_c}, while for $N < N_c$, the number is $\sum_{k=0}^{N} \binom{N_c}{k}$. The sub-sectors $\mathcal{P} = -1$, like the sub-sectors $\mathcal{P} = 0$ in Fig. 6.2(a), have only one particle in the dispersive chain, while all the other particles occupy distinct CLSs. These particles can not access the two-particle tunneling in Eq. (6.5) and thus, are trapped in the CLSs. Therefore, these sub-sectors are effectively single-particle systems with a non-uniform on-site potential distribution. For the larger sub-sectors, there are at least two particles in the dispersive chain, making these sub-sectors sensitive to interactions. Note that the different sub-sectors with the same eigenvalue $\mathcal{P}$ for the total CLS number parity are not degenerate due to the different positioning of the diagonal terms. This will prove to be an important factor in distinguishing between the different domes of the distribution of entanglement entropies, as we discuss below in Sec. 6.1.4.

As an example of a sub-sector with a large dimension, we represent the largest sub-sector of $\hat{\mathcal{H}}_1'$, with $N = 4$ particles in $N_c = 4$ unit cells in Fig. 6.2(c). The color of each basis state represents the total number of particles that are in a CLS, $N_{CLS}|f\rangle = \sum_k \hat{n}_{a,k}|f\rangle$. Most of the basis states have zero particles in a CLS. However, there are also some basis states with four-particles in a CLS (either four-particles in the same CLS or two pairs of particles in different CLSs), and many-more with two particles in the same CLS. This embedding of special basis states has some consequences on the distribution of entanglement entropies of the system, which will be discussed in Section 6.1.4.

It is important to note that the Hilbert space fractures into a series of uncoupled sub-sectors only on the rotated or entangled basis. Meanwhile, the Hilbert space in the original or product-state basis exhibits a connected adjacency graph. Thus, the results of this section show how this system exhibits quantum Hilbert space fragmentation, a distinction recently proposed in [249]. In contrast, the Hilbert space of classically fragmented systems is shattered in the product-state basis. While the fracture is only revealed on the rotated basis, it still has some dramatic consequences on the thermalization properties of this family of models, which we explore in Section 6.1.4.

Another recently proposed classification of Hilbert space fragmentation distinguishes between strongly and weakly fragmented systems in the context of dipole conserving models [110, 111, 387]. The ratio between the dimension of the largest sector $\mathcal{D}_{max}$ and the dimension of the full Hilbert space $\mathcal{D}$ either tends to one in the thermodynamic limit, signaling weak fragmentation, or tends to zero, signaling strong fragmentation. Typical initial states of a weakly fragmented system belong to the largest sector, and thus, completely thermalize, while only a vanishing subset of initial states are non-thermal. For strongly fragmented systems, most initial states only have access to a small subset of the Hilbert space, which precludes full thermalization. Thus, these two types of fragmentation are associated with a weak or a strong violation of the ETH, respectively. For our model, the dimension of each sub-sector in a sector

$\mathcal{P}$ is

$$\mathcal{D}_{\mathcal{P}} = \sum_{\varrho=0}^{\lfloor \frac{N-m}{2} \rfloor} \binom{(n+1)N_c + N - 2\varrho - m - 1}{N - 2\varrho - m} \binom{N_c + \varrho - 1}{\varrho}, \tag{6.7}$$

where the integer ϱ counts the number of pairs of particles that populate the CLSs and m is defined as $m = (N_c - \mathcal{P})/2$. The dimension of the largest sub-sector $\mathcal{D}_{max}$ corresponds to $\mathcal{P} = N_c$. Given the dimension of the full Hilbert space,

$$\mathcal{D} = \binom{(n+2)N_c + N - 1}{N}, \tag{6.8}$$

the ratio $\mathcal{D}_{max}/\mathcal{D}$ tends to zero at the thermodynamic limit, indicating strong Hilbert space fragmentation for this family of models. Thus, this result points to a strong violation of the ETH, as we will numerically argue in the next section.

Finally, this system exhibits local Hilbert space fragmentation, a term recently coined in [250], as the fragmentation stems from a local conservation law, namely, the local CLS number parity, $[\hat{\mathcal{H}}'_n, \hat{\mathcal{P}}_k] = 0$.

6.1.4   Exact diagonalization results

Level statistics

In order to characterize the properties of the different sub-sectors of the Hilbert space, we analyze their level statistics using exact diagonalization. For each sub-sector, we consider the ordered eigenvalues E_n, and the nearest-neighbor gaps $s_n = E_{n+1} - E_n$. From those, one can define the level spacing ratios for each pair of gaps [388],

$$r_n = \frac{\min(s_n, s_{n+1})}{\max(s_n, s_{n+1})}, \tag{6.9}$$

and the corresponding average $\langle r \rangle$. Non-integrable systems with time-reversal symmetry are expected to approximate the probability distribution $P(r)$ of the Gaussian orthogonal ensemble, with an average value $\langle r \rangle_{GOE} = 0.536$ [389]. For integrable systems, a Poisson distribution is expected, with a characteristic value $\langle r \rangle_P = 0.386$. In Fig. 6.3, we represent the average spacing ratio for $\hat{\mathcal{H}}'_4$ with $N = 4$ particles in $N_c = 4$ unit cells for the sub-sectors $\mathcal{P} = 4, 2, 0$ and $U = \mathcal{J} = 1$. We observe how most sub-sectors are within a few error bars of $\langle r \rangle_{GOE}$. The value of $\langle r \rangle$ increases with the total CLS number parity, $\mathcal{P}$, as less particles are trapped in a CLS. Additionally, the lowest values of $\langle r \rangle$ correspond to the sub-sectors with the smallest dimension (i.e., smaller $\mathcal{P}$), for which the $P(r)$ distribution is not so well-defined. Besides the sub-sectors shown in Fig. 6.3, the system also presents the integrable sub-sectors with $\mathcal{P} = -2$, the effectively single-particle sub-sectors, and $\mathcal{P} = -4$, the frozen, one-dimensional sub-sector.
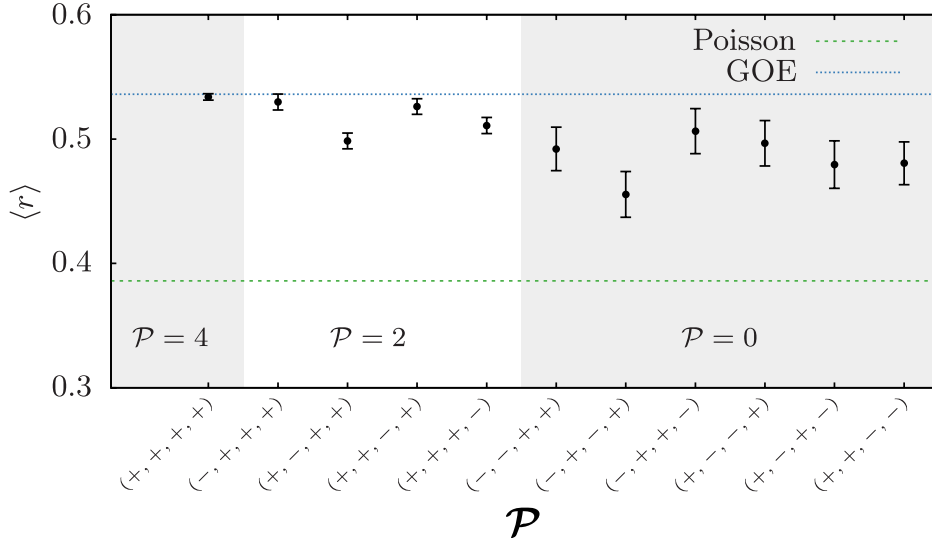
Figure 6.3: Mean level spacing ratio for the sub-sectors with $\mathcal{P} = 4, 2, 0$ of $\hat{\mathcal{H}}'_4$, with $N = 4$ particles in $N_c = 4$ unit cells and $U = \mathcal{J} = 1$. The blue dotted line indicates the value corresponding to the Gaussian orthogonal ensemble, $\langle r \rangle_{GOE} = 0.536$, and the dashed green line, the value for a Poisson distribution, $\langle r \rangle_P = 0.386$. The error bars are standard errors of the mean. The sub-sectors $\mathcal{P} = -2$ and $\mathcal{P} = -4$, which are not included, correspond to the integrable effective single-particle sub-sectors and the integrable frozen state, respectively.

Entanglement entropy and evolution

In this section, we calculate the bipartite von Neumann entanglement entropy, S, for each eigenstate of the full Hilbert space by partitioning the lattice into two subsystems: left, L; and right, R. The entanglement entropy is then $S = -\operatorname{tr}(\rho_L \ln \rho_L)$, where ρ_L is the reduced density matrix of the left subsystem. We consider the half-chain entanglement entropy by partitioning the lattice in the middle, with the same number of sites in each subsystem and such that the cut never falls between the U and D sites of a single diamond.

Fig. 6.4(a) represents the entanglement entropy of all eigenstates of the system for $\hat{\mathcal{H}}'_2$ with $N = 4$ particles in $N_c = 4$ unit cells and $U = \mathcal{J} = 1$. We give the results in terms of the normalized entanglement entropy, $\tilde{S} = S/\mathcal{N}_L$ where $\mathcal{N}_L$ is the number of sites subsystem L. The entanglement entropy is not a continuous function of the energy density but presents a nested-dome structure. Similar structures have been found in the distribution of entanglement entropies of systems with [106, 366, 390] or without frustration [391], as a similar shattering mechanism is known to arise in spin systems [392]. In Fig. 6.4(a), each dome corresponds to a sector with a given value for the total CLS number parity, $\mathcal{P}$.

- The upper dome corresponds to the largest sub-sector, with $\mathcal{P} = 4$, where most basis states have all particles in the dispersive chain and none is trapped in a CLS.

- The second dome from above corresponds to the sub-sectors with $\mathcal{P} = 2$, where most basis states have one particle in a CLS and the other three are in the dispersive chain.
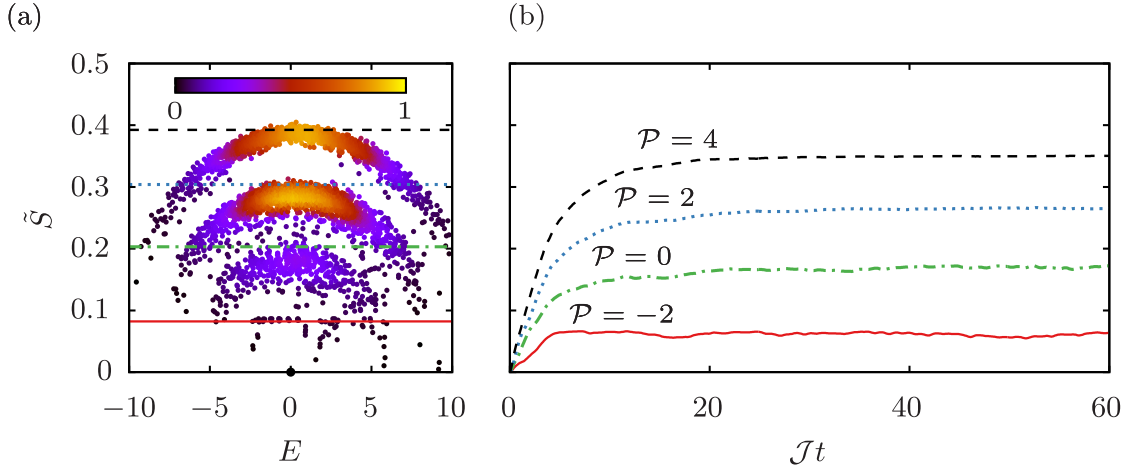
(a)

(b)

Figure 6.4: Distribution of entanglement entropies and entanglement evolution of a trial state for $\hat{\mathcal{H}}_2'$, with $N = 4$ particles in $N_c = 4$ unit cells and $U = \mathcal{J} = 1$. (a) Half-chain bipartite von Neumann entanglement entropy of each eigenstate as a function of the energy. The horizontal lines are the sector-restricted Page values for each sector and the color of the dots indicates the normalized density of data points, increasing with warming colors. (b) Average of the entanglement entropy evolution for ten random rotated basis states of each sector with eigenvalue $\mathcal{P}$. In both figures, the entropy is normalized to the number of sites in the subsystem, $\tilde{S} = S/\mathcal{N}_L$.

As the subsystem partition does not fall between the sites U and D of any diamond, the contribution to the entanglement of the particle occupying a CLS is exactly zero. Thus, the eigenstates belonging to the sector $\mathcal{P} = 2$ have an upper bound for the entanglement entropy given by the maximum number of particles in the dispersive chain of the corresponding basis states.

- The third dome corresponds to $\mathcal{P} = 0$, where most basis states have two particles in a CLS and two in the dispersive chain. Consequently, those sub-sectors have an even lower bound for the entanglement entropy.

- The sub-sectors with $\mathcal{P} = -2$ have only one particle in the dispersive chain, making them effectively single-particle systems. As a result, their distribution of entanglement entropies does not form a dome structure. Most eigenstates accumulate at a constant value, which one would expect for a linear chain, while some fall below as a consequence of the interaction-induced on-site potentials, e.g., a particle occupying the $|A_k\rangle$ CLS can be translated into an effective on-site potential of strength U acting on a second particle located at $|S_k\rangle$ of the dispersive chain, due to the first term of $\mathcal{H}_{n,diam.}'^{int}$ in Eq. (6.5). These potentials act as impurities that either attract or repel the wavefunctions, and they induce an asymmetry between the L and R subsystems that lowers the half-chain entanglement entropy.

- Finally, there is a single state with exactly zero entanglement entropy and zero energy

that corresponds to the sub-sector with $\mathcal{P} = -4$, for which all the particles are trapped in a CLS.

The interaction-induced on-site potentials are the origin of the many-body localization transition observed in [126, 393] for the diamond chain with nearest-neighbor interactions and spinless fermions. For spinless fermions, the two-particle tunneling is not present, thus completely decoupling the CLSs from the dispersive chain, and the random on-site potentials cause a transition to a many-body localized phase when the interaction, i.e., the effective disorder, is increased.

Additionally, we plot in Fig. 6.4(a) the sector-restricted Page value (horizontal lines), for each of the sectors with a given total CLS number parity $\mathcal{P}$. The Page value is the average entanglement entropy of a random vector, for which Don N. Page derived an analytical expression for a generic bipartite quantum system [394]. We find the Page value using normalized random vectors $|\psi\rangle$ of the form

$$\langle f \mid \psi \rangle = \frac{\alpha_{f,\psi} + i\beta_{f,\psi}}{\mathcal{N}_{\psi}}, \tag{6.10}$$

where the basis states $|f\rangle$ belong to a particular sub-sector $\mathcal{P}$, $\alpha_{f,\psi}$ and $\beta_{f,\psi}$ are taken from a normal distribution with zero mean, and $\mathcal{N}_{\psi}$ is the normalization constant. The entanglement entropy of each random state is computed by projecting $|\psi\rangle$ onto the full Hilbert space. Then, we compute the average of the entanglement entropy for one thousand random vectors belonging to a particular sub-sector, such that the sector-restricted Page value is given by the average value of the corresponding sub-sectors. Each sector-restricted Page value coincides with the top of each dome [see Fig. 6.4(a)]. In Fig. 6.4(b), we take ten random basis states for each sector and let them evolve through time (in dimensionless units, $\mathcal{J}t$). The evolved wavefunctions are computed numerically using the time-evolution unitary operator defined through the rotated Hamiltonian, Eqs. (6.4) and (6.5). We observe how the average entanglement entropy at which the evolved states saturate is bounded by the corresponding sector-restricted Page value indicated in Fig. 6.4(a). This sub-sector-restricted thermalization induced by the fragmentation of the Hilbert space suggests a violation of the ETH.

Entanglement scaling

In order to further characterize the properties of the different sectors of the Hamiltonian, we compute the scaling of the entanglement entropy S with system size for each of the sectors $\mathcal{P}$. In Fig. 6.5, we plot the average entanglement entropy for the eigenstates of each sector as one increases the number of unit cells of the Hamiltonian $\hat{\mathcal{H}}_2'$ with $N = 3$ particles and $U = \mathcal{J} = 1$. The eigenstates of each sector are identified by diagonalizing the system in the rotated basis, applying the $\hat{\mathcal{P}}$ operator to the rotated basis states, and determining the sector from the amplitudes of each eigenstate. The sectors $\mathcal{P} = 3$ and $\mathcal{P} = 1$ exhibit logarithmic entanglement growth, thus demonstrating subthermal behavior within each sector [95, 395]. However, the growth rate of both sectors is different, as most basis states in sector $\mathcal{P} = 3$ contain three particles in the dispersive chain while none are trapped in a CLS. In contrast,
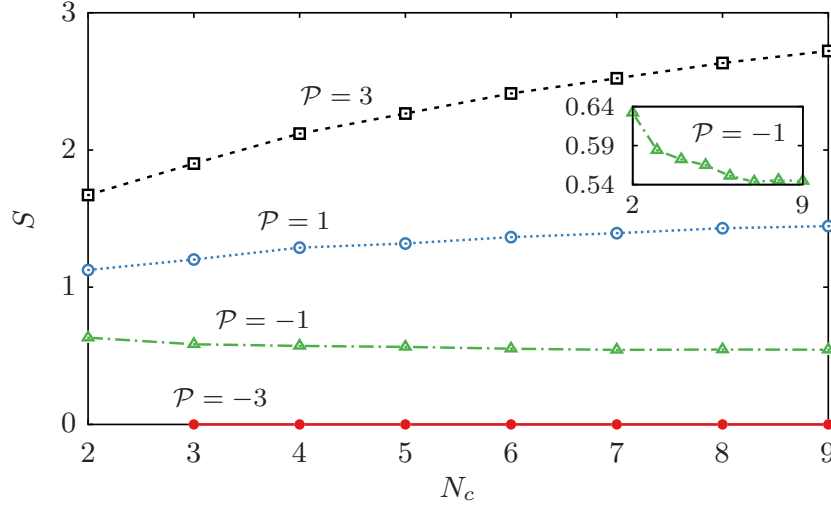
Figure 6.5: Average entanglement entropy for each sector $\mathcal{P}$ as a function of the number of unit cells N_c for $\hat{\mathcal{H}}_2'$ with $N = 3$ particles and $U = \mathcal{J} = 1$. The inset shows sector $\mathcal{P} = -1$. The lines are represented as a guide to the eye.

most basis states in sector $\mathcal{P} = 1$ only have two particles in a dispersive state while one is trapped in a CLS. Both sectors present a logarithmic growth of the form $S = \sigma \ln(N_c) + \upsilon$ with $\{\sigma = 0.708 \pm 0.016, \upsilon = 1.148 \pm 0.027\}$ for $\mathcal{P} = 3$ and $\{\sigma = 0.217 \pm 0.006, \upsilon = 0.973 \pm 0.010\}$ for $\mathcal{P} = 1$.

The sector $\mathcal{P} = -1$ corresponds to the effectively single-particle sub-sectors, for which one observes a surprising slight decrease in the entanglement entropy as the size of the system increases (see inset in Fig. 6.5). This is due to the on-site potential terms that arise in the dispersive chain reflecting the presence of one particle in $|A_k\rangle$ and one in $|S_k\rangle$. Any left-right subsystem asymmetries in the location of the two nodes of the adjacency graph with an on-site potential will lower the entanglement entropy. For $N_c = 2$, there is a single sub-sector where the two basis states that have an on-site potential fall in opposite subsystems L and R. As the size of the system increases, more CLSs are available and thus there are more sub-sectors where there is some asymmetry in the location of the on-site potential (e.g., the two potentials may fall in the same subsystem L or R). Thus, the average entanglement entropy of the sector $\mathcal{P} = -1$ slightly decreases with system size. The decrease is more pronounced for small numbers of unit cells, and it seems to tend to an asymptotic value. This constitutes an anti-volume correction that should also play a role in sectors $\mathcal{P} = 1, 3$, though it is not noticeable there as the logarithm term dominates.

The sector with $\mathcal{P} = -3$ includes the one-dimensional sub-sectors where all the particles are trapped in a CLS. This sector follows an area law scaling, which in one dimension corresponds to a constant value. As a particle in a CLS does not contribute to the entanglement entropy, the average entanglement entropy for these sub-sectors is zero for any system size. For this sector, the diagonalization of the full Hilbert space results in a series of degenerate states that correspond to the different CLSs that the three particles can occupy. Then, the

entanglement entropy obtained through this method is higher than the one shown in Fig. 6.5, as it corresponds to an arbitrary numerical superposition of those states. Consequently, one should compute the entanglement entropy of this sector in the rotated basis analytically. Note that this sector does not exist for $N_c = 2$ unit cells: as the number of particles is $N = 3$, one particle will always occupy the linear chain.

These results demonstrate that the system exhibits weak thermalization with respect to the full Hilbert space through its fragmentation, while also exhibiting subthermal behavior within each non-integrable sector.

Model comparison and boundary conditions

In this subsection, we analyze the effect that the number of central sites of the lattice has in the distribution of entanglement entropies by comparing the different models of the family of diamond necklaces. Fig. 6.6 shows the distributions of entanglement entropies and the adjacency graphs of different models for $N = 4$ particles in $N_c = 4$ unit cells and $U = \mathcal{J} = 1$. The represented models are: (a,e) $\hat{\mathcal{H}}'_1$, (b,f) $\hat{\mathcal{H}}'_2$, (c,g) $\hat{\mathcal{H}}'_3$, (d,h) $\hat{\mathcal{H}}'_4$. The subplots in the left column show the normalized entanglement entropy $\tilde{S}$ for each eigenstate as a function of the energy. The color indicates the density of data points. The subplots in the center column represent the density of data points η as a function of $\tilde{S}$ for the eigenstates around $E = 0$. To obtain a clear picture, we take the eigenstates whose energy fulfills $-|E_0| \cdot 0.2 < E < |E_0| \cdot 0.2$, where E_0 is the ground-state energy, and normalize the density η to 1. The plots in the right column show the second and third largest sub-sectors in the adjacency graph of the rotated Hamiltonian. The color of the nodes indicates the total number of particles that occupy a CLS, as given by $N_{CLS}|f\rangle = \sum_k \hat{n}_{a,k}|f\rangle$.

We see how increasing the number of central sites in the lattice, going from $\hat{\mathcal{H}}'_1$ to $\hat{\mathcal{H}}'_4$, increases the visibility of the different domes. This can be understood in terms of the adjacency graphs of the different models. In Figs. 6.6(e-h), most of the basis states of the bottom sub-sectors have two particles in different CLSs, in purple, although there are some special basis states, in yellow, where an additional pair of particles also occupies a CLS. A similar pattern occurs in the top sub-sectors, for which most basis states have one-particle in a CLS, in green, while some have three particles occupying CLSs, in red. These special basis states appear due to the two-particle tunneling term in the rotated Hamiltonian of Eq. (6.5), and thus are present in all sectors except for the integrable ones. The eigenstates that have some weight on those basis states will have a lower entanglement entropy than those that do not, and they might fall below the dome of the sub-sector, thus obscuring the visibility of the nested-dome pattern. When one increases the number of central sites in the lattice, these special basis states become more sparse compared to the main basis states, which have a lower number of particles in a CLS [see Figs. 6.6(e-h)]. Therefore, the visibility of the nested-dome structure in the distribution of entanglement entropies can be enhanced by increasing the sparsity of the CLSs. This, in turn, increases the sparsity of the special basis states with a higher number of particles in a CLS due to the two-particle tunneling.

Let us consider what would occur for different numbers of particles. For each particle added with respect to a fixed number of unit cells, an extra dome appears on top and one
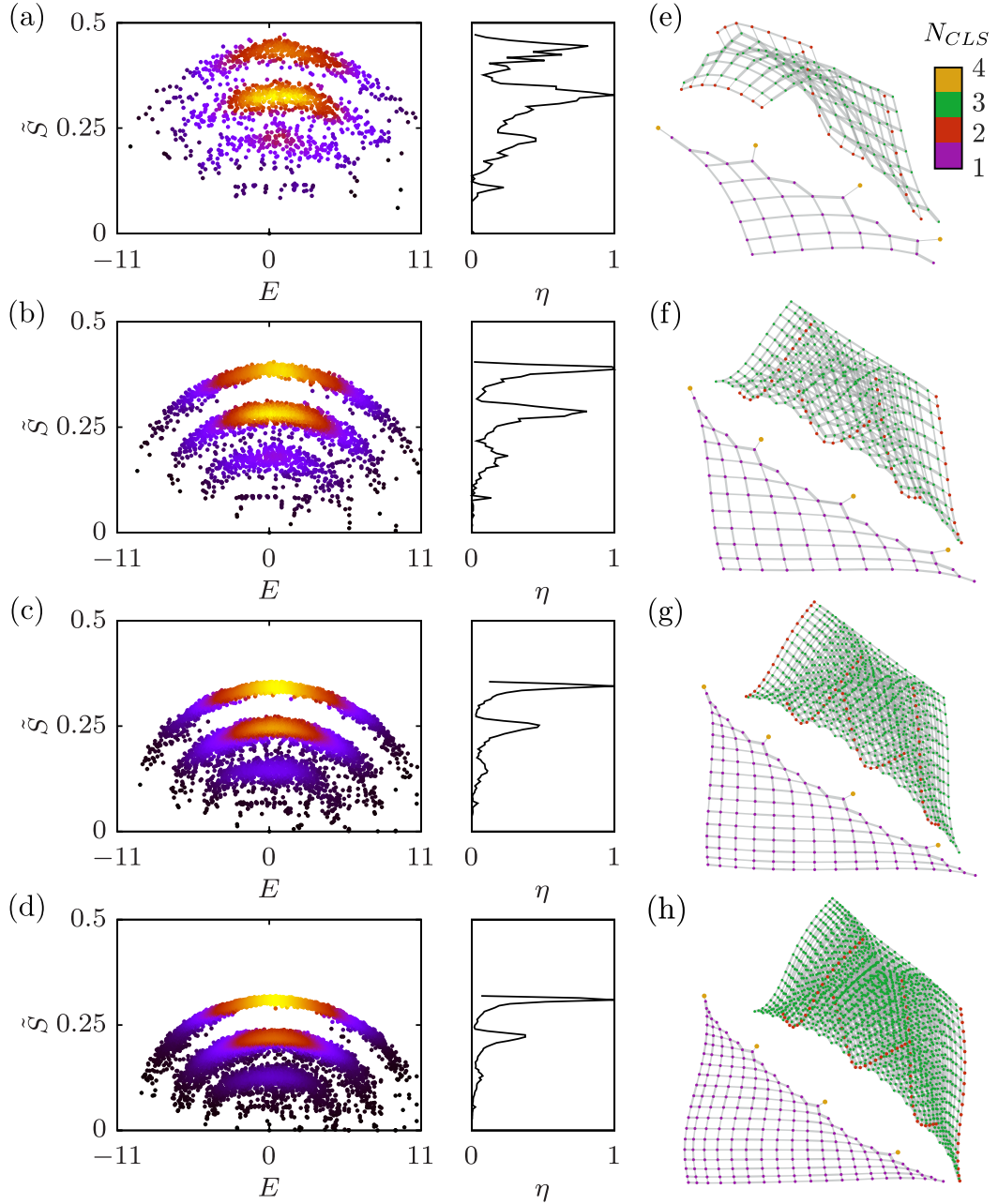
Figure 6.6: Distribution of entanglement entropies and adjacency graphs for $N = 4$ particles in $N_c = 4$ unit cells and $U = \mathcal{J} = 1$ for the following models: (a,e) $\hat{\mathcal{H}}'_1$, (b,f) $\hat{\mathcal{H}}'_2$, (c,g) $\hat{\mathcal{H}}'_3$, (d,h) $\hat{\mathcal{H}}'_4$. (a-d) Left plots: normalized entanglement entropy $\tilde{S}$ as a function of the energy, where color represents the density of data points. (a-d) Center plots: normalized density of data points as a function of $\tilde{S}$ for the middle region of the spectrum, $-|E_0| \cdot 0.2 < E < |E_0| \cdot 0.2$. Plots (e-h): second and third largest sub-sectors in the adjacency graphs of the rotated Hamiltonians with the color of the nodes indicating the total number of particles occupying a CLS, N_{CLS}.

dome (or sector) is removed from below. For example, for $N = 5$ and $N_c = 4$ unit cells, the frozen sub-sector is unavailable. However, the number of domes for $N \geq N_c$ is conserved, as it corresponds to the number of sectors. As one increases the number of particles, there is a global shift to the right in the distribution of entanglement entropies, which corresponds to an increased energy of the eigenstates due to the repulsive interaction. For each particle removed, keeping the number of unit cells fixed, the upper dome disappears, as there are less particles populating the dispersive chain. Additionally, the frozen sub-sectors multiply, due to the different CLSs that the particles can occupy, and become degenerate.

Up to now, we have assumed open boundary conditions, however, this analysis also holds for periodic boundary conditions. The visibility of the domes when one introduces periodic boundary conditions is notably worse than for open boundary conditions. This is due to the fact that periodic boundary conditions make the system translation invariant, which introduces degeneracies in the spectrum between sub-sectors belonging to the same sector. As a result, one numerically finds arbitrary superpositions of the degenerate eigenstates which have arbitrary entanglement entropies. The cause of the deteriorated visibility can be corroborated by introducing vertical couplings between the U and D sites of each diamond and making their strength different for each unit cell. In that case, although the system still has periodic boundary conditions, it is no longer translation invariant, and the visibility of the domes is restored.

In the second part of this chapter, we will consider arbitrary flat-band lattices in order to determine if this instance of local Hilbert space fragmentation is a broader phenomenon. In particular, we will concentrate in a class of flat-band lattices that exhibit commutative local symmetries and we will explore the effect of both on-site and nearest-neighbor bosonic interactions.

6.2   Arbitrary flat-band lattices

6.2.1   Commutative local symmetries

Let us consider the real symmetric matrix associated with a time-reversal invariant and Hermitian Hamiltonian $\hat{\mathcal{H}}$. One might interpret this matrix as an adjacency matrix representing an undirected weighted graph that might contain loops. The vertices of such a graph represent the basis states of the Hamiltonian, while the edges are the adjacency relations between the vertices, i.e., the non-zero matrix elements of $\hat{\mathcal{H}}$. Graphs might present automorphisms, permutations of vertices such that the adjacency relations of the associated matrix are left invariant. Let us take for example a single unit cell of the diamond chain, shown in black in Fig. 6.7(a), where we have numbered the vertices as 1, 2, and 3. The permutation of the vertices (or sites) 2 and 3 leaves the graph invariant. This automorphism can be represented as a permutation that in cyclic notation reads as follows

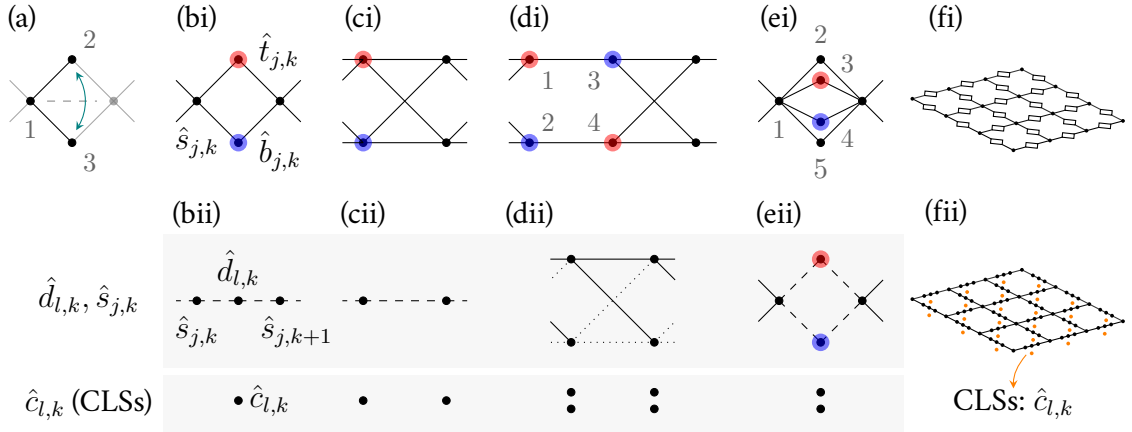$$\mathcal{S} = (1)(2, 3), \tag{6.11}$$

Figure 6.7: (a) Adjacency graph exhibiting a commutative local symmetry $\mathcal{S} = (1)(2, 3)$ which corresponds to a local reflection of the sites 2 and 3, where the sites of a unit cell are shown in black. (i) Examples of flat-band lattices with underlying basic commutative local symmetries of order two and (ii) their rotated models composed of dispersive states and spinal sites (top row) and CLSs decoupled at the single-particle level (bottom row). (b) Diamond chain, (c) Creutz ladder, (d) 1D Pyrochlore chain, (e) double diamond chain (f) 2D diamond necklace lattice. Examples of CLSs for the lattices (b-e) are given in color, with the radius representing the amplitude and the color representing the phase, where red is a π phase and blue is a phase zero. We also indicate the annihilation operators associated with the spinal, top, bottom, dispersive, and CLS sites for a given unit cell k.

where each parenthesis indicates an *orbit* whose size is the number of elements it contains. An orbit of size 1 is called a trivial orbit, as it leaves its element unchanged. A permutation $\mathcal{S}$ can also be represented in matrix form $\Pi_{\mathcal{S}}$, which in the above example would read, in the ordered $\{|1\rangle, |2\rangle, |3\rangle\}$ basis,

$$\Pi_{\mathcal{S}} = \begin{pmatrix} 1 & 0 & 0 \\ 0 & 0 & 1 \\ 0 & 1 & 0 \end{pmatrix}. \tag{6.12}$$

One might consider an enlarged Hamiltonian by taking the black sites that form a diamond in Fig. 6.7(a) as a unit cell and constructing a lattice from it [Fig. 6.7(a) including the gray sites and couplings]. We will adopt the definition of a *commutative local symmetry* of a Hamiltonian $\hat{\mathcal{H}}$ proposed in [358] as a permutation symmetry $\mathcal{S}$ that fulfills

$$\hat{\mathcal{H}}_{p,q} = \hat{\mathcal{H}}_{\mathcal{S}(p),\mathcal{S}(q)} \,\forall p, q \quad \Longleftrightarrow \quad [\hat{\mathcal{H}}, \Pi_{\mathcal{S}}] = 0. \tag{6.13}$$

A commutative local symmetry is *basic* and of order o if all the non-trivial orbits of $\mathcal{S}$ have the same size o. For basic commutative local symmetries of order two, the permutation matrix fulfills $\Pi_{\mathcal{S}}^2 = \mathbb{I}$. Then, if $\mathcal{S}$ is a commutative local symmetry, the eigenstates of $\hat{\mathcal{H}}$ are also eigenstates of $\Pi_{\mathcal{S}}$ and have a well-defined parity ± 1 with respect to this symmetry.

The equitable partition theorem (EPT) provides a symmetry-induced decomposition of a matrix associated with a graph exhibiting an automorphism into a direct sum of smaller matri-

ces that determine its spectrum and eigenstates [181]. It was originally stated for unweighted graphs, which can be represented by unweighted adjacency matrices, but was later generalized to complex square matrices, thus representing generic Hamiltonians [355, 357]. There are two consequences of the EPT that are of interest here. The EPT states that a system with a commutative local symmetry has two classes of eigenstates: eigenstates that are symmetric under the action of $\mathcal{S}$ and eigenstates that are not symmetric and that have support only on the permuted sites [355, 356]. Therefore, the EPT ensures the presence of one or more CLSs (depending on the geometry of the Hamiltonian). If the commutative local symmetry $\mathcal{S}$ is basic and of order two, these CLSs will have a well-defined negative parity while all the other states will have a positive parity. Such a permutation can be interpreted visually as a local reflection symmetry with respect to an axis in the adjacency graph of the Hamiltonian [as shown in Fig. 6.7(a) for the diamond chain]. This interpretation depends on the depiction of the Hamiltonian as a graph but provides an intuitive picture of the destructive interference mechanism that generates the CLSs.

In this section, we will consider lattice models exhibiting CLSs that stem from commutative local symmetries of order two in each unit cell. We represent an arbitrary lattice model with n sites per unit cell as a set of pairs of sites, that we call top and bottom and form a rung. These make explicit the permutation symmetries of the Hamiltonian as a local y-reflection symmetry in the Hamiltonian graph. Additionally, each unit cell may present spinal sites that remain invariant under the reflection. Our lattice will have $n = n_1 + n_2$ sites per unit cell, where n_1 is the number of spinal sites, with associated annihilation operators $\hat{s}_{j,k}$ ($j = 1, ..., n_1$), and n_2 is the number of top and bottom sites, with annihilation operators $\hat{t}_{j,k}$ and $\hat{b}_{j,k}$ ($j = 1, ..., n_2/2$), respectively. The EPT theorem ensures that such a system presents $n_2/2$ negative-parity CLSs that have support only on the top and bottom sites. Some examples of lattices containing this class of CLSs and an example of their CLSs are given in the top row of Fig. 6.7: (bi) diamond chain (a diamond necklace, studied in Sec. 6.1, with zero spinal sites), (ci) Creutz ladder, (di) one-dimensional (1D) Pyrochlore chain, (ei) double diamond chain (fi) two-dimensional (2D) diamond necklace lattice. Note that while some of these lattices [(ai) and (bi)] present one CLS per unit cell, the 1D Pyrochlore chain presents two and the double diamond chain presents three. Also, the double diamond chain can be recast into a top-bottom configuration by reordering the sites. Other examples not depicted in Fig. 6.7 include the square root versions of the diamond chain [386] or the 2D Creutz ladder [390].

6.2.2 Hilbert space fragmentation

One can also classify CLSs phenomenologically in terms of the number of unit cells that they occupy. In many lattice models, CLSs extending to more than a single unit cell appear as a consequence of inserting a finite magnetic flux per plaquette [147, 153, 327, 336, 396]. In these models, adjacent CLSs of a flat band have spatial overlap, which can be used to generate interaction-driven dynamics [330] and topological effects [150, 397] in many-body systems. CLSs that occupy a single unit cell can form an orthogonal basis that allows one to detangle each CLSs at the single-particle level [123]. For CLSs with underlying commutative local

symmetries, this is ensured by the EPT theorem, which restricts the support of the CLSs to the permuted sites. Thus, there is no overlap with the CLSs in adjacent unit cells and they can form an orthogonal basis. Negative parity CLSs, those with an associated basic commutative local symmetry $\mathcal{S}$ of order two, constitute a new basis that is completed by their symmetric counterparts. The corresponding annihilation operators are

$$\hat{c}_{l,k} = \sum_{j=1}^{n_2/2} \alpha_{j,k}^l \left(\hat{t}_{j,k} - \hat{b}_{j,k} \right), \ \ \hat{d}_{l,k} = \sum_{j=1}^{n_2/2} \alpha_{j,k}^l \left(\hat{t}_{j,k} + \hat{b}_{j,k} \right), \tag{6.14}$$

where k labels the unit cell, j labels the rung, and the coefficients $\alpha_{j,k}^l$ determine the amplitudes at each rung for each CLS and dispersive state $l = 1, ..., n_2/2$ in unit cell k. In this basis, the CLSs become decoupled at the single-particle level while the symmetric states, which we refer to as dispersive states, remain coupled and compose a dispersive chain supporting extended states. In our notation, the dispersive chain can also include spinal sites, which remain invariant under this rotation. Figures 6.7(ii) represent the rotated models of the (bii) diamond chain, (cii) Creutz ladder, (dii) 1D Pyrochlore chain, (eii) double diamond chain, and (fii) 2D diamond necklace lattice. Each model presents one or more decoupled CLSs for each unit cell.

The many-body Hamiltonian includes the independent-particle Hamiltonian and the interaction Hamiltonian, $\hat{\mathcal{H}} = \hat{\mathcal{H}}^0 + \hat{\mathcal{H}}^{int}$. The term $\hat{\mathcal{H}}^0$ can be written as a sum of local operators in each unit cell $\hat{\mathcal{H}}^0 = \mathcal{J} \sum_k \hat{f}_k$, where the operators $\hat{f}_k$ include particle-conserving products of the operators $\hat{\nu}_{j,k}$, with $\nu = t, b, s$. We consider the addition of on-site bosonic interactions of the form $\hat{n}_{\nu_{j,k}}(\hat{n}_{\nu_{j,k}} - 1)$, where $\hat{n}_{\nu_{j,k}} = \hat{\nu}_{j,k}^\dagger \hat{\nu}_{j,k}$, are the number operators at each site. The interaction Hamiltonian at the top and bottom sites can be written as

$$\hat{\mathcal{H}}_{t,b}^{int} = \frac{U}{2} \sum_k \sum_{j=1}^{n_2/2} \left[\hat{t}_{j,k}^\dagger \hat{t}_{j,k}^\dagger \hat{t}_{j,k} \hat{t}_{j,k} + \hat{b}_{j,k}^\dagger \hat{b}_{j,k}^\dagger \hat{b}_{j,k} \hat{b}_{j,k} \right]. \tag{6.15}$$

In Section 6.1 of this chapter, we showed that the parity of the number of particles in each CLS commutes with the Hamiltonian of a diamond necklace or diamond chain [154]. However, the associated conservation quantity remains hidden in the product state basis. We denote the rotated basis using its associated collection of annihilation operators, $\{\hat{c}_{l,k}, \hat{d}_{l,k}\}$, and the product state basis as $\{\hat{t}_{j,k}, \hat{b}_{j,k}\}$. We will show that a similar mechanism occurs for arbitrary flat-band lattices with basic commutative local symmetries of order two, which may have more than one CLS per unit cell. In this general case, we postulate that the conserved quantity is the parity of the number of particles *in all CLSs of a unit cell*. Thus, the operator

$$\hat{\mathcal{P}}_k = e^{i\pi \sum_{l=1}^{n_2/2} \hat{n}_{c_{l,k}}} \tag{6.16}$$

commutes with the Hamiltonian, $[\hat{\mathcal{P}}_k, \hat{\mathcal{H}}'] = 0$, where $\hat{\mathcal{H}}'$ is the total Hamiltonian in the rotated basis, $\hat{n}_{c_{l,k}} = \hat{c}_{l,k}^\dagger \hat{c}_{l,k}$, and $n_2/2$ is the number of CLSs in each unit cell. This conservation law leads to the fragmentation of the Hilbert space in the rotated or entangled basis, while it

remains hidden in the product-state basis. Therefore, this is again an instance of quantum Hilbert space fragmentation, as discussed in Section 6.1.3.

Given that the CLSs only have support on the top and bottom sites, the spinal part of the interaction Hamiltonian trivially commutes with $\hat{\mathcal{P}}_k$. The rotated interaction Hamiltonian on the top and bottom sites can be obtained by expressing the top and bottom operators in terms of CLSs and dispersive operators [Eq. (6.14)]. Due to the periodicity of the lattice, it is enough to consider a single unit cell k. Thus, we omit the unit cell index k in the demonstration, for ease of reading. The reduced interaction Hamiltonian in the rotated basis reads

$$\hat{\mathcal{H}}_{t,b}^{int\prime} = \frac{U}{2} \sum_{\hat{\rho},\hat{\sigma},\hat{\tau},\hat{v}} \sum_{\{l_i\}=1}^{n_2/2} \left(\Theta_{\hat{\rho},\hat{\sigma},\hat{\tau},\hat{v}}^{l_1,l_2,l_3,l_4} \right) \hat{\rho}_{l_1}^\dagger \hat{\sigma}_{l_2}^\dagger \hat{\tau}_{l_3} \hat{v}_{l_4}, \tag{6.17}$$

where $\{\hat{\rho}, \hat{\sigma}, \hat{\tau}, \hat{v}\} = \{\hat{c}, \hat{d}\}$ are the annihilation operators of either a CLS or a dispersive state, respectively, $\{l_i\} = 1, ..., n_2/2$ are the CLS and dispersive state indices (with $i = 1, 2, 3, 4$), and $\Theta_{\hat{\rho},\hat{\sigma},\hat{\tau},\hat{v}}^{l_1,l_2,l_3,l_4}$ are the coefficients of each term. Only those terms with an odd number of $\hat{c}_l^{(\dagger)}$ and of $\hat{d}_l^{(\dagger)}$ operators do not commute with $\hat{\mathcal{P}}_k$. Those terms, e.g., $\hat{c}_{l_1}^\dagger \hat{d}_{l_2}^\dagger \hat{d}_{l_3} \hat{d}_{l_4}$, exchange one particle between the CLSs and the dispersive states, thus violating parity. Then, it is enough to prove that the coefficient $\Theta_{\hat{\rho},\hat{\sigma},\hat{\tau},\hat{v}}^{l_1,l_2,l_3,l_4}$ vanishes for terms of this form.

The rotation matrix from the product-state basis $\{\hat{t}_j, \hat{b}_j\}$ to the rotated basis $\{\hat{c}_l, \hat{d}_l\}$ in each unit cell can be written as a Kronecker product $\mathcal{K} = \mathcal{L} \otimes \mathcal{M}$, with

$$\mathcal{L} = \begin{pmatrix} \alpha_1^1 & \alpha_2^1 \\ \alpha_1^2 & \alpha_2^2 & \cdots \\ & \vdots & \ddots \end{pmatrix} \qquad \text{and} \qquad \mathcal{M} = \begin{pmatrix} 1 & 1 \\ -1 & 1 \end{pmatrix}. \tag{6.18}$$

where we have ordered the basis as $\{\hat{b}_1, \hat{t}_1, \hat{b}_2, \hat{t}_2, ...\}$ and $\{\hat{d}_1, \hat{c}_1, \hat{d}_2, \hat{c}_2, ...\}$, and made use of Eq. (6.14). The inverse of matrix $\mathcal{K}$ is $\mathcal{K}^{-1} = (\mathcal{L} \otimes \mathcal{M})^{-1} = \mathcal{L}^{-1} \otimes \mathcal{M}^{-1}$, and indicates the expressions of $\{\hat{t}_j, \hat{b}_j\}$ in terms of $\{\hat{c}_l, \hat{d}_l\}$. By writing $\mathcal{L}^{-1}$ as an arbitrary matrix, $\mathcal{K}^{-1}$ takes the following general form

$$\mathcal{K}^{-1} = \begin{pmatrix} \beta_1^1 & -\beta_1^1 & \beta_2^1 & -\beta_2^1 \\ \beta_1^1 & \beta_1^1 & \beta_2^1 & \beta_2^1 \\ \beta_1^2 & -\beta_1^2 & \beta_2^2 & -\beta_2^2 \\ \beta_1^2 & \beta_1^2 & \beta_2^2 & \beta_2^2 & \cdots \\ & & & \vdots & \ddots \end{pmatrix}. \tag{6.19}$$

Thus, one can express the annihilation operators $\hat{t}_j$ and $\hat{b}_j$ in terms of $\hat{c}_l$ and $\hat{d}_l$

$$\hat{t}_{j,k} = \sum_{l=1}^{n_2/2} \beta_{l,k}^j \left(\hat{d}_{l,k} + \hat{c}_{l,k} \right), \quad \hat{b}_{j,k} = \sum_{l=1}^{n_2/2} \beta_{l,k}^j \left(\hat{d}_{l,k} - \hat{c}_{l,k} \right). \tag{6.20}$$

Then, the coefficient $\Theta^{l_1,l_2,l_3,l_4}_{\hat{\rho},\hat{\sigma},\hat{\tau},\hat{\upsilon}}$ for the terms containing an odd number of CLS and dispersive operators takes two forms: (i) for the terms with one CLS operator and three dispersive state operators and (ii) for the terms with three CLS operators and one dispersive state operator. These two terms are

$$
\begin{aligned}
(i) \quad & \sum_{j=1}^{n_2/2} \left[\beta^j_r \beta^j_m \beta^j_p \beta^j_o + (-\beta^j_r)\beta^j_m \beta^j_p \beta^j_o \right] = 0, \\
(ii) \quad & \sum_{j=1}^{n_2/2} \left[\beta^j_r \beta^j_m \beta^j_p \beta^j_o + \beta^j_r(-\beta^j_m)(-\beta^j_p)(-\beta^j_o) \right] = 0.
\end{aligned}
\tag{6.21}
$$

For both cases, it vanishes at each rung j. As all the other terms commute with $\hat{\mathcal{P}}_k$, the parity of the number of particles in all the CLSs in a unit cell is conserved. The only terms in the rotated Hamiltonian that produce a particle exchange between the CLSs and the dispersive states are of the form $\hat{d}^\dagger_{l_1,k}\hat{d}^\dagger_{l_2,k}\hat{c}_{l_3,k}\hat{c}_{l_4,k}$ and $\hat{c}^\dagger_{l_1,k}\hat{c}^\dagger_{l_2,k}\hat{d}_{l_3,k}\hat{d}_{l_4,k}$. These denote a two-particle tunneling between CLSs and dispersive states that preserves $\hat{\mathcal{P}}_k$. This mechanism is a direct consequence of the commutative local symmetry of these lattices: the well-defined parities of the eigenstates determine the structure of the basis states (6.14) which in turn determines the form of $\mathcal{M}^{-1}$. Note that this result is not restricted to one dimension, as the underlying permutations can exchange sites in any axis [see Fig. 6.7(f)].

As the operator $\hat{\mathcal{P}}_k$ in each unit cell k commutes with the rotated Hamiltonian $\hat{\mathcal{H}}'$, one can also define the total CLS number parity as $\hat{\mathcal{P}} = \sum_k \hat{\mathcal{P}}_k$, which also commutes with $\hat{\mathcal{H}}'$. As in the diamond necklace of Sec. 6.1, the rotated Hamiltonian is composed of a series of sectors defined by the eigenvalues of $\hat{\mathcal{P}}$ and within those, one or more sub-sectors determined by the eigenvalues of $\hat{\mathcal{P}}_k$. The eigenvalues of $\hat{\mathcal{P}}$ and $\hat{\mathcal{P}}_k$ are given in Table 6.1 as well as the number of sectors and sub-sectors in terms of the number of particles N and the number of unit cells N_c. The number of sub-sectors grows exponentially with system size, signaling Hilbert space fragmentation [249], while the locality of the conservation law, $[\hat{\mathcal{P}}_k, \hat{\mathcal{H}}'] = 0$, indicates that this mechanism produces local Hilbert space fragmentation [250].

We measure the degree of fragmentation by calculating the ratio of the dimension of the largest sector of the Hilbert space to the total dimension of the space [110]. For this general class of models, the dimension of the largest sub-sector is

$$
\mathscr{D}_{max} = \sum_{\varrho=0}^{\lfloor \frac{N}{2} \rfloor} \left[\binom{(n_1 + \frac{n_2}{2})N_c + N - 2\varrho - 1}{N - 2\varrho} \cdot \sum_{(\delta_1,...,\delta_{N_c}) \in \mathcal{Q}} \prod_{k=1}^{N_c} \binom{\frac{n_2}{2} + 2\delta_k - 1}{2\delta_k} \right],
\tag{6.22}
$$

where the indices ϱ and δ_k count the number of pairs of particles that populate the CLSs, in total and for a unit cell k, respectively, N is the number of particles, and the set $\mathcal{Q}$ fulfills $\mathcal{Q}(\varrho, N_c) = \{(\delta_1,...,\delta_{N_c}) | \varrho = \delta_1 + \delta_2 + ... + \delta_{N_c}\}$. Then, using the dimension of the full Hilbert space, Eq. (6.8), the ratio $\mathscr{D}_{max}/\mathscr{D}$ tends to zero at the thermodynamic limit, indicating strong Hilbert space fragmentation.

	No. sectors and sub-sectors	
Eigenvalue	$N > N_c$	$N \leq N_c$
$\mathcal{P}_k = \pm 1$	2^{N_c}	$\sum_{k=0}^{N-1} \binom{N_c}{k} + \binom{N_c}{N}(\frac{n_2}{2})^N$
$\mathcal{P} = -N_c, -N_c + 2, ..., N_c$	$N_c + 1$	$N + 1$

Table 6.1: Eigenvalues of the local, $\hat{\mathcal{P}}_k$, and total, $\hat{\mathcal{P}}$, parities, and number of associated sub-sectors, $\mathcal{P}_k$ and sectors $\mathcal{P}$ for a number of particles N larger, equal, or smaller than the number of unit cells N_c.

Let us consider some examples. For the class of models with only one CLSs per unit cell [Fig. 6.7(bi) diamond chain and (ci) Creutz ladder], the conserved quantity simplifies to $\hat{\mathcal{P}}_k = e^{i\pi\hat{n}_{c_k}}$, in agreement with the analysis of the diamond necklace of Sec. 6.1. The double diamond chain, Fig. 6.7(ei), is an unusual example, it presents multiple commutative local symmetries of order two, such as

$$\begin{aligned} \mathcal{S}_1 &= (1)(4)(5)(2,3), \quad \mathcal{S}_2 = (1)(2)(3)(4,5), \\ \mathcal{S}_3 &= (1)(2)(5)(3,4), \quad \mathcal{S}_4 = (1)(2)(4)(3,5). \end{aligned} \quad (6.23)$$

Taking for example $\mathcal{S}_1$ and $\mathcal{S}_2$, these are *independent* commutative local symmetries that lead to non-overlapping CLSs and thus to independently conserved quantities. However, after decoupling these CLSs the dispersive lattice still presents an unresolved local symmetry [see Fig. 6.7(eii)]. The third CLS occupies all diamond sites in Fig. 6.7(ei) and corresponds to the permutation $\mathcal{S} = (1)(2,5)(3,4)$. One can perform a second rotation to decouple this state at the single-particle level. However, the third CLS will not be decoupled from the dispersive chain at the many-body level due to the presence of interaction-induced one-particle tunnelings between the dispersive chain and the CLS. In contrast, the 1D Pyrochlore chain presents the symmetry $\mathcal{S} = (1,2)(3,4)$ [see Fig. 6.7(di)], which cannot be decomposed into two independent permutations. As a consequence, it presents two overlapping CLSs per unit cell that lead to a single conserved quantity $\hat{\mathcal{P}}_k = e^{i\pi(\hat{n}_{c_{1,k}} + \hat{n}_{c_{2,k}})}$. Therefore, each independent local reflection symmetry with an underlying basic commutative local symmetry $\mathcal{S}$ of order two leads to a conserved quantity. These require a single rotation to detangle the associated CLSs and thus lead to the conservation of parity and fragmentation. Some lattices, such as the double diamond chain, might present more than one independent local symmetry per unit cell, which leads to a multiplicity of conserved quantities. For example, one might create an enlarged unit cell by uniting Creutz and 1D Pyrochlore unit cells, which will lead to two independent sets of conserved quantities per unit cell.

6.2.3 Long-range interactions

Let us consider how the block-diagonal structure of the Hamiltonian is affected by the presence of long-range interactions. There are mainly three classes of long-range interaction terms for

a 1D system. Considering interactions that respect the y-reflection symmetry of the system, these read

$$(i)\ \hat{\mathcal{H}}_1^{int} = \sum_{k,k'} \sum_{j,j'} \xi_{k,k'}^{j,j'} \left(\hat{n}_{s_{j,k}} \hat{n}_{t_{j',k'}} + \hat{n}_{s_{j,k}} \hat{n}_{b_{j',k'}} \right),$$

$$(ii)\ \hat{\mathcal{H}}_2^{int} = \sum_{k} \sum_{j} \vartheta_j \hat{n}_{t_{j,k}} \hat{n}_{b_{j,k}}, \tag{6.24}$$

$$(iii)\ \hat{\mathcal{H}}_3^{int} = \sum_{k,k'} \sum_{j,j'} \Omega_{k,k'}^{j,j'} \left(\hat{n}_{t_{j,k}} \hat{n}_{t_{j',k'}} + \hat{n}_{t_{j,k}} \hat{n}_{b_{j',k'}} + \hat{n}_{b_{j,k}} \hat{n}_{t_{j',k'}} + \hat{n}_{b_{j,k}} \hat{n}_{b_{j',k'}} \right).$$

In term (iii), we have assumed that the cross terms, e.g., $\hat{n}_{t_{j,k}} \hat{n}_{b_{j',k'}}$, have the same strength than the horizontal terms, e.g., $\hat{n}_{t_{j,k}} \hat{n}_{t_{j',k'}}$. There can also be interactions between spinal sites, which remain invariant under the basis rotation and thus preserve fragmentation. In order to understand the effect of these terms, we can write them in the rotated basis determined by the annihilation operators $\hat{\tilde{c}}_{j,k} = \left(\hat{t}_{j,k} - \hat{b}_{j,k} \right)/\sqrt{2}$, and $\hat{\tilde{d}}_{j,k} = \left(\hat{t}_{j,k} + \hat{b}_{j,k} \right)/\sqrt{2}$. In contrast with the basis considered before [see Eq. (6.14)], the states annihilated by $\hat{\tilde{c}}_{j,k}$ are not eigenstates of the system, i.e., they are not the CLSs, except for the cases of the diamond chain and Creutz ladder, where the CLSs occupy a single rung j [see Fig. 6.7(bi) and (ci) and Eq. (6.3)]. Thus, the CLSs do not generally become decoupled through this rotation. For arbitrary lattices, the antisymmetric states represented by $\hat{\tilde{c}}_{j,k}$ are superpositions of the CLSs of unit cell k, and thus remain coupled between them within a unit cell at the single-particle level. The symmetric states given by $\hat{\tilde{d}}_{j,k}$ form a dispersive chain that is decoupled from the states given by $\hat{\tilde{c}}_{j,k}$. The rotated interaction Hamiltonians in this basis read

$$(i)\ \hat{\mathcal{H}}_1^{int\prime} = \sum_{k,k'} \sum_{j,j'} \xi_{k,k'}^{j,j'} \left(\hat{n}_{\tilde{d}_{j,k}} \hat{n}_{s_{j',k'}} + \hat{n}_{\tilde{c}_{j,k}} \hat{n}_{s_{j',k'}} \right),$$

$$(ii)\ \hat{\mathcal{H}}_2^{int\prime} = \sum_{k} \sum_{j} \frac{\vartheta_j}{4} \left[\hat{n}_{\tilde{d}_{j,k}} (\hat{n}_{\tilde{d}_{j,k}} - 1) + \hat{n}_{\tilde{c}_{j,k}} (\hat{n}_{\tilde{c}_{j,k}} - 1) \right.$$
$$\left. - \hat{\tilde{c}}_{j,k}^{\dagger} \hat{\tilde{c}}_{j,k}^{\dagger} \hat{\tilde{d}}_{j,k} \hat{\tilde{d}}_{j,k} - \hat{\tilde{d}}_{j,k}^{\dagger} \hat{\tilde{d}}_{j,k}^{\dagger} \hat{\tilde{c}}_{j,k} \hat{\tilde{c}}_{j,k} \right], \tag{6.25}$$

$$(iii)\ \hat{\mathcal{H}}_3^{int\prime} = \sum_{k,k'} \sum_{j,j'} \Omega_{k,k'}^{j,j'} \left(\hat{n}_{\tilde{d}_{j,k}} \hat{n}_{\tilde{d}_{j',k'}} + \hat{n}_{\tilde{c}_{j,k}} \hat{n}_{\tilde{c}_{j',k'}} + \hat{n}_{\tilde{d}_{j,k}} \hat{n}_{\tilde{c}_{j',k'}} + \hat{n}_{\tilde{c}_{j,k}} \hat{n}_{\tilde{d}_{j',k'}} \right).$$

The Hamiltonians (i) and (iii) are defined for any distance between the first, k, and second, k', unit cells, and might involve different pairs of rungs j, j'. Thus, they represent not only nearest-neighbor (NN) interactions but arbitrary long-range interactions. These only include density-density interaction terms in the rotated basis. Thus, they conserve the number of particles in all CLSs of a unit cell, as particles are free to move between the states given by $\hat{\tilde{c}}_{j,k}$ of a single unit cell. The Hamiltonian (ii) also includes two particle tunnelings between the states annihilated by $\hat{\tilde{c}}_{j,k}$ and $\hat{\tilde{d}}_{j,k}$, such that only the parity of the number of particles in all CLSs of a unit cell is conserved. Therefore, all these terms preserve the fragmentation of the Hilbert

space and the parity sectors determined by on-site interactions. If one considers the case where there are no on-site interactions and only long-range interactions of the form (i) and (iii), then, the structure of the fragmented Hilbert space changes, as each sub-sector is given by the number of particles in each CLS (not the parity), and the number of sub-sectors proliferates, leading to a stronger fragmentation. As the authors of [332] point out, all density-density interactions invariant under the graph automorphism associated with the local symmetry will preserve fragmentation. In particular, they study the Creutz ladder, diamond chain, and dice lattice with flux. Their formalism can be used to analyze the generic class of flat-band lattices with commutative local symmetries studied here, as we show in Appendix C.1. Similar considerations have been pointed out for the case of all-bands-flat lattices [384].

6.2.4 Example: Pyrochlore lattice

In this section, we numerically study the 1D Pyrochlore chain [Fig. 6.7(di)] as an example of a model with more than one CLS per unit cell. There are two CLSs per unit cell that, together with two dispersive states, form a new basis. The associated annihilation operators are given by

$$\hat{c}_1 = \frac{1}{2}\left(\hat{t}_1 + \hat{t}_2 - \hat{b}_1 - \hat{b}_2\right), \quad \hat{c}_2 = \frac{1}{2}\left(\hat{t}_1 - \hat{t}_2 - \hat{b}_1 + \hat{b}_2\right),$$
$$\hat{d}_1 = \frac{1}{2}\left(\hat{t}_1 + \hat{t}_2 + \hat{b}_1 + \hat{b}_2\right), \quad \hat{d}_2 = \frac{1}{2}\left(\hat{t}_1 - \hat{t}_2 + \hat{b}_1 - \hat{b}_2\right),$$

(6.26)

where we have omitted the unit cell index k. Note that these CLSs occupy two rungs, in contrast to the states defined by $\hat{\tilde{c}}_{j,k}$ in the previous section. The single-particle energies of the CLSs are $E_{c_1} = 1$ and $E_{c_2} = -1$, and thus the states $\hat{\tilde{c}}_{j,k}$ are not eigenstates of the single-particle Hamiltonian. If the CLSs were degenerate, the states given by $\hat{\tilde{c}}_{j,k}$ would also be eigenstates. In this basis, the interaction Hamiltonian contains only terms that commute with $\hat{\mathcal{P}}_k$, thus conserving the parity of the number of particles in the two CLSs, $\hat{\mathcal{P}}_k = e^{i\pi(\hat{n}_{c_1,k} + \hat{n}_{c_2,k})}$. In a unit cell k, it reads

$$\hat{\mathcal{H}}^{int\prime} = U\left[\frac{1}{8}\sum_{l,l'}\left(\hat{d}_l^\dagger \hat{d}_l^\dagger \hat{c}_{l'}\hat{c}_{l'} + \text{H.c.}\right) + \frac{1}{8}\sum_{l,l'}\left(\hat{d}_l^\dagger \hat{d}_l^\dagger \hat{d}_{l'}\hat{d}_{l'} + \hat{c}_l^\dagger \hat{c}_l^\dagger \hat{c}_{l'}\hat{c}_{l'}\right)\right.$$
$$\left. + \frac{1}{2}\left(\hat{n}_{d_1}\hat{n}_{d_2} + \hat{n}_{c_1}\hat{n}_{c_2} + \sum_{l,l'}\hat{n}_{d_l}\hat{n}_{c_{l'}}\right) + \frac{1}{2}\left[\sum_{l,l'}\hat{c}_l^\dagger \hat{d}_{l'}^\dagger \hat{c}_{\bar{l}}\hat{d}_{\bar{l'}} + \left(\hat{c}_1^\dagger \hat{c}_2^\dagger \hat{d}_1\hat{d}_2 + \text{H.c.}\right)\right]\right].$$

(6.27)

where $\bar{l}^{(\prime)}$ indicates the opposite index of $l^{(\prime)}$, i.e., $\bar{l}^{(\prime)} \neq l^{(\prime)}$. The terms include on-site interactions, two-particle tunnelings, and NN interactions in the basis $\{\hat{c}_l, \hat{d}_l\}$. The two-particle tunnelings and NN interactions both include terms between the dispersive states and the CLSs and within these two groups.

Figure 6.8 presents the numerical results for the 1D Pyrochlore chain with $N = 4$ particles in $N_c = 4$ unit cells, with $\mathcal{J} = U = 1$, and open boundary conditions. The lattice starts with the sites hosting the CLSs, presents an integer number of unit cells, and one spinal site [see inset in Fig. 6.8(c)]. Fig. 6.8(a) shows the von Neumann half-chain bipartite entanglement entropy

of each eigenstate as a function of the energy. The horizontal lines are the sector-restricted Page values [see Eq. (6.10)] [394] and we represent the entanglement entropy normalized to the number of sites in the left subsystem, $\tilde{S} = S/\mathcal{N}_L$. The entanglement entropies present a nested-dome structure that can be understood by analyzing the adjacency graph of the many-body Hamiltonian in the rotated basis, shown in Fig. 6.8(b). The eigenstates that compose each dome correspond to a total sector of the Hamiltonian with eigenvalue $\mathcal{P}$, composed of one or more sub-sectors with eigenvalues $\boldsymbol{\mathcal{P}} = (\mathcal{P}_1, \cdots, \mathcal{P}_{N_c})$, where the vector $\boldsymbol{\mathcal{P}}$ contains the eigenvalues of $\hat{\mathcal{P}}_k$ at each unit cell k. The color of the nodes in Fig. 6.8(b) represents the diagonal terms of the rotated Hamiltonian, $\varepsilon = \langle f|\hat{\mathcal{H}}'|f\rangle$, where $|f\rangle$ is a basis state, which highlights that the different sub-sectors of a given sector are not degenerate. The entanglement entropies of the CLSs are exactly zero along several bipartitions of the lattice, one of which coincides with the half-chain cut considered in Fig. 6.8(a). Thus, particles located in a CLS do not contribute to the entanglement entropy of the eigenstates. The two-particle tunneling terms in Eq. (6.27) allow pairs of particles to jump to a CLS. However, those special basis states form a small fraction of the basis states in each sub-sector, and thus the main basis states determine the structure of the entanglement entropies. As a result, the entanglement entropies form the same nested-dome pattern also present in the diamond necklace (Fig. 6.4). The main difference resides in the sector with $\mathcal{P} = -4$, where all particles occupy CLSs in distinct unit cells. There are two single-particle CLSs available [Eq. (6.26)] instead of only one, with energies $E_{c_1} = 1$ and $E_{c_2} = -1$, and thus, the available energies for the frozen states are $\{-4, -2, 0, -2, 4\}$, with degeneracies $\{1, 4, 6, 4, 1\}$. The two non-degenerate states with energies ± 4 have exactly zero entanglement entropy and correspond to the case where all particles populate the same CLS in distinct unit cells. The additional frozen states are degenerate and thus a higher value of $\tilde{S}$ is obtained numerically.

The nested-dome structure of the entanglement entropies is a direct consequence of the fragmentation of the Hilbert space and the low entanglement of the CLSs. Thus, it is generally present in the class of flat-band lattices with commutative local symmetries. However, the distinguishability of the different domes is not guaranteed, as it depends on several factors such as the presence of symmetries, the particle filling, the boundary conditions, and the sparsity of the CLS compared to the dispersive states (see Sec. 6.1.4). Here, the visibility of the domes is enhanced by introducing one spinal site that makes the CLSs more sparse while also breaking the x-reflection symmetry of the model [see inset in Fig. 6.8(c)].

In analogy with the diamond necklace, the Hilbert space of the 1D Pyrochlore chain presents both integrable and non-integrable sub-sectors. The integrable sub-sectors comprise the frozen states and those in sector $\mathcal{P} = -2$, for which only one particle is free to move in the dispersive chain, thus forming an effective single-particle model. All the other sub-sectors are non-integrable, as they present Wigner-Dyson statistics (numerical evidence is given in Appendix C.2). Figure 6.8(c) shows the evolution of the average entanglement entropy for 20 random initial states belonging to particular sectors. The entanglement entropy grows for all cases while remaining bounded by the sector-restricted Page value indicated in Fig. 6.8(a). This is a direct consequence of the fragmentation of the Hilbert space, which restricts thermalization within each sub-sector.
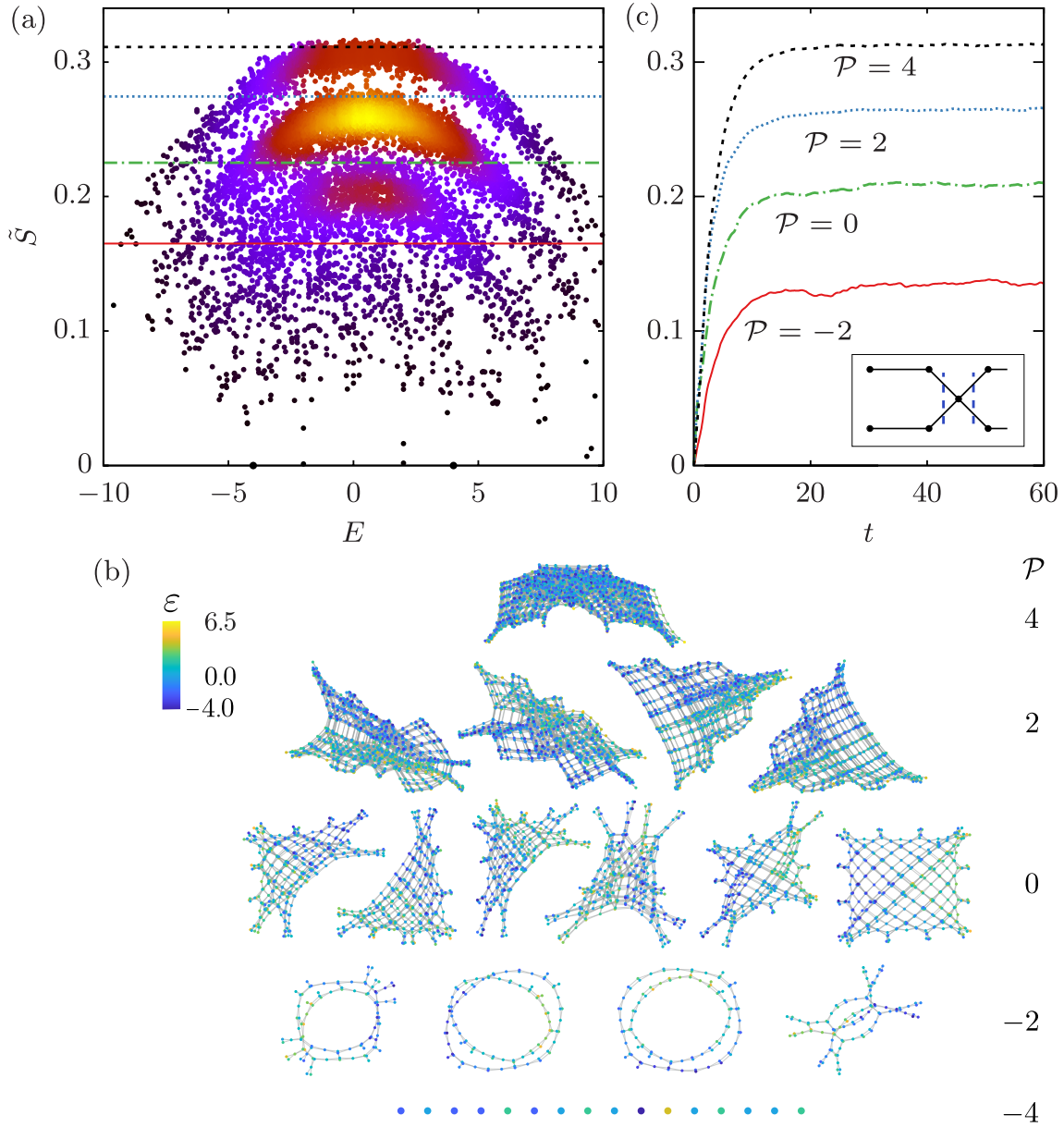
Figure 6.8: Numerical results for the 1D Pyrochlore chain with $N = 4$ particles in $N_c = 4$ unit cells and $\mathcal{J} = U = 1$. (a) Half-chain bipartite von Neumann entanglement entropy of each eigenstate as a function of the energy. The horizontal lines are the sector-restricted Page values for each sector and the color of the dots indicates the normalized density of data points, increasing with warming colors. (b) Adjacency graphs corresponding to the dome structures in (a) for each sector $\mathcal{P}$, where the color of the nodes represents the diagonal terms of the rotated Hamiltonian, ε. (c) Average of the entanglement entropy evolution for 20 random rotated basis states of each sector with eigenvalue $\mathcal{P}$. Inset: beginning of the 1D Pyrochlore chain with one spinal site and bipartitions (dashed blue lines) resulting in a zero entanglement entropy for the CLSs. In (a) and (c), the entropy is normalized to the number of sites in the subsystem, $\tilde{S} = S/\mathcal{N}_L$.

The numerical and analytical results presented in this chapter suggest a strong violation of the ETH that stems from the strong fragmentation of the Hilbert space. Eigenstates at nearby energies present a wide range of properties, which is reflected in the wide variance of the entanglement entropies at a given energy, and thermalization only occurs within each sub-sector. Such behavior is consistent with the extension of the eigenstate thermalization hypothesis through the use of generalized Gibbs ensembles [89], which are usually employed to characterize the behavior of integrable models. Instead of the microcanonical ensemble, one uses a generalized grand canonical ensemble that can be obtained by maximizing the entropy while taking into account the constraints imposed by the conserved quantities that lead to integrability [398]. Although the conserved quantities in the systems we study here are not enough to make the system integrable, they restrict thermalization in an analog way, and make it depend critically on the initial state.

6.3   Conclusions

We have studied local Hilbert space fragmentation in Bose-Hubbard flat-band lattices. In the first part of the chapter, we analyze in depth a family of diamond necklace lattices with n central sites. Such models possess a single-particle spectrum with a flat band, which is composed of compact localized states (CLSs) located in each diamond. Due to the presence of these CLSs, when adding more bosons with on-site interactions, the Hilbert space becomes locally fragmented. We have demonstrated how this fragmentation is revealed in the adjacency graph of the Hamiltonian when applying an appropriate basis rotation that decouples the CLSs at the single-particle level, making it an instance of quantum local Hilbert space fragmentation. Also, by analyzing the dimension of the largest sector, we have shown that the system exhibits strong fragmentation, which leads to a strong violation of the eigenstate thermalization hypothesis. We have found a conserved quantity that uniquely identifies each sub-sector of the Hamiltonian, the local CLS number parity. The sub-sectors present a wide range of dimensions, including one-dimensional sub-sectors, and also entanglement entropy scalings ranging from area-law to logarithmic growth, while also including one sector with an anti-volume correction. As a result of the fragmentation, the distribution of entanglement entropies presents a nested-dome structure, that stems from the number of particles that are trapped in a CLS. We have found weak thermalization through sub-sector-restricted entanglement evolution and subthermal entanglement growth within each non-integrable sector. Additionally, we have shown how the visibility of the nested-dome structure can be enhanced by increasing the sparsity of the CLSs, and how the results hold both for open and periodic boundary conditions.

In the second part of this chapter, we have demonstrated that this mechanism for local Hilbert space fragmentation also arises in a large class of flat-band lattices exhibiting commutative local symmetries. These lattices obey the equitable partition theorem, which ensures the presence of CLSs and extended states with distinct parities. Upon rotating the basis, such CLSs become decoupled at the single-particle level, and in the presence of bosonic on-site interactions, we have demonstrated that this leads to the fragmentation of the Hilbert space, which is again local, quantum and strong. In this case, a generalized conserved quantity arises:

the parity of the number of particles in all the CLSs in a single unit cell. For lattices presenting more than one set of independent local symmetries, multiple conserved quantities per unit cell can arise. Additionally, the mechanism for local Hilbert space fragmentation studied here is robust to large classes of long-range interactions, which in some cases causes the conserved quantity to change from the parity to the total number of particles in the CLSs. By studying one particular example numerically, the 1D Pyrochlore chain, we have shown that the sub-sector-restricted thermalization and the nested-dome structure in the entanglement entropies are a hallmark for this mechanism of fragmentation, and are a consequence of the low entanglement of the CLSs.

This chapter leaves open the study of other classes of flat-band lattices which might present similar mechanisms of fragmentation. One could consider for instance lattices with flux, where conserved quantities were observed in the diamond chain, Creutz ladder, and dice lattice [332].

7

CONCLUSIONS AND OUTLOOK

The main aim of this thesis has been the study of ultracold bosons in two particular types of systems: ring-trapping potentials and flat-band lattices. On the one hand, we have focused on orbital angular momentum (OAM) states in ring potentials, both studying Bose-Einstein condensates (BECs) and strongly correlated regimes hosting non-trivial topological phases in optical lattices of ring potentials. On the other hand, we have concentrated on signatures of thermalization in bosonic flat-band lattices. In this chapter, we summarize the main conclusions of the thesis and discuss possible future lines of research that stem from this work.

In Chapter 2, we have given an overview of the theoretical background and physical models used throughout this thesis. We have started by discussing the basics of Bose-Einstein condensation, including the role of particle statistics and the mean-field description of BECs at zero temperature through the Gross-Pitaevskii equation (GPE). We have also reviewed the generation of optical lattice potentials and the single-particle solutions that arise in such systems, the Bloch wavefunctions. This has served as a preliminary step to introduce the bosonic many-body scenario by describing the Bose-Hubbard model. Then, we have developed the physical models used to study ring trapping potentials. First, we have described the single-particle solutions to the Schrödinger equation for a single ring and then we have shown how coplanar ring geometries lead to complex tunnelings that critically depend on the geometry of the system. The two- and three-ring toy models we have considered allow us to describe arbitrary geometries of lattices of identical coplanar rings. In addition, we have presented the main concepts necessary to characterize topology in discrete systems, such as the Berry phase and the bulk-boundary correspondence, while also describing in detail a one-dimensional example of a topological insulator, the Su-Schrieffer-Heeger (SSH) model. Finally, we have explored the concept of thermalization, which we have first discussed in a classical setting to later compare it with the quantum approach to the problem. For an isolated quantum many-body system, we have reviewed the eigenstate thermalization hypothesis and the systems that violate it and thus fail to thermalize.

Chapters 3, 4, and 5 have been devoted to the study of ultracold bosons in ring potentials, starting with the analysis of a BEC in a two-stacked ring geometry in Chapter 3. In this chapter, we have studied the condensate in the mean-field regime through the GPE by reducing the

dimensionality of the problem to 1D [151]. In particular, we have derived the evolution equations for the amplitudes of each orbital angular momentum mode, which highlight the interplay between the OAM-specific tunneling between rings and the cross-OAM interactions within each ring. We have focused on populating the same OAM mode in both rings, which yields stationary solutions when there is the same population in both rings and dynamical regimes when there is a population imbalance. For both cases, we have analyzed numerically the stability of the stationary states and the dynamical regimes against small perturbations in higher-order modes, and have also developed analytically two-state models for both cases. For the stationary solutions, the two-state model not only predicts the regime of stationary states, thus agreeing with the results obtained through Bogoliubov analysis, but also describes the destabilization dynamics of the unstable solutions. For the dynamical regimes, we have established that the self-trapping and Josephson oscillation regimes are independent of the OAM mode, and thus reproduce the dynamics of a weakly-coupled double-well potential. However, these regimes are susceptible to perturbations in other OAM modes and we have shown that the destabilization dynamics mimic those of the stationary states. This work could be continued by studying a two-component BEC in the miscible regime [168, 399], where the dynamics now depend on the interplay between the inter- and intra-component interactions and the tunneling, which has lead to fascinating dynamics in double-well potentials [400–402]. For example, it would be interesting to populate different OAM modes in each component to explore angular momentum transfer between them.

The rest of the thesis, from Chapters 4 to 6, has dealt with the study of ultracold bosons in optical lattices through the use of exact diagonalization. In Chapters 4 and 5, we have transitioned from a 1D to a 2D description of the ring trapping geometry to address lattices where each site is formed by a ring potential. In particular, we have considered the local eigenstates of each ring with orbital angular momentum $l = 1$, which provides each site with two internal states with circulations $+$ and $-$. We have studied these systems through Bose-Hubbard-type models with a focus on strongly interacting regimes and perturbation theory techniques.

In Chapter 4, we have explored the simplest geometry yielding non-trivial topological phases in one dimension, a Su-Schrieffer-Heeger (SSH)-like model with alternating distances d and d' [152]. First, we have investigated the single-particle case by performing a basis rotation that decouples the system into two SSH chains with correlated topological phases. This has allowed us to characterize the system topologically in terms of the separation distances d and d'. Then, we have considered the case of two interacting bosons to study doublon states, in which the interactions bind the two particles together in the same site, and the interplay between topology and interactions. We have used two regimes to characterize the system analytically: the dimerized limit, where a single strong link describes the doublon bands, and the strongly interacting regime, where each doublon subspace can be analyzed independently. The model of the first regime accurately predicts the energy of the doublon bands and agrees with the exact diagonalization results for a large range of interactions. The second set of models have allowed us to map the different subspaces to effective single-particle SSH and Creutz ladder models exhibiting Tamm-Shockley states. Additionally, we have shown how

one can modify the edge potentials of the lattice to promote these states, which arise due to impurities at the edge sites, to topologically protected edge states.

In Chapter 5, we have increased the complexity of the problem by considering a staggered lattice with a tilting angle ϕ populated by a few bosons [153]. While a 1D lattice of inline rings presents real tunneling amplitudes between OAM states, for a staggered lattice with $\phi \neq 0$, some of the tunneling amplitudes can take complex values. Therefore, the synthetic Creutz ladder, which is comprised of the OAM states with circulations $+$ and $-$ at each site, can present a nonzero flux that is tuned through the angle ϕ. First, we have considered the single-particle case with a π flux, which causes the appearance of compact localized states (CLSs) that form a flat-band spectrum. The wavefunction of these states has a nonzero amplitude only on a few nearby sites and is exactly zero on the rest due to the destructive interference induced by the flux. This phenomenon is known as Aharonov-Bohm caging [121, 122].

In the rest of this chapter, we have explored the effect of on-site interactions on Aharonov-Bohm caging by focusing on the strongly interacting regime using perturbation theory and exact diagonalization. For nonzero interactions, the number of subspaces with more than one boson per site rapidly proliferates with the number of particles. We have shown how most of these subspaces can be mapped to an effective single-particle Creutz ladder with a flux, in analogy with the single particle case. This allows one to generate many-body CLSs by appropriately choosing the real-space angle ϕ. Remarkably, this instance of Aharonov-Bohm caging is a purely many-body effect, as it exists even in the absence of a flat-band single-particle spectrum. Additionally, we have studied the possibility of tuning the spatial extent of the Aharonov-Bohm cage by modifying the periodicity τ at which the angle ϕ is introduced. Increasing this periodicity yields more flat bands and their associated CLSs, which generally have a larger spatial extent. As a result, particles can explore a larger region of the lattice before encountering the destructive interference that enforces particle caging. To summarize, we have demonstrated how the geometry of the lattice can be engineered to select which N-particle subspaces exhibit caging (through the angle ϕ) and the spatial extent of the cage (through the periodicity τ). The results of this chapter could be further extended to the diamond chain with a flux, which has already been shown to host single-particle Aharonov-Bohm caging [147], through the use of nonidentical ring potentials. Also, one could consider Aharonov-Bohm caging in non-hermitian lattices, which has already been demonstrated in the diamond chain [403] and the Creutz ladder [404] by introducing gain and loss terms. In this case, one could generate many-body CLSs and Aharonov-Bohm caging in the strongly interacting regime by appropriately tuning the gain and loss coefficients.

In Chapter 6, we have continued with the theme of bosons in optical lattices hosting CLSs, but with two main differences: we have considered conventional optical lattices, where only the local ground state of each site can be occupied, and CLSs induced by local symmetry instead of Aharonov-Bohm caging. Within this type of lattice, we have focused on thermalization and the presence of Hilbert space fragmentation. In the first part of the chapter, we have analyzed in-depth a family of diamond necklaces [154], while in the second, we have generalized our findings to a complete class of flat-band lattices [155]. The diamond necklaces present CLS in each diamond, which can be decoupled from the dispersive chain at the single-particle

level by a basis rotation. We have shown that the addition of on-site interactions leads to a conserved quantity which is revealed in this rotated basis, the parity of the number of particles occupying each CLS. As a result, the Hilbert space is fragmented in the rotated basis, which can be observed in the adjacency graphs of the Hamiltonian. This is an example of quantum fragmentation, which in contrast to classical fragmentation, it is only visible in an entangled basis, but not on the product state basis. Also, this instance of fragmentation is local, a result of a local conservation law, and strong, such that no sector predominates in the thermodynamic limit. We have also studied this phenomenon numerically, finding sectors with a large range of dimensions, entanglement scalings (including volume and area law), and that include both integrable and non-integrable sectors. All these characteristics and the exponential growth of the number of sectors with the size of the system are typical of fragmented systems. Additionally, we have found a nested-dome distribution entanglement entropies that can be understood through the adjacency graphs of the Hamiltonian, and that thermalization is restricted within each sub-sector.

In the second part of Chapter 6, we have evidenced that this instance of Hilbert space fragmentation is not a particular feature of the diamond chain, but a general mechanism that arises in a certain class of flat-band lattices. The diamond lattice is a particular example of a flat-band lattice with local permutation symmetries in the single-particle graph of the Hamiltonian. For such lattices, the equitable partition theorem from graph theory guarantees opposite parities between the CLS and the extended states of the system. We have used this result to demonstrate the presence of a generalized conserved quantity for arbitrary lattices of this class, the parity of the total number of particles in all CLSs of a unit cell. As in the case of the diamond necklace, this instance of Hilbert space fragmentation is strong, quantum, and local, and its hallmark is the presence of the nested-dome pattern of entanglement entropies that leads to sub-sector-restricted thermalization. Finally, we have also shown that this mechanism for Hilbert space fragmentation is robust to a broad class of long-range interactions, which in some cases cause the structure of the fragmented Hilbert space to change, from the parity to the number of particles in the CLSs of a unit cell. The sensitivity of the CLSs to perturbations makes these systems ideal candidates for the study of prethermalization [244]. Any small perturbation that lifts the degeneracy of the flat bands will lead to approximate CLSs yielding approximate conserved quantities. As a result, one can expect the presence of (possibly multiple) prethermalization plateaus in the entanglement entropy, due to the presence of the quasi-conserved quantities, and full thermalization at a much longer time scale. Alternatively, one could extend this line of research by studying under which conditions flat-band lattices lead to time crystals, which have already been shown to appear in a spin 1/2 Creutz ladder [185, 250].

A

APPENDIX

A.1 Properties of the critical points

For the two-state model derived in Sec. 3.2.2, the behavior of the system around the critical points can be obtained by studying the eigenvalues of the Jacobian at the critical points. The Jacobian reads

$$
DF = \begin{pmatrix} \dfrac{\partial(|\dot{\alpha_\nu}|^2)}{\partial(|\alpha_\nu|^2)} & \dfrac{\partial\dot{\zeta}}{\partial(|\alpha_\nu|^2)} \\ \dfrac{\partial(|\dot{\alpha_\nu}|^2)}{\partial\zeta} & \dfrac{\partial\dot{\zeta}}{\partial\zeta} \end{pmatrix}
$$

$$
= \begin{pmatrix} \gamma\left(8|\alpha_\nu|^2 - N\right)\sin 2\zeta & 3\gamma + 4\gamma\cos 2\zeta \\ 4\gamma|\alpha_\nu|^2\left(2|\alpha_\nu|^2 - \frac{N}{2}\right)\cos 2\zeta & -2\gamma\left(4\gamma|\alpha_\nu|^2 - \frac{N}{2}\right)\sin 2\zeta \end{pmatrix}. \tag{A.1}
$$

For the critical point $(\mathcal{A}, |\alpha_\nu|^2 = 0)$,

$$
DF(\mathcal{A}, |\alpha_\nu|^2 = 0) = \begin{pmatrix} -\gamma N\sin 2\zeta & 3\gamma + 4\gamma\cos 2\zeta \\ 0 & \gamma N\sin 2\zeta \end{pmatrix}. \tag{A.2}
$$

The corresponding eigenvalues are real and have opposite sign, $\lambda = \pm\gamma N\sin 2\zeta$, thus, the critical point is a saddle point. For the limiting values of κ in the existence condition of the critical point, Eq. (3.17), $\nu^2/2$ and $(\nu^2 + 2\epsilon)/2$, ζ takes the values $(2a+1)\pi/2$ and $a\pi$, respectively. In those cases, the eigenvalues become zero and the behavior around the critical point can not be inferred from this method.

Similarly, for $(\mathcal{B}, |\alpha_\nu|^2 = N/4)$,

$$
DF\left(\mathcal{B}, |\alpha_\nu|^2 = \frac{N}{4}\right) = \begin{pmatrix} \gamma N\sin 2\zeta & 3\gamma + 4\gamma\cos 2\zeta \\ 0 & -\gamma N\sin 2\zeta \end{pmatrix}, \tag{A.3}
$$

and the eigenvalues are real numbers of opposite sign $\lambda = \pm\gamma N\sin 2\zeta$. Thus, this critical point is a saddle point, except for the limiting cases in Eq. (3.18).

For the critical point $(\zeta = a\pi, \mathcal{C})$,

$$DF(\zeta = a\pi, \mathcal{C}) = \begin{pmatrix} 0 & 7\gamma \\ 4\gamma|\alpha_\nu|^2 \left(2|\alpha_\nu|^2 - \frac{N}{2}\right) & 0 \end{pmatrix}, \tag{A.4}$$

and the eigenvalues are

$$\lambda = \pm\sqrt{28\gamma^2|\alpha_\nu|^2 \left(2|\alpha_\nu|^2 - \frac{N}{2}\right)}. \tag{A.5}$$

Using the $|\alpha_\nu|^2$ value of the critical point in Eq. (3.19a), these eigenvalues are imaginary, and thus the stationary point is a center, the trajectories precede around it. For the limiting values of κ in Eq. (3.20), $(\nu^2 - 3\epsilon/2)/2$ and $(\nu^2 + 2\epsilon)/2$, $|\alpha_\nu|^2$ becomes $N/4$ or 0, respectively, in which case both eigenvalues are zero and the behavior around the critical point can not be determined.

For $(\zeta = (2a + 1)\frac{\pi}{2}, \mathcal{D})$,

$$DF\left(\zeta = (2a + 1)\frac{\pi}{2}, \mathcal{D}\right) = \begin{pmatrix} 0 & -\gamma \\ -4\gamma|\alpha_\nu|^2 \left(2|\alpha_\nu|^2 - \frac{N}{2}\right) & 0 \end{pmatrix}, \tag{A.6}$$

with eigenvalues

$$\lambda = \pm\sqrt{4\gamma^2|\alpha_\nu|^2 \left(2|\alpha_\nu|^2 - \frac{N}{2}\right)}. \tag{A.7}$$

As before, these stationary points are centers, and the trajectories precede around them, except for the limiting values of κ in Eq. (3.21).

B

APPENDIX

B.1 Eigenvectors of the strong-link Hamiltonian

The eigenvectors of the strong-link Hamiltonian discussed in Sec. 4.3 are given in Table B.1 below. These correspond to the eigenvalues in Eq. (4.17), where we consider the limit of large distances where $J_2' \simeq J_3' \equiv J$. We have defined the factors

$$A^{+(-)} = \frac{U \overset{+}{(-)} \sqrt{U^2 + 16J^2}}{2\sqrt{2}J}, \quad V = \frac{U}{2\sqrt{2}J}, \quad W_i = \sqrt{2}(E_i^2 - E_i V - 1), \quad \text{(B.1)}$$

for $i = 4, 5, 6$, and the norms of the eigenvectors $\tilde{v}_{7,8,9,10}$ take the following simple forms

$$\|\tilde{v}_7\| = \|\tilde{v}_8\| = (8 + 4V^2 + 4V\sqrt{V^2 + 2})^{1/2}$$
$$\|\tilde{v}_9\| = \|\tilde{v}_{10}\| = (8 + 4V^2 - 4V\sqrt{V^2 + 2})^{1/2}. \quad \text{(B.2)}$$

v_n	$|A_s^+ A_s^+\rangle$	$|A_s^+ A_s^-\rangle$	$|A_s^+ B_k^+\rangle$	$|A_s^+ B_k^-\rangle$	$|A_s^- A_s^-\rangle$	$|A_s^- B_k^+\rangle$	$|A_s^- B_k^-\rangle$	$|B_k^+ B_k^+\rangle$	$|B_k^+ B_k^-\rangle$	$|B_k^- B_k^-\rangle$
v_1	0	0	$\frac{1}{2}$	$-\frac{1}{2}$	0	$-\frac{1}{2}$	$\frac{1}{2}$	0	0	0
v_2	$-\frac{1}{2}$	0	0	0	$-\frac{1}{2}$	0	0	$\frac{1}{2}$	0	$\frac{1}{2}$
v_3	0	$-\frac{1}{\sqrt{2}}$	0	0	0	0	0	0	$\frac{1}{\sqrt{2}}$	0
$\tilde{v}_4$	1	W_4	$E_4 - V$	$E_4 - V$	1	$E_4 - V$	$E_4 - V$	1	W_4	1
$\tilde{v}_5$	1	W_5	$E_5 - V$	$E_5 - V$	1	$E_5 - V$	$E_5 - V$	1	W_5	1
$\tilde{v}_6$	1	W_6	$E_6 - V$	$E_6 - V$	1	$E_6 - V$	$E_6 - V$	1	W_6	1
$\tilde{v}_7$	1	0	0	$-A^+$	-1	A^+	0	-1	0	1
$\tilde{v}_8$	1	0	$-A^+$	0	-1	0	A^+	1	0	-1
$\tilde{v}_9$	1	0	0	$-A^-$	-1	A^-	0	-1	0	1
$\tilde{v}_{10}$	1	0	$-A^-$	0	-1	0	A^-	1	0	-1

Table B.1: Eigenvectors v_n of the strong-link Hamiltonian $\hat{\mathcal{H}}_{SL}$ in the regime of large distances. The normalized eigenvectors are $v_n = \tilde{v}_n / \|\tilde{v}_n\|$ and we use the factors $A^{+(-)}$, V, and W_i with $i = 4, 5, 6$ defined in Eq. (25).

C

APPENDIX

C.1 Intertwining operators

In this section, we apply the argument used in [332] for the Creutz ladder, diamond chain, and dice lattice with flux, to arbitrary flat-band lattices with basic commutative local symmetries of order two. The authors in [332] define the so-called intertwining operators $\mathcal{U}_{j,k}$, which realize the automorphisms of the single-particle graph in the field operators. In our notation, they swap the top and bottom operators in a rung j of a unit cell k while leaving the other operators invariant,

$$\begin{cases} \mathcal{U}_{j,k}\hat{t}_{j,k}\mathcal{U}_{j,k}^{\dagger} = \hat{b}_{j,k} \\ \mathcal{U}_{j,k}\hat{b}_{j,k}\mathcal{U}_{j,k}^{\dagger} = \hat{t}_{j,k} \end{cases} \text{and} \begin{cases} \mathcal{U}_{j,k}\hat{t}_{j',k}\mathcal{U}_{j,k}^{\dagger} = \hat{t}_{j',k} \\ \mathcal{U}_{j,k}\hat{b}_{j',k}\mathcal{U}_{j,k}^{\dagger} = \hat{b}_{j',k} \end{cases} \text{for } j \neq j', \tag{C.1}$$

while $\mathcal{U}_{j,k}\hat{s}_{j',k'}\mathcal{U}_{j,k}^{\dagger} = \hat{s}_{j',k'}$ for a spinal site in any rung j' and any unit cell k'. For each lattice, the Hamiltonian will remain invariant under a set of local permutations represented by the combined action $\mathcal{R}_k = \prod_{j=1}^{n_2/2} \mathcal{U}_{j,k}$, such that $\mathcal{R}_k\hat{\mathcal{H}}\mathcal{R}_k^{\dagger} = \hat{\mathcal{H}}$. Note that, in contrast with [332], here we deal with flat-band lattices without flux. As a consequence, the intertwining operators do not cause the insertion of a π flux and the conserved quantity does not include an additional gauge transformation.

The effect of the intertwining operators on the CLSs and the dispersive states we defined in Eq. (6.14) is the following,

$$\prod_{j_1=1}^{n_2/2} \mathcal{U}_{j_1,k}\hat{c}_{l,k} \left[\prod_{j_2=1}^{n_2/2} \mathcal{U}_{j_2,k}\right]^{\dagger} = \prod_{j_1=1}^{n_2/2} \mathcal{U}_{j_1,k} \sum_{j=1}^{n_2/2} \alpha_{j,k}^l \left(\hat{t}_{j,k} - \hat{b}_{j,k}\right) \left[\prod_{j_2=1}^{n_2/2} \mathcal{U}_{j_2,k}\right]^{\dagger}$$

$$= \sum_{j=1}^{n_2/2} \alpha_{j,k}^l \left(\hat{b}_{j,k} - \hat{t}_{j,k}\right) = -\hat{c}_{l,k}. \tag{C.2}$$

If the intertwining operators are applied to a different unit cell, the CLS operators remain invariant $\prod_{j_1=1}^{n_2/2} \mathcal{U}_{j_1,k}\hat{c}_{l,k'} \prod_{j_2=1}^{n_2/2} \mathcal{U}_{j_2,k}^{\dagger} = \hat{c}_{l,k'}$, for $k \neq k'$. Due to the positive sign in the

expression of the dispersive states, Eq. (6.14), they remain invariant under such operation, $\prod_{j_1=1}^{n_2/2} \mathcal{U}_{j_1,k} \hat{d}_{l,k'} \prod_{j_2=1}^{n_2/2} \mathcal{U}_{j_2,k}^\dagger = \hat{d}_{l,k'}$ for any pair k, k'. For an on-site bosonic interaction, the Hamiltonian is composed of a series of terms of the form $\hat{\rho}_{l_1,k}^\dagger \hat{\sigma}_{l_2,k}^\dagger \hat{\tau}_{l_3,k} \hat{v}_{l_4,k}$, where $\{\hat{\rho}, \hat{\sigma}, \hat{\tau}, \hat{v}\} = \{\hat{c}, \hat{d}\}$ are the annihilation operators of either a CLS or a dispersive state [see Eq. (6.17)]. The terms with an odd number of CLS creation or annihilation operators change sign under the action of the intertwining operators, while the others remain invariant. As we showed in the main text, those terms always vanish, such that

$$\hat{\mathcal{P}}_k = e^{i\pi \sum_{l=1}^{n_2/2} \hat{n}_{c_{l,k}}} \tag{C.3}$$

is a conserved quantity of the complete system.

C.2   Level statistics and non-integrability in the 1D Pyrochlore chain

Below we give numerical results on the energy level statistics of the 1D Pyrochlore chain [Fig. 6.7(di)]. In Table C.1, we show the mean value of the spacing ratio [Eq. (6.9)] for each sub-sector $\mathcal{P} = (\mathcal{P}_1, \cdots, \mathcal{P}_{N_c})$ of the Pyrochlore chain considered in Section 6.2.4, with $N = 4$ particles in $N_c = 4$ unit cells, open boundary conditions, and one spinal site per unit cell. Most sub-sectors tend to the Wigner-Dyson value signaling non-integrability within each sub-sector. The sub-sectors belonging to $\mathcal{P} = -2$, for which the dimension of the sub-sectors is very small, tend to the Poisson regime, as those correspond to the integrable effective single-particle sub-sectors. The sectors $\mathcal{P} = -4$, not included in the table, correspond to the frozen states.

Sector $\mathcal{P}$	Subsector $\mathcal{P}_k$	$\langle r \rangle$	Standard error
4	$(+,+,+,+)$	0.520	0.005
2	$(-,+,+,+)$	0.508	0.008
2	$(+,-,+,+)$	0.515	0.008
2	$(+,+,-,+)$	0.524	0.008
2	$(+,+,+,-)$	0.526	0.008
0	$(-,-,+,+)$	0.538	0.014
0	$(-,+,-,+)$	0.529	0.014
0	$(-,+,+,-)$	0.531	0.014
0	$(+,-,-,+)$	0.538	0.013
0	$(+,-,+,-)$	0.515	0.014
0	$(+,+,-,-)$	0.503	0.013
-2	$(-,-,-,+)$	0.40	0.03
-2	$(-,-,+,-)$	0.40	0.03
-2	$(-,+,-,-)$	0.36	0.03
-2	$(+,-,-,-)$	0.43	0.03

Table C.1: Mean level spacing ratio for the sub-sectors with $\mathcal{P} = 4, 2, 0, -2$ of the 1D Pyrochlore chain, with $N = 4$ particles in $N_c = 4$ unit cells, open boundary conditions, and one spinal site. The value corresponding to the Gaussian orthogonal ensemble is $\langle r \rangle_{GOE} = 0.536$, while the value for a Poisson distribution is $\langle r \rangle_P = 0.386$. We also indicate the standard errors of the mean. The plus and minus signs indicate the positive or negative parity of the vector $\mathcal{P} = (\mathcal{P}_1, \cdots, \mathcal{P}_{N_c})$ in each unit cell k.

Bibliography

[1]   M. H. Anderson, J. R. Ensher, M. R. Matthews, C. E. Wieman, and E. A. Cornell, "Observation of Bose-Einstein Condensation in a Dilute Atomic Vapor", Science **269**, 198–201 (1995).

[2]   K. B. Davis, M.-O. Mewes, M. R. Andrews, N. J. van Druten, D. S. Durfee, D. M. Kurn, and W. Ketterle, "Bose-Einstein Condensation in a Gas of Sodium Atoms", Physical Review Letters **75**, 3969–3973 (1995).

[3]   C. C. Bradley, C. A. Sackett, J. J. Tollett, and R. G. Hulet, "Evidence of Bose-Einstein Condensation in an Atomic Gas with Attractive Interactions", Physical Review Letters **75**, 1687–1690 (1995).

[4]   Bose, "Plancks Gesetz und Lichtquantenhypothese", Zeitschrift für Physik **26**, 178–181 (1924).

[5]   A. Einstein, "Quanten theorie des einatomigen idealen gases", Sitzungsberichte der Königlich Preussischen Akademie der Wissenschaften zu Berlin, 261–267 (1924).

[6]   A. Einstein, "Quanten theorie des einatomigen idealen gases", Sitzungsberichte der Königlich Preussischen Akademie der Wissenschaften zu Berlin, 3–14 (1925).

[7]   F. London, "On the Bose-Einstein Condensation", Physical Review **54**, 947–954 (1938).

[8]   C. Cohen-Tannoudji, "Laser cooling and trapping of neutral atoms: theory", Physics Reports **219**, 153–164 (1992).

[9]   M. R. Andrews, C. G. Townsend, H.-J. Miesner, D. S. Durfee, D. M. Kurn, and W. Ketterle, "Observation of Interference Between Two Bose Condensates", Science **275**, 637–641 (1997).

[10] A. Ramanathan, K. C. Wright, S. R. Muniz, M. Zelan, W. T. Hill, C. J. Lobb, K. Helmerson, W. D. Phillips, and G. K. Campbell, "Superflow in a toroidal bose-einstein condensate: An atom circuit with a tunable weak link", Physical Review Letters **106**, 130401 (2011).

[11] M. R. Matthews, B. P. Anderson, P. C. Haljan, D. S. Hall, C. E. Wieman, and E. A. Cornell, "Vortices in a Bose-Einstein Condensate", Physical Review Letters **83**, 2498–2501 (1999).

[12]   S. Burger, K. Bongs, S. Dettmer, W. Ertmer, K. Sengstock, A. Sanpera, G. V. Shlyapnikov, and M. Lewenstein, "Dark Solitons in Bose-Einstein Condensates", Physical Review Letters **83**, 5198–5201 (1999).

[13]   J. Denschlag, J. E. Simsarian, D. L. Feder, C. W. Clark, L. A. Collins, J. Cubizolles, L. Deng, E. W. Hagley, K. Helmerson, W. P. Reinhardt, S. L. Rolston, B. I. Schneider, and W. D. Phillips, "Generating Solitons by Phase Engineering of a Bose-Einstein Condensate", Science **287**, 97–101 (2000).

[14]   L. Khaykovich, F. Schreck, G. Ferrari, T. Bourdel, J. Cubizolles, L. D. Carr, Y. Castin, and C. Salomon, "Formation of a Matter-Wave Bright Soliton", Science **296**, 1290–1293 (2002).

[15]   K. E. Strecker, G. B. Partridge, A. G. Truscott, and R. G. Hulet, "Formation and propagation of matter-wave soliton trains", Nature **417**, 150–153 (2002).

[16]   B. DeMarco and D. S. Jin, "Onset of Fermi Degeneracy in a Trapped Atomic Gas", Science **285**, 1703–1706 (1999).

[17]   B. DeMarco, S. B. Papp, and D. S. Jin, "Pauli Blocking of Collisions in a Quantum Degenerate Atomic Fermi Gas", Physical Review Letters **86**, 5409–5412 (2001).

[18]   A. G. Truscott, K. E. Strecker, W. I. McAlexander, G. B. Partridge, and R. G. Hulet, "Observation of Fermi Pressure in a Gas of Trapped Atoms", Science **291**, 2570–2572 (2001).

[19]   R. Grimm, M. Weidemüller, and Y. B. Ovchinnikov, "Optical Dipole Traps for Neutral Atoms", in *Advances in atomic, molecular and optical physics*, Vol. 42, C (2000), pp. 95–170.

[20]   M. P. A. Fisher, P. B. Weichman, G. Grinstein, and D. S. Fisher, "Boson localization and the superfluid-insulator transition", Physical Review B **40**, 546–570 (1989).

[21]   D. Jaksch, C. Bruder, J. I. Cirac, C. W. Gardiner, and P. Zoller, "Cold Bosonic Atoms in Optical Lattices", Physical Review Letters **81**, 3108–3111 (1998).

[22]   M. Greiner, O. Mandel, T. Esslinger, T. W. Hänsch, and I. Bloch, "Quantum phase transition from a superfluid to a Mott insulator in a gas of ultracold atoms", Nature **415**, 39–44 (2002).

[23]   M. Lewenstein, A. Sanpera, and V. Ahufinger, *Ultracold atoms in optical lattices: simulating quantum many-body systems* (Oxford University Press, 2012).

[24]   I. Bloch, J. Dalibard, and W. Zwerger, "Many-body physics with ultracold gases", Reviews of Modern Physics **80**, 885–964 (2008).

[25]   P. O. Fedichev, Y. Kagan, G. V. Shlyapnikov, and J. T. M. Walraven, "Influence of Nearly Resonant Light on the Scattering Length in Low-Temperature Atomic Gases", Physical Review Letters 77, 2913–2916 (1996).

[26]   M. Theis, G. Thalhammer, K. Winkler, M. Hellwig, G. Ruff, R. Grimm, and J. H. Denschlag, "Tuning the Scattering Length with an Optically Induced Feshbach Resonance", Physical Review Letters **93**, 123001 (2004).

[27] O. Thomas, C. Lippe, T. Eichert, and H. Ott, "Experimental realization of a Rydberg optical Feshbach resonance in a quantum many-body system", Nature Communications **9**, 2238 (2018).

[28] S. L. Cornish, N. R. Claussen, J. L. Roberts, E. A. Cornell, and C. E. Wieman, "Stable ^{85}Rb Bose-Einstein Condensates with Widely Tunable Interactions", Physical Review Letters **85**, 1795–1798 (2000).

[29] S. E. Pollack, D. Dries, M. Junker, Y. P. Chen, T. A. Corcovilos, and R. G. Hulet, "Extreme Tunability of Interactions in a ^{7}Li Bose-Einstein Condensate", Physical Review Letters **102**, 090402 (2009).

[30] C. Chin, R. Grimm, P. Julienne, and E. Tiesinga, "Feshbach resonances in ultracold gases", Reviews of Modern Physics **82**, 1225–1286 (2010).

[31] M. Baranov, "Theoretical progress in many-body physics with ultracold dipolar gases", Physics Reports **464**, 71–111 (2008).

[32] M. Baranov, L. Dobrek, K. Góral, L. Santos, and M. Lewenstein, "Ultracold Dipolar Gases - a Challenge for Experiments and Theory", Physica Scripta **T102**, 74 (2002).

[33] T. Lahaye, C. Menotti, L. Santos, M. Lewenstein, and T. Pfau, "The physics of dipolar bosonic quantum gases", Reports on Progress in Physics **72**, 126401 (2009).

[34] C. Becker, P. Soltan-Panahi, J. Kronjäger, S. Dörscher, K. Bongs, and K. Sengstock, "Ultracold quantum gases in triangular optical lattices", New Journal of Physics **12**, 065025 (2010).

[35] P. Soltan-Panahi, J. Struck, P. Hauke, A. Bick, W. Plenkers, G. Meineke, C. Becker, P. Windpassinger, M. Lewenstein, and K. Sengstock, "Multi-component quantum gases in spin-dependent hexagonal lattices", Nature Physics 7, 434–440 (2011).

[36] L. Santos, M. Baranov, J. Cirac, H.-U. Everts, H. Fehrmann, and M. Lewenstein, "Atomic Quantum Gases in Kagomé Lattices", Physical Review Letters **93**, 030601 (2004).

[37] L. Pricoupenko, H. Perrin, and M. Olshanii, "Quantum Gases in Low Dimensions", in Journal de Physique IV (proceedings) (2004).

[38] C. Gross and I. Bloch, "Quantum simulations with ultracold atoms in optical lattices", Science **357**, 995–1001 (2017).

[39] R. P. Feynman, "Simulating physics with computers", International Journal of Theoretical Physics **21**, 467–488 (1982).

[40] P. A. Lee, "From high temperature superconductivity to quantum spin liquid: progress in strong correlation physics", Reports on Progress in Physics **71**, 012501 (2008).

[41] A. J. Kollár, M. Fitzpatrick, and A. A. Houck, "Hyperbolic lattices in circuit quantum electrodynamics", Nature **571**, 45–50 (2019).

[42] T. Ozawa and H. M. Price, "Topological quantum matter in synthetic dimensions", Nature Reviews Physics **1**, 349–357 (2019).

[43] E. Altman, K. R. Brown, G. Carleo, L. D. Carr, E. Demler, C. Chin, B. DeMarco, S. E. Economou, M. A. Eriksson, K.-M. C. Fu, M. Greiner, K. R. Hazzard, R. G. Hulet, A. J. Kollár, B. L. Lev, M. D. Lukin, R. Ma, X. Mi, S. Misra, C. Monroe, K. Murch, Z. Nazario, K.-K. Ni, A. C. Potter, P. Roushan, M. Saffman, M. Schleier-Smith, I. Siddiqi, R. Simmonds, M. Singh, I. Spielman, K. Temme, D. S. Weiss, J. Vučković, V. Vuletić, J. Ye, and M. Zwierlein, "Quantum Simulators: Architectures and Opportunities", PRX Quantum **2**, 017003 (2021).

[44] C. J. Kennedy, W. C. Burton, W. C. Chung, and W. Ketterle, "Observation of Bose–Einstein condensation in a strong synthetic magnetic field", Nature Physics **11**, 859–864 (2015).

[45] L. Landau, "The Theory of Phase Transitions", Nature **138**, 840–841 (1936).

[46] C. Kittel, *Introduction to Solid State Physics* (Wiley, 2004).

[47] E. D. Bloch, *A First Course in Geometric Topology and Differential Geometry* (Birkhäuser Boston, 1997).

[48] K. V. Klitzing, G. Dorda, and M. Pepper, "New Method for High-Accuracy Determination of the Fine-Structure Constant Based on Quantized Hall Resistance", Physical Review Letters **45**, 494–497 (1980).

[49] P. G. Harper, "Single Band Motion of Conduction Electrons in a Uniform Magnetic Field", Proceedings of the Physical Society. Section A **68**, 874–878 (1955).

[50] D. R. Hofstadter, "Energy levels and wave functions of Bloch electrons in rational and irrational magnetic fields", Physical Review B **14**, 2239–2249 (1976).

[51] M. den Nijs, "Quantized Hall conductance in a two dimensional periodic potential", Physica A: Statistical Mechanics and its Applications **124**, 199–210 (1984).

[52] F. D. M. Haldane, "Model for a Quantum Hall Effect without Landau Levels: Condensed-Matter Realization of the "Parity Anomaly"", Physical Review Letters **61**, 2015–2018 (1988).

[53] C. L. Kane and E. J. Mele, "Z_2 Topological Order and the Quantum Spin Hall Effect", Physical Review Letters **95**, 146802 (2005).

[54] C.-K. Chiu, J. C. Teo, A. P. Schnyder, and S. Ryu, "Classification of topological quantum matter with symmetries", Reviews of Modern Physics **88**, 035005 (2016).

[55] A. Kitaev, "Periodic table for topological insulators and superconductors", in AIP Conference Proceedings, Vol. 1134 (2009), pp. 22–30.

[56] T. Neupert and F. Schindler, "Topological Crystalline Insulators", in *Topological matter* (Springer, 2018), pp. 31–61.

[57] S.-Y. Xu, I. Belopolski, D. S. Sanchez, C. Zhang, G. Chang, C. Guo, G. Bian, Z. Yuan, H. Lu, T.-R. Chang, P. P. Shibayev, M. L. Prokopovych, N. Alidoust, H. Zheng, C.-C. Lee, S.-M. Huang, R. Sankar, F. Chou, C.-H. Hsu, H.-T. Jeng, A. Bansil, T. Neupert, V. N. Strocov, H. Lin, S. Jia, and M. Z. Hasan, "Experimental discovery of a topological Weyl semimetal state in TaP", Science Advances **1**, 1501092 (2015).

[58] E. J. Meier, F. A. An, A. Dauphin, M. Maffei, P. Massignan, T. L. Hughes, and B. Gadway, "Observation of the topological Anderson insulator in disordered atomic wires", Science **362**, 929–933 (2018).

[59] M. S. Rudner and N. H. Lindner, "Band structure engineering and non-equilibrium dynamics in Floquet topological insulators", Nature Reviews Physics **2**, 229–244 (2020).

[60] S. Rachel, "Interacting topological insulators: a review", Reports on Progress in Physics **81**, 116501 (2018).

[61] A. Celi, P. Massignan, J. Ruseckas, N. Goldman, I. B. Spielman, G. Juzeliūnas, and M. Lewenstein, "Synthetic Gauge Fields in Synthetic Dimensions", Physical Review Letters **112**, 043001 (2014).

[62] T. Ozawa and H. M. Price, "Topological quantum matter in synthetic dimensions", Nature Reviews Physics **1**, 349–357 (2019).

[63] N. Goldman, G. Juzeliūnas, P. Öhberg, and I. B. Spielman, "Light-induced gauge fields for ultracold atoms", Reports on Progress in Physics 77, 126401 (2014).

[64] N. Goldman and J. Dalibard, "Periodically Driven Quantum Systems: Effective Hamiltonians and Engineered Gauge Fields", Physical Review X **4**, 031027 (2014).

[65] M. Aidelsburger, S. Nascimbene, and N. Goldman, "Artificial gauge fields in materials and engineered systems", Comptes Rendus Physique **19**, 394–432 (2018).

[66] N. Goldman, J. C. Budich, and P. Zoller, "Topological quantum matter with ultracold gases in optical lattices", Nature Physics **12**, 639–645 (2016).

[67] G. Jotzu, M. Messer, R. Desbuquois, M. Lebrat, T. Uehlinger, D. Greif, and T. Esslinger, "Experimental realization of the topological Haldane model with ultracold fermions", Nature **515**, 237–240 (2014).

[68] H. Miyake, G. A. Siviloglou, C. J. Kennedy, W. C. Burton, and W. Ketterle, "Realizing the Harper Hamiltonian with Laser-Assisted Tunneling in Optical Lattices", Physical Review Letters **111**, 185302 (2013).

[69] M. Aidelsburger, M. Atala, M. Lohse, J. T. Barreiro, B. Paredes, and I. Bloch, "Realization of the Hofstadter Hamiltonian with Ultracold Atoms in Optical Lattices", Physical Review Letters **111**, 185301 (2013).

[70] M. Aidelsburger, M. Lohse, C. Schweizer, M. Atala, J. T. Barreiro, S. Nascimbène, N. R. Cooper, I. Bloch, and N. Goldman, "Measuring the Chern number of Hofstadter bands with ultracold bosonic atoms", Nature Physics **11**, 162–166 (2015).

[71]   T. Langen, R. Geiger, and J. Schmiedmayer, "Ultracold Atoms Out of Equilibrium", Annual Review of Condensed Matter Physics **6**, 201–217 (2015).

[72]   J. M. Deutsch, "Quantum statistical mechanics in a closed system", Physical Review A **43**, 2046–2049 (1991).

[73]   M. Srednicki, "Chaos and quantum thermalization", Physical Review E **50**, 888–901 (1994).

[74]   M. Rigol, V. Dunjko, and M. Olshanii, "Thermalization and its mechanism for generic isolated quantum systems", Nature **452**, 854–858 (2008).

[75]   L. F. Santos and M. Rigol, "Localization and the effects of symmetries in the thermalization properties of one-dimensional quantum systems", Physical Review E **82**, 031130 (2010).

[76]   M. Rigol and L. F. Santos, "Quantum chaos and thermalization in gapped systems", Physical Review A **82**, 011604 (2010).

[77]   E. Khatami, G. Pupillo, M. Srednicki, and M. Rigol, "Fluctuation-Dissipation Theorem in an Isolated System of Quantum Dipolar Bosons after a Quench", Physical Review Letters **111**, 050403 (2013).

[78]   M. Rigol, "Breakdown of Thermalization in Finite One-Dimensional Systems", Physical Review Letters **103**, 100403 (2009).

[79]   M. Rigol, "Quantum quenches and thermalization in one-dimensional fermionic systems", Physical Review A **80**, 053607 (2009).

[80]   R. Steinigeweg, J. Herbrych, and P. Prelovšek, "Eigenstate thermalization within isolated spin-chain systems", Physical Review E **87**, 012118 (2013).

[81]   C. Neuenhahn and F. Marquardt, "Thermalization of interacting fermions and delocalization in Fock space", Physical Review E **85**, 060101 (2012).

[82]   M. Rigol, "Quantum quenches and thermalization in one-dimensional fermionic systems", Physical Review A **80**, 053607 (2009).

[83]   E. Khatami, M. Rigol, A. Relaño, and A. M. García-García, "Quantum quenches in disordered systems: Approach to thermal equilibrium without a typical relaxation time", Physical Review E **85**, 050102 (2012).

[84]   S. Genway, A. F. Ho, and D. K. K. Lee, "Thermalization of local observables in small Hubbard lattices", Physical Review A **86**, 023609 (2012).

[85]   W. Beugeling, R. Moessner, and M. Haque, "Finite-size scaling of eigenstate thermalization", Physical Review E **89**, 042112 (2014).

[86]   W. Beugeling, R. Moessner, and M. Haque, "Off-diagonal matrix elements of local operators in many-body quantum systems", Physical Review E **91**, 012144 (2015).

[87]   G. Biroli, C. Kollath, and A. M. Läuchli, "Effect of Rare Fluctuations on the Thermalization of Isolated Quantum Systems", Physical Review Letters **105**, 250401 (2010).

[88] G. Roux, "Finite-size effects in global quantum quenches: Examples from free bosons in an harmonic trap and the one-dimensional Bose-Hubbard model", Physical Review A **81**, 053604 (2010).

[89] L. D'Alessio, Y. Kafri, A. Polkovnikov, and M. Rigol, "From quantum chaos and eigenstate thermalization to statistical mechanics and thermodynamics", Advances in Physics **65**, 239–362 (2016).

[90] R. Nandkishore and D. A. Huse, "Many-Body Localization and Thermalization in Quantum Statistical Mechanics", Annual Review of Condensed Matter Physics **6**, 15–38 (2015).

[91] H. Bernien, S. Schwartz, A. Keesling, H. Levine, A. Omran, H. Pichler, S. Choi, A. S. Zibrov, M. Endres, M. Greiner, V. Vuletić, and M. D. Lukin, "Probing many-body dynamics on a 51-atom quantum simulator", Nature **551**, 579–584 (2017).

[92] C. J. Turner, A. A. Michailidis, D. A. Abanin, M. Serbyn, and Z. Papić, "Weak ergodicity breaking from quantum many-body scars", Nature Physics **14**, 745–749 (2018).

[93] C. J. Turner, A. A. Michailidis, D. A. Abanin, M. Serbyn, and Z. Papić, "Quantum scarred eigenstates in a Rydberg atom chain: Entanglement, breakdown of thermalization, and stability to perturbations", Physical Review B **98**, 155134 (2018).

[94] I. Affleck, T. Kennedy, E. H. Lieb, and H. Tasaki, "Rigorous results on valence-bond ground states in antiferromagnets", Physical Review Letters **59**, 799–802 (1987).

[95] S. Moudgalya, N. Regnault, and B. A. Bernevig, "Entanglement of exact excited states of Affleck-Kennedy-Lieb-Tasaki models: Exact results, many-body scars, and violation of the strong eigenstate thermalization hypothesis", Physical Review B **98**, 235156 (2018).

[96] S. Moudgalya, S. Rachel, B. A. Bernevig, and N. Regnault, "Exact excited states of nonintegrable models", Physical Review B **98**, 235155 (2018).

[97] T. Iadecola and M. Žnidarič, "Exact Localized and Ballistic Eigenstates in Disordered Chaotic Spin Ladders and the Fermi-Hubbard Model", Physical Review Letters **123**, 036403 (2019).

[98] M. Schecter and T. Iadecola, "Weak Ergodicity Breaking and Quantum Many-Body Scars in Spin-1 XY Magnets", Physical Review Letters **123**, 147201 (2019).

[99] T. Iadecola and M. Schecter, "Quantum many-body scar states with emergent kinetic constraints and finite-entanglement revivals", Physical Review B **101**, 024306 (2020).

[100] D. K. Mark, C.-J. Lin, and O. I. Motrunich, "Unified structure for exact towers of scar states in the Affleck-Kennedy-Lieb-Tasaki and other models", Physical Review B **101**, 195131 (2020).

[101] D. K. Mark and O. I. Motrunich, "η-pairing states as true scars in an extended Hubbard model", Physical Review B **102**, 075132 (2020).

[102] S. Moudgalya, N. Regnault, and B. A. Bernevig, "η-pairing in Hubbard models: From spectrum generating algebras to quantum many-body scars", Physical Review B **102**, 085140 (2020).

[103] N. Shibata, N. Yoshioka, and H. Katsura, "Onsager's Scars in Disordered Spin Chains", Physical Review Letters **124**, 180604 (2020).

[104] S. Chattopadhyay, H. Pichler, M. D. Lukin, and W. W. Ho, "Quantum many-body scars from virtual entangled pairs", Physical Review B **101**, 174308 (2020).

[105] N. O'Dea, F. Burnell, A. Chandran, and V. Khemani, "From tunnels to towers: Quantum scars from Lie algebras and q -deformed Lie algebras", Physical Review Research **2**, 043305 (2020).

[106] K. Lee, R. Melendrez, A. Pal, and H. J. Changlani, "Exact three-colored quantum scars from geometric frustration", Physical Review B **101**, 241111(R) (2020).

[107] Y. Kuno, T. Mizoguchi, and Y. Hatsugai, "Multiple quantum scar states and emergent slow thermalization in a flat-band system", Physical Review B **104**, 085130 (2021).

[108] J. Jeyaretnam, J. Richter, and A. Pal, "Quantum scars and bulk coherence in a symmetry-protected topological phase", Physical Review B **104**, 014424 (2021).

[109] S. Moudgalya, B. A. Bernevig, and N. Regnault, "Quantum many-body scars and Hilbert space fragmentation: a review of exact results", Reports on Progress in Physics **85**, 086501 (2022).

[110] P. Sala, T. Rakovszky, R. Verresen, M. Knap, and F. Pollmann, "Ergodicity Breaking Arising from Hilbert Space Fragmentation in Dipole-Conserving Hamiltonians", Physical Review X **10**, 011047 (2020).

[111] V. Khemani, M. Hermele, and R. Nandkishore, "Localization from Hilbert space shattering: From theory to physical realizations", Physical Review B **101**, 174204 (2020).

[112] S. R. Taylor, M. Schulz, F. Pollmann, and R. Moessner, "Experimental probes of Stark many-body localization", Physical Review B **102**, 054206 (2020).

[113] S. Moudgalya, A. Prem, R. Nandkishore, N. Regnault, and B. A. Bernevig, "Thermalization and Its Absence within Krylov Subspaces of a Constrained Hamiltonian", in *Memorial Volume for Shoucheng Zhang* (World Scientific, 2021), pp. 147–209.

[114] E. V. H. Doggen, I. V. Gornyi, and D. G. Polyakov, "Stark many-body localization: Evidence for Hilbert-space shattering", Physical Review B **103**, L100202 (2021).

[115] A. Chattopadhyay, B. Mukherjee, K. Sengupta, and A. Sen, "Strong Hilbert space fragmentation via emergent quantum drums in two dimensions", SciPost Physics **14**, 146 (2023).

[116] M. A. Nielsen and I. L. Chuang, *Quantum Computation and Quantum Information* (Cambridge University Press, 2012).

[117] C. H. Bennett and D. P. DiVincenzo, "Quantum information and computation", Nature **404**, 247–255 (2000).

[118] D. A. Abanin, E. Altman, I. Bloch, and M. Serbyn, "Colloquium: Many-body localization, thermalization, and entanglement", Reviews of Modern Physics **91**, 021001 (2019).

[119] P. W. Anderson, "Absence of Diffusion in Certain Random Lattices", Physical Review **109**, 1492–1505 (1958).

[120] L. Landau, "Diamagnetismus der Metalle", Zeitschrift für Physik **64**, 629–637 (1930).

[121] J. Vidal, R. Mosseri, and B. Douçot, "Aharonov-Bohm Cages in Two-Dimensional Structures", Physical Review Letters **81**, 5888–5891 (1998).

[122] J. Vidal, B. Douçot, R. Mosseri, and P. Butaud, "Interaction Induced Delocalization for Two Particles in a Periodic Potential", Physical Review Letters **85**, 3906–3909 (2000).

[123] S. Flach, D. Leykam, J. D. Bodyfelt, P. Matthies, and A. S. Desyatnikov, "Detangling flat bands into Fano lattices", Europhysics Letters **105**, 30001 (2014).

[124] Y. Kuno, T. Mizoguchi, and Y. Hatsugai, "Flat band quantum scar", Physical Review B **102**, 241115 (2020).

[125] C. Danieli, A. Andreanov, and S. Flach, "Many-body flatband localization", Physical Review B **102**, 041116(R) (2020).

[126] C. Danieli, A. Andreanov, and S. Flach, "Many-body localization transition from flat-band fine tuning", Physical Review B **105**, L041113 (2022).

[127] M. Röntgen, C. V. Morfonios, I. Brouzos, F. K. Diakonos, and P. Schmelcher, "Quantum Network Transfer and Storage with Compact Localized States Induced by Local Symmetries", Physical Review Letters **123**, 1–6 (2019).

[128] L. Amico, M. Boshier, G. Birkl, A. Minguzzi, C. Miniatura, L.-C. Kwek, D. Aghamalyan, V. Ahufinger, D. Anderson, N. Andrei, A. S. Arnold, M. Baker, T. A. Bell, T. Bland, J. P. Brantut, D. Cassettari, W. J. Chetcuti, F. Chevy, R. Citro, S. De Palo, R. Dumke, M. Edwards, R. Folman, J. Fortagh, S. A. Gardiner, B. M. Garraway, G. Gauthier, A. Günther, T. Haug, C. Hufnagel, M. Keil, P. Ireland, M. Lebrat, W. Li, L. Longchambon, J. Mompart, O. Morsch, P. Naldesi, T. W. Neely, M. Olshanii, E. Orignac, S. Pandey, A. Pérez-Obiol, H. Perrin, L. Piroli, J. Polo, A. L. Pritchard, N. P. Proukakis, C. Rylands, H. Rubinsztein-Dunlop, F. Scazza, S. Stringari, F. Tosto, A. Trombettoni, N. Victorin, W. von Klitzing, D. Wilkowski, K. Xhani, and A. Yakimenko, "Roadmap on Atomtronics: State of the art and perspective", AVS Quantum Science **3**, 039201 (2021).

[129] L. Amico, D. Anderson, M. Boshier, J.-P. Brantut, L.-C. Kwek, A. Minguzzi, and W. von Klitzing, "Colloquium: Atomtronic circuits: From many-body physics to quantum technologies", Reviews of Modern Physics **94**, 041001 (2022).

[130] A. Kumar, R. Dubessy, T. Badr, C. De Rossi, M. de Goër de Herve, L. Longchambon, and H. Perrin, "Producing superfluid circulation states using phase imprinting", Physical Review A **97**, 043615 (2018).

[131] J. Polo, R. Dubessy, P. Pedri, H. Perrin, and A. Minguzzi, "Oscillations and Decay of Superfluid Currents in a One-Dimensional Bose Gas on a Ring", Physical Review Letters **123**, 1–6 (2019).

[132] S. Beattie, S. Moulder, R. J. Fletcher, and Z. Hadzibabic, "Persistent Currents in Spinor Condensates", Physical Review Letters **110**, 025301 (2013).

[133] M. F. Andersen, C. Ryu, P. Cladé, V. Natarajan, A. Vaziri, K. Helmerson, and W. D. Phillips, "Quantized rotation of atoms from photons with orbital angular momentum", Physical Review Letters **97**, 170406 (2006).

[134] M. Cominotti, D. Rossini, M. Rizzi, F. Hekking, and A. Minguzzi, "Optimal Persistent Currents for Interacting Bosons on a Ring with a Gauge Field", Physical Review Letters **113**, 025301 (2014).

[135] M. Cominotti, M. Rizzi, D. Rossini, D. Aghamalyan, L. Amico, L. C. Kwek, F. Hekking, and A. Minguzzi, "Optimal scaling of persistent currents for interacting bosons on a ring", The European Physical Journal Special Topics **224**, 519–524 (2015).

[136] G. Pecci, G. Aupetit-Diallo, M. Albert, P. Vignolo, and A. Minguzzi, "Persistent currents in a strongly interacting multicomponent Bose gas on a ring", Comptes Rendus. Physique **24**, 1–13 (2023).

[137] T. Schulte, L. Santos, A. Sanpera, and M. Lewenstein, "Vortex-vortex interactions in toroidally trapped Bose-Einstein condensates", Physical Review A **66**, 033602 (2002).

[138] S. Eckel, J. G. Lee, F. Jendrzejewski, N. Murray, C. W. Clark, C. J. Lobb, W. D. Phillips, M. Edwards, and G. K. Campbell, "Hysteresis in a quantized superfluid 'atomtronic' circuit", Nature **506**, 200–203 (2014).

[139] S. Eckel, F. Jendrzejewski, A. Kumar, C. J. Lobb, and G. K. Campbell, "Interferometric Measurement of the Current-Phase Relationship of a Superfluid Weak Link", Physical Review X **4**, 031052 (2014).

[140] C. Ryu, P. W. Blackburn, A. A. Blinova, and M. G. Boshier, "Experimental Realization of Josephson Junctions for an Atom SQUID", Physical Review Letters **111**, 205301 (2013).

[141] F. Jendrzejewski, S. Eckel, N. Murray, C. Lanier, M. Edwards, C. J. Lobb, and G. K. Campbell, "Resistive Flow in a Weakly Interacting Bose-Einstein Condensate", Physical Review Letters **113**, 045305 (2014).

[142] D. Aghamalyan, M. Cominotti, M. Rizzi, D. Rossini, F. Hekking, A. Minguzzi, L.-C. Kwek, and L. Amico, "Coherent superposition of current flows in an atomtronic quantum interference device", New Journal of Physics **17**, 045023 (2015).

[143] A. Kumar, N. Anderson, W. D. Phillips, S. Eckel, G. K. Campbell, and S. Stringari, "Minimally destructive, Doppler measurement of a quantized flow in a ring-shaped Bose–Einstein condensate", New Journal of Physics **18**, 025001 (2016).

[144] J. Clarke and A. I. Braginski, *The SQUID Handbook* (Wiley, 2004).

[145] J. L. Helm, S. L. Cornish, and S. A. Gardiner, "Sagnac Interferometry Using Bright Matter-Wave Solitons", Physical Review Letters **114**, 134101 (2015).

[146] J. Polo, J. Mompart, and V. Ahufinger, "Geometrically induced complex tunnelings for ultracold atoms carrying orbital angular momentum", Physical Review A **93**, 033613 (2016).

[147] G. Pelegrí, A. M. Marques, R. G. Dias, A. J. Daley, V. Ahufinger, and J. Mompart, "Topological edge states with ultracold atoms carrying orbital angular momentum in a diamond chain", Physical Review A **99**, 023612 (2019).

[148] G. Pelegrí, J. Mompart, V. Ahufinger, and A. J. Daley, "Quantum magnetism with ultracold bosons carrying orbital angular momentum", Physical Review A **100**, 023615 (2019).

[149] G. Pelegrí, A. M. Marques, V. Ahufinger, J. Mompart, and R. G. Dias, "Second-order topological corner states with ultracold atoms carrying orbital angular momentum in optical lattices", Physical Review B **100**, 205109 (2019).

[150] G. Pelegrí, A. M. Marques, V. Ahufinger, J. Mompart, and R. G. Dias, "Interaction-induced topological properties of two bosons in flat-band systems", Physical Review Research **2**, 033267 (2020).

[151] E. Nicolau, J. Mompart, B. Juliá-Díaz, and V. Ahufinger, "Orbital angular momentum dynamics of Bose-Einstein condensates trapped in two stacked rings", Physical Review A **102**, 023331 (2020).

[152] E. Nicolau, A. M. Marques, J. Mompart, R. G. Dias, and V. Ahufinger, "Bosonic orbital Su-Schrieffer-Heeger model in a lattice of rings", Physical Review A **108**, 023317 (2023).

[153] E. Nicolau, A. M. Marques, R. G. Dias, J. Mompart, and V. Ahufinger, "Many-body Aharonov-Bohm caging in a lattice of rings", Physical Review A **107**, 023305 (2023).

[154] E. Nicolau, A. M. Marques, J. Mompart, V. Ahufinger, and R. G. Dias, "Local Hilbert space fragmentation and weak thermalization in Bose-Hubbard diamond necklaces", Physical Review B **107**, 094312 (2023).

[155] E. Nicolau, A. M. Marques, R. G. Dias, and V. Ahufinger, "Flat-band induced local Hilbert space fragmentation", (2023), arXiv:2306.15660.

[156] M. Fierz, "Über die relativistische Theorie kräftefreier Teilchen mit beliebigem Spin", Helvetica Physica Acta **12**, 3–37 (1939).

[157] W. Pauli, "The Connection Between Spin and Statistics", Physical Review **58**, 716–722 (1940).

[158] J. Schwinger, "The Theory of Quantized Fields. I", Physical Review **82**, 914–927 (1951).

[159] M. Ueda, *Fundamentals and New Frontiers of Bose-Einstein Condensation* (World Scientific, 2010).

[160] C. Pethick and H. Smith, *Bose Einstein Condensation in Dilute Gases* (Cambridge University Press, 2008).

[161] C. N. Yang, "Concept of Off-Diagonal Long-Range Order and the Quantum Phases of Liquid He and of Superconductors", Reviews of Modern Physics **34**, 694–704 (1962).

[162]   J. W. Kane and L. P. Kadanoff, "Long-Range Order in Superfluid Helium", Physical Review **155**, 80–83 (1967).

[163]   D. S. Petrov, G. V. Shlyapnikov, and J. T. M. Walraven, "Regimes of Quantum Degeneracy in Trapped 1D Gases", Physical Review Letters **85**, 3745–3749 (2000).

[164]   D. S. Petrov, M. Holzmann, and G. V. Shlyapnikov, "Bose-Einstein Condensation in Quasi-2D Trapped Gases", Physical Review Letters **84**, 2551–2555 (2000).

[165]   L. Pitaevskii and S. Stringari, *Bose-Einstein condensation* (Oxford University Press, 2003).

[166]   F. Dalfovo, S. Giorgini, L. P. Pitaevskii, and S. Stringari, "Theory of Bose-Einstein condensation in trapped gases", Reviews of Modern Physics **71**, 463–512 (1999).

[167]   J. J. Sakurai, *Modern Quantum Mechanics* (Addison Wesley, 1985).

[168]   E. P. Gross, "Unified Theory of Interacting Bosons", Physical Review **106**, 161–162 (1957).

[169]   V. L. Ginzburg, L. P. Pitaevskii, and P. N. Lebedev, "On the theory of superfluidity", J. Exptl. Theoret. Phys. (U.S.S.R.) **34**, 1240–1245 (1958).

[170]   M. Greiner, "Ultracold quantum gases in three-dimensional optical lattice", PhD thesis (Ludwig Maxmilian University, Munich, 2003).

[171]   J. M. Ziman, *Principles of the Theory of Solids* (Cambridge University Press, 1964).

[172]   M. Born and V. Fock, "Beweis des Adiabatensatzes", Zeitschrift für Physik **51**, 165–180 (1928).

[173]   M. Lewenstein, A. Sanpera, V. Ahufinger, B. Damski, A. Sen(De), and U. Sen, "Ultracold atomic gases in optical lattices: mimicking condensed matter physics and beyond", Advances in Physics **56**, 243–379 (2007).

[174]   P. Sierant and J. Zakrzewski, "Many-body localization of bosons in optical lattices", New Journal of Physics **20**, 043032 (2018).

[175]   O. Dutta, M. Gajda, P. Hauke, M. Lewenstein, D.-S. Lühmann, B. A. Malomed, T. Sowiński, and J. Zakrzewski, "Non-standard Hubbard models in optical lattices: a review", Reports on Progress in Physics **78**, 066001 (2015).

[176]   X. Li and W. V. Liu, "Physics of higher orbital bands in optical lattices: a review", Reports on Progress in Physics **79**, 116401 (2016).

[177]   V. Fock, "Konfigurationsraum und zweite Quantelung", Zeitschrift für Physik **75**, 622–647 (1932).

[178]   D. Raventós, T. Graß, M. Lewenstein, and B. Juliá-Díaz, "Cold bosons in optical lattices: a tutorial for exact diagonalization", Journal of Physics B: Atomic, Molecular and Optical Physics **50**, 113001 (2017).

[179]   R. Orús, "Tensor networks for complex quantum systems", Nature Reviews Physics **1**, 538–550 (2019).

[180] U. Schollwöck, "The density-matrix renormalization group in the age of matrix product states", Annals of Physics **326**, 96–192 (2011).

[181] R. J. Trudeau, *Introduction to Graph Theory* (Dover Publications, 1994).

[182] E. Estrada and P. A. Knight, *A First Course in Network Theory* (Oxford University Press, 2015).

[183] D. Cvetkovic, P. Rowlinson, and S. Simic, *Eigenspaces of Graphs* (Cambridge University Press, 1997).

[184] A. Hudomal, I. Vasić, N. Regnault, and Z. Papić, "Quantum scars of bosons with correlated hopping", Communications Physics **3**, 99 (2020).

[185] D. Hahn, P. A. McClarty, and D. J. Luitz, "Information dynamics in a model with Hilbert space fragmentation", SciPost Physics **11**, 074 (2021).

[186] J. Polo, A. Benseny, T. Busch, V. Ahufinger, and J. Mompart, "Transport of ultracold atoms between concentric traps via spatial adiabatic passage", New Journal of Physics **18**, 015010 (2016).

[187] G. Pelegrí, "Ultracold atoms carrying orbital angular momentum", PhD thesis (Universitat Autònoma de Barcelona, 2020).

[188] B. E. Sherlock, M. Gildemeister, E. Owen, E. Nugent, and C. J. Foot, "Time-averaged adiabatic ring potential for ultracold atoms", Physical Review A **83**, 043408 (2011).

[189] A. S. Arnold, "Extending dark optical trapping geometries", Optics Letters **37**, 2505 (2012).

[190] T. A. Bell, J. A. Glidden, L. Humbert, M. W. Bromley, S. A. Haine, M. J. Davis, T. W. Neely, M. A. Baker, and H. Rubinsztein-Dunlop, "Bose-Einstein condensation in large time-averaged optical ring potentials", New Journal of Physics **18**, 035003 (2016).

[191] S. K. Schnelle, E. D. van Ooijen, M. J. Davis, N. R. Heckenberg, and H. Rubinsztein-Dunlop, "Versatile two-dimensional potentials for ultra-cold atoms", Optics Express **16**, 1405 (2008).

[192] K. Henderson, C. Ryu, C. MacCormick, and M. G. Boshier, "Experimental demonstration of painting arbitrary and dynamic potentials for Bose-Einstein condensates", New Journal of Physics **11**, 043030 (2009).

[193] E. M. Wright, J. Arlt, and K. Dholakia, "Toroidal optical dipole traps for atomic Bose-Einstein condensates using Laguerre-Gaussian beams", Physical Review A **63**, 013608 (2000).

[194] S. Gupta, K. W. Murch, K. L. Moore, T. P. Purdy, and D. M. Stamper-Kurn, "Bose-Einstein Condensation in a Circular Waveguide", Physical Review Letters **95**, 143201 (2005).

[195] O. Morizot, Y. Colombe, V. Lorent, H. Perrin, and B. M. Garraway, "Ring trap for ultracold atoms", Physical Review A **74**, 023617 (2006).

[196] C. Ryu, M. Andersen, P. Cladé, V. Natarajan, K. Helmerson, and W. Phillips, "Observation of Persistent Flow of a Bose-Einstein Condensate in a Toroidal Trap", Physical Review Letters **99**, 260401 (2007).

[197] A. Turpin, J. Polo, Y. V. Loiko, J. Küber, F. Schmaltz, T. K. Kalkandjiev, V. Ahufinger, G. Birkl, and J. Mompart, "Blue-detuned optical ring trap for Bose-Einstein condensates based on conical refraction", Optics Express **23**, 1638 (2015).

[198] K. C. Wright, R. B. Blakestad, C. J. Lobb, W. D. Phillips, and G. K. Campbell, "Driving Phase Slips in a Superfluid Atom Circuit with a Rotating Weak Link", Physical Review Letters **110**, 025302 (2013).

[199] S. Franke-Arnold, "Optical angular momentum and atoms", Philosophical Transactions of the Royal Society A: Mathematical, Physical and Engineering Sciences **375**, 20150435 (2017).

[200] L. Corman, L. Chomaz, T. Bienaimé, R. Desbuquois, C. Weitenberg, S. Nascimbène, J. Dalibard, and J. Beugnon, "Quench-Induced Supercurrents in an Annular Bose Gas", Physical Review Letters **113**, 135302 (2014).

[201] G. Gauthier, I. Lenton, N. McKay Parry, M. Baker, M. J. Davis, H. Rubinsztein-Dunlop, and T. W. Neely, "Direct imaging of a digital-micromirror device for configurable microscopic optical potentials", Optica **3**, 1136 (2016).

[202] J. Küber, "Dynamics of Bose-Einstein condensates in novel optical potentials", PhD thesis (Technische Universität Darmstadt, 2014).

[203] F. Moscatelli, C. Sackett, S. Du, and E. Oh, "Far-off-resonant ring trap near the ends of optical fibers", Physical Review A **76**, 043404 (2007).

[204] G. Wirth, M. Ölschläger, and A. Hemmerich, "Evidence for orbital superfluidity in the P-band of a bipartite optical square lattice", Nature Physics 7, 147–153 (2011).

[205] X. Li and W. V. Liu, "Physics of higher orbital bands in optical lattices: a review", Reports on Progress in Physics **79**, 116401 (2016).

[206] A. Kiely, A. Benseny, T. Busch, and A. Ruschhaupt, "Shaken not stirred: creating exotic angular momentum states by shaking an optical lattice", Journal of Physics B: Atomic, Molecular and Optical Physics **49**, 215003 (2016).

[207] T. Kock, C. Hippler, A. Ewerbeck, and A. Hemmerich, "Orbital optical lattices with bosons", Journal of Physics B: Atomic, Molecular and Optical Physics **49**, 042001 (2016).

[208] M. A. Armstrong, *Basic Topology* (Springer New York, 1983).

[209] N. R. Cooper, J. Dalibard, and I. B. Spielman, "Topological bands for ultracold atoms", Reviews of Modern Physics **91**, 015005 (2019).

[210] J. K. Asbóth, L. Oroszlány, and A. Pályi, *A Short Course on Topological Insulators* (Springer International Publishing, 2016).

[211] D. Vanderbilt, *Berry Phases in Electronic Structure Theory* (Cambridge University Press, 2018).

[212] M. Berry, "Quantal phase factors accompanying adiabatic changes", Proceedings of the Royal Society of London. A. Mathematical and Physical Sciences **392**, 45–57 (1984).

[213] M. Berry, "The quantum phase, five years after", in *Geometric phases in physics* (1989), pp. 7–28.

[214] M. Z. Hasan and C. L. Kane, "Colloquium: Topological insulators", Reviews of Modern Physics **82**, 3045–3067 (2010).

[215] F. Wilczek and A. Zee, "Appearance of Gauge Structure in Simple Dynamical Systems", Physical Review Letters **52**, 2111–2114 (1984).

[216] M. Kremer, I. Petrides, E. Meyer, M. Heinrich, O. Zilberberg, and A. Szameit, "A square-root topological insulator with non-quantized indices realized with photonic Aharonov-Bohm cages", Nature Communications **11**, 907 (2020).

[217] X.-L. Qi and S.-C. Zhang, "Topological insulators and superconductors", Reviews of Modern Physics **83**, 1057–1110 (2011).

[218] J. Zak, "Berry's phase for energy bands in solids", Physical Review Letters **62**, 2747–2750 (1989).

[219] L. Wang, W. Cai, M. Bie, X. Zhang, and J. Xu, "Zak phase and topological plasmonic Tamm states in one-dimensional plasmonic crystals", Optics Express **26**, 28963 (2018).

[220] H.-X. Wang, G.-Y. Guo, and J.-H. Jiang, "Band topology in classical waves: Wilson-loop approach to topological numbers and fragile topology", New Journal of Physics **21**, 093029 (2019).

[221] S. Deng, G. Ortiz, and L. Viola, "Multiband s-wave topological superconductors: Role of dimensionality and magnetic field response", Physical Review B **87**, 205414 (2013).

[222] W. Zhu, Y.-q. Ding, J. Ren, Y. Sun, Y. Li, H. Jiang, and H. Chen, "Zak phase and band inversion in dimerized one-dimensional locally resonant metamaterials", Physical Review B **97**, 195307 (2018).

[223] C. Bena and G. Montambaux, "Remarks on the tight-binding model of graphene", New Journal of Physics **11**, 095003 (2009).

[224] J. Cayssol and J. N. Fuchs, "Topological and geometrical aspects of band theory", Journal of Physics: Materials **4**, 034007 (2021).

[225] J.-N. Fuchs and F. Piéchon, "Orbital embedding and topology of one-dimensional two-band insulators", Physical Review B **104**, 235428 (2021).

[226] J. Zurita, C. Creffield, and G. Platero, "Tunable zero modes and quantum interferences in flat-band topological insulators", Quantum **5**, 591 (2021).

[227] W. P. Su, J. R. Schrieffer, and A. J. Heeger, "Solitons in Polyacetylene", Physical Review Letters **42**, 1698–1701 (1979).

[228] S. Ryu and Y. Hatsugai, "Topological Origin of Zero-Energy Edge States in Particle-Hole Symmetric Systems", Physical Review Letters **89**, 077002 (2002).

[229] J.-W. Rhim, J. H. Bardarson, and R.-J. Slager, "Unified bulk-boundary correspondence for band insulators", Physical Review B **97**, 115143 (2018).

[230] M. Ueda, "Quantum equilibration, thermalization and prethermalization in ultracold atoms", Nature Reviews Physics **2**, 669–681 (2020).

[231] J. M. Deutsch, "Eigenstate thermalization hypothesis", Reports on Progress in Physics **81**, 082001 (2018).

[232] J. V. José and E. J. Saletan, *Classical Dynamics: A Contemporary Approach* (Cambridge University Press, 1998).

[233] J. Berkovitz, R. Frigg, and F. Kronz, "The ergodic hierarchy, randomness and Hamiltonian chaos", Studies in History and Philosophy of Science Part B: Studies in History and Philosophy of Modern Physics **37**, 661–691 (2006).

[234] K. T. Alligood, T. D. Sauer, and J. A. Yorke, *Chaos* (Springer New York, 1996).

[235] I. P. Cornfeld, S. V. Fomin, and Y. G. Sinai, *Ergodic Theory* (Springer New York, 1982).

[236] G. Belot and J. Earman, "Chaos out of order: Quantum mechanics, the correspondence principle and chaos", Studies in History and Philosophy of Science Part B: Studies in History and Philosophy of Modern Physics **28**, 147–182 (1997).

[237] C. Werndl, "What Are the New Implications of Chaos for Unpredictability?", The British Journal for the Philosophy of Science **60**, 195–220 (2009).

[238] N. Chernov and R. Markarian, *Chaotic Billiards* (American Mathematical Society, 2006).

[239] S. Zelditch and M. Zworski, "Ergodicity of eigenfunctions for ergodic billiards", Communications in Mathematical Physics **175**, 673–682 (1996).

[240] Mehran Kardar, *Statistical Physics of Particles* (Cambridge University Press, 2007).

[241] J. v. Neumann, "Beweis des Ergodensatzes und desH-Theorems in der neuen Mechanik", Zeitschrift für Physik **57**, 30–70 (1929).

[242] O. Lychkovskiy, "Dependence of decoherence-assisted classicality on the way a system is partitioned into subsystems", Physical Review A **87**, 022112 (2013).

[243] B. Sutherland, *Beautiful models: 70 years of exactly solved quantum many-body problems* (World Scientific, 2004).

[244] T. Mori, T. N. Ikeda, E. Kaminishi, and M. Ueda, "Thermalization and prethermalization in isolated quantum systems: a theoretical overview", Journal of Physics B: Atomic, Molecular and Optical Physics **51**, 112001 (2018).

[245] F. Alet and N. Laflorencie, "Many-body localization: An introduction and selected topics", Comptes Rendus Physique **19**, 498–525 (2018).

[246] I. V. Gornyi, A. D. Mirlin, and D. G. Polyakov, "Interacting Electrons in Disordered Wires: Anderson Localization and Low-T Transport", Physical Review Letters **95**, 206603 (2005).

[247] D. Basko, I. Aleiner, and B. Altshuler, "Metal–insulator transition in a weakly interacting many-electron system with localized single-particle states", Annals of Physics **321**, 1126–1205 (2006).

[248] N. Shiraishi and T. Mori, "Systematic Construction of Counterexamples to the Eigenstate Thermalization Hypothesis", Physical Review Letters **119**, 030601 (2017).

[249] S. Moudgalya and O. I. Motrunich, "Hilbert Space Fragmentation and Commutant Algebras", Physical Review X **12**, 011050 (2022).

[250] B. Buča, "Out-of-Time-Ordered Crystals and Fragmentation", Physical Review Letters **128**, 100601 (2022).

[251] B. T. Seaman, M. Krämer, D. Z. Anderson, and M. J. Holland, "Atomtronics: Ultracold-atom analogs of electronic devices", Physical Review A **75**, 023615 (2007).

[252] L. Amico, G. Birkl, M. Boshier, and L.-C. Kwek, "Focus on atomtronics-enabled quantum technologies", New Journal of Physics **19**, 020201 (2017).

[253] G. Pelegrí, J. Mompart, and V. Ahufinger, "Quantum sensing using imbalanced counter-rotating Bose–Einstein condensate modes", New Journal of Physics **20**, 103001 (2018).

[254] B. Barrett, R. Geiger, I. Dutta, M. Meunier, B. Canuel, A. Gauguet, P. Bouyer, and A. Landragin, "The Sagnac effect: 20 years of development in matter-wave interferometry", Comptes Rendus Physique **15**, 875–883 (2014).

[255] F. I. Moxley, J. P. Dowling, W. Dai, and T. Byrnes, "Sagnac interferometry with coherent vortex superposition states in exciton-polariton condensates", Physical Review A **93**, 053603 (2016).

[256] S. P. Nolan, J. Sabbatini, M. W. J. Bromley, M. J. Davis, and S. A. Haine, "Quantum enhanced measurement of rotations with a spin-1 Bose-Einstein condensate in a ring trap", Physical Review A **93**, 023616 (2016).

[257] P. Navez, S. Pandey, H. Mas, K. Poulios, T. Fernholz, and W. von Klitzing, "Matter-wave interferometers using TAAP rings", New Journal of Physics **18**, 075014 (2016).

[258] S. Safaei, L.-C. Kwek, R. Dumke, and L. Amico, "Monitoring currents in cold-atom circuis", Physical Review A **100**, 013621 (2019).

[259] B. P. Anderson, K. Dholakia, and E. M. Wright, "Atomic-phase interference devices based on ring-shaped Bose-Einstein condensates: Two-ring case", Physical Review A **67**, 033601 (2003).

[260] L. Amico, D. Aghamalyan, F. Auksztol, H. Crepaz, R. Dumke, and L. C. Kwek, "Superfluid qubit systems with ring shaped optical lattices", Scientific Reports **4**, 4298 (2015).

[261] Y.-H. Wang, A. Kumar, F. Jendrzejewski, R. M. Wilson, M. Edwards, S. Eckel, G. K. Campbell, and C. W. Clark, "Resonant wavepackets and shock waves in an atomtronic SQUID", New Journal of Physics **17**, 125012 (2015).

[262]   L. Corman, L. Chomaz, T. Bienaimé, R. Desbuquois, C. Weitenberg, S. Nascimbène, J. Dalibard, and J. Beugnon, "Quench-Induced Supercurrents in an Annular Bose Gas", Physical Review Letters **113**, 135302 (2014).

[263]   B. Josephson, "Possible new effects in superconductive tunnelling", Physics Letters **1**, 251–253 (1962).

[264]   P. W. Anderson and J. M. Rowell, "Probable Observation of the Josephson Superconducting Tunneling Effect", Physical Review Letters **10**, 230–232 (1963).

[265]   A. Smerzi, S. Fantoni, S. Giovanazzi, and S. R. Shenoy, "Quantum Coherent Atomic Tunneling between Two Trapped Bose-Einstein Condensates", Physical Review Letters **79**, 4950–4953 (1997).

[266]   M. Albiez, R. Gati, J. Fölling, S. Hunsmann, M. Cristiani, and M. K. Oberthaler, "Direct Observation of Tunneling and Nonlinear Self-Trapping in a Single Bosonic Josephson Junction", Physical Review Letters **95**, 010402 (2005).

[267]   Y. Shin, G.-B. Jo, M. Saba, T. A. Pasquini, W. Ketterle, and D. E. Pritchard, "Optical Weak Link between Two Spatially Separated Bose-Einstein Condensates", Physical Review Letters **95**, 170402 (2005).

[268]   S. Levy, E. Lahoud, I. Shomroni, and J. Steinhauer, "The a.c. and d.c. Josephson effects in a Bose–Einstein condensate", Nature **449**, 579–583 (2007).

[269]   G. Ferrini, A. Minguzzi, and F. W. J. Hekking, "Number squeezing, quantum fluctuations, and oscillations in mesoscopic Bose Josephson junctions", Physical Review A **78**, 023606 (2008).

[270]   G. Ferrini, D. Spehner, A. Minguzzi, and F. W. J. Hekking, "Noise in Bose Josephson junctions: Decoherence and phase relaxation", Physical Review A **82**, 033621 (2010).

[271]   T. Schumm, S. Hofferberth, L. M. Andersson, S. Wildermuth, S. Groth, I. Bar-Joseph, J. Schmiedmayer, and P. Krüger, "Matter-wave interferometry in a double well on an atom chip", Nature Physics **1**, 57–62 (2005).

[272]   B. V. Hall, S. Whitlock, R. Anderson, P. Hannaford, and A. I. Sidorov, "Condensate splitting in an asymmetric double well for atom chip based sensors", Physical Review Letters **98**, 030402 (2007).

[273]   G.-B. Jo, Y. Shin, S. Will, T. A. Pasquini, M. Saba, W. Ketterle, D. E. Pritchard, M. Vengalattore, and M. Prentiss, "Long Phase Coherence Time and Number Squeezing of Two Bose-Einstein Condensates on an Atom Chip", Physical Review Letters **98**, 030407 (2007).

[274]   J. Estève, C. Gross, A. Weller, S. Giovanazzi, and M. K. Oberthaler, "Squeezing and entanglement in a Bose-Einstein condensate", Nature **455**, 1216–1219 (2008).

[275]   D. Aghamalyan, L. Amico, and L. C. Kwek, "Effective dynamics of cold atoms flowing in two ring-shaped optical potentials with tunable tunneling", Physical Review A **88**, 063627 (2013).

[276]   A. Escrivà, A. M. Mateo, M. Guilleumas, and B. Juliá-Díaz, "Tunneling vortex dynamics in linearly coupled Bose-Hubbard rings", Physical Review A **100**, 063621 (2019).

[277]   I. Lesanovsky and W. von Klitzing, "Spontaneous Emergence of Angular Momentum Josephson Oscillations in Coupled Annular Bose-Einstein Condensates", Physical Review Letters **98**, 050401 (2007).

[278]   J. Brand, T. J. Haigh, and U. Zülicke, "Sign of coupling in barrier-separated Bose-Einstein condensates and stability of double-ring systems", Physical Review A **81**, 025602 (2010).

[279]   N. V. Hung, K. Zegadlo, A. Ramaniuk, V. V. Konotop, and M. Trippenbach, "Modulational instability of coupled ring waveguides with linear gain and nonlinear loss", Scientific Reports 7, 4089 (2017).

[280]   A. Richaud and V. Penna, "Quantum dynamics of bosons in a two-ring ladder: Dynamical algebra, vortexlike excitations, and currents", Physical Review A **96**, 013620 (2017).

[281]   A. Ramaniuk, N. Hung, M. Giersig, K. Kempa, V. Konotop, and M. Trippenbach, "Vortex Creation without Stirring in Coupled Ring Resonators with Gain and Loss", Symmetry **10**, 195 (2018).

[282]   K. Zegadlo, H. V. Nguyen, V. V. Konotop, J. Zakrzewski, and M. Trippenbach, "Route to chaos in a coupled microresonator system with gain and loss", Nonlinear Dynamics **97**, 559–569 (2019).

[283]   A. Oliinyk, I. Yatsuta, B. Malomed, and A. Yakimenko, "Symmetry Breaking in Interacting Ring-Shaped Superflows of Bose–Einstein Condensates", Symmetry **11**, 1312 (2019).

[284]   A. Oliinyk, A. Yakimenko, and B. Malomed, "Tunneling of persistent currents in coupled ring-shaped Bose–Einstein condensates", Journal of Physics B: Atomic, Molecular and Optical Physics **52**, 225301 (2019).

[285]   A. Oliinyk, B. Malomed, and A. Yakimenko, "Nonlinear dynamics of Josephson vortices in merging superfluid rings", Communications in Nonlinear Science and Numerical Simulation **83**, 105113 (2020).

[286]   X.-F. Zhang, R.-F. Dong, T. Liu, W. M. Liu, and S.-G. Zhang, "Spin-orbit-coupled Bose-Einstein condensates confined in concentrically coupled annular traps", Physical Review A **86**, 063628 (2012).

[287]   T. Bland, Q. Marolleau, P. Comaron, B. A. Malomed, and N. P. Proukakis, "Persistent current formation in double-ring geometries", Journal of Physics B: Atomic, Molecular and Optical Physics **53**, 115301 (2020).

[288]   L. Lin, Y. Ke, and C. Lee, "Topological invariants for interacting systems: From twisted boundary conditions to center-of-mass momentum", Physical Review B **107**, 125161 (2023).

[289]   J. Hubbard, "Electron correlations in narrow energy bands", Proceedings of the Royal Society of London. Series A. Mathematical and Physical Sciences **276**, 238–257 (1963).

[290]   D. C. Mattis, "The few-body problem on a lattice", Reviews of Modern Physics **58**, 361–379 (1986).

[291]   K. Winkler, G. Thalhammer, F. Lang, R. Grimm, J. Hecker Denschlag, A. J. Daley, A. Kantian, H. P. Büchler, and P. Zoller, "Repulsively bound atom pairs in an optical lattice", Nature **441**, 853–856 (2006).

[292]   C. E. Creffield and G. Platero, "Localization of two interacting electrons in quantum dot arrays driven by an ac field", Physical Review B **69**, 165312 (2004).

[293]   C. E. Creffield and G. Platero, "Coherent Control of Interacting Particles Using Dynamical and Aharonov-Bohm Phases", Physical Review Letters **105**, 086804 (2010).

[294]   M. Bello, G. Platero, and S. Kohler, "Doublon lifetimes in dissipative environments", Physical Review B **96**, 045408 (2017).

[295]   S. Wall, D. Brida, S. R. Clark, H. P. Ehrke, D. Jaksch, A. Ardavan, S. Bonora, H. Uemura, Y. Takahashi, T. Hasegawa, H. Okamoto, G. Cerullo, and A. Cavalleri, "Quantum interference between charge excitation paths in a solid-state Mott insulator", Nature Physics 7, 114–118 (2011).

[296]   M. Valiente and D. Petrosyan, "Scattering resonances and two-particle bound states of the extended Hubbard model", Journal of Physics B: Atomic, Molecular and Optical Physics **42**, 121001 (2009).

[297]   M. Valiente, "Lattice two-body problem with arbitrary finite-range interactions", Physical Review A **81**, 042102 (2010).

[298]   S. Longhi, "Bloch-Zener oscillations of strongly correlated electrons", Physical Review B **86**, 075144 (2012).

[299]   M. Di Liberto, A. Recati, I. Carusotto, and C. Menotti, "Two-body bound and edge states in the extended SSH Bose-Hubbard model", The European Physical Journal Special Topics **226**, 2751–2762 (2017).

[300]   M. Valiente, M. Küster, and A. Saenz, "Frustrated collisions and unconventional pairing on a quantum superlattice", Europhysics Letters **92**, 10001 (2010).

[301]   C. Menotti, F. Minganti, and A. Recati, "Momentum-dependent pseudospin dimers of coherently coupled bosons in optical lattices", Physical Review A **93**, 033602 (2016).

[302]   Y. Zhang, H. Lin, and C. Wu, "Bond order wave and energy gap in a 1D SSH-Hubbard model of conjugated polymers", Synthetic Metals **135-136**, 449–450 (2003).

[303]   M. Di Liberto, A. Recati, I. Carusotto, and C. Menotti, "Two-body physics in the Su-Schrieffer-Heeger model", Physical Review A **94**, 062704 (2016).

[304]   A. M. Marques and R. G. Dias, "Multihole edge states in Su-Schrieffer-Heeger chains with interactions", Physical Review B **95**, 115443 (2017).

[305] A. M. Marques and R. G. Dias, "Topological bound states in interacting Su–Schrieffer–Heeger rings", Journal of Physics: Condensed Matter **30**, 305601 (2018).

[306] P. St-Jean, V. Goblot, E. Galopin, A. Lemaître, T. Ozawa, L. Le Gratiet, I. Sagnes, J. Bloch, and A. Amo, "Lasing in topological edge states of a one-dimensional lattice", Nature Photonics **11**, 651–656 (2017).

[307] S.-L. Zhang and Q. Zhou, "Two-leg Su-Schrieffer-Heeger chain with glide reflection symmetry", Physical Review A **95**, 061601(R) (2017).

[308] M. Bello, C. E. Creffield, and G. Platero, "Long-range doublon transfer in a dimer chain induced by topology and ac fields", Scientific Reports **6**, 22562 (2016).

[309] M. A. Gorlach and A. N. Poddubny, "Topological edge states of bound photon pairs", Physical Review A **95**, 053866 (2017).

[310] G. Salerno, M. Di Liberto, C. Menotti, and I. Carusotto, "Topological two-body bound states in the interacting Haldane model", Physical Review A **97**, 013637 (2018).

[311] G. L. Bir and G. E. Pikus, *Symmetry and Strain-Induced Effects in Semiconductors* (Wiley, 1974).

[312] C. Cohen-Tannoudji, J. Dupont-Roc, and G. Grynberg, *Atom–Photon Interactions: Basic Processes and Applications* (Wiley, 1992).

[313] J. Zurita, C. E. Creffield, and G. Platero, "Topology and Interactions in the Photonic Creutz and Creutz-Hubbard Ladders", Advanced Quantum Technologies **3**, 1900105 (2020).

[314] C. W. Hsu, B. Zhen, A. D. Stone, J. D. Joannopoulos, and M. Soljačić, "Bound states in the continuum", Nature Reviews Materials **1**, 16048 (2016).

[315] J. Dalibard, F. Gerbier, G. Juzeliunas, and P. Öhberg, "Colloquium: Artificial gauge potentials for neutral atoms", Reviews of Modern Physics **83**, 1523–1543 (2011).

[316] Y. Aharonov and D. Bohm, "Significance of Electromagnetic Potentials in the Quantum Theory", Physical Review **115**, 485–491 (1959).

[317] T. T. Wu and C. N. Yang, "Concept of nonintegrable phase factors and global formulation of gauge fields", Physical Review D **12**, 3845–3857 (1975).

[318] D. Bercioux, D. F. Urban, H. Grabert, and W. Häusler, "Massless Dirac-Weyl fermions in a $\mathcal{T}_3$ optical lattice", Physical Review A **80**, 063603 (2009).

[319] D. Bercioux, N. Goldman, and D. F. Urban, "Topology-induced phase transitions in quantum spin Hall lattices", Physical Review A **83**, 023609 (2011).

[320] C. C. Abilio, P. Butaud, T. Fournier, B. Pannetier, J. Vidal, S. Tedesco, and B. Dalzotto, "Magnetic Field Induced Localization in a Two-Dimensional Superconducting Wire Network", Physical Review Letters **83**, 5102–5105 (1999).

[321] C. Naud, G. Faini, and D. Mailly, "Aharonov-Bohm cages in 2D normal metal networks", Physical Review Letters **86**, 5104–5107 (2001).

[322]   K. Shinohara, T. Aoki, and A. Morinaga, "Scalar Aharonov-Bohm effect for ultracold atoms", Physical Review A **66**, 042106 (2002).

[323]   S. Mukherjee, M. Di Liberto, P. Öhberg, R. R. Thomson, and N. Goldman, "Experimental Observation of Aharonov-Bohm Cages in Photonic Lattices", Physical Review Letters **121**, 075502 (2018).

[324]   C. Jörg, G. Queraltó, M. Kremer, G. Pelegrí, J. Schulz, A. Szameit, G. von Freymann, J. Mompart, and V. Ahufinger, "Artificial gauge field switching using orbital angular momentum modes in optical waveguides", Light: Science & Applications **9**, 150 (2020).

[325]   M. Di Liberto, S. Mukherjee, and N. Goldman, "Nonlinear dynamics of Aharonov-Bohm cages", Physical Review A **100**, 043829 (2019).

[326]   G. Gligorić, P. P. Beličev, D. Leykam, and A. Maluckov, "Nonlinear symmetry breaking of Aharonov-Bohm cages", Physical Review A **99**, 013826 (2019).

[327]   G. Pelegrí, A. M. Marques, R. G. Dias, A. J. Daley, J. Mompart, and V. Ahufinger, "Topological edge states and Aharanov-Bohm caging with ultracold atoms carrying orbital angular momentum", Physical Review A **99**, 023613 (2019).

[328]   T. Zhang and G.-B. Jo, "One-dimensional sawtooth and zigzag lattices for ultracold atoms", Scientific Reports **5**, 16044 (2015).

[329]   S. Takayoshi, H. Katsura, N. Watanabe, and H. Aoki, "Phase diagram and pair Tomonaga-Luttinger liquid in a Bose-Hubbard model with flat bands", Physical Review A **88**, 063613 (2013).

[330]   M. Tovmasyan, E. P. L. van Nieuwenburg, and S. D. Huber, "Geometry-induced pair condensation", Physical Review B **88**, 220510(R) (2013).

[331]   M. Tovmasyan, S. Peotta, P. Törmä, and S. D. Huber, "Effective theory and emergent SU(2) symmetry in the flat bands of attractive Hubbard models", Physical Review B **94**, 245149 (2016).

[332]   M. Tovmasyan, S. Peotta, L. Liang, P. Törmä, and S. D. Huber, "Preformed pairs in flat Bloch bands", Physical Review B **98**, 134513 (2018).

[333]   D. Sticlet, L. Seabra, F. Pollmann, and J. Cayssol, "From fractionally charged solitons to Majorana bound states in a one-dimensional interacting model", Physical Review B **89**, 115430 (2014).

[334]   J. Jünemann, A. Piga, S.-J. Ran, M. Lewenstein, M. Rizzi, and A. Bermudez, "Exploring Interacting Topological Insulators with Ultracold Atoms: The Synthetic Creutz-Hubbard Model", Physical Review X **7**, 031057 (2017).

[335]   Y. Kuno, T. Orito, and I. Ichinose, "Flat-band many-body localization and ergodicity breaking in the Creutz ladder", New Journal of Physics **22**, 013032 (2020).

[336]   A. Mukherjee, A. Nandy, S. Sil, and A. Chakrabarti, "Engineering topological phase transition and Aharonov–Bohm caging in a flux-staggered lattice", Journal of Physics: Condensed Matter **33**, 035502 (2021).

[337] S. Ganeshan, K. Sun, and S. Das Sarma, "Topological Zero-Energy Modes in Gapless Commensurate Aubry-André-Harper Models", Physical Review Letters **110**, 180403 (2013).

[338] O. Mansikkamäki, S. Laine, A. Piltonen, and M. Silveri, "Beyond Hard-Core Bosons in Transmon Arrays", PRX Quantum **3**, 040314 (2022).

[339] S. Li, Z.-Y. Xue, M. Gong, and Y. Hu, "Non-Abelian Aharonov-Bohm caging in photonic lattices", Physical Review A **102**, 023524 (2020).

[340] W. Maimaiti, A. Andreanov, H. C. Park, O. Gendelman, and S. Flach, "Compact localized states and flat-band generators in one dimension", Physical Review B **95**, 115135 (2017).

[341] J.-W. Rhim and B.-J. Yang, "Classification of flat bands according to the band-crossing singularity of Bloch wave functions", Physical Review B **99**, 045107 (2019).

[342] R. G. Dias and J. D. Gouveia, "Origami rules for the construction of localized eigenstates of the Hubbard model in decorated lattices", Scientific Reports **5**, 16852 (2015).

[343] A. Nandy and A. Chakrabarti, "Engineering flat electronic bands in quasiperiodic and fractal loop geometries", Physics Letters, Section A: General, Atomic and Solid State Physics **379**, 2876–2882 (2015).

[344] B. Pal and K. Saha, "Flat bands in fractal-like geometry", Physical Review B **97**, 195101 (2018).

[345] A. Ramachandran, A. Andreanov, and S. Flach, "Chiral flat bands: Existence, engineering, and stability", Physical Review B **96**, 161104(R) (2017).

[346] L. Morales-Inostroza and R. A. Vicencio, "Simple method to construct flat-band lattices", Physical Review A **94**, 043831 (2016).

[347] A. Mielke, "Ferromagnetism in the Hubbard model on line graphs and further considerations", Journal of Physics A: Mathematical and General **24**, 3311–3321 (1991).

[348] C. V. Morfonios, M. Röntgen, M. Pyzh, and P. Schmelcher, "Flat bands by latent symmetry", Physical Review B **104**, 035105 (2021).

[349] W. Maimaiti, S. Flach, and A. Andreanov, "Universal $d = 1$ flat band generator from compact localized states", Physical Review B **99**, 125129 (2019).

[350] W. Maimaiti, A. Andreanov, and S. Flach, "Flat-band generator in two dimensions", Physical Review B **103**, 165116 (2021).

[351] W. Maimaiti and A. Andreanov, "Non-Hermitian flat-band generator in one dimension", Physical Review B **104**, 035115 (2021).

[352] C. Xu, G. Wang, Z. H. Hang, J. Luo, C. T. Chan, and Y. Lai, "Design of full-k-space flat bands in photonic crystals beyond the tight-binding picture", Scientific Reports **5**, 18181 (2015).

[353] P. Sathe, F. Harper, and R. Roy, "Compactly supported Wannier functions and strictly local projectors", Journal of Physics A: Mathematical and Theoretical **54**, 335302 (2021).

[354]   P. Sathe and R. Roy, "Compact Wannier Functions in One Dimension", (2023), arXiv:2302.11608.

[355]   W. Barrett, A. Francis, and B. Webb, "Equitable decompositions of graphs with symmetries", Linear Algebra and Its Applications **513**, 409–434 (2017).

[356]   A. Francis, D. Smith, D. Sorensen, and B. Webb, "Extensions and applications of equitable decompositions for graphs with symmetries", Linear Algebra and Its Applications **532**, 432–462 (2017).

[357]   M. Thüne, "Exploiting Equitable Partitions for Efficient Block Triangularization", (2016), arXiv:1605.05924.

[358]   M. Röntgen, C. V. Morfonios, and P. Schmelcher, "Compact localized states and flat bands from local symmetry partitioning", Physical Review B **97**, 035161 (2018).

[359]   T. Rakovszky, P. Sala, R. Verresen, M. Knap, and F. Pollmann, "Statistical localization: From strong fragmentation to strong edge modes", Physical Review B **101**, 125126 (2020).

[360]   G. De Tomasi, D. Hetterich, P. Sala, and F. Pollmann, "Dynamics of strongly interacting systems: From Fock-space fragmentation to many-body localization", Physical Review B **100**, 214313 (2019).

[361]   P. Frey, L. Hackl, and S. Rachel, "Hilbert space fragmentation and interaction-induced localization in the extended Fermi-Hubbard model", Physical Review B **106**, L220301 (2022).

[362]   B. Mukherjee, D. Banerjee, K. Sengupta, and A. Sen, "Minimal model for Hilbert space fragmentation with local constraints", Physical Review B **104**, 155117 (2021).

[363]   W. H. Li, X. Deng, and L. Santos, "Hilbert Space Shattering and Disorder-Free Localization in Polar Lattice Gases", Physical Review Letters **127**, 260601 (2021).

[364]   P. Brighi, M. Ljubotina, and M. Serbyn, "Hilbert space fragmentation and slow dynamics in particle-conserving quantum East models", (2022), arXiv:2210.15607.

[365]   S. N. Kempkes, P. Capiod, S. Ismaili, J. Mulkens, L. Eek, I. Swart, and C. Morais Smith, "Compact localized boundary states in a quasi-1D electronic diamond-necklace chain", Quantum Frontiers **2**, 1 (2023).

[366]   E. Chertkov and B. K. Clark, "Motif magnetism and quantum many-body scars", Physical Review B **104**, 104410 (2021).

[367]   A. Smith, J. Knolle, D. L. Kovrizhin, and R. Moessner, "Disorder-Free Localization", Physical Review Letters **118**, 266601 (2017).

[368]   A. Smith, J. Knolle, R. Moessner, and D. L. Kovrizhin, "Dynamical localization in Z2 lattice gauge theories", Physical Review B **97**, 245137 (2018).

[369]   A. Russomanno, S. Notarnicola, F. M. Surace, R. Fazio, M. Dalmonte, and M. Heyl, "Homogeneous Floquet time crystal protected by gauge invariance", Physical Review Research **2**, 012003(R) (2020).

[370] J. C. Halimeh, P. Hauke, J. Knolle, and F. Grusdt, "Temperature-Induced Disorder-Free Localization", (2022), arXiv:2206.11273.

[371] U. Borla, R. Verresen, F. Grusdt, and S. Moroz, "Confined Phases of One-Dimensional Spinless Fermions Coupled to Z2 Gauge Theory", Physical Review Letters **124**, 120503 (2020).

[372] B. Buča, "Unified Theory of Local Quantum Many-Body Dynamics: Eigenoperator Thermalization Theorems", Physical Review X **13**, 031013 (2023).

[373] N. Ivanov and J. Richter, "Competition between plaquette and dimer phases in Heisenberg chains", Physics Letters A **232**, 308–312 (1997).

[374] J. Richter, N. B. Ivanov, and J. Schulenburg, "The antiferromagnetic spin- chain with competing dimers and plaquettes: numerical versus exact results", Journal of Physics: Condensed Matter **10**, 3635–3649 (1998).

[375] A. Koga, K. Okunishi, and N. Kawakami, "First-order quantum phase transition in the orthogonal-dimer spin chain", Physical Review B **62**, 5558–5563 (2000).

[376] A. Honecker, J. Schulenburg, and J. Richter, "Magnetization plateaus in frustrated antiferromagnetic quantum spin models", Journal of Physics: Condensed Matter **16**, S749–S758 (2004).

[377] L. Čanová, J. Strečka, and M. Jaščur, "Exact Results of the Ising-Heisenberg Model on the Diamond Chain with Spin-1/2", Czechoslovak Journal of Physics **54**, 579–582 (2004).

[378] H. G. Paulinelli, S. M. de Souza, and O. Rojas, "Thermal entanglement in an orthogonal dimer-plaquette chain with alternating Ising–Heisenberg coupling", Journal of Physics: Condensed Matter **25**, 306003 (2013).

[379] T. Verkholyak and J. Strečka, "Exact solution for a quantum spin-$\frac{1}{2}$ Ising-Heisenberg orthogonal-dimer chain with Heisenberg intradimer and Ising interdimer interactions", Physical Review B **88**, 134419 (2013).

[380] A. Nandy, "Analytical Study of Quasi-One-Dimensional Flat Band Networks and Slow Light Analogue", Acta Physica Polonica A **136**, 164–173 (2019).

[381] O. Rojas, J. Strečka, M. L. Lyra, and S. M. de Souza, "Universality and quasicritical exponents of one-dimensional models displaying a quasitransition at finite temperatures", Physical Review E **99**, 042117 (2019).

[382] L. Gálisová, J. Strečka, T. Verkholyak, and S. Havadej, "Magnetization plateaus and bipartite entanglement of an exactly solved spin-1/2 Ising-Heisenberg orthogonal-dimer chain", Physica E: Low-dimensional Systems and Nanostructures **125**, 114089 (2021).

[383] B. Douçot and J. Vidal, "Pairing of Cooper Pairs in a Fully Frustrated Josephson-Junction Chain", Physical Review Letters **88**, 227005 (2002).

[384]   C. Danieli, A. Andreanov, T. Mithun, and S. Flach, "Quantum caging in interacting many-body all-bands-flat lattices", Physical Review B **104**, 085132 (2021).

[385]   A. Metavitsiadis, A. Pidatella, and W. Brenig, "Thermal transport in a two-dimensional Z2 spin liquid", Physical Review B **96**, 205121 (2017).

[386]   A. M. Marques, L. Madail, and R. G. Dias, "One-dimensional 2^n-root topological insulators and superconductors", Physical Review B **103**, 235425 (2021).

[387]   A. Morningstar, V. Khemani, and D. A. Huse, "Kinetically constrained freezing transition in a dipole-conserving system", Physical Review B **101**, 214205 (2020).

[388]   V. Oganesyan and D. A. Huse, "Localization of interacting fermions at high temperature", Physical Review B **75**, 155111 (2007).

[389]   Y. Y. Atas, E. Bogomolny, O. Giraud, and G. Roux, "Distribution of the Ratio of Consecutive Level Spacings in Random Matrix Ensembles", Physical Review Letters **110**, 084101 (2013).

[390]   P. A. McClarty, M. Haque, A. Sen, and J. Richter, "Disorder-free localization and many-body quantum scars from magnetic frustration", Physical Review B **102**, 224303 (2020).

[391]   J. Richter and A. Pal, "Anomalous hydrodynamics in a class of scarred frustration-free Hamiltonians", Physical Review Research **4**, L012003 (2022).

[392]   G. Sierra, M. A. Martín-Delgado, S. R. White, D. J. Scalapino, and J. Dukelsky, "Diagonal ladders: A class of models for strongly coupled electron systems", Physical Review B **59**, 7973–7989 (1999).

[393]   M. Daumann, R. Steinigeweg, and T. Dahm, "Many-body localization in translationally invariant diamond ladders with flat bands", Physical Review B **108**, 045129 (2023).

[394]   D. N. Page, "Average entropy of a subsystem", Physical Review Letters **71**, 1291–1294 (1993).

[395]   Z. Papić, "Weak Ergodicity Breaking Through the Lens of Quantum Entanglement", in *Entanglement in spin chains: from theory to quantum technology applications* (Springer International Publishing Cham, 2022), pp. 341–395.

[396]   A. A. Lopes and R. G. Dias, "Interacting spinless fermions in a diamond chain", Physical Review B **84**, 085124 (2011).

[397]   Y. Kuno, T. Mizoguchi, and Y. Hatsugai, "Interaction-induced doublons and embedded topological subspace in a complete flat-band system", Physical Review A **102**, 063325 (2020).

[398]   M. Rigol, V. Dunjko, V. Yurovsky, and M. Olshanii, "Relaxation in a Completely Integrable Many-Body Quantum System: An Ab Initio Study of the Dynamics of the Highly Excited States of 1D Lattice Hard-Core Bosons", Physical Review Letters **98**, 050405 (2007).

[399]   T.-L. Ho and V. B. Shenoy, "Binary Mixtures of Bose Condensates of Alkali Atoms", Physical Review Letters **77**, 3276–3279 (1996).

[400] M. Guilleumas, B. Juliá-Díaz, M. Melé-Messeguer, and A. Polls, "Josephson tunneling of binary mixtures of spinor BECs", Laser Physics **20**, 1163–1168 (2010).

[401] M. Melé-Messeguer, B. Juliá-Díaz, M. Guilleumas, A. Polls, and A. Sanpera, "Weakly linked binary mixtures of $F = 1$ ^{87}Rb Bose–Einstein condensates", New Journal of Physics **13**, 033012 (2011).

[402] M. Melé-Messeguer, B. Juliá-Díaz, M. Guilleumas, and A. Polls, "Two component bosonic Josephson junctions in elongated traps", Molecular Physics **109**, 2763–2771 (2011).

[403] S. M. Zhang and L. Jin, "Localization in non-Hermitian asymmetric rhombic lattice", Physical Review Research **2**, 033127 (2020).

[404] S. M. Zhang and L. Jin, "Non-Hermitian Aharonov-Bohm Cage", (2020), arXiv:2005. 01044.